University of Cincinnati

Date: 4/15/2015

I, Wei Zeng , hereby submit this original work as part of the requirements for the degree of Doctor of Philosophy in Engineering Mechanics.

It is entitled:

Advanced Development of Smoothed Finite Element Method (S-FEM) and Its Applications

Student's name: **Wei Zeng**

This work and its defense approved by:

Committee chair: Guirong Liu, Ph.D.

Committee member: Shaaban Abdallah, Ph.D.

Committee member: Yijun Liu, Ph.D.

Committee member: Francesco Simonetti, Ph.D.

16146

Advanced Development of Smoothed Finite Element Method (S-FEM) and Its Applications

A dissertation submitted to the
Graduate School
of the University of Cincinnati
in partial fulfillment of the
requirements for the degree of

Doctor of Philosophy

in the Department of Aerospace Engineering and Engineering Mechanics
of the College of Engineering and Applied Science

April 2015
by

Wei Zeng

M.S., Hunan University, 2008
B.S., Hunan University, 2005

Committee: Dr. G.R. Liu, Dr. S. Abdallah
Dr. Y.J. Liu, Dr. F. Simonetti

Abstract

The smoothed finite element method (S-FEM) was recently proposed to bring softening effects into and improve the accuracy of the standard FEM. In the S-FEM, the system stiffness matrix is obtained using strain smoothing technique over the smoothing domains associated with cells, nodes, edges or faces to establish models of desired properties. In this dissertation, it will introduce several aspects of advanced development and applications of S-FEM in solid mechanics. The idea, main work and contribution are included in four aspects as following:

(1) A Generalized Stochastic Cell-based S-FEM (GS_CS-FEM): The cell-based S-FEM is extended for stochastic analysis based on the generalized stochastic perturbation technique. Numerical examples are presented and the obtained results are compared with the solution of Monte Carlo simulations. It is found that the present GS_CS-FEM method can improve the solution accuracy with high-efficiency for stochastic problems with large uncertainties.

(2) An effective fracture analysis method based on the VCCT implemented in CS-FEM: The VCCT is formulated in the framework of CS-FEM for evaluating SIF's and for modeling the crack propagation in solids. The one-step-analysis approach of the VCCT is utilized based on the assumption of stress field equivalence under infinitesimal perturbations. The significant feature of the present approach is that it requires no domain integration but attains same level of accuracy compared to the standard FEM using the interaction integral method. Numerical examples are provided to validate the effectiveness of fracture parameter evaluation as well as to predict the crack growth trajectories.

(3) Smoothing techniques based crystal plasticity finite element modeling of crystalline materials: A framework and numerical implementation for modeling anisotropic crystalline plasticity using strain smoothing techniques is presented to model anisotropic crystalline plasticity with rate-independence. The edge-based strain smoothing technique is extended to deal with finite strains in a nonlinear incremental integration procedure based on the Newton-Raphson scheme. Several representative examples are studied to demonstrate the capability of proposed method as well as the integration algorithm for capturing the strain localization and dealing with plastic incompressibility. The proposed method is also implemented to explore the mesoscopic and macroscopic elaso-plastic behavior of polycrystalline aggregates.

(4) A novel beta finite element method (βFEM) of coupled edge/face and node based smoothing techniques: Smoothing domains generated upon both edges (faces for 3D) and nodes are employed to construct a smoothed model. In this work, a novel S-FEM is proposed, in which an adjustable parameter β is introduced to control the ratio of the area of edge-based/face-based and node-based smoothing domains. It is found that the nearly exact solution in strain energy can be obtained by tuning the parameter, making use of the important property that the exact solution is bonded by the solutions of ES/FS-FEM and NS-FEM. A number of examples have shown that the developed βFEM method is found to be ultra-accurate, insensitive to mesh quality, temporal stable and capable for modeling complex geometry and offers alleviation of volumetric locking. The βFEM is also applied in modeling crystal plasticity with monocrystalline, bi-crystalline and polycrystalline materials.

Acknowledgements

I would like to thank Professor Guirong Liu, my academic advisor and the chair of my doctoral committee, for his motivation, guidance and suggestions. I would also like to thank Professor Shaaban Abdallah, Professor Yijun Liu, Dr. Francesco Simonetti and Dr. Grant Schaffner for serving as my committee members and for their time and valuable suggestions in my oral exam and final defense.

Furthermore, I would like to acknowledge the financial support provided by the UC P&G Simulation Center. I am especially grateful to my P&G advisor Mr. Russel Clem, and to Dr. Brent Rudd, Mr. Fred Murrell and Dr. Kelly Anderson, for their career advice.

In addition, I want to thank all my colleagues and friends at our research laboratory at the University of Cincinnati for their friendship. I am also very thankful to the friends and people at the Department of Aerospace Engineering and Engineering Mechanics. My special thanks goes to Mr. Robert Ogden for his assistance and help.

Finally, I would like to take this opportunity to express my greatest appreciation to my parents and my family for their consistent love, support and encouragement.

Contents

List of Figures

List of Tables

Chapter 1. Introduction

In essence, the finite element method (FEM) or also termed as the finite element analysis (FEA), is a numerical technique for solving field problems. A field problem could be the displacement field or the stress field in stress analysis, or be temperature field or the heat flux in thermal analysis, or even be the stream function or the velocity potential function in fluid flow analysis, and so on. Usually an actual physical problem with certain boundary conditions specified over arbitrary two- and three-dimensional domain would be very difficult or unable to find the exact/analytical solution or sometimes even an approximate solution. The basic idea of FEM is to find the approximate solution of a complicated problem through a simpler numerical approach.

Before an analysis is carried out, the problem domain has to be discretized into a set of discrete, non-overlapping subdomains, usually called finite elements. In each element a continuous function of an unknown field variable/quantity is approximated by simple local functions, generally described by polynomials. Elements are connected at points called nodes, at which the unknowns are then the discrete values of the field variable [1]. The elements are arranged and collected to one another according to some proper principles, which construct the FEM mesh, or named grid interchangeably. This process can be represented numerically by a system of simultaneous algebraic equations to be solved for unknowns at nodes. In a mathematical view, firstly, FEM is a numerical means for solving general boundary and/or initial value problems characterized by partial differential equations, which can be applied to various

physical phenomena. Secondly, these general boundary and/or initial value problems are formulated in a so-called weak, or integral form, so as to assemble the contributions of each subdomain to the global integrals and then generate an integral characterizing the problem over the entire problem domain [2]. Moreover, based on the FEM fashion, the approximate solutions can be improved or refined by spending more computational effort, such as using more elements to represent the domain, or increasing the order of the interpolation polynomial, etc.

The stress analysis of elastic solid and structures in civil and aeronautical engineering was the first application area of the finite element method [3]. Indeed, the subdivision of a whole domain into "elements" in FEM can be traced back to the earlier work on matrix analysis of beams and frames. In the early 1960s, FEM was viewed as sound and versatile, and since then both the theoretical explorations and engineering applications of FEM have been developed and extended explosively. Its various areas of application contain structural engineering, mechanical and aeronautical engineering, material engineering, fluid mechanics, biomechanics, soil mechanics, thermodynamics, electromagnetism, and so on.

Though FEM has been widely used as a reliable numerical tool, standard FEM still exists several inherent issues. The first issue is the well-known overly stiff behavior of a fully compatible FEM model of displacement based on the Galerkin weak form, which may cause the shear and volumetric locking problems in some cases. The second is the instability, inaccuracy and locking phenomenon for large deformation problems involving severe mesh distortion. Large deformation problems and other varying configuration problems (e.g., crack propagations) are often solved with some adaptive mesh regeneration/rezoning method. But it is impossible to remesh arbitrary deformed 2D or 3D domains with quadrilateral (Q4) or hexahedral (H8) elements automatically. Only T-mesh, i.e., triangular (T3) elements for 2D or tetrahedral (T4)

elements for 3D, can be generated and refined quickly and easily without much manual operations, even for complicated or arbitrary deformed shapes of geometry. Then another issue arises: T-mesh models often suffer from poor accuracy: excessive stiffness in shearing/bending, sensitivity of mesh distortion and the entire mesh behaves rigidly (or "locked") especially in incompressible materials, etc. This is the reason for analysts to be warned when opting for T-mesh or adopting high percentage of T-mesh elements in some commercial software packages.

1.1 Background and Motivation

The main reason of the accuracy issues such as overly stiff behavior are attributed to the nature of the fully compatible displacement approach based on the standard variational principle [4]. Many numerical strategies have been sought to resolving these issues, for example, hybrid FEM techniques [5] and mesh-free methods [6]. These remedial methods are able to treat different kinds of problems with remarkable accuracy. However, for hybrid FEM, there is no sufficient formulation for triangular/tetrahedral presented so far; for mesh-free methods, the programming efforts and costs of computing are much more expensive than FEM and it still has a long way to be commercialized and solve large-scale practical problems.

By examining FEM and mesh-free methods, a smoothed FEM (or S-FEM) was formulated through combining the FEM procedures and a generalized gradient smoothing (GGS) technique for discontinuous functions by Liu et al [7,8] recently. S-FEM was proposed as a special linear version of smoothed point interpolation methods, theoretically founded by the generalized smoothed Galerkin weak form (it can be named as "weakened weak form", or W2 form) on G space theory [4]. The essential idea in the S-FEM is to utilize a standard finite

element mesh (in particular T-mesh) to build numerical models with good performance [9]. This is performed by modifying/constructing the compatible strain field in a Galerkin weak form model to deliver some good properties. Other than element based implementation in standard FEM, the S-FEM techniques evaluate the weak form based on smoothing domains, which can be located within the elements: CS-FEM [7,10], but more often beyond elements: acquiring the information from the adjacent elements, such as NS-FEM, ES-FEM and FS-FEM [11–13]. And the strain field has naturally to satisfy certain conditions such as linear independence to guarantee the stability and convergence for the W2 scheme.

Compared to the standard linear displacement finite element method (LFEM), S-FEM can overcome some inherited drawbacks exhibited in LFEM, such as stress inaccuracies [4], sensitivity to element distortion [14], unstable/volumetric locking phenomena [15–16], etc. Detailed theoretical aspects including properties of stability and convergence about S-FEM can be found in [9,17]. Various kinds of S-FEM models have been applied to a wide class of practical mechanics problems such as vibration [11], acoustic [18], plates and shells [19–21], fracture mechanics [22–24], piezoelectricity [25], viso-elasto [26], limit and shakedown analysis [27], contact problems [28,29], fluid–structure interaction [30,31], etc.

Different kinds of S-FEM models may possess different properties and it has been proved that they can solve different specific problems. Generally, numerical investigations have shown that S-FEM models have some features/merits compared to the standard FEM using linear elements. For example, (1) S-FEM models are created using the linear PIM for assuming the displacement field without isoparametric mapping; (2) field gradients are computed directly using shape functions themselves, other than the shape function derivatives; (3) As long as a minimum number of linearly independent smoothing domains are adopted, the S-FEM models

are proved to be stable and convergent [32]; (4) S-FEM models generate desiredly more accurate outcomes and higher convergence rates than those of FEM in displacement solution or stress solution or both, as the stiffness of S-FEM is softer than that of FEM; (5) S-FEM models are displacement-like models using the same background mesh or DoF's of corresponding FEM, and many existing algorithms of FEM are compatible or easily extended and applied to S-FEM [33].

Since these good features already have been discussed for S-FEM models in the past few years, it deserves to explore new S-FEM models or extend the possible application areas of some available S-FEM approaches, especially in computational solid mechanics. In this work, it will develop and extend S-FEM in stochastic analysis, fracture mechanics, and modeling crystal plasticity. And most importantly, an ultra-accurate and most versatile S-FEM approach so far will be proposed and developed for solid mechanics. A large number of examples will be provided to illustrate the numerical implementations, verify or confirm the numerical models, and show the applications in various areas, including stochastic problems, frature parameter evaluations, prediction of crack growth trajectories, simulation of crystalline behavior, static, dynamic, linear and nonlinear problems, etc. Due to the limit of the length of the thesis, it will focus several aspects in mechanics based on the crucial properties already obtained in S-FEM, such as accuracy, insensitive to mesh quality, temporal stability and capabilty for modeling objects with complex geometry and alleviation of volumetric locking, and so on.

1.2 Study Outline

The work is organized in eight chapters. A brief introduction, research background and motivation are given in chapter 1. A brief introduction of historical background, governing

equations and general steps of FEM are presented in chapter 2. The general formulations of strain smoothing operations, numerical procedure and general properties of S-FEM are introduced in Chapter 3. Chapter 4 presents a generalized stochastic cell-based smoothed finite element method (GS_CS-FEM) for stochastic analysis. The solution accuracy and efficiency will be compared with those obtained from Monte Carlo simulation. Chapter 5 introduces an effective fracture analysis method for evaluating SIF's and modeling the crack propagation, which is based on the virtual crack closure-integral technique (VCCT) implemented in CS-FEM scheme. Chapter 6 proposes the framework of smoothed technique based crystal plasticity finite element method for modeling of rate-independent crystalline materials. The method will be demonstrated by the capability of modeling strain localization and dealing with plastic incompressibility of single crystals. It would be also implemented to explore the mechanical behavior of polycrystalline aggregates. Chapter 7 develops a novel class of smoothing techniques based beta finite element method (βFEM) for both 2D and 3D mechanics problems. Some attractive features are expected to be found numerically, such as high accuracy, insensitivity to mesh quality, immunity of volumetric locking, temporal stability and capability for modeling complex geometry. Then the proposed βFEM is performed to simulate crystal plasticity for monocrystalline, bi-crystalline and polycrystalline materials. Finally, a brief summary is included in the last chapter.

References

[1] Liu GR and Quek SS. 2003. The finite element method: A practical course. Butterworth-Heinemann, Oxford.

[2] Oden JT and Reddy JN. 1976. An introduction to the mathematical theory of finite elements. John Wiley and Sons, New York.

[3] Stein E, Borst R de, and Hughes T JR. 2004. Encyclopedia of computational mechanics. Volume 2. Solid and structures. John Wiley and Sons, New York.

[4] Liu GR. 2010. A G space theory and a weakened weak (W2) form for a unified formulation of compatible and incompatible methods: Part I theory and Part II applications to solid mechanics problem. International Journal for Numerical Methods in Engineering; 81(9): 1093–1156.

[5] Pian THH and Wu CC. 2006. Hybrid and incompatible finite element methods. CRC Press, Boca Raton.

[6] Liu GR. 2009. Meshfree methods: Moving beyond the finite element method, 2nd edition. CRC Press, Boca Raton.

[7] Liu GR, Dai KY, and Nguyen-Thoi T. 2007. A smoothed finite element method for mechanics problems. Computational Mechanics 39; 859–877.

[8] Liu GR and Zhang GY. 2007. Upper bound solution to elasticity problems: A unique property of the linearly conforming point interpolation method (LC-PIM). International Journal for Numerical Methods in Engineering; 74: 1128–1161.

[9] Liu GR and Nguyen-Thoi T. 2010. Smoothed finite element methods. CRC Press (Taylor & Francis), Boca Raton.

[10] Liu GR, Zeng W, and Nguyen-Xuan H. 2013. Generalized stochastic cell-based smoothed finite element method (GS CS-FEM) for solid mechanics. Finite Elements in Analysis and Design; 63(0): 51–61.

[11] Liu GR, Nguyen-Thoi T, and Lam KY, 2009. An edge-based smoothed finite element method (ES-FEM) for static, free and forced vibration analyses of solids. Journal of Sound and Vibration; 320(45): 1100–1130.

[12] Liu GR, Nguyen-Thoi T, Nguyen-Xuan H., and Lam KY. 2009. A node-based smoothed finite element method (NS-FEM) for upper bound solutions to solid mechanics problems. Computers and Structures; 87(12): 14–26.

[13] Nguyen-Thoi T., Liu GR, Lam KY, and Zhang GY. 2009. A face-based smoothed finite element method (FS-FEM) for 3D linear and geometrically non-linear solid mechanics problems using 4-node tetrahedral elements. International Journal for Numerical Methods in Engineering; 78(3): 324–353.

[14] Dai KY and Liu GR. 2007. Free and forced vibration analysis using the smoothed finite element method (SFEM). Journal of Sound and Vibration; 301(35): 803–820.

[15] Nguyen-Xuan H, Liu GR, Thai-Hoang C, and Nguyen-Thoi T. 2010. An edge-based smoothed finite element method (ES-FEM) with stabilized discrete shear gap technique for analysis of reissnermindlin plates. Computer Methods in Applied Mechanics and Engineering; 199(912): 471–489.

[16] Chen L, Zhang YW, Liu GR, Nguyen-Xuan H, and Zhang ZQ. 2012. A stabilized finite element method for certified solution with bounds in static and frequency analyses of piezoelectric structures. Computer Methods in Applied Mechanics and Engineering; 241-244(0): 65–81.

[17] Dai KY, Liu GR, and Nguyen TT. 2007. An n-sided polygonal smoothed finite element method (nSFEM) for solid mechanics. Finite Elements in Analysis and Design; 43: 847–860.

[18] He ZC, Liu GR, Zhong ZH, Zhang GY, and Cheng AG. 2010. Coupled analysis of 3D structural-acoustic problems using the edge-based smoothed finite element method/finite element method. Finite Elements in Analysis and Design; 46: 1114–1121.

[19] Nguyen-Xuan H, Rabczuk T, Bordas S, and Debongnie JF. 2008. A smoothed finite element method for plate analysis. Computer Methods in Applied Mechanics and Engineering; 197: 1184–203.

[20] Nguyen-Thanh N, Rabczuk T, Nguyen-Xuan H, and Bordas S. 2008. A smoothed finite element method for shell analysis. Computer Methods in Applied Mechanics and Engineering;198: 165–177.

[21] Cui XY, Liu GR, Li GY, Zhao X, Zhang GY, and Zheng G. 2009. Analysis of plates and shells using edge-based smoothed finite element method. Computational Mechanics; 45: 141–156.

[22] Liu GR, Nourbakhshnia N, and Zhang YW. 2011. A novel singular ES-FEM method for simulating singular stress fields near the crack tips for linear fracture problems. Engineering Fracture Mechanics; 78: 863–876.

[23] Chen L, Liu GR, Jiang Y, Zeng K, and Zhang J. 2011. A singular edge-based smoothed finite element method (ES-FEM) for crack analyses in anisotropic media. Engineering Fracture Mechanics; 78: 85–109.

[24] Nguyen-Xuan H, Liu GR, Nourbakhshnia N, Chen L. 2012. A novel singular ES-FEM for crack growth simulation. Engineering Fracture Mechanics; 84: 41–46.

[25] Nguyen-Xuan H., Liu GR, Nguyen-Thoi T, and Nguyen-Tran C. 2009. An edge-based smoothed finite element method for analysis of two dimensional piezoelectric structures. Smart Materials and Structures; 18(6): 065015.

[26] Nguyen-Thoi T, Liu GR, Vu-Do HC, and Nguyen-Xuan H. 2009. An edge-based smoothed finite element method (ES-FEM) for visco-elastoplastic analyses in 2D solids using triangular mesh. Computational Mechanics; 45: 23-44.

[27] Tran TN, Liu GR, Nguyen-Xuan H, and Nguyen-Thoi T. 2010. An edge-based smoothed finite element method for primal-dual shakedown analysis of structures. International Journal for Numerical Methods in Engineering; 82: 917–938.

[28] Li Y, Liu GR, and Zhang GY. 2011. An adaptive NS/ES-FEM approach for 2D contact problems using triangular elements. Finite Elements in Analysis and Design; 47: 256–275.

[29] Kumar V and Metha R. 2013. Impact simulations using smoothed finite element method. International Journal of Computational Methods; 10(4): 1350012.

[30] He ZC, Liu GR, Zhong ZH, Zhang GY, and Chen AG. 2011. A coupled ES-FEM/BEM method for fluid–structure interaction problems. Engineering Analysis with Boundary Elements. 35: 140–147.

[31] Nguyen-Thoi T, Phung-Van P, Nguyen-Hoang S, and Lieu-Xuan Q. 2014. A coupled alpha-FEM for dynamic analyses of 2D fluid–solid interaction problems. Journal of Computational and Applied Mathematics; 271(1): 130–149.

[32] Liu GR, Nguyen-Xuan H, and Nguyen-Thoi T. 2010. A theoretical study on the smoothed FEM (S-FEM) models: Properties, accuracy and convergence rates. International Journal for Numerical Methods in Engineering; 84(10): 1222–1256.

[33] Liu GR, Nguyen TT, Dai KY and Lam KY. 2007. Theoretical aspects of the smoothed finite element method (SFEM), International Journal for Numerical Methods in Engineering; 72(1): 902–930.

Chapter 2. Brief Introduction of the Finite Element Method

Mathematically, the governing equations in FEM are integrated over each finite element and the contributions of each element to the global integrals will be summed or assembled over the whole problem domain. As the FEM has a long history of development, it has various ways of formulating the properties of individual elements. Basically it has three different approaches: direct approach, variational approach and weighted residuals approach. The direct approach establishes the element properties in terms of relevant variables. It was originated from the direct stiffness method of structural analysis and is only applicable to some simple problems [1]. The variational approach involves calculus of variations and extremizing a functional, including the potential energy, complementary enegry, or some variant forms formulated from physical or engineering problems. This is the most popular and widely used method and the displacement-based standard FEM introduced in this thesis for solid mechanics is also regarded to rely on the minimum potential energy principle. The weighted residual approach derives the governing equations of the problem directly and proceeds without any need of a variational statement. This method is versatile and widely used for nonstructural areas such as fluid mechanics and heat transfer. This is mainly because it offers the most general procedure to derive the FE equations and extends the FEM to the problems in which the functional(s) is/are not available [2]. It contains four main categories of weight or test functions applied in this method: subdomain method, collocation method, least squares method and Galerkin method. In this chapter, a brief history, governing equations, variational formulations and general procedures of the FEM will be introduced.

2.1 Historical Background

The idea and concept of FEM is traceable to several centuries ago, e.g., ancient mathematicians used a polygon to approximate the circumference of a circle. The exact date of the origination of modern FEM is difficult to know, and its development can be traced back to several independent research groups in the fields of applied mathematics, physics or engineering: Courant [3], Synge [4], Argyris and Kelsey [5,6] and Feng [7,8]. The applied mathematicians wanted to find numerical methods for partial differential equations (PDE's), and the corresponding convergence, error estimation, etc. The physicists were motivated by how to find piecewise approximate functions to represent their continuous functions for boundary value problems (BVP's) in continuum mechanics. While in engineering, people were interested in the structural analysis of rods, beams and frames [5,9].

The phrase "finite element" was first coined and introduced by Clough [10] in 1960 for plane stress analysis using both triangle and rectangular elements. Later, Melosh [11] developed rectangular-plate bending-element stiffness matrix for thin plates in bending in 1961. Grafton and Strome [12] then proposed the curved-shell bending element stiffness matrix for analysis of axisymmetric shells in 1963. In 1960s, the FEM was extended to three-dimensional (3D) problems by Martin [13], Gallagher et al. [14], Melosh [15], Argyris [16], Clough and Rashid [17], Wilson [18], etc. It was also widely developed to treat large deflection and thermal analysis by Turner et al. [19], material nonlinearities by Gallagher et al. [14], buckling problems by Gallagher and Padlog [20], dynamic analysis [21] and visco-elasticity problems by Zienkiewicz et al. [22].

On the applications of general field problems, including fluid flow, heat transfer and other areas, we can refer to the work presented by Zienkiewicz and Cheung [23], Martin [24], and Wilson and Nickel [25]. Researchers then found the FE equations can be derived by utilizing a weighted residual approach such as the Galerkin method [26] or the least squares method [27,28]. Many practitioners of the FEM are now apt to adopt Galerkin's method to establish the approximations for the governing equations. And this approach is widely extended to nonstructural applications, especially to the problems where the functional(s) is/are not available.

Belytschko [29,30] explored the efficient large-scale nonlinear dynamic analysis by FE programs. Besides, much of the early work on nonlinear problems can be found in Oden [31], and Hughes [32,33] and Simo [34] presented a few models for inelastic and finite deformation problems. A brief history of the early development of the FEM can be found in Gupta and Meek [35]. In the past half century, enormous advances for various types of FEMs have been made in most engineering disciplines and lots of applied sciences. Today, we can find hundreds of books and numerous papers that deal with the basic theory, applied mathematics, product design, and applications to structure and solid, fluid mechanics, heat transfer, electromagnetics, bioengineering, and so on [24, 36–47].

2.2 General Procedures of the FEM

This section presents the procedures of FEM for the continuum problem. For simplicity's sake, only the general steps for solid mechanics problems will be summarized as follows.

Step 1 Establish the Weak Form

The strong form, i.e., governing partial differential equations (PDEs) for solid mechanics problems, requires strong continuity on the displacement field variables. The trial approximation functions defined the field variables (e.g., displacement in solid mechanics) in strong form have to be differentiable up to the highest order of the PDEs. This is not always efficient and there may not be smooth (classical) solutions to a particular problem because of the requirement for the strong continuity, especially for complex domains/boundary conditions and/or different material interfaces, etc. In order to overcome these difficulties the weak forms are preferred in FEM. Weak forms reduce the continuity requirements (the order of differentiation) on the trial functions thereby allowing the use of easy-to-construct and implement polynomials including the widely used Lagrange polynomials. In solid mechanics, such a weak form can be derived from the well-known principle of minimum potential energy and the Neumann boundary conditions would be naturally satisfied.

Step 2 Discretize the Continuum and Select the Element Types

Once the weak form has been established, the problem domain/region will be divided into elements according to a certain discretization or called meshing guidelines. The total amount, type, size and arrangement of the elements are decided by specific engineering or physical purposes. By and large, a fine mesh with more elements may match the geometry more accurately and give more accurate or usable results but may consume more computational resources. Designers/analysts can create an appropriate mesh for a particular problem with mesh-generation programs or some pre-processor software according to their experience and engineering judgement.

Step 3 Select Shape Functions

Since the displacement solution of a complex problem is not easy to obtain exactly, we assume some proper functions expressed in terms of the nodal unknowns within an element to approximate the solution. They are named as “shape functions” as they define the “shape” of the variation of the displacements within the element if the nodal displacements are given. Linear, quadratic, and cubic polynomials are often selected as displacement functions because they can be integrated and differentiated easily. The shape functions should satisfy certain requirements such as continuity requirement at the nodes and along the element boundaries, partitions of unity and linear reproducibility [48].

Step 4 Define the Constitutive Relations

To derive the equations for each finite element, it is necessary to define the stress/strain relationship, or generally called the constitutive relations. For linear materials, the constitutive relation is the commonly known Hooke's law. And it would be involved to define the constitutive models to describe the response behavior of other materials such as viscoelastic, plastic, hyperelastic materials, etc.

Step 5 Find the Characteristic Element Properties

Once the weak form, shape functions and constitutive relations are formulated/defined, we are ready to determine the characteristic matrices (stiffness, mass) and vectors (force, etc.) expressing the properties of the individual elements. They can be derived by three different approaches as mentioned: direct approach, variational approach and weighted residuals approach.

Step 6 Assemble the System/Global Equations from Element Equations

This step involves the assemblage of element equations to generate the overall equilibrium equations. The individual element properties, such as stiffness and mass matrices and force vectors, obtained from step 5 now can be assembled together as the properties of the overall system using a method of superposition based on nodes. The basis for the assembly procedure stems from the fact that the continuity or compatibility condition ensures the field variable at a node is identical for each element sharing that node and no gaps occurring anywhere in the problem domain.

Step 7 Impose Boundary Conditions (BC's)

Before the system of equations is ready to be solved, proper boundary conditions (or called constraints or supports) have to be imposed into them, which involves modification of the system or the global stiffness matrix and force vectors. This is due to the system stiffness matrix obtained from step 6 is a singular matrix and certain force or displacement BC's should be incorporated so as to ensure the problem is well-posed.

Step 8 Solve the System Equations

The modified system equations determined from step 7 can now be solved to find the nodal displacements, and the function of the displacement field for the overall problem domain will be obtained. For linear problems, the displacement field can be determined easily. For nonlinear or unsteady problems, the solution is time-dependent and may involve the modification of the (tangent) stiffness matrix and/or the force vectors.

Step 9 Solve for Additional Quantities

From the previous computed nodal displacements, if required, the important secondary quantities of element strains and stresses can be calculated as they can be expressed in terms of nodal displacements.

2.3 Brief Description on Governing Equations and Variational Formulations

To illustrate the idea and formulations in a simple way, we consider a 2D static elasticity problem, the governing equation in the problem domain Ω bounded by Γ ($\Gamma = \Gamma_D \bigcup \Gamma_t,\ \Gamma_D \bigcap \Gamma_t = \varnothing$) can be expressed in terms of stresses as

$$\nabla_s^T \cdot \boldsymbol{\sigma} + \mathbf{f}^b = 0 \quad \text{or} \quad \partial_j \sigma_{ij} + f_i^b = 0 \text{ in } \Omega \tag{2.1}$$

subjects to the boundary conditions $\mathbf{u} = \hat{\mathbf{u}}$ on Γ_u and $\boldsymbol{\sigma} \cdot \mathbf{n} = \mathbf{f}^t$ on Γ_t. Here, boundary Γ is consisted of two parts: $\Gamma_{\mathbf{t}}$ where external tractions $\mathbf{t}$ are applied (Neumann conditions), and Γ_D where the displacements $\mathbf{u}$ are prescribed (Dirichlet conditions). $\mathbf{f}^b$ and $\mathbf{f}^t$ denotes the body force and the prescribed traction vector, and $\mathbf{n}$ stands for the outward unit normal vector on the boundary Γ, σ_{ij} denotes the component of stress tensor and f_i^b denotes the component of body force; n_j is the unit vector normal to the boundary Γ. The ∇_s represents a matrix of differential operators given by

$$\nabla_s = \begin{bmatrix} \partial/\partial x & 0 & \partial/\partial y \\ 0 & \partial/\partial y & \partial/\partial x \end{bmatrix}^T \tag{2.2}$$

The relation between strain and displacement or the compatibility equation can be expressed by

$$\boldsymbol{\varepsilon} = \nabla_s \mathbf{u} \tag{2.3}$$

The stress tensor $\boldsymbol{\sigma}$ in Eq. (2.3) is defined in terms of the strain tensor $\boldsymbol{\varepsilon}$ from the constitutive relations:

$$\boldsymbol{\sigma} = \mathbf{D}\boldsymbol{\varepsilon} \tag{2.4}$$

where $\mathbf{D}$ is the Hooke's matrix of elastic constants for a solid which is related to modulus E and Poisson's ratio ν.

Now let us multiply the equilibrium equation (Eq. (2.1)) by an arbitrary test function defined in Hilbert space $\mathbf{v} \in \mathbb{H}_0^1$ and integrate it over the entire problem domain Ω, which leads to

$$\int_\Omega \mathbf{v}^T \nabla_s^T \boldsymbol{\sigma} d\Omega + \int_\Omega \mathbf{v}^T \mathbf{f}^b d\Omega = 0 \tag{2.5}$$

Application of classical differentiation rules together with the divergence theorem and boundary conditions may result in the variational statement

$$\underbrace{\int_\Omega \delta\left(\nabla_s \mathbf{v}\right)^T \mathbf{D}\left(\nabla_s \mathbf{u}\right) d\Omega}_{a(\mathbf{u},\mathbf{v})} - \underbrace{\left(\int_\Omega \delta \mathbf{v}^T \mathbf{f}^b d\Omega + \int_{\Gamma_t} \delta \mathbf{v}^T \mathbf{f}^t d\Gamma\right)}_{f(\mathbf{v})} = 0 \tag{2.6}$$

The above equation is referred to as the principle of the virtual potentials, which would be the basis of the FEM standard discretization procedure for a 2D solid mechanics problem. The discrete solution of the problem described in Eq. (2.1) is then to find $\mathbf{u} \in \mathbb{H}_0^1$ such that the following Galerkin weak form is satisfied

$$a\left(\mathbf{u},\mathbf{v}\right) = f\left(\mathbf{v}\right), \quad \forall \mathbf{v} \in \mathbb{H}_0^1 \tag{2.7}$$

where $a(\mathbf{u},\mathbf{v})$ is a bilinear form of derivatives of functions with the following form

$$a(\mathbf{u},\mathbf{v}) = \int_{\Omega} \delta(\nabla_s \mathbf{v})^T \mathbf{D}(\nabla_s \mathbf{u}) d\Omega \tag{2.8}$$

and $f(\mathbf{v})$ is the linear functional

$$f(\mathbf{v}) = \int_{\Omega} \delta \mathbf{v}^T \mathbf{f}^b d\Omega + \int_{\Gamma_t} \delta \mathbf{v}^T \mathbf{f}^t d\Gamma \tag{2.9}$$

References

[1] Rao SS. 2005. The finite element method in engineering, 4ed edition. Butterworth-Heinemann, Burlington.

[2] Huebner KH, Dewhirst DL, Smith DE, and Byrom TG. 2001. The finite element method for engineers. John Wiley and Sons, New York.

[3] Courant R. 1943. Variational methods for the solution of problems of equilibrium and vibrations. Bulletin of the American Mathematical Society; 49: 1–23.

[4] Synge JL. 1957. The hypercircle in mathematical physics. Cambridge University Press, London.

[5] Argyris JH. 1954. Energy theorems and structural analysis. Aircraft engineering: Part 1; 26.

[6] Argyris JH and Kelsey S. 1954. Energy Theorems and Structural Analysis. Aircraft Engineering: Part 2; 27.

[7] Feng K. 1965. Finite difference schemes based on variational principles (In Chinese). Applied Mathematics and Computational Mathematics; 2: 238–262.

[8] Lax P. 1993. "Feng Kang", Society for Industrial and Applied Mathematics (SIAM News). 26.

[9] Turner MJ, Clough RW, Martin HC, and Topp LJ. 1956. Stiffness and deflection analysis of complex structures. Journal of Aeronautical Sciences; 23: 805–824.

[10] Clough RW. 1960. The finite element method in plane stress analysis. Proceedings, American Society of Civil Engineers, 2nd Conference on Electronic Computation, Pittsburgh; 345–378.

[11] Melosh RJ. 1961. A stiffness matrix for the analysis of thin plates in bending. Journal of the Aerospace Sciences; 28(1): 34–42.

[12] Grafton PE and Strome DR. 1963. Analysis of axisymmetric shells by the direct stiffness method. Journal of the American Institute of Aeronautics and Astronautics; 1(10): 2342–2347.

[13] Martin HC. 1961. Plane elasticity problems and the direct stiffness method. The Trend in Engineering. 13: 5–19.

[14] Gallagher RH, Padlog J, and Bijlaard PP. 1962. Stress analysis of heated complex shapes. Journal of the American Rocket Society; 32: 700–707.

[15] Melosh RJ. 1963. Structural analysis of solids. Journal of the Structural Division, Proceedings of the American Society of Civil Engineers; 205–223.

[16] Argyris JH. 1964. Recent advances in matrix methods of structural analysis. In *Progress in Aeronautical Science*; 4. Pergamon Press, New York.

[17] Clough RW and Rashid Y. 1965. Finite element analysis of axisymmetric solids. Journal of the Engineering Mechanics Division, Proceedings of the American Society of Civil Engineers; 91: 71–85.

[18] Wilson EL. 1965. Structural analysis of axisymmetric solids. Journal of the American Institute of Aeronautics and Astronautics; 3(12): 2269–2274.

[19] Turner MJ, Dill EH, Martin HC, and Melosh RJ. 1960. Large deflections of structures subjected to heating and external loads. Journal of Aeronautical Sciences; 27(2): 97–107.

[20] Gallagher RH and Padlog J. 1963. Discrete element approach to structural stability analysis. Journal of the American Institute of Aeronautics and Astronautics; 1(6): 1437–1439.

[21] Archer JS. 1965. Consistent matrix formulations for structural analysis using finite-element techniques. Journal of the American Institute of Aeronautics and Astronautics; 3(10): 1910–1918.

[22] Zienkiewicz OC, Watson M, and King IP. 1968. A numerical method of visco-elastic stress analysis. International Journal of Mechanical Sciences; 10: 807–827.

[23] Zienkiewicz OC and Cheung YK. 1965. Finite elements in the solution of field problems. The Engineer; 507–510.

[24] Martin HC. 1968. Finite element analysis of fluid flows. Proceedings of the Second Conference on Matrix Methods in Structural Mechanics, Wright-Patterson Air Force Base, Ohio; 517–535.

[25] Wilson EL and Nickel RE. 1966. Application of the finite element method to heat conduction analysis. Nuclear Engineering and Design; 4: 276–286.

[26] Szabo BA and Lee GC. 1969. Derivation of stiffness matrices for problems in plane elasticity by Galerkin's method. International Journal of Numerical Methods in Engineering. 1: 301–310.

[27] Fix GJ, Gunzburger MD, and Nicolaides MA. 1979. On finite element methods of the least squares type. Computers and Mathematics with Applications; 5(2): 87–98.

[28] Hughes TJR, Franca LP, and Hulbert GM. 1989. A new finite element formulation for computational fluid dynamics: VIII. The Galerkin least squares method for advective-diffusive equations. Computer Methods in Applied Mechanics and Engineering; 73: 173–189.

[29] Belytschko T. 1976. A survey of numerical methods and computer programs for dynamic structural analysis. Nuclear Engineering and Design; 37(1): 23–34.

[30] Belytschko T. 1976. Efficient large-scale nonlinear transient analysis by finite elements. International Journal of NumericalMethods in Engineering; 10(3): 579–596.

[31] Oden JT. 1972. Finite elements of nonlinear continua. McGraw-Hill, New York.

[32] Hughes TJR. 1980. Generalization of selective integration procedures to anisotropic and nonlinear media. International Journal for Numerical Methods in Engineering; 15: 1413–1418.

[33] Hughes TJR. 1984. Numerical implementation of constitutive models: Rate-independent deviatoric plasticity. In Theoretical Foundations for Large Scale Computations of Nonlinear Material Behavior, Eds., Nemat-Nasser S, Asaro R, and Hegemier G. Martinus Nijhoff Publishers, Dordrecht (The Netherlands); 29–57.

[34] Simo JC. 1987. A J2-flow theory exhibiting a corner-like effect and suitable for large-scale computation. Computer Methods in Applied Mechanics and Engineering; 62: 169–194.

[35] Gupta KK and Meek JL. 1996. A brief history of the beginning of the finite element method. International Journal for Numerical Methods in Engineering; 39: 3761–3774.

[36] Aziz AK. 1972. The mathematical foundations of the finite element method with applications to partial differential equations. Academic Press, New York.

[37] Oden JT and Reddy JN. 1976. An introduction to the mathematical theory of finite elements. Wiley, New York.

[38] Ladeveze P and Leguillon D. 1983. Error estimate procedure in the finite element method and applications. SIAM Journal on Numerical Analysis; 20: 485–509.

[39] Huiskies R and Chao EYS. 1983. A survey of finite element analysis in orthopedic biomechanics: The first decade. Journal of Biomechanics; 16(6): 385–409.

[40] Hughs TJR. 1987. The finite element method: Linear static and dynamic finite element analysis. Prentice-Hall, Englewood Cliffs.

[41] Silvester PP and Ferrari RL. 1990. Finite elements for electrical engineers. 2nd edition. Cambridge University Press, Cambridge.

[42] Jin JM. 1993. The finite element method in electromagnetics. Wiley, New York.

[43] Zhong ZH. 1993. Finite element procedures for contact-impact problems. Oxford University Press, Oxford.

[44] Salon SJ. 1995. Finite element analysis of electrical machines. Kluwer, Boston.

[45] Bathe KJ. 1996. Finite element procedures. Prentice-Hall, Englewood Cliffs.

[46] Logan DL. 2002. A first course in the finite element method, 3rd edition. Thomson Learning Inc. Pacific Grove, CA.

[47] Zienkiewicz OC, Taylor RL, and Zhu JZ. 2005. The finite element method: Its basis and fundamentals, 6th edition. Butterworth-Heinemann, Burlington.

[48] Liu GR, Quek SS. 2003. The finite element method: A practical course. Butterworth-Heinemann, Oxford.

Chapter 3. Fundamental Theories of the Smoothed Finite Element Method (S-FEM)

In some meshfree methods, sometimes the derivatives of the shape functions vanish at the nodes, which result in spurious modes [1,2]. To eliminate such spatial instability in nodal integration, the strain smoothing technique (SST) was introduced by Chen et al [3] and later extended by Yoo and Moran [4] to the natural element method (NEM). The SST applied in Galerkin mesh-free methods in [1] involves the moving least-squares (MLS) and reproducing kernel approximations. Subsequently, the so-called weakened weak (W2) formulation based on the G space theory [5] was developed by extending the gradient smoothing technique to a class of discontinuous shape functions. The strain is expressed as the divergence of a spatial average of the standard (compatible) strain field, i.e. symmetric gradient of the displacement field [2].

This chapter will introduce the general formulations, procedures, theoretical aspects and properties of strain smoothing techniques [6]. The discussions here are mainly performed for 2D problems. The extension to three-dimensional (3D) domains, if necessary, will be presented in next few chapters.

3.1 General Formulations

3.1.1 Local Gradient Smoothing Operation

The smoothing techniques were widely applied in computational mechanics, such as the nonlocal continuum mechanics to consider the size effects [7], and smoothed particle hydrodynamics (SPH) [8,9] to approximate field functions. The strain smoothing technique (SST) is the most frequently utilized technique to modify the compatible strain field, i.e., the strain is expressed as the divergence of a spatial average of the standard (compatible) strain field. In a compatible model, the standard (compatible) strain can be evaluated by the assumed displacement field $\mathbf{u}^h(\mathbf{x})$,

$$\boldsymbol{\varepsilon}^h(\mathbf{x}) = \nabla_s \mathbf{u}^h(\mathbf{x}) \tag{3.1}$$

The strain smoothing operation is carried out over the so-called local smoothing domain which can be created within elements but more often beyond the elements. The smoothed strain field $\tilde{\boldsymbol{\varepsilon}}_k$, for computation of stiffness matrix, will be in generally computed by a weighted average of the standard strain field $\boldsymbol{\varepsilon}^h(\mathbf{x})$. For example, the smoothed strain field at a point in a smoothed domain Ω_k^s as shown in Figure 3.1 can be defined by the following operation

$$\tilde{\boldsymbol{\varepsilon}}_k(\mathbf{x}_C) = \int_{\Omega_k^s} \boldsymbol{\varepsilon}^h(\mathbf{x}) \Phi(\mathbf{x}-\mathbf{x}_C) \mathrm{d}\Omega = \int_{\Omega_k^s} \nabla^s \mathbf{u}^h(\mathbf{x}) \Phi(\mathbf{x}-\mathbf{x}_C) \mathrm{d}\Omega \tag{3.2}$$

where $\Phi(\mathbf{x}-\mathbf{x}_C)$ is an assumed smoothing function which satisfies the properties of Heaviside-type function such as

$$\Phi^{(k)}(\mathbf{x}-\mathbf{x}_C) \geq 0 \text{ and } \int_{\Omega_k^s} \Phi^{(k)}(\mathbf{x}-\mathbf{x}_C) \mathrm{d}\Omega = 1 \tag{3.3}$$

$$\Phi^{(k)}(\mathbf{x}-\mathbf{x}_C) = \begin{cases} 1/A_k^s, & \mathbf{x} \in \Omega_k^s \\ 0, & \mathbf{x} \notin \Omega_k^s \end{cases} \tag{3.4}$$

where $A_k^s = \int_{\Omega_k^s} \mathrm{d}\Omega$ is the area of the smoothing domain Ω_k^s. The smoothed strain field will become constant in the smoothing domain Ω_k^s and defined by

$$\tilde{\boldsymbol{\varepsilon}}_k(\mathbf{x}) = \frac{1}{A_k^s}\int_{\Omega_k^s} \boldsymbol{\varepsilon}^h(\mathbf{x})\mathrm{d}\Omega = \frac{1}{A_k^s}\int_{\Omega_k^s} \nabla_s \mathbf{u}^h(\mathbf{x})\mathrm{d}\Omega \tag{3.5}$$

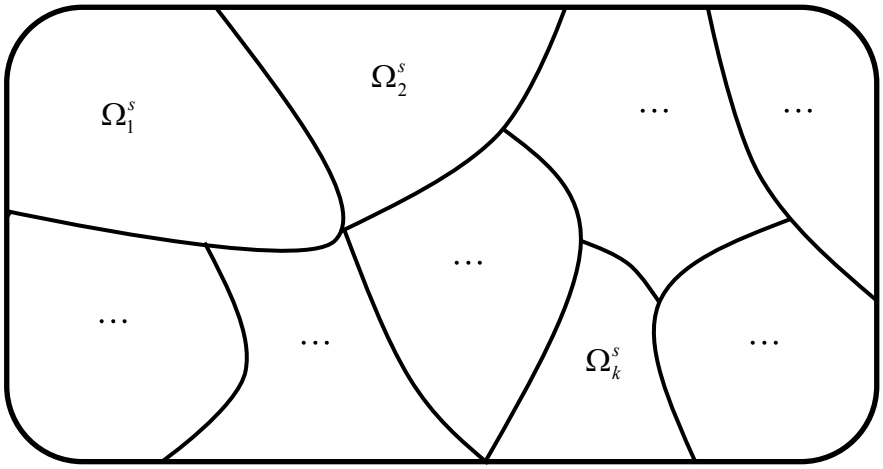

Figure 3.1. Division of problem domain into N_s "non-overlap" and "no-gap" smoothing domains: Ω_1^s, Ω_2^s, …, Ω_k^s, …, $\Omega_{N_s}^s$.

3.1.2 Types of Smoothing Domains

In this thesis, the strain smoothing operation represented in Eq. (3.4) will be employed for modifying the compatible strain field in finite element settings, viz. S-FEM schemes. To do so, a background mesh is required, which could be generated in the same fashion as standard FEM. However, other than element-based implementations in FEM, S-FEM models evaluate the weak form based on the smoothing domain, which can be constructed within the elements: CS-FEM [10,11], but more often beyond the elements: bringing the information from the adjacent

elements, such as NS-FEM, ES-FEM and FS-FEM [12–14]. Upon the element mesh, the entire problem domain Ω will be divided into a set of N_s "non-overlap" and "no-gap" smoothing domains (Figure 3.1) such that $\Omega \approx \bigcup_{k=1}^{N_s} \Omega_k^s$ and $\Omega_i^s \cap \Omega_j^s = \varnothing$ for $i \neq j$. To guarantee the stability and convergence for W2 scheme [5], the number of the smoothing domain created has to satisfy certain conditions such as linearly independence [15].

Table 3.1 Some representative smoothing domains (SD's)

Name	Method for creation and number of SD's (N_s)	S-FEM models	Dimension of problem
Cell-based SD (CSD)	SD's or smoothing cells (SC's) are divided from and located within the elements ($N_s = \sum_{i=1}^{N_e} n_{sc}^i$, $n_i^s = 1, 2, 3, 4, \ldots$)	CS-FEM [10–11]	1D, 2D, 3D
Node-based SD (NSD)	SD's are created based on nodes by connecting portions of the surrounding elements sharing the associated node ($N_s = N_{node}$)	NS-FEM [12]	1D, 2D, 3D
Edge-based SD (ESD)	SD's are created based on edges by connecting portions of the surrounding elements sharing the associated edge ($N_s = N_{edge}$)	ES-FEM [13]	2D, 3D
Face-based SD (FSD)	SD's are created based on faces by connecting portions of the surrounding elements sharing the associated face ($N_s = N_{face}$)	FS-FEM [14]	3D

In Table 3.1, several typical smoothing domains for S-FEM models are collected. Take for example, in the CS-FEM using quadrilateral elements, the basic elements (e.g., element i) in Figure 3.2 can be further subdivided into several numbers ($n_{sc}^i = 1, 2, 3, 4, \ldots$) of smoothing domains or specially termed as the "smoothing cells" (SC's), where n_{sc}^i depends on the stability condition [16] and accuracy requirements. For the 2D ES-FEM using triangular elements, the

smoothing domain Ω_k^s associated with the edge k is created by connecting two endpoints of the edge to centroids of corresponding adjacent elements as sketched in Figure 3.3. It is noted that for inner edges there are two elements involved for the creation of smoothing domains as an inner edge is shared by two connected elements. More details of construction of smoothing domains for different S-FEM models will be introduced in following chapters.

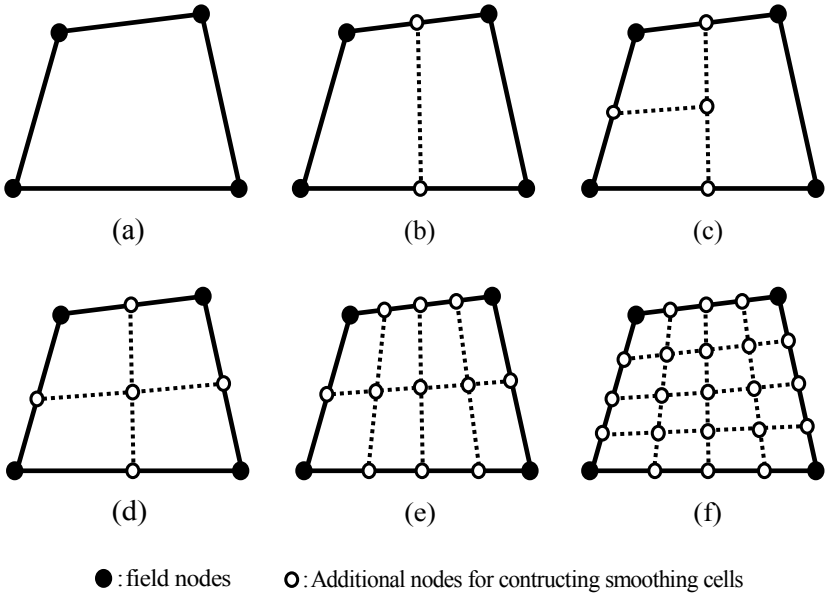

Figure 3.2. Division of a quadrilateral element into smoothing cells (SCs) in CS-FEM by connecting the mid-segment-points of opposite segments of smoothing domains: (a) $n_{SC}=1$; (b) $n_{SC}=2$; (c) $n_{SC}=3$; (d) $n_{SC}=4$; (e) $n_{SC}=8$; and (f) $n_{SC}=16$.

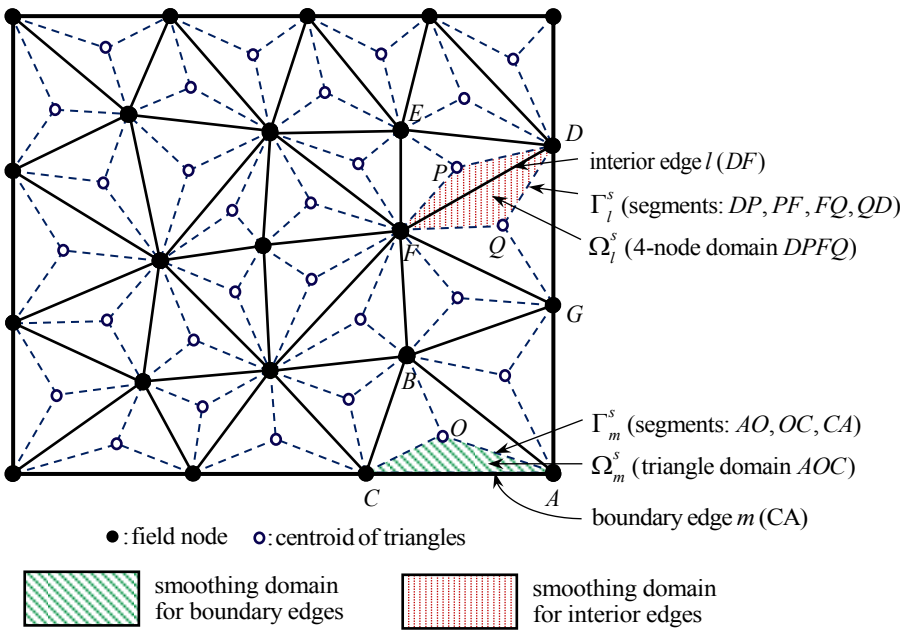

Figure 3.3. Division of a problem domain into triangular elements and edge-based smoothing domains. For example, the smoothing domain Ω_m^s for boundary edge m is a triangle AOC, and the smoothing domain Ω_l^s for interior edge l is four-sided convex polygon $DPFQ$.

3.1.3 Smoothed Strain Field

For an S-FEM model as listed in Table 3.1, the weak form is evaluated based on smoothing domains (Ω_k^s), which can be regarded as $n_s \geq 1$ sub-smoothing cells $\Omega_{k,t}^s$. The displacement field, i.e., primary variables of the problem $\mathbf{u}^h(\mathbf{x})$, is always continuous over the entire problem domain. However, the compatible strain field, i.e., differentials of displacements $\boldsymbol{\varepsilon}^h(\mathbf{x}) = \nabla_s \mathbf{u}^h(\mathbf{x})$, is continuous inside each of the sub-smoothing cells $\Omega_{k,t}^s$, but can be discontinuous on the inner boundaries for different sub-smoothing cells in domains Ω_k^s. Take 2D ES-FEM as shown in Figure 3.3 for example, the smoothing domain for inner edge k contains two sub-smoothing cells $\Omega_{k,1}^s$ and $\Omega_{k,2}^s$. The compatible strain field $\boldsymbol{\varepsilon}^h(\mathbf{x})$ would be piecewise

constants and discontinuous along this edge. Applying the Divergence theorem of Gauss, the smoothed strain $\tilde{\boldsymbol{\varepsilon}}_k(\mathbf{x})$ for smoothing domain Ω_k^s in Eq. (3.5) can be evaluated along the boundary of the sub-smoothing cells $\Omega_{k,t}^s$, which gives

$$\tilde{\boldsymbol{\varepsilon}}_k(\mathbf{x}) = \frac{1}{A_k^s}\int_{\Omega_k^s} \nabla_s \mathbf{u}^h(\mathbf{x})\mathrm{d}\Omega = \frac{1}{A_k^s}\sum_{t=1}^{n_s}\int_{\Omega_{k,t}^s} \nabla_s \mathbf{u}^h(\mathbf{x})\mathrm{d}\Omega = \frac{1}{A_k^s}\sum_{t=1}^{n_s}\int_{\Gamma_{k,t}^s} \mathbf{n}_{k,t}^s(\mathbf{x})\mathbf{u}^h(\mathbf{x})\mathrm{d}\Gamma \tag{3.6}$$

where Γ_k^s is the boundary of the smoothing domain Ω_k^s, and $\mathbf{n}_{k,t}^s(\mathbf{x})$ denotes the outward normal matrix on the boundary $\Gamma_{k,t}^s$.

Since the displacement field is continuous along the shared boundary for the sub-smoothing cells $\Omega_{k,1}^s$ and $\Omega_{k,2}^s$ (i.e., the edge k or the boundary inside the smoothing domain), we have

$$\mathbf{n}_{k,1}^s(\mathbf{x}) = -\mathbf{n}_{k,2}^s(\mathbf{x}) \quad \text{or} \quad \mathbf{n}_{k,1}^s(\mathbf{x})\mathbf{u}^h(\mathbf{x}) + \mathbf{n}_{k,2}^s(\mathbf{x})\mathbf{u}^h(\mathbf{x}) = 0 \quad \text{on } \Gamma_{k,1-2}^s \tag{3.7}$$

where $\mathbf{n}_{k,1}^s(\mathbf{x})$ and $\mathbf{n}_{k,2}^s(\mathbf{x})$ represent the outward normal matrix on the boundary $\Gamma_{k,1-2}^s$ for sub-smoothing cells $\Omega_{k,1}^s$ and $\Omega_{k,2}^s$. Obviously the Eq. (3.7) may let the integration of $\mathbf{n}_{k,t}^s(\mathbf{x})\mathbf{u}^h(\mathbf{x})$ for the neighboring sub-smoothing cells to be eliminated along the shared boundary k inside the smoothing domain in Eq. (3.6). Then the integrations in Eq. (3.6) will only comprise the outer boundaries of the smoothing domain, which implies

$$\tilde{\boldsymbol{\varepsilon}}_k(\mathbf{x}) = \frac{1}{A_k^s}\sum_{t=1}^{n_s}\int_{\Gamma_{k,t}^s} \mathbf{n}_{k,t}^s(\mathbf{x})\mathbf{u}^h(\mathbf{x})\mathrm{d}\Gamma = \frac{1}{A_k^s}\int_{\Gamma_k^s} \mathbf{n}_k^s(\mathbf{x})\mathbf{u}^h(\mathbf{x})\mathrm{d}\Gamma \tag{3.8}$$

in which $\Gamma_k^s = \sum_{t=1}^{n_s} \Gamma_{k,t(\text{outer})}^s$ is the outer boundary of smoothing domain Ω_k^s, and $\mathbf{n}_k^s(\mathbf{x})$ is the outward normal matrix on the boundary Γ_k^s defined by

$$\mathbf{n}_k^s(\mathbf{x}) = \begin{bmatrix} n_{kx}^s & 0 & n_{ky}^s \\ 0 & n_{ky}^s & n_{kx}^s \end{bmatrix}^T \tag{3.9}$$

where n_x^s and n_y^s denote the unit outward normal components in x and y directions, respectively.

If the matrix of shape function $\mathbf{N}_I(\mathbf{x})$, which is similar as in a finite element scheme obtained from the background triangular mesh, is introduced, the trial displacement $\mathbf{u}^h(\mathbf{x})$ will have the following form

$$\mathbf{u}^h = \sum_{I=1}^{N_n} \mathbf{N}_I(\mathbf{x})\mathbf{d}_I \tag{3.10}$$

where $\mathbf{x} = [x \quad y]^T$, nodal displacement vector at node I is $\mathbf{d}_I = \mathbf{u}^h(\mathbf{x}_I)$, and the shape function has the form

$$\mathbf{N}_I(\mathbf{x}) = \begin{bmatrix} N_I(\mathbf{x}) & 0 \\ 0 & N_I(\mathbf{x}) \end{bmatrix} \tag{3.11}$$

Now the trial function $\mathbf{u}^h(\mathbf{x})$ expressed in Eq. (3.10) can be substituted into Eq. (3.8), with respect to nodal displacement giving

$$\tilde{\boldsymbol{\varepsilon}}_k(\mathbf{x}) = \sum_{I \in S_k^s} \tilde{\mathbf{B}}_I \mathbf{d}_I \tag{3.12}$$

where $\mathbf{d}_I$ is the vector of the associated nodal displacements, S_k^s is the set of "supporting" nodes for the smoothing domain Ω_k^s, i.e., the set of all nodes of the elements that share the common edge k. For ES-FEM using triangle elements with sample smoothing domains as shown in Fig. 1, S_k^s is the set of nodes $\{A,B,C\}$ for boundary edge AC, and $\{D,E,F,G\}$ for the interior edge DF. $\tilde{\mathbf{B}}_I$ is the smoothed strain-displacement matrix evaluated by

$$\tilde{\mathbf{B}}_I = \frac{1}{A_k^s}\int_{\Gamma_k^s} \mathbf{n}_k^s(\mathbf{x})\mathbf{N}_I(\mathbf{x})\mathrm{d}\Gamma = \begin{bmatrix} \tilde{b}_{Ix} & 0 & \tilde{b}_{Iy} \\ 0 & \tilde{b}_{Iy} & \tilde{b}_{Ix} \end{bmatrix}^T \tag{3.13}$$

with components

$$\tilde{b}_{Ih} = \frac{1}{A_k^s}\int_{\Gamma_k^s} N_I(\mathbf{x}) n_{kh}^s(\mathbf{x})\mathrm{d}\Gamma\,,\ h = x, y \tag{3.14}$$

From the above equation, it is noted that only the values of $N_I(\mathbf{x})$ (not the derivatives) are involved on the boundary of the smoothing domain Γ_k^s. If a linearly compatible displacement field is utilized along Γ_k^s, then a single Gaussian point is sufficient for numerical integration along each segment $\Gamma_{k,t}^s$ of the boundary Γ_k^s. It is now possible to obtain the form by Gauss quadrature

$$\tilde{b}_{Ih} = \frac{1}{A_k^s}\sum_{t=1}^{n_{eg}^s} N_I(\mathbf{x}_t^{GP}) n_{kh,t}^s l_{k,t}^s\,,\ h = x, y \tag{3.15}$$

where n_Γ^s is the total number of the boundary segments $\Gamma_{k,t}^s \subset \Gamma_k^s$, For example, in Figure 3.3 the smoothing domain for boundary edge $m\,(AC)$ has three boundary segments (AO, OC, CA), i.e.,

$n_\Gamma^s = 3$; and for interior edge $l\,(DF)$ it has four segments (DP, PF, FQ, QD), i.e., $n_\Gamma^s = 4$. $\mathbf{x}_t^{GP}$ is the midpoint (Gaussian point) of the piecewise boundary segment $\Gamma_{k,t}^s$, $n_{kh,t}^s$ and $l_{k,t}^s$ are the outward unit normal and length of $\Gamma_{k,t}^s$, respectively. In the above equations, A_k^s is the area of smoothing domain computed by

$$A_k^s = \int_{\Omega_k^s} d\Omega = \frac{1}{3}\sum_{j=1}^{n_k^e} A_j^e \tag{3.16}$$

where n_k^e is the number of elements attached to the edge ($n_k^e = 1$ for the boundary edges and $n_k^e = 2$ for interior edges as shown in Figure 3.3).

Consider the assumed displacement field is continuous/smooth and the definition of the smoothed strain field expressed in Eq. (3.6) and Eq. (3.8), we can rewrite the smoothed strain-displacement matrix $\tilde{\mathbf{B}}_I$ in Eq. (3.13) by the average of strain-displacement matrix $\mathbf{B}_I(\mathbf{x})$ yielded from the involved element(s) by linear FEM, which gives

$$\tilde{\mathbf{B}}_I = \frac{1}{A_k^s}\int_{\Gamma_k^s} \mathbf{n}_k^s(\mathbf{x})\mathbf{N}_I(\mathbf{x})\mathrm{d}\Gamma = \frac{1}{A_k^s}\int_{\Omega_k^s} \nabla_s \mathbf{N}_I(\mathbf{x})\mathrm{d}\Omega = \frac{1}{A_k^s}\int_{\Omega_k^s} \mathbf{B}_I(\mathbf{x})\mathrm{d}\Omega \tag{3.17}$$

where the line integral along Γ_k^s is converted to region integration in Γ_k^s. It is worthwhile to note that the expression in Eq. (3.17) reveals the relationship between smoothed strain-displacement matrix $\tilde{\mathbf{B}}_I$ and the standard strain-displacement matrix $\mathbf{B}_I(\mathbf{x})$ calculated from linear FEM.

In FEM, the global/total stiffness matrix is an assembly of the element stiffness matrix that relates the displacements of the nodes on the mesh to applied external forces. Similar to

FEM, the global smoothed stiffness matrix $\tilde{\mathbf{K}}$ is assembled from the individual smoothing domain's stiffness contributions, and its entries can be computed by

$$\tilde{\mathbf{K}}_{IJ} = \int_{\Omega} \tilde{\mathbf{B}}_I^T \mathbf{D} \tilde{\mathbf{B}}_J \mathrm{d}\Omega = \sum_{k=1}^{N_s} \int_{\Omega_k^s} \tilde{\mathbf{B}}_I^T \mathbf{D} \tilde{\mathbf{B}}_J \mathrm{d}\Omega = \sum_{k=1}^{N_s} \tilde{\mathbf{B}}_I^T \mathbf{D} \tilde{\mathbf{B}}_J A_k^s \tag{3.18}$$

where N_s is the total number of smoothing domains. $\tilde{\mathbf{K}}$ is a symmetric positive definite (SPD) matrix and $\tilde{\mathbf{K}}_{IJ}$ involves only these nodes which have contributions to the smoothed domain. Note that a smoothing domain in S-FEM usually includes parts of adjacent elements, which means it may have more supporting nodes for a smoothing domain than those in an element. This leads to increasing the bandwidth of the global stiffness matrix and higher computational cost for S-FEM models, compared to the corresponding standard FEM with the same sets of nodes.

3.2 Numerical Procedure for the S-FEM Models

Analogous to the general procedures of the FEM, the steps in S-FEM procedure can be summarized as follows.

1. Domain discretization: define the problem and discretize the problem domain with proper background mesh;

2. Creation of smoothing domains: select an S-FEM model type and generate the corresponding smoothing domains;

3. Computation of stiffness matrix and load vector for smoothing domains:

   1) Evaluate the smoothed strain-displacement matrix $\tilde{\mathbf{B}}_I$;

2) Calculate the smoothed stiffness matrix $\tilde{\mathbf{K}}_{IJ}$ and load vector of the smoothing domain.

4. Assemblage for overall equilibrium equations: Assemble the stiffness matrix and the load vector of the smoothing domains into the global stiffness matrix and load vector;

5. Incorporation of the external loads and boundary conditions;

6. Solution for the unknown nodal displacements;

7. Retrieval of reaction force, stress/strain, internal forces, strain energy.

3.3 General Properties of S-FEM models

In the past few years, several different S-FEM models using different types of smoothing domains have been proposed and further investigated for a wide range of mechanics problems. These numerical studies have demonstrated that S-FEM shows some attractive properties in comparison with conventional FEM, including softened behavior, upper bounds and ultra-accuracy, etc. In this section, we will only list some basic properties of S-FEM, which were laid out in Reference [15]. Some other promising properties such as handling complex geometry and immunity from volumetric locking issues will be discussed in application problems in the next few chapters.

3.3.1 Smoothed Strain Field: Incompatible

As mentioned previously, the modification/construction of compatible strain field for S-FEM can be performed within elements (CS-FEM) but more often beyond the elements (NS-FEM, ES-FEM, or FS-FEM). For the operation within elements (i.e., smoothing domain locates

within the element), the assumed smoothed strains defined in Eq. (3.8) will not be compatible in terms of strain–displacement relations unless the linear displacement field is assumed. When bringing in the information from the neighboring elements, for any assumed continuous displacement field the smoothed strains would not be compatible in terms of the strain–displacement relation. Generally, an S-FEM model can be regarded as partially compatible compared to the fully compatible FEM models. Due to the violations of compatibility in terms of strain–displacement relations, S-FEM models process the very important softening effects and hence some other special properties.

3.3.2 Stress Equilibrium State within Smoothing Domains: Softening Effect and Bound Property

Consider the definition of smoothed strains in Eq. (3.8), the assumed smoothing strains become constants for any point in a smoothing domain [17]. According to the constitutive relations for elastic solid, the stresses obtained in the smoothing domain will also be constants. The equilibrium equation, i.e., Eq. (2.1) for finite element scheme, will be naturally satisfied when these constant stresses are substituted with free external loadings, i.e., $\mathbf{f}^b = 0$. Therefore, an important property can be revealed: the stress equilibrium status can be reached in a smoothing domain when the strain smoothing technique is applied to the smoothing domain for a specific problem. The smoothing operation hereby is referred to as a local stress equilibrator in S-FEM models.

Moreover, based on minimum complementary principle [18], if the stress field satisfies exactly the equilibrium equations and boundary conditions, an exact upper bound solution would be rendered. Since the S-FEM models satisfy the equilibrium equation for every point in the

problem domain and the smoothed domains as a whole in some given boundary conditions, proper S-FEM models with sufficient softening effects can offer the possibility to obtain both lower and upper bound solutions, ultra-accurate solutions, and even 'exact' solutions [5].

3.3.3 Energy Conservation

When a constant smoothing function is adopted, area integrations over a smoothed domain in the weak form become line integrations along the domain boundaries. S-FEM models are energy consistent if the assumed displacement field (or the nodal shape functions according to Eq. (3.10)) is continuous and linear compatible along the boundary segments of the smoothing domains.

The property of energy conservation can be verified by considering a unique "complementary" situation for S-FEM models. As discussed already, in a smoothing domain the equilibrium is ensured as described but compatibility is violated. And on the boundary segments of the smoothing domain, equilibrium and stress continuity are not guaranteed, but displacement continuity is satisfied owing to the utilization of continuous nodal shape functions. Thus, this unique complementary satisfaction of equilibrium or compatibility conditions guarantees energy consistency without energy loss even if there exist violations of equilibrium or compatibility conditions [15]. This is the reason that the S-FEM models are variationally consistent: energy conservation when they adopt the linear compatible shape functions along the boundaries of smoothing domains.

3.3.4 Elements Selection: Preference for Simplicity and Robustness

It is easiser to mesh and re-mesh an arbitrary geometry domain with simplex T-mesh elements (triangular for 2D and tetrahedral for 3D), than other meshes (e.g., quadrilateral elements in 2D or hexahedron elements in 3D). Moreover, S-FEM models will not induce inaccuracy issues (compared to standard FEM) when using the standard (constant strain) T-mesh. Therefore, generally a simplex T-mesh with T3 or T4 elements for S-FEM models is preferred as it takes advantages of the following: (1) low cost in grid/mesh generation; (2) robustness for arbitrary geometries; (3) possibility of remeshing for deformed/changed configurations; (4) simplicity in formulation and implementation as when using constant strain triangles and no derivatives of shape function involved in S-FEM; and (5) S-FEM works effectively with T-elements. The philosophy of S-FEM is obvious: being a powerful and versatile numerical technique which is simple, effective and robust.

Regarding the theoretical proof of features such as the softening effect, upper bound to the FEM solution, monotonic convergence, we can refer to the references [6] and [15].

References

[1] Chen L, Nguyen-Xuan H, Nguyen-Thoi T, Zeng KY and Wu SC. 2010. Assessment of smoothed point interpolation methods for elastic mechanics. Communications in Numerical Methods in Engineering; 89: 1635–1655.

[2] Bordas S, Rabczuk T, Nguyen-Xuan H, Nguyen-Vinh P, Natarajan S, Bog T, Do-Minh Q, and Nguyen-Vinh H. 2010. Strain smoothing in FEM and XFEM. Computers and Structures; 88: 1419–1443.

[3] Chen JS, Wu CT, Yoon S and You Y. 2001. A stabilized conforming nodal integration for Galerkin meshfree method. International Journal for Numerical Methods in Engineering; 50: 435–466.

[4] Yoo JW, Moran B, Chen JS. 2004. Stabilized conforming nodal integration in the natural-element method, International Journal for Numerical Methods in Engineering; 60: 861–890.

[5] Liu GR. 2010. A G space theory and a weakened weak (W2) form for a unified formulation of compatible and incompatible methods: Part I theory and Part II applications to solid mechanics problem. International Journal for Numerical Methods in Engineering; 81(9): 1093–1156.

[6] Nguyen-Thoi T. 2009. Development of smoothed finite element method (SFEM). PhD thesis, National University of Singapore.

[7] Eringen AC. 1972. Nonlocal polar elastic continua. International Journal of Engineering Science; 10(1): 1-16.

[8] Lucy LB. 1977. A numerical approach to the testing of the fission hypothesis.Astronomical Journal; 82: 1013–1024.

[9] Liu GR, Liu MB. 2003. Smoothed particle hydrodynamics - A meshfree particle method. World Scientific, Singapore.

[10] Liu GR, Dai KY, and Nguyen-Thoi T. 2007. A smoothed finite element method for mechanics problems. Computational Mechanics 39; 859–877.

[11] Liu GR, Zeng W, and Nguyen-Xuan H. 2013. Generalized stochastic cell-based smoothed finite element method (GS CS-FEM) for solid mechanics. Finite Elements in Analysis and Design; 63(0): 51–61.

[12] Liu GR, Nguyen-Thoi T, Nguyen-Xuan H., and Lam KY. 2009. A node-based smoothed finite element method (NS-FEM) for upper bound solutions to solid mechanics problems. Computers and Structures; 87(12): 14–26.

[13] Liu GR, Nguyen-Thoi T, and Lam KY, 2009. An edge-based smoothed finite element method (ES-FEM) for static, free and forced vibration analyses of solids. Journal of Sound and Vibration; 320(45): 1100–1130.

[14] Nguyen-Thoi T., Liu GR, Lam KY, and Zhang GY. 2009. A face-based smoothed finite element method (FS-FEM) for 3D linear and geometrically non-linear solid mechanics problems using 4-node tetrahedral elements. International Journal for Numerical Methods in Engineering; 78(3): 324–353.

[15] Liu GR and Nguyen-Thoi T. 2010. Smoothed finite element methods. CRC Press (Taylor & Francis), Boca Raton.

[16] Dai KY, Liu GR, and Nguyen TT. 2007. An n-sided polygonal smoothed finite element method (nSFEM) for solid mechanics. Finite Elements in Analysis and Design; 43: 847–860.

[17] Liu GR, Nguyen TT, Dai KY and Lam KY. 2007. Theoretical aspects of the smoothed finite element method (SFEM), International Journal for Numerical Methods in Engineering; 72(1): 902–930.

[18] Veubeke BF. 1965. Displacement and equilibrium models in the finite element method. In *Stress Analysis*, OC Zienkiewicz and GS Holister, Eds. Wiley, London.

Chapter 4. Generalized Stochastic Cell-based Smoothed Finite Element Method (GS_CS-FEM) for Solid Mechanics

4.1 Introduction

Randomness of parameters is a natural characteristic in many engineering systems, and should be properly dealt with in computational modeling and simulations. Such randomness could lead to uncertainty in the outputs of the numerical models. Deterministic FEM fails to consider the uncertainty, which limits its application [1]. From early 1980s, the concept of the stochastic FEM has been established, by combining the approaches of reliability evaluation into FEM technology. During the last several decades, the stochastic FEM has become a powerful tool in computational stochastic mechanics, in dealing with large-scale realistic engineering problems. Regarding the state-of-the-art review of the past and recent developments in stochastic FEM area, we can refer to Ref [2]. The stochastic perturbation FEM, which is based on stochastic moment techniques, is an efficient and accurate approach for approximation of the response and reliability in some practical enginnering problems. However, the commonly used second order perturbation expansion was found ineffective when the uncertainties are too large. M. Kamiński [3] proposed an *n*th order generalized stochastic finite element (GS-FEM) based on perturbation technique. In Ref. [3], a 1D linear elastostatics problem with a single random variable showed that the accuracy of the expected values and variances can be improved using GS-FEM. In addition, the approach using higher order makes it possible to compute the probabilistic moments of the solution with a priori given accuracy [4].

In this chapter, we establish a generalized stochastic CS-FEM (GS_CS-FEM), which develops the generalized n^{th} order stochastic perturbation technique under the framework of the cell-based smoothed finite element method (CS-FEM) for 2D solid mechanics problems. To demonstrate the effectiveness of the present method, two numerical examples are presented and verified by Monte Carlo simulations.

The chapter is organized as follows. In sections 4.2 and 4.3, the probability theory and the CS-FEM are briefly presented, respectively. The formulation of GS_CS-FEM using the generalized *n*th order perturbation stochastic approach is derived in section 4.4. Section 4.5 shows two numerical examples. Finally, some concluding remarks are made in section 4.6.

4.2 Briefing of Probability Theory

For a given set of random fields $b(\mathbf{x})$ and its probability density function (PDF) $p_i(b_r)$, $r=1,2,\cdots,R$, $i=1,2$, the first two probabilistic moments for the random fields $b_r(x_k)$ are defined as [5-6]

$$E[b_r]=b_r^0=\int_{-\infty}^{+\infty} b_r p_1(b_r)db_r \tag{4.1}$$

$$\mathrm{Cov}(b_r,b_s)=S_{rs}=\int_{-\infty}^{+\infty}\int_{-\infty}^{+\infty}(b_r-b_r^0)(b_s-b_s^0)p_2(b_r,b_s)db_r db_s \tag{4.2}$$

where b_r^0 represents the first probabilistic moment of the random variable, $\mathrm{Cov}(b_r,b_s)$ or S_{rs} represents the covariance, $p_1(b_r)$ and $p_2(b_r,b_s)$ denote the PDF and the joint PDF, respectively.

For a real, single-valued continuous function of a random variable b, the expectation becomes the expected value, or mean of the variable b

$$E[b] = b^0 = \int_{-\infty}^{+\infty} bp(b)db \tag{4.3}$$

The variance of b, expressed as $\mathrm{Var}(b)$, or σ_b^2 is defined as the mean square value of b about the mean

$$\mathrm{Var}(b) = E[(b-b^0)^2] = \int_{-\infty}^{+\infty}\int_{-\infty}^{+\infty} (b-b^0)^2\, p(b)db \tag{4.4}$$

Then the standard deviation (denoted by σ_b) and the coefficient of variation (denoted by γ or COV) of a random variable b can be defined as

$$\sigma_b = \sqrt{\mathrm{Var}(b)} \quad \text{and} \quad \gamma = \left[\frac{\mathrm{Var}(b)}{(E[b])^2}\right]^{\frac{1}{2}} \tag{4.5}$$

Based on stochastic perturbation technique, if a small perturbation parameter ε related to spatial expectations is adopted, the n th order truncated Taylor series expansion of the limit state function of a structural reliability analysis [3] can be expressed as

$$f(b) = f^0(b) + \sum_{n=1}^{\infty} \frac{1}{n!}\varepsilon^n f^{(n)}(b)(\Delta b)^n \cong f^0(b) + \varepsilon f^{,b}(b)\Delta b + \ldots + \frac{1}{n!}\varepsilon^n f^{(n)}(b)(\Delta b)^n \tag{4.6}$$

where $f^{(n)}(b) = \dfrac{\partial^n f(b)}{\partial b^n}$, $\varepsilon\Delta b = \varepsilon(b-b^0)$ and $\varepsilon^2(\Delta b)^2 = \varepsilon^2(b-b^0)^2$ are the first and second variations of b concerning the corresponding expected value b^0, respectively. The n th order variation can be similarly written as

$$\varepsilon^n (\Delta b)^n = \varepsilon^n (b - b^0)^n \tag{4.7}$$

where $(\cdot)^0$ denotes the mean value of the function value $(\cdot)$ taken at the expected value b^0, and $(\cdot)^{,b}$, $(\cdot)^{,bb}$ represents the first and second order partial derivative with respect to b at the point b^0. Replacing b_r in Eq. (4.1) using $f(b)$ with the expression in Eq. (4.6), we will obtain the expected value of a limit state function $f(b)$ with a specified small perturbation parameter ε by expansion of Taylor series [3]:

$$\begin{aligned} E\left[f(b);b\right] &= \int_{-\infty}^{+\infty} f(b)\, p(b)\, db = \int_{-\infty}^{+\infty} \left(f^0(b) + \sum_{n=1}^{\infty} \frac{1}{n!} \varepsilon^n f^{(n)}(b)(\Delta b)^n \right) p(b)\, db \\ &\cong \begin{cases} \displaystyle\int_{-\infty}^{+\infty} \left(f^0(b) + \sum_{n=1}^{M} \frac{1}{(2n)!} \varepsilon^{2n} f^{(2n)}(b)(\Delta b)^{2n} \right) p(b)\, db \\ \qquad \textit{for symmetric distribution functions} \\ \displaystyle\int_{-\infty}^{+\infty} \left(f^0(b) + \sum_{n=1}^{N} \frac{1}{(n)!} \varepsilon^{n} f^{(n)}(b)(\Delta b)^{n} \right) p(b)\, db \\ \qquad \textit{for asymmetric distribution functions} \end{cases} \end{aligned} \tag{4.8}$$

It is noted that the approximation of expected values or variances satisfies a given priori precision with an admissible error via a proper selection of number of terms, M or N.

For a small variation of the random variable with the symmetric PDF around its mean value, the expected value for the input random variable with symmetric probability density function in the second order perturbation approach can be expressed as [4]

$$\begin{aligned} E\left[f(b);b\right] &= \int_{-\infty}^{+\infty} f(b)\, p(b)\, db \cong \int_{-\infty}^{+\infty} \left(f^0(b) + f^{,b}(b)\varepsilon\Delta b + \frac{1}{2} f^{,bb}(b)\varepsilon^2 (\Delta b)^2 \right) p(b)\, db \\ &= f^0(b) + 0 \times f^{,b}(b)\varepsilon + \frac{1}{2} f^{,bb}(b)\varepsilon^2 S_{bb} \end{aligned} \tag{4.9}$$

where S_{bb} stands for the second-order central moments, which is unique for a given random variable b. When the input random variable with the symmetric PDF is considered in a large variation, the following extension with a perturbation parameter ε can be preferably adopted [4–8]:

$$\begin{aligned} E\left[f(b);b\right] &= f^0(b)+\frac{1}{2}f^{,bb}(b)\varepsilon^2\mu_2(b)+\frac{1}{4!}f^{,bbbb}(b)\varepsilon^2\mu_4(b)+\frac{1}{6!}f^{,bbbbbb}(b)\varepsilon^6\mu_6(b)+\ldots \\ &\cong f^0(b)+\frac{1}{2}\frac{\partial^2 f}{\partial b^2}\varepsilon^2\mu_2(b)+\frac{1}{4!}\frac{\partial^4 f}{\partial b^4}\varepsilon^2\mu_4(b)+\frac{1}{6!}\frac{\partial^6 f}{\partial b^6}\varepsilon^6\mu_6(b)+\ldots \end{aligned} \tag{4.10}$$

where $\mu_n(b)$ denotes the n^{th} order central probabilistic moment of b and the odd order terms vanish for a symmetry PDF (such as Gaussian random distribution), and where higher than sixth-order terms are neglected. The sixth-order truncated expansion for a variance can be analogously employed [3]:

$$\begin{aligned} Var\left[f(b)\right] &= \int_{-\infty}^{+\infty}\Bigg(f^0+f^{,b}\varepsilon\Delta b+\frac{1}{2}f^{,bb}(\varepsilon\Delta b)^2+\frac{1}{3!}f^{,bbb}(\varepsilon\Delta b)^3+\frac{1}{4!}f^{,bbbb}(\varepsilon\Delta b)^4 \\ &\quad +\frac{1}{5!}f^{,bbbbb}(\varepsilon\Delta b)^3-E(f)\Bigg)^2 p(b)db \\ &\cong \int_{-\infty}^{+\infty}\left(f^{,b}\right)^2(\varepsilon\Delta b)^2\,p\left(f(b)\right)db+\frac{1}{4}\int_{-\infty}^{+\infty}\left(f^{,bb}\right)^2(\varepsilon\Delta b)^4\,p(b)db \\ &\quad 2\times\frac{1}{3!}\int_{-\infty}^{+\infty}f^{,b}f^{,bbb}(\varepsilon\Delta b)^4\,p\left(f(b)\right)db+\left(\frac{1}{3!}\right)^2\int_{-\infty}^{+\infty}\left(f^{,bbb}\right)^2(\varepsilon\Delta b)^6\,p(b)db \\ &\quad +\frac{1}{4!}\int_{-\infty}^{+\infty}f^{,bb}f^{,bbbb}(\varepsilon\Delta b)^6\,p\left(f(b)\right)db+2\times\frac{1}{5!}\int_{-\infty}^{+\infty}f^{,b}f^{,bbbbb}(\varepsilon\Delta b)^6\,p(b)db \\ &= \left(f^{,b}\right)^2\varepsilon^2\mu_2(b)+\left(\frac{1}{4}(f^{,bb})^2+\frac{2}{3!}f^{,b}f^{,bbb}\right)\varepsilon^4\mu_4(b)+ \\ &\quad \left(\left(\frac{1}{3!}\right)^2(f^{,bbb})^2+\frac{1}{4!}f^{,bb}f^{,bbbb}+\frac{2}{5!}f^{,b}f^{,bbbbb}\right)\varepsilon^6\mu_6(b) \end{aligned} \tag{4.11}$$

when the state function does not possess a symmetric feature, the odd orders of probabilistic moments should be nonzero. Even so, the procedure would be implemented in a similar fashion.

4.3 Briefing of the Cell-based Smoothed Finite Element Method (CS-FEM)

4.3.1 Governing Equations

Consider a two-dimensional (2D) linear isotropic elastic solid $\Omega \in \mathscr{R}^2$ bounded by a boundary Γ such that $\Gamma = \Gamma_D \bigcup \Gamma_t$, $\Gamma_D \bigcap \Gamma_t = \varnothing$. Here, boundary Γ is consisted of two parts: Γ_t where external tractions **t** are applied (Neumann conditions), and Γ_D where the displacements **u** are prescribed (Dirichlet conditions). The governing equation in the problem domain Ω bounded by Γ can be expressed in terms of stresses as

$$\begin{aligned} \nabla \cdot \boldsymbol{\sigma} + \mathbf{f}^b = 0 \quad &\text{or} \quad \partial_j \sigma_{ij} + f_i^b = 0 \text{ in } \Omega \\ \boldsymbol{\sigma} \cdot \mathbf{n} = \mathbf{f}^t \quad &\text{or} \quad \sigma_{ij} n_j = f_i^t \text{ on } \Gamma_t \\ \mathbf{u} = \hat{\mathbf{u}} \quad &\text{or} \quad u_i = \hat{u}_i \text{ on } \Gamma_D \end{aligned} \tag{4.12}$$

where $\mathbf{f}^b$ and $\mathbf{f}^t$ denotes the body force and the prescribed traction vector, and **n** is the outward unit normal vector on the boundary Γ. $\partial_i = \partial / \partial x_i$ represents the first partial derivatives corresponding to $x_i \in \{x, y, z\}$ and ∇ denotes a matrix of differential operators:

$$\nabla = \begin{bmatrix} \partial/\partial x & 0 & \partial/\partial y \\ 0 & \partial/\partial y & \partial/\partial x \end{bmatrix}^T \tag{4.13}$$

The stress tensor $\boldsymbol{\sigma}$ in Eq. (4.12) is defined in terms of the strain tensor $\boldsymbol{\varepsilon}$ from the constitutive relations for solid:

$$\boldsymbol{\sigma} = \mathbf{D}\boldsymbol{\varepsilon} \text{ in } \Omega \text{ or } \sigma_{ij} = D_{ijkl}\varepsilon_{kl} \text{ in } \Omega \tag{4.14}$$

where **D** is the Hooke's matrix of elastic constants which is related to modulus E and Poisson's ratio ν.

In Eq. (4.14), $\boldsymbol{\varepsilon}$ is the strain tensor which can be expressed by displacement $\mathbf{u}$ using compatibility relation:

$$\boldsymbol{\varepsilon} = \nabla^s \mathbf{u}(\mathbf{x}) \quad \text{or} \quad \varepsilon_{ij} = \frac{1}{2}(\partial_j u_i + \partial_i u_j) \text{ in } \Omega, \ \forall i, j = 1,2 \tag{4.15}$$

$$\mathbf{u}(\mathbf{x}) = \mathbf{u}_\Gamma(\mathbf{x}) \quad \text{or} \quad u_i = u_{\Gamma i} \text{ on } \Gamma_{\mathbf{D}} \tag{4.16}$$

where ∇^s is the symmetric gradient of the displacement field.

4.3.2 Local Gradient Smoothing Operation of CS-FEM

Consider an element Ω_e selected from the discretized domain Ω_h. In order to manipulate the strain smoothing operation, the element Ω_e is partitioned into several number (n_{SC}) of smoothing cells noted as Ω_C, as depicted in Figure 3.2, Here the value of n_{SC} depends on the stability condition and accuracy requirements [9–11] and Ref. [11] proved that the solution of CS-FEM using one single-strain smoothing cell ($n_{SC} = 1$) has equivalent properties as those of FEM using reduced integration (one Gauss point).

Now consider a point x_C in an element Ω_e, and assume $x_C \in \Omega_C$ ($\Omega_C \subset \Omega_e \subset \Omega_h$). The gradient of displacement for the smoothing cell Ω_C in the element Ω_e, which reads the form

$$\nabla u^h(\mathbf{x}_C) = \int_\Omega \nabla u^h(\mathbf{x}) \Phi(\mathbf{x} - \mathbf{x}_C) \mathrm{d}\Omega \tag{4.17}$$

By employing the divergence theorem to the right-hand side, the equation can be rewritten as

$$\nabla u^h(\mathbf{x}_C) = \int_{\Gamma_C} u^h(\mathbf{x})\mathbf{n}_C(\mathbf{x})\Phi(\mathbf{x}-\mathbf{x}_C)\mathrm{d}\Gamma - \int_{\Omega_C} u^h(\mathbf{x})\nabla\Phi(\mathbf{x}-\mathbf{x}_C)\mathrm{d}\Omega \tag{4.18}$$

where Γ_C is the boundary of the smoothing cell Ω_C, and $\mathbf{n}_C(\mathbf{x})$ denotes the outward normal matrix on the boundary Γ_C. The matrix for boundary segment p ($p = 1,2,3,4$ and $\Gamma_{C,p} \subset \Gamma_C$) is defined as

$$\mathbf{n}_C^p(\mathbf{x}) = \begin{bmatrix} n_x^p & 0 & n_y^p \\ 0 & n_y^p & n_x^p \end{bmatrix}^T \tag{4.19}$$

In Eq. (4.18), $\Phi(\mathbf{x}-\mathbf{x}_C)$ is a distribution function or a smoothing function that satisfies at least unity property such as

$$\Phi(\mathbf{x}-\mathbf{x}_C) \geq 0 \text{ and } \int_{\Omega_C} \Phi(\mathbf{x}-\mathbf{x}_C)\mathrm{d}\Omega = 1 \tag{4.20}$$

The most frequently adopted smoothing function is the Heaviside-type piecewise constant function defined in the following form

$$\Phi(\mathbf{x}-\mathbf{x}_C) = \begin{cases} 1/A_C, & \mathbf{x} \in \Omega_C \\ 0, & \mathbf{x} \notin \Omega_C \end{cases} \tag{4.21}$$

where $A_C = \int_{\Omega_C} \mathrm{d}\Omega$ is the area of the smoothing cell Ω_C.

Introducing Eq. (4.21) into Eq. (4.18) gives the smoothed gradient of displacement

$$\tilde{\nabla} u^h(\mathbf{x}_C) = \int_{\Gamma_C} u^h(\mathbf{x})\mathbf{n}_C(\mathbf{x})\Phi(\mathbf{x}-\mathbf{x}_C)\mathrm{d}\Gamma = \frac{1}{A_C}\int_{\Gamma_C} u^h(\mathbf{x})\mathbf{n}_C(\mathbf{x})\mathrm{d}\Gamma \tag{4.22}$$

where the second term in the right-hand side of Eq. (4.18) vanishes due to the selection of function Φ and the area integration becomes boundary integration around the smoothing cell Γ_C. The smoothed strain can then be easily obtained as

$$\tilde{\boldsymbol{\varepsilon}}^h = \frac{1}{A_C}\int_{\Omega_C} \nabla_S \mathbf{d}^h \mathrm{d}\Omega = \frac{1}{A_C}\int_{\Gamma_C} \mathbf{n}_C(\mathbf{x})\mathbf{d}^h(\mathbf{x})\mathrm{d}\Gamma \tag{4.23}$$

4.3.3 Calculation of Stiffness Matrix

If the FEM procedure [9] is followed, the discretized displacement of system can be approximated upon field discretization, which is expressed as

$$u^h(\mathbf{x}) = \sum_{I=1}^{n} N_I(\mathbf{x})\mathbf{d}_I \tag{4.24}$$

where n denotes the number of nodes in an element ($n = 4$ for a quadrilateral element) and $\mathbf{d}_I$ is the nodal displacement vector. Substituting Eq. (4.24) into Eq. (4.22), it yields the form as following

$$\tilde{\nabla} u^h(\mathbf{x}_C) = \frac{1}{A_C}\sum_{I=1}^{n}\int_{\Gamma_C} N_I(\mathbf{x})\mathbf{n}_C(\mathbf{x})\mathrm{d}\Gamma\mathbf{d}_I \tag{4.25}$$

Similarly the smoothed strain in Eq. (4.23) can be obtained as

$$\tilde{\boldsymbol{\varepsilon}} = \sum_{I=1}^{n} \tilde{\mathbf{B}}_I(\mathbf{x}_C)\mathbf{d}_I \tag{4.26}$$

where $\tilde{\mathbf{B}}_I$ is the smoothed strain-displacement matrix which can be evaluated by

$$\tilde{\mathbf{B}}_I(\mathbf{x}_C)=\begin{bmatrix}\tilde{b}_{Ix}(\mathbf{x}_C) & 0 & \tilde{b}_{Iy}(\mathbf{x}_C)\\ 0 & \tilde{b}_{Iy}(\mathbf{x}_C) & \tilde{b}_{Ix}(\mathbf{x}_C)\end{bmatrix}^T \tag{4.27}$$

with

$$\tilde{b}_{Ih}(\mathbf{x}_C)=\frac{1}{A_C}\int_{\Gamma_C} N_I(\mathbf{x})n_{Ch}(\mathbf{x})\mathrm{d}\Gamma,\ h=x,y \tag{4.28}$$

From the above equation, we know that only the values of shape functions $N_I(\mathbf{x})$ (not the derivatives) are involved on the boundary of the smoothing cell Γ_C. If a linearly compatible displacement field is utilized along Γ_C, then a single Gaussian point is sufficient for numerical integration along each segment $\Gamma_{C,p}$ of the boundary Γ_C. It is now possible to obtain the form by Gauss quadrature

$$\tilde{b}_{Ih}(\mathbf{x}_C)=\frac{1}{A_C}\sum_{t=1}^{n_\Gamma} N_I(\mathbf{x}_t^{GP})n_{Ch,t}l_{C,t},\ h=x,y \tag{4.29}$$

where n_Γ is the total number of the boundary segments $\Gamma_{C,p}\subset\Gamma_C$, For 2D CS-FEM shown in Figure 3.2(d), the smoothing cells has four segments, i.e., $n_\Gamma=4$. $\mathbf{x}_t^{GP}$ is the midpoint (Gaussian point) of the piecewise boundary segment $\Gamma_{C,p}$, and $n_{Ch,t}$ and $l_{C,t}$ are the outward unit normal and length of $\Gamma_{C,p}$, respectively.

Once the smoothed strain-displacement matrices over each smoothing cell have been evaluated, the smoothed element stiffness matrix can be obtained by assembly from those of all the smoothing cells in the element, which reads the form as

$$\tilde{\mathbf{K}}_e = \sum_{q=1}^{n_{SC}} \tilde{\mathbf{B}}_q^T \mathbf{D} \tilde{\mathbf{B}}_q A_{Cq} \tag{4.30}$$

The smoothed global stiffness matrix $\tilde{\mathbf{K}}$ is assembled from each of element stiffness matrix $\tilde{\mathbf{K}}_e$. Then the discrete global CS-FEM equilibrium equations in displacement format can be written as

$$\tilde{\mathbf{K}}\mathbf{d} = \mathbf{f} \tag{4.31}$$

where $\mathbf{f}$ is the general nodal force vector.

4.4 The Formulation of the Generalized Stochastic CS-FEM

The general perturbation approach can be now applied based on smoothed FEM settings. For simplicity, we will name the present method as generalized stochastic cell-based smoothed finite element method (GS_CS-FEM), an analogous of the GS-FEM [12].

Consider the smoothed strain matrix $\tilde{\mathbf{B}}_I(\mathbf{x}_C)$ that is stochastically independent from random variables. In general, the partial derivative of the smoothed strain $\tilde{\varepsilon}^h(\mathbf{x}_C)$ with respect to a random variable b can then be derived from Eq. (4.26):

$$\frac{\partial^n \tilde{\varepsilon}^h(\mathbf{x}_C)}{\partial b^n} = \sum_I^n \tilde{\mathbf{B}}_I(\mathbf{x}_C) \frac{\partial \mathbf{d}_I}{\partial b^n} \tag{4.32}$$

In the discrete global CS-FEM equilibrium in Eq. (4.31), if some random quantities are integrated into the smoothed stiffness matrix $\tilde{\mathbf{K}}$ and the force vector $\mathbf{f}$, the following

hierarchical GS_CS-FEM equations for elastostatics are obtained by employing the standard procedure:

- Zeroth-order (ε^0 terms)

$$\tilde{\mathbf{K}}^0\mathbf{d}^0 = \mathbf{f}^0 \tag{4.33}$$

- First-order (ε^1 terms)

$$\tilde{\mathbf{K}}^0\mathbf{d}^{,b} + \tilde{\mathbf{K}}^{,b}\mathbf{d}^0 = \mathbf{f}^{,b} \tag{4.34}$$

- Second-order (ε^2 terms)

$$\tilde{\mathbf{K}}^0\mathbf{d}^{,bb} + 2\tilde{\mathbf{K}}^{,b}\mathbf{d}^{,b} + \tilde{\mathbf{K}}^{,bb}\mathbf{d}^0 = \mathbf{f}^{,bb} \tag{4.35}$$

- Third-order (ε^3 terms)

$$\tilde{\mathbf{K}}^0\mathbf{d}^{,bbb} + 3\tilde{\mathbf{K}}^{,b}\mathbf{d}^{,bb} + 3\tilde{\mathbf{K}}^{,bb}\mathbf{d}^{,b} + \tilde{\mathbf{K}}^{,bbb}\mathbf{d}^0 = \mathbf{f}^{,bbb} \tag{4.36}$$

……

- N th-order (ε^N terms, notation using Pascal's rule)

$$\sum_{k=0}^{N}\binom{N}{k}\tilde{\mathbf{K}}^{(k)}\mathbf{d}^{(N-k)} = \mathbf{f}^{(N)} \tag{4.37}$$

where the symbol $(\cdot)^{(k)}$ denotes $(\cdot)^{,\overbrace{bb\ldots b}^{k}}$, what means k th order partial derivative with respect to b evaluated at $(\cdot)^0$.

Recall now that the smoothed global stiffness matrix $\tilde{\mathbf{K}}$ is assembled from element stiffness matrix $\tilde{\mathbf{K}}_e$ from Eq. (4.30), i.e.

$$\tilde{\mathbf{K}} = \sum_{e=1}^{n_e} \sum_{\mathrm{C}}^{n_{\mathrm{SC}}} \tilde{\mathbf{B}}_{\mathrm{C}}^{\mathrm{T}} \mathbf{D} \tilde{\mathbf{B}}_{\mathrm{C}} A_{\mathrm{C}} \tag{4.38}$$

where n_e is the total number of elements in domain Ω. If Young's modulus $\mathcal{E}$ is considered as the random variable, the k th order derivatives of smoothed global stiffness matrix with respect to $\mathcal{E}$ are then written as

$$\frac{\partial \tilde{\mathbf{K}}}{\partial \mathcal{E}} = \sum_{e=1}^{n_e} \sum_{\mathrm{C}=1}^{n_{\mathrm{SC}}} \tilde{\mathbf{B}}_{\mathrm{C}}^{\mathrm{T}} \frac{\partial \mathbf{D}}{\partial \mathcal{E}} \tilde{\mathbf{B}}_{\mathrm{C}} A_{\mathrm{C}} \tag{4.39}$$

when $k \geq 2$, the result $\frac{\partial^k \tilde{\mathbf{K}}}{\partial \mathcal{E}^k} = 0$ can be derived for elastic problems apparently. Note that $\frac{\partial^k \mathbf{f}}{\partial \mathcal{E}^k} = 0$ for any $k \geq 1$ as the Young's modulus E has no effect on the force vector $\mathbf{f}$. Then the corresponding GS_CS-FEM equilibrium equations can be simplified into

- Zeroth-order (ε^0 terms)

$$\tilde{\mathbf{K}}^0 \mathbf{d}^0 = \mathbf{f}^0 \tag{4.40}$$

- First-order (ε^1 terms)

$$\tilde{\mathbf{K}}^0 \mathbf{d}^{,\mathcal{E}} = -\tilde{\mathbf{K}}^{,\mathcal{E}} \mathbf{d}^0 \tag{4.41}$$

- Second-order (ε^2 terms)

$$\tilde{\mathbf{K}}^0 \mathbf{d}^{,\varepsilon\varepsilon} = -2\tilde{\mathbf{K}}^{,\varepsilon} \mathbf{d}^{,\varepsilon} \tag{4.42}$$

- Third-order (ε^3 terms)

$$\tilde{\mathbf{K}}^0 \mathbf{d}^{,\varepsilon\varepsilon\varepsilon} = -3\tilde{\mathbf{K}}^{,\varepsilon} \mathbf{d}^{,\varepsilon\varepsilon} \tag{4.43}$$

……

- N th-order (ε^N terms)

$$\tilde{\mathbf{K}}^0 \frac{\partial^N \mathbf{d}}{\partial \varepsilon^N} = -N\tilde{\mathbf{K}}^{,\varepsilon} \frac{\partial^{N-1} \mathbf{d}}{\partial \varepsilon^{N-1}} \tag{4.44}$$

A recursive procedure can be implemented to acquire the N th-order solution from the above equation series.

4.5 Numerical Illustrations

In order to analysis the properties of the GS_CS-FEM, two numerical examples will be presented to study the probabilistic output moments. The first example is a simple rectangular cantilever subjected to a parabolic traction at the free end and a plane stress condition is assumed. For the second problem, the infinite plate with a circular hole subjected to unidirectional tension is under a plane strain condition.

4.5.1 Cantilever Beam Subjected to a Tip Load

In this example, a rectangular cantilever linear elastic beam with length L and height H is studied here. The beam is fixed along the left side edge and subjected to a parabolic traction P

at free end as shown in Figure 4.1. The beam is assumed to be a plane stress problem with unit thickness. The analytical solution of displacements can be found in Ref. [13], which reads as follows:

$$u_x = \frac{P}{6EI}\left[(6L-3x)xy+(2+\nu)y\left(y^2-\frac{H^2}{4}\right)\right]$$

$$u_y = -\frac{P}{6EI}\left[(4+5\nu)\frac{H^2x}{4}+(3L-x)x^2+3\nu y^2(L-x)\right] \tag{4.45}$$

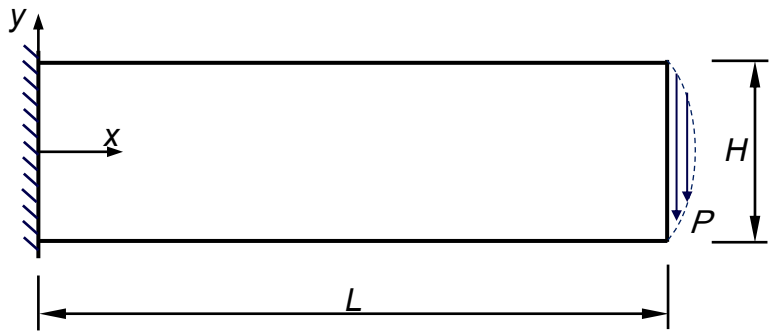

Figure 4.1. A cantilever subjected to a parabolic traction at the free end.

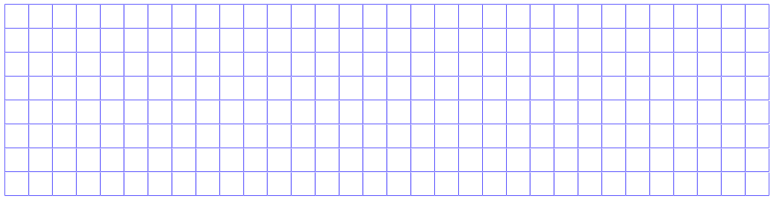

Figure 4.2. Domain discretization using 4-node quadrilateral elements of the cantilever (mesh 32×8).

The corresponding stresses can be expressed as

$$\sigma_{xx}(x,y)=\frac{P(L-x)y}{I};\ \sigma_{yy}(x,y)=0;\ \tau_{xy}(x,y)=\frac{P}{2I}\left(y^2-\frac{D^2}{4}\right) \tag{4.46}$$

where the moment of inertia I of the beam is given by $I=H^3/12$ for this problem. The related geometry/loading parameters and material properties are given as: $L=2.4$ m, $H=0.6$ m, $P=5000$ N, Young's modulus $\mathcal{E}=3.0\times10^7$ Pa (here the script letter "$\mathcal{E}$" is adopted to distinguish it from the notation of the expectation "E"), and the Poisson's ratio $v=0.3$. The perturbation parameter ε is chosen as an interval $\varepsilon\in[0.8,1.2]$, and the input coefficient of variation of the randomized modulus is set as $\gamma(\mathcal{E})\in[0.0,0.3]$.

In Figure 4.2, the domain is discretized by 4-noded quadrilateral elements and these elements can be further divided into different SCs, n_{SC}=1, 2, 3, 4, 8, 16, as shown in Figure 3.2. The relative errors of deflection along centerline obtained from FEM, CS-FEM (mesh: 32×8) and the analytical solution are demonstrated in Figure 4.3. It is seen the deflection v computed by CS-FEM with 4, 8, and 16 smoothing cells can be more accurate than the result of FEM using 4 Gauss points for full integration. It is noted that the model with elements using $n_{SC}=4$ will produce the most accurate results. To study the convergence rate of the present method, the two norms called displacement norm and energy norm can be provided as following:

$$\begin{aligned} Error_d &= \sum_{ndof}\left|u_i-u_i^h\right| \Big/ \sum_{ndof}\left|u_i\right| \\ Error_e &= \frac{1}{2LD}\left[\int_\Omega(\varepsilon^h-\varepsilon)^{\mathrm{T}}\mathbf{D}(\varepsilon^h-\varepsilon)\right]^{1/2} \end{aligned} \tag{4.47}$$

In Figure 4.4, the depicted convergence rate shows CS-FEM can give almost comparable convergence rates compared to FEM in both displacement and energy norms, i.e., CS-FEM preserves the full super-convergence feature similar to FEM. Furthermore, the error in energy norm for the CS-FEM is always smaller than that of FEM, as plotted in Figure 4.4(b).

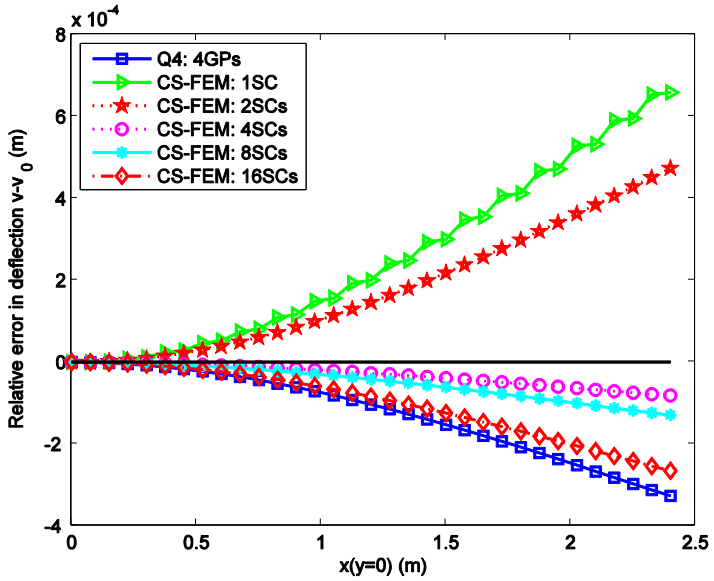

Figure 4.3. Comparison of the relative error in displacement v between FEM and CS-FEM using different number of smoothing cells.

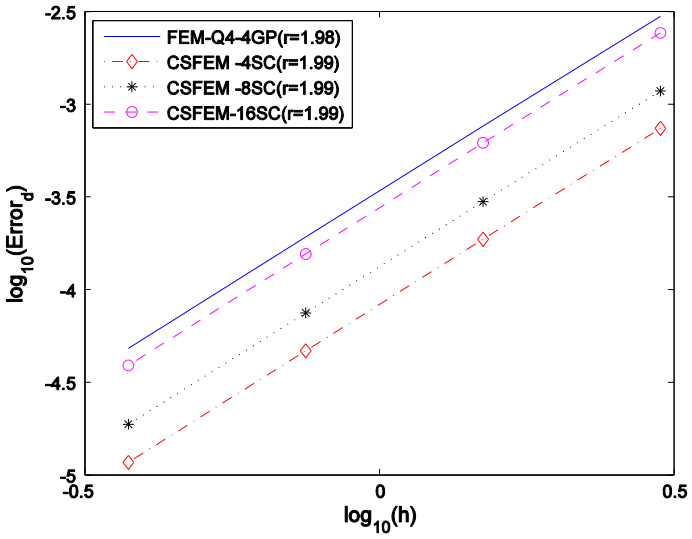

(a)

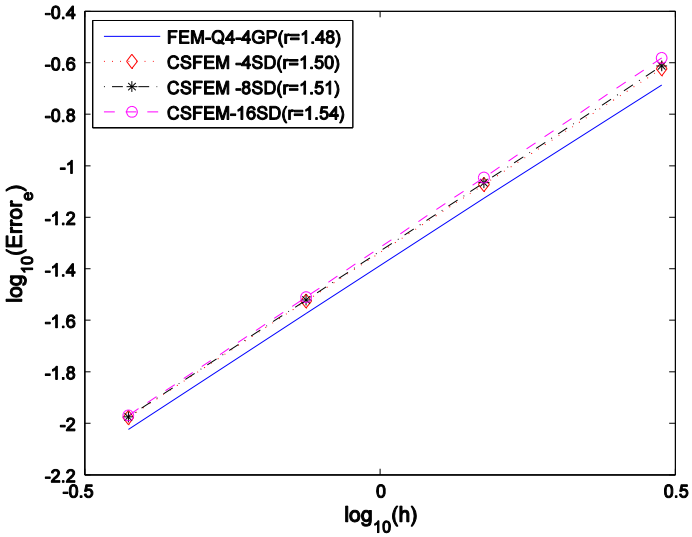

(b)

Figure 4.4. Comparison of convergence rate between S-FEM and FEM: (a) displacement norm; (b) energy norm.

If the input quantity $\mathcal{E}$ consists of Gaussian random distribution, then all the central probabilistic moments can be obtained from the formulae [3]

$$\mu_{2m+1}(\mathcal{E})=0,\ \mu_{2m}(\mathcal{E})=1\cdot 3\cdot 5...(2m-1)\sigma^{2m}(\mathcal{E})=(2m-1)!\,(\mathrm{Var}(\mathcal{E}))^{m} \tag{4.48}$$

Obviously, the maximum vertical deflection v in the centerline is at the center point of the free end. Applying Eqs (4.10) and (4.11), the expectation and variance for this maximum vertical deflection v_m should be

$$E\left[\mathrm{v}_m\left(\varepsilon,\gamma(\mathcal{E})\right)\right]\cong \mathrm{v}_m^0(\mathcal{E})+\frac{1}{2}\frac{\partial^2\mathrm{v}_m}{\partial\mathcal{E}^2}\varepsilon^2(\gamma\mathcal{E})^2+\frac{1}{4!}\frac{\partial^4\mathrm{v}_m}{\partial\mathcal{E}^4}\varepsilon^4(3\gamma\mathcal{E})^4+\frac{1}{6!}\frac{\partial^6\mathrm{v}_m}{\partial\mathcal{E}^6}\varepsilon^6(3\cdot 5\gamma\mathcal{E})^6+... \tag{4.49}$$

$$\begin{aligned}Var\left[\mathrm{v}_m\left(\varepsilon,\gamma(\mathcal{E})\right)\right]=&\left(\frac{\partial\mathrm{v}_m}{\partial\mathcal{E}}\right)^2\varepsilon^2(\gamma\mathcal{E})^2+\left(\frac{1}{4}\left(\frac{\partial\mathrm{v}_m}{\partial\mathcal{E}}\right)^2+\frac{2}{3!}\left(\frac{\partial\mathrm{v}_m}{\partial\mathcal{E}}\right)\left(\frac{\partial^3\mathrm{v}_m}{\partial\mathcal{E}^3}\right)\right)\varepsilon^4(3\gamma\mathcal{E})^4\\&+\left(\left(\frac{1}{3!}\right)^2\left(\frac{\partial^3\mathrm{v}_m}{\partial\mathcal{E}^3}\right)^2+\frac{1}{4!}\left(\frac{\partial^2\mathrm{v}_m}{\partial\mathcal{E}^2}\right)\left(\frac{\partial^4\mathrm{v}_m}{\partial\mathcal{E}^4}\right)+\frac{2}{5!}\left(\frac{\partial\mathrm{v}_m}{\partial\mathcal{E}}\right)\left(\frac{\partial^5\mathrm{v}_m}{\partial\mathcal{E}^5}\right)\right)\varepsilon^6(3\cdot 5\gamma\mathcal{E})^6+...\end{aligned} \tag{4.50}$$

The expected values of the maximum vertical deflection in centerline for $2nd$, $4th$, $6th$, $8th$, $10th$ order stochastic smoothed finite element approximation are provided in Figure 4.5. The corresponding standard deviations are collected in Figure 4.6, and the output variances are presented in Figure 4.7. The expected values, standard deviations and the output variances are shown with respect to (w.r.t.) only perturbation parameter ε (while the input coefficient of variation γ is set as 0.10 and 0.25, separately) in Figure 4.8–Figure 4.13.

From Figure 4.5–Figure 4.7, it is observed that the expected values and standard deviations increase nonlinearly along with the increasing of the perturbation parameter ε or the input coefficient of variation γ. Besides, it is apparent that the convergence of the GS_CS-FEM

depends on the input γ. The 2^{nd} order Taylor expansion perturbation is suitable for the situation when the input $\gamma(E)$ is no more than 0.10. Otherwise, it requires an approximation with a higher perturbation order. In addition, the input coefficient of variation will play more crucial impact on these probabilistic characteristics than the perturbation parameter, especially as $\gamma \leq 0.10$.

The comparison of the expected values, standard deviations and the output variances are plotted in Figure 4.8–Figure 4.13, for $\gamma = 0.10$ and $\gamma = 0.25$. It is obviously that for a smaller value of input coefficient of variation, such as 0.10, the 4^{th} order perturbation approximation can satisfy the accuracy/convergence requirement. However, even 10^{th} order perturbation is not enough for the case using γ=0.25, especially for standard deviations and the variances. In conclusion, the 2^{nd} order expansion perturbation technique works well in precision when the input γ is less than 0.10 and may be effective for $0.10 \leq \gamma \leq 0.15$, but may lead to low accuracy for larger γ.

In Figure 4.14 and Figure 4.15, the expected values for 2, 4, 6, 8, 10^{th} order GS_CS-FEM approximation are compared to the results of Monte Carlo simulation (MCs). It is evident that the GS_CS-FEM using higher order perturbations provides higher accuracy of solution compared to the results obtained from the MCs. Referring to computational efficiency, the CPU time for the GS_CS-FEM is only 15.5 seconds, while it requires more than thousands times of computation time for MCs calculation in a reasonable accuracy as a reference solution (even only 2000 times picked as the number of analysis for MCs, more than 7760 seconds required). If other randomized variables are considered, one can also apply similar implementations using the GS_CS-FEM approach.

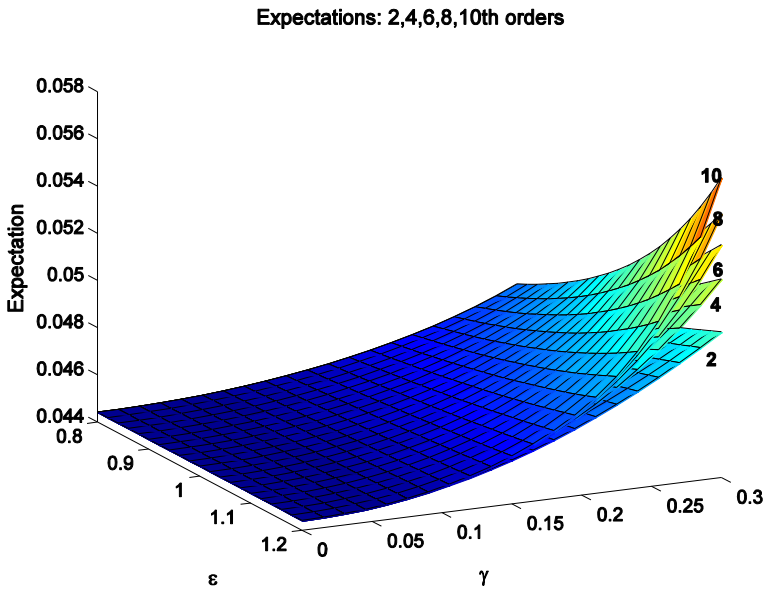

Figure 4.5. Expected values for 2, 4, 6, 8, 10th orders.

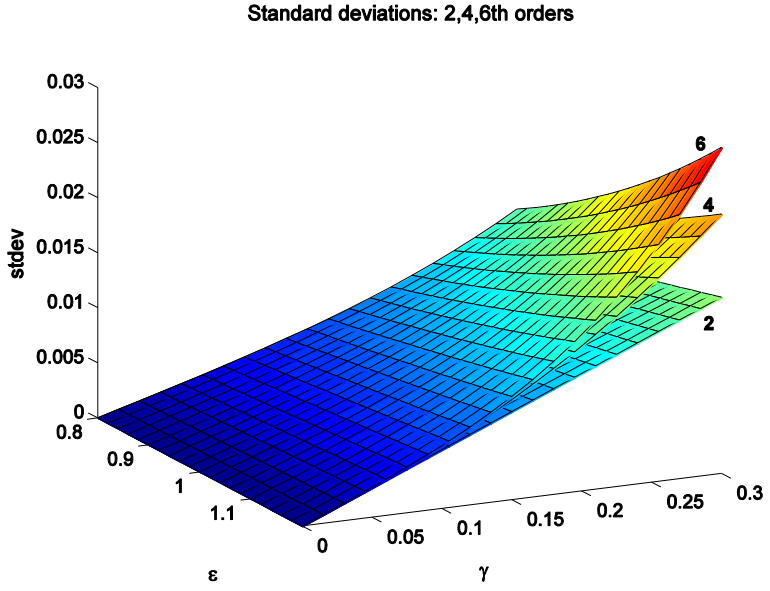

Figure 4.6. Standard deviations for 2, 4, 6th orders.

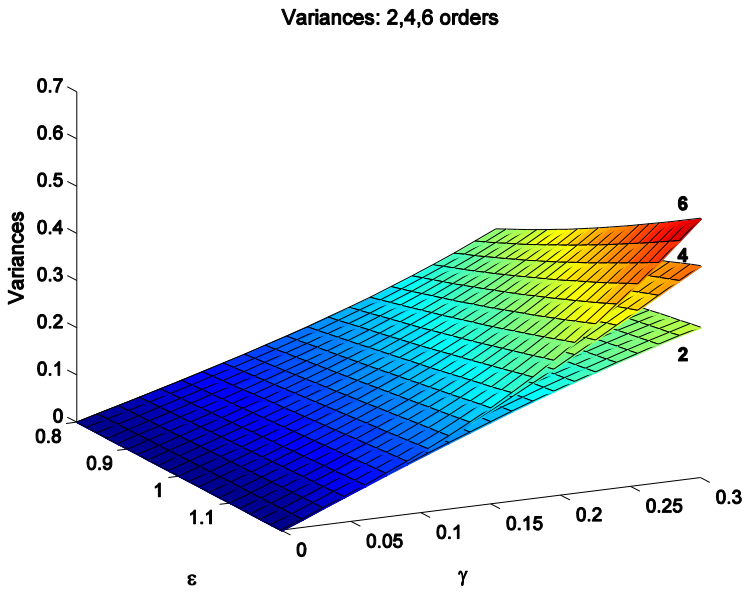

Figure 4.7. Variances for 2, 4, 6th orders.

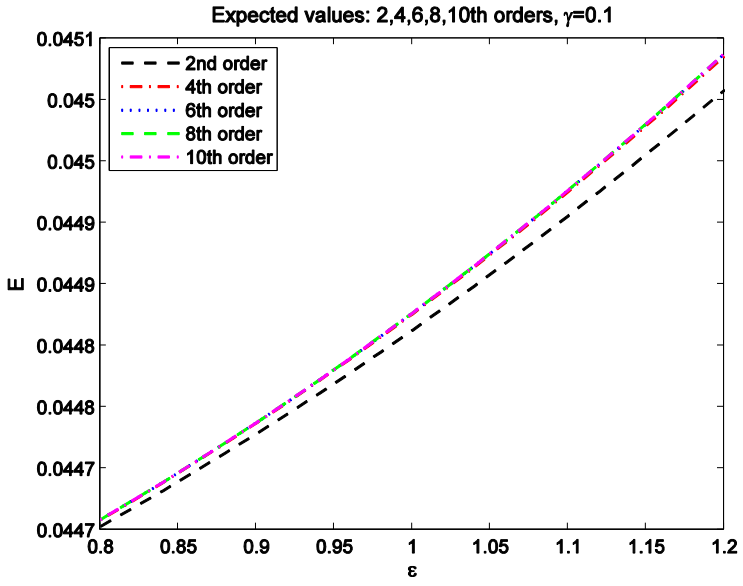

Figure 4.8. Expected values: 2, 4, 6, 8, 10th orders; γ : 0.10 .

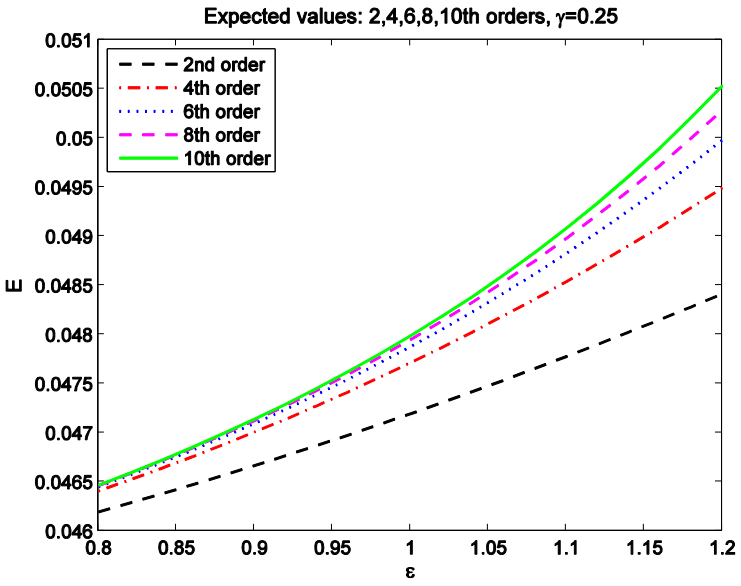

Figure 4.9. Expected values: 2, 4, 6, 8, 10th orders; γ : 0.25 .

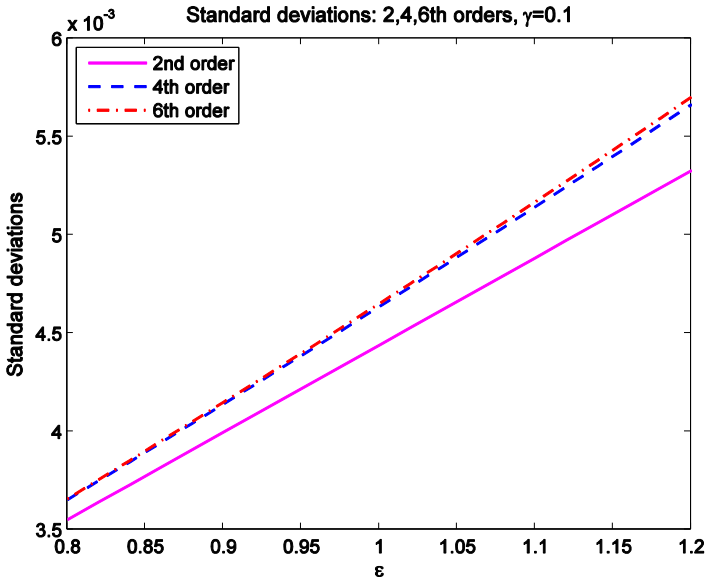

Figure 4.10. Standard deviations: 2, 4, 6th orders; γ : 0.10 .

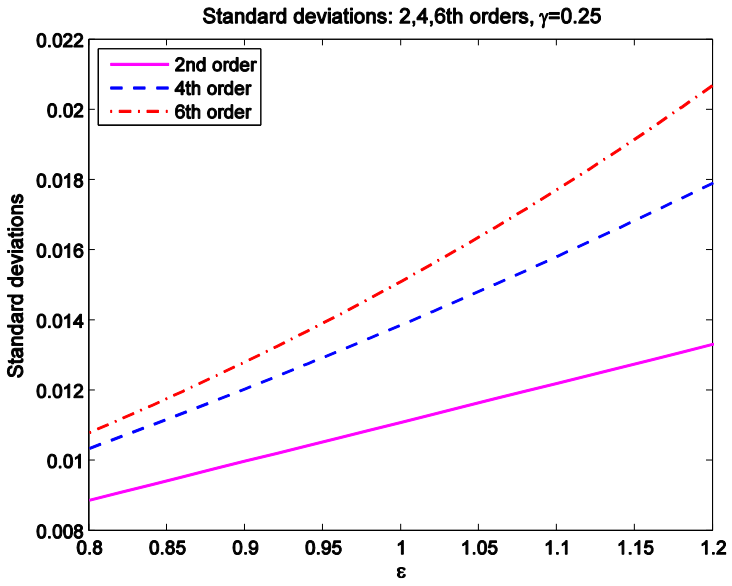

Figure 4.11. Standard deviations: 2, 4, 6th orders; $\gamma : 0.25$.

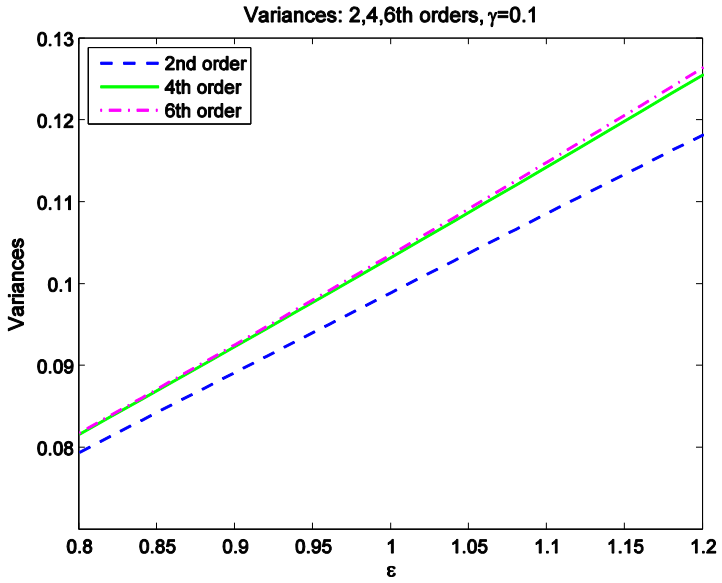

Figure 4.12. Variances: 2, 4, 6th orders; $\gamma : 0.10$.

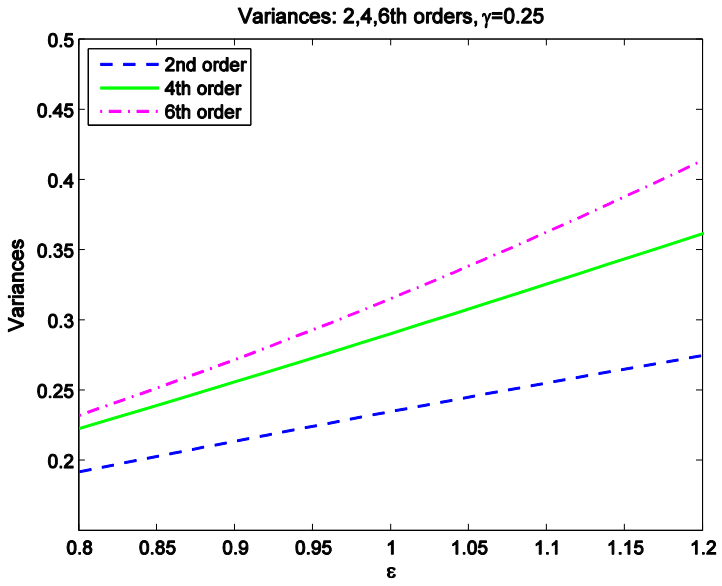

Figure 4.13. Variances: 2, 4, 6th orders; $\gamma : 0.25$.

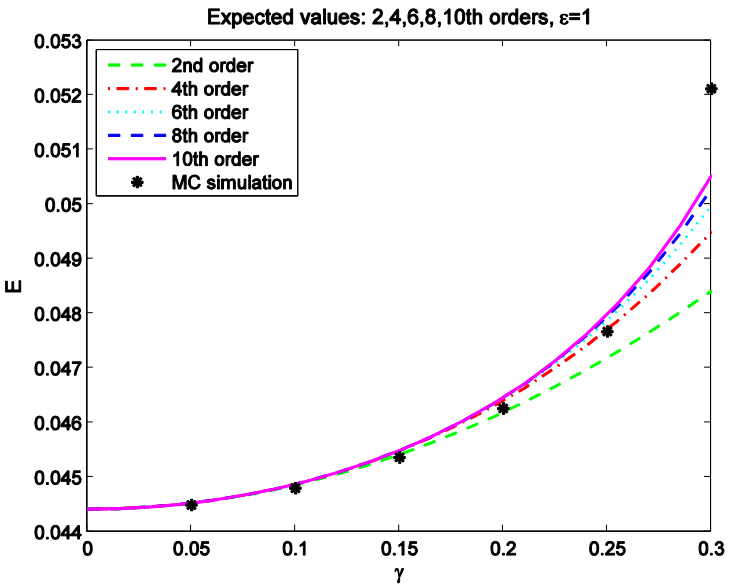

Figure 4.14. Expected values; GS_CS-FEM vs. MCs.

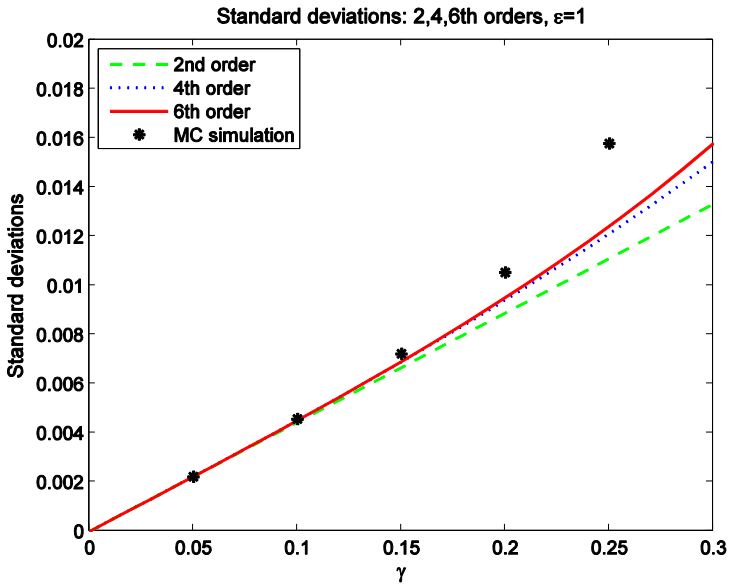

Figure 4.15. Standard deviations; GS_CS-FEM vs. MCs.

4.5.2 Infinite Plate with Circular Hole

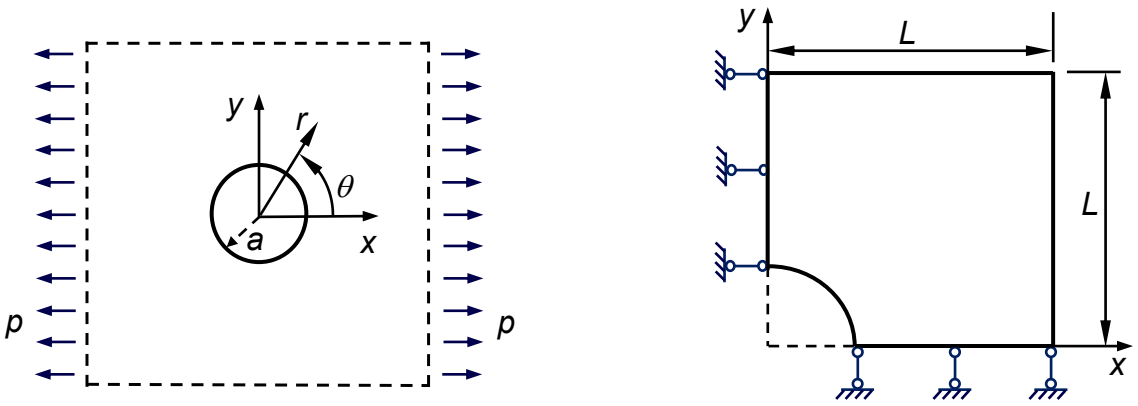

Figure 4.16. Infinite plate with a circular hole subjected to x-directional tension and a symmetric geometry.

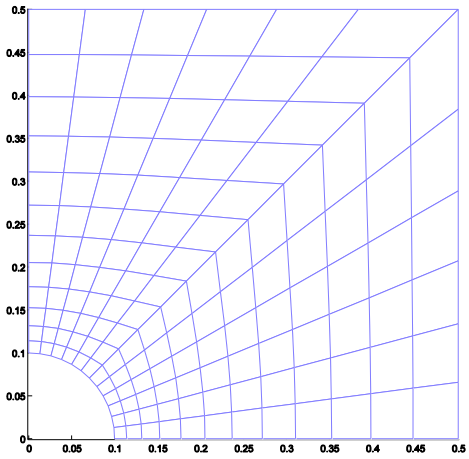

Figure 4.17. Domain discretization using 4-node quadrilateral elements of the infinite plate with a circular hole.

Figure 4.16 represents a plate with a central circular hole subjected to a unidirectional tensile load of $p = 1.16 \times 10^6$ N/m at infinity in the x direction. Since the stress concentration around the hole is highly localized and decays very rapidly, essentially disappearing when the distance to the center is greater than $5a$, only a finite plate with $l = 5a$ needs to be modeled. Due to its symmetry, only the upper right quadrant of the plate is selected and discretized by 144 elements. The case is considered as a plane strain problem and Young's modulus $E = 90 \times 10^6$ N/m^2, Poisson's ratio $\nu = 0.3$. The inner edge of the hole is traction free and symmetric conditions are set along the left and bottomed edges. On the right ($x = 0.5$ m) and top ($y = 0.5$ m) edges, traction boundary conditions are imposed according to the exact solution [13]. The analytical solution for displacement components is [14,15]

$$u_x = \frac{pa}{8\mu'}\left[\left(2\frac{a}{r}+\frac{r}{a}\right)(1+\kappa)\cos\theta + 2\frac{a}{r}\left(1-\frac{a^2}{r^2}\right)\cos 3\theta\right]$$
$$u_y = \frac{pa}{8\mu'}\left[\left(2\frac{a}{r}-\frac{r}{a}\right)(1-\kappa)\sin\theta + 2\frac{a}{r}\left(1-\frac{a^2}{r^2}\right)\sin 3\theta\right] \tag{4.51}$$

where the shear modulus $\mu' = \frac{\mathcal{E}}{2(1+\nu)}$ and bulk modulus $\kappa = 3-4\nu$ for plane strain cases, (r,θ) are the polar coordinates and θ is measured counterclockwise from the positive x-axis. The exact solution for the stress is given as [14,15]

$$\sigma_{11} = p\left[1-\frac{a^2}{r^2}\left(\frac{3}{2}\cos 2\theta+\cos 4\theta\right)+\frac{3a^4}{2r^4}\cos 4\theta\right]$$
$$\sigma_{22} = p\left[-\frac{a^2}{r^2}\left(\frac{1}{2}\cos 2\theta-\cos 4\theta\right)-\frac{3a^4}{2r^4}\cos 4\theta\right] \tag{4.52}$$
$$\tau_{12} = p\left[-\frac{a^2}{r^2}\left(\frac{1}{2}\sin 2\theta+\sin 4\theta\right)+\frac{3a^4}{2r^4}\sin 4\theta\right]$$

In order to avoid the redundancy, it's unnecessary to repeat the plots for convergence rate of displacement and energy, as these performances are quite similar to the cantilever example. Figure 4.17 describes 4-noded quadrilateral elements mesh used to discretize the problem domain. Similar to plane stress example, the modulus $\mathcal{E}$ is adopted as the input random variable, the perturbation parameter ε is chosen as the interval of $[0.8,1.2]$, and the input coefficient of variation of the randomized modulus is set as $\gamma(\mathcal{E}) \in [0.0,0.3]$. The horizontal displacement at point $(0.1,0)$ is adopted as the output probabilistic variable. The expected values, standard deviations and output coefficients of variation are collected respectively in Figure 4.18, Figure 4.19 and Figure 4.20. The expected values, standard deviations and output coefficients of variation are plotted w.r.t. only perturbation parameter ε (while the input γ is set as 0.10 and 0.25, separately) in Figure 4.21–

Figure 4.26. In Figure 4.27 and Figure 4.28, the expected values and standard deviations obtained from GS_CS-FEM are compared to the corresponding results from MCs. It is shown again that the GS_CS-FEM using higher order perturbations yields higher accuracy approximation. Several other properties of GS_CS-FEM in this problem are quite similar to those in the previous example.

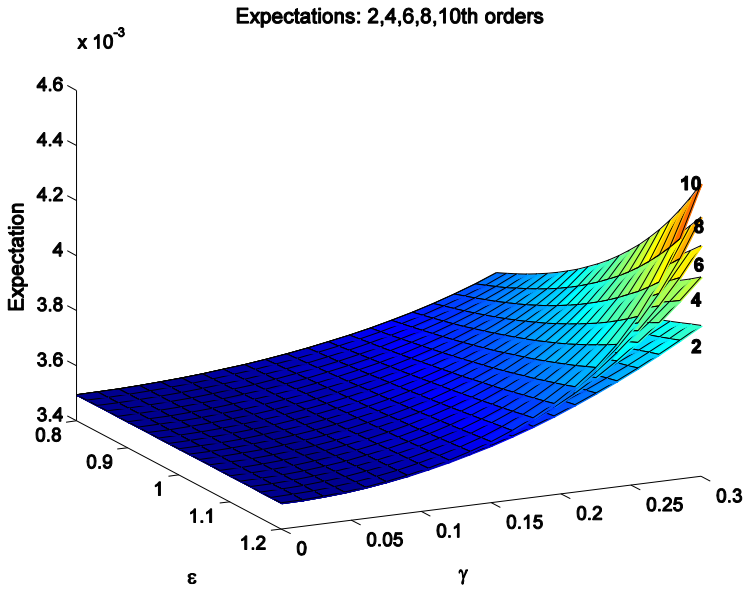

Figure 4.18. Expected values for 2, 4, 6, 8, 10th orders

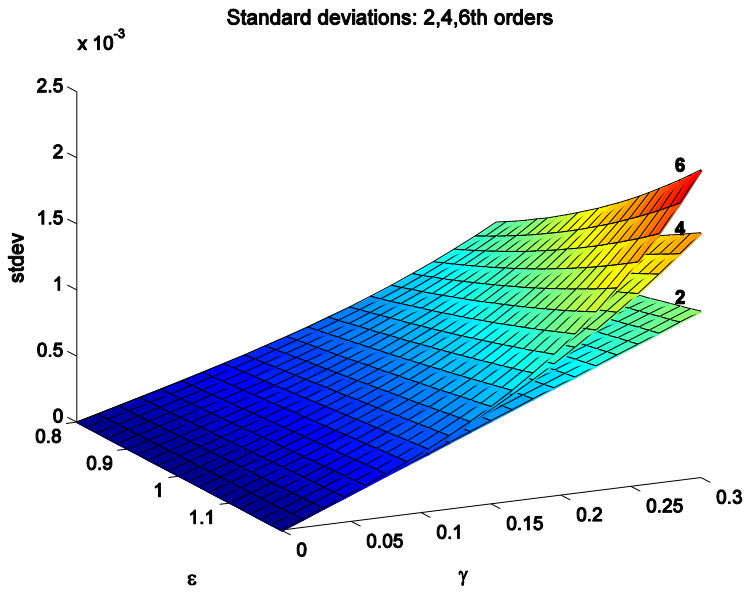

Figure 4.19. Standard deviations for 2, 4, 6th orders

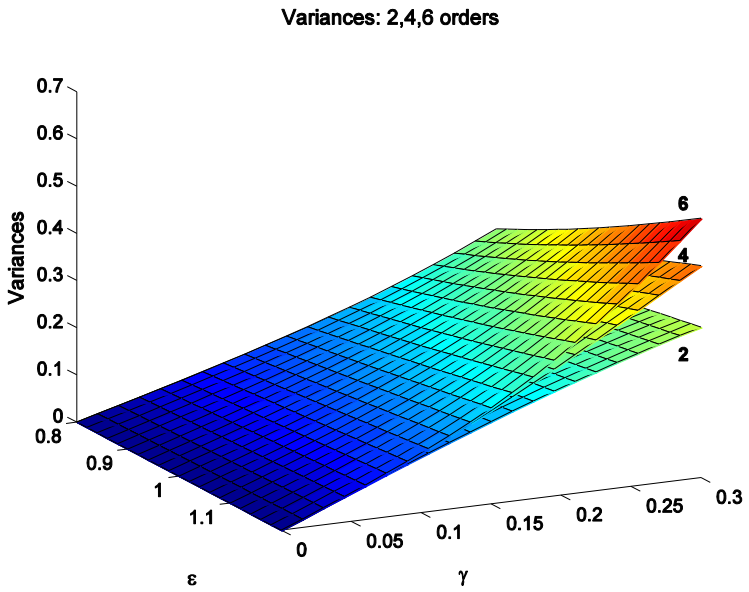

Figure 4.20. Variances for 2, 4, 6th orders

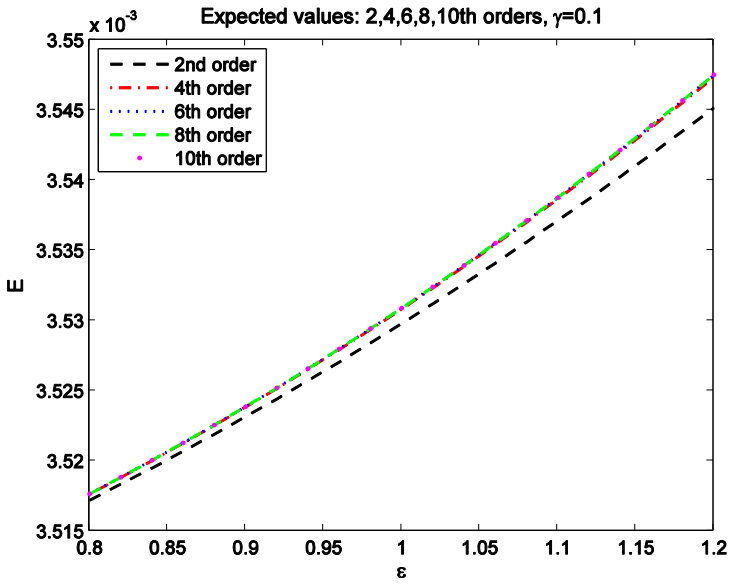

Figure 4.21. Expected values: 2, 4, 6, 8, 10th orders; γ : 0.10

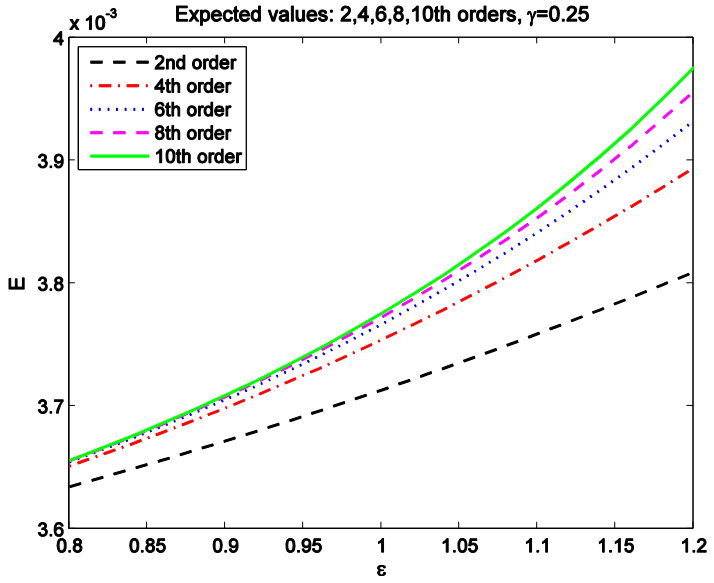

Figure 4.22. Expected values: 2, 4, 6, 8, 10th orders; γ : 0.25

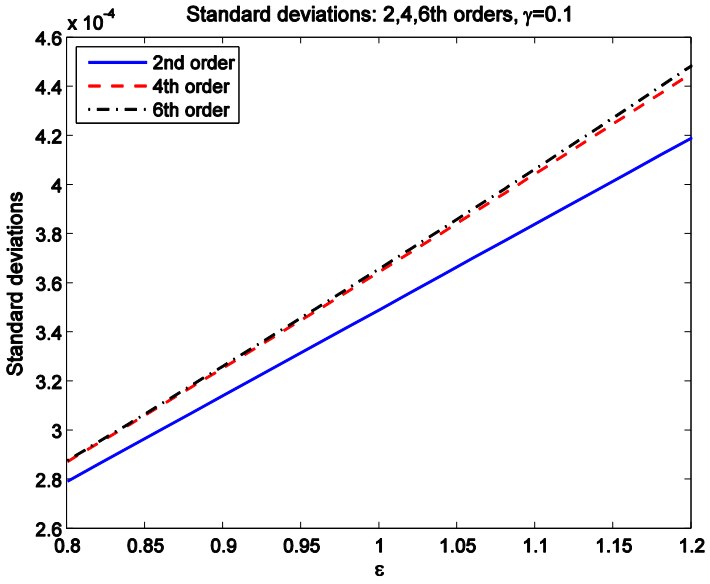

Figure 4.23. Standard deviations: 2, 4, 6th orders; γ : 0.10

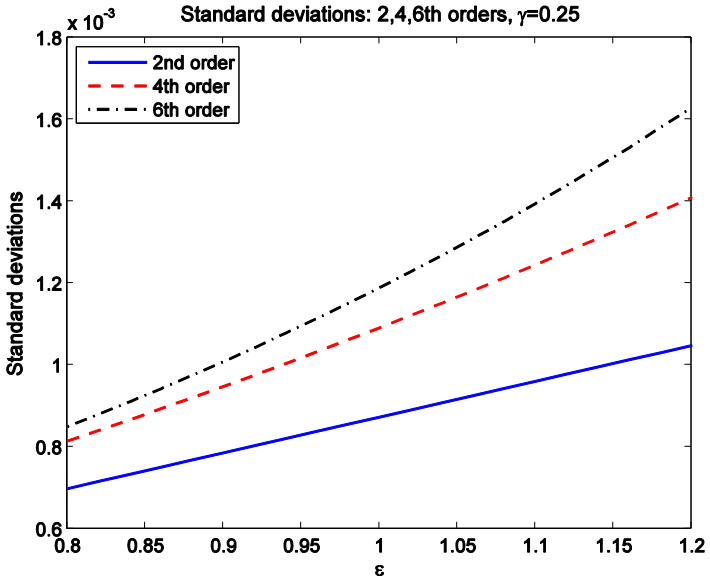

Figure 4.24. Standard deviations: 2, 4, 6th orders; γ : 0.25

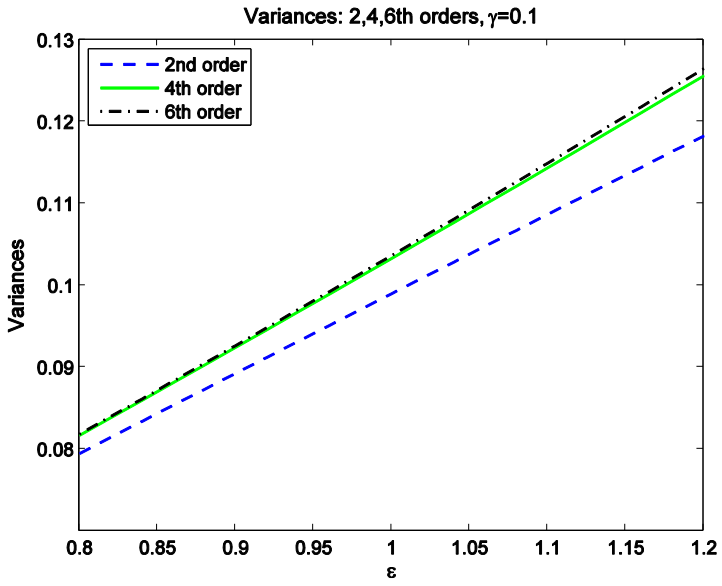

Figure 4.25. Variances: 2, 4, 6th orders; γ : 0.10

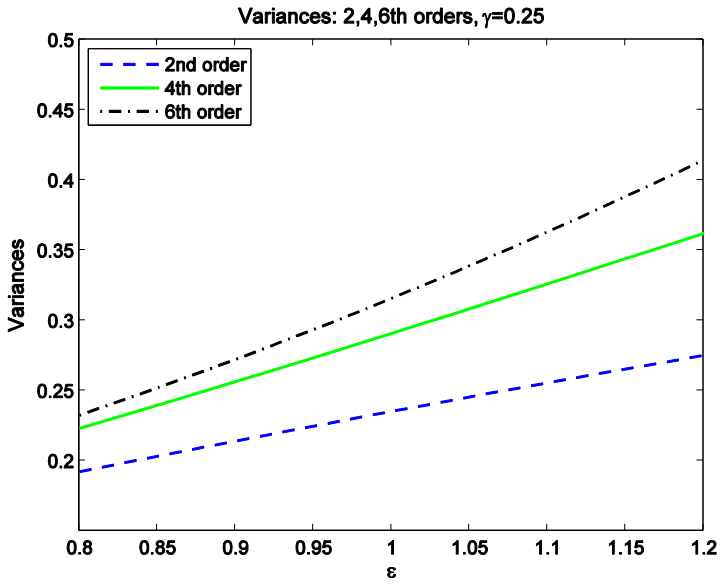

Figure 4.26. Variances: 2, 4, 6th orders; γ : 0.25

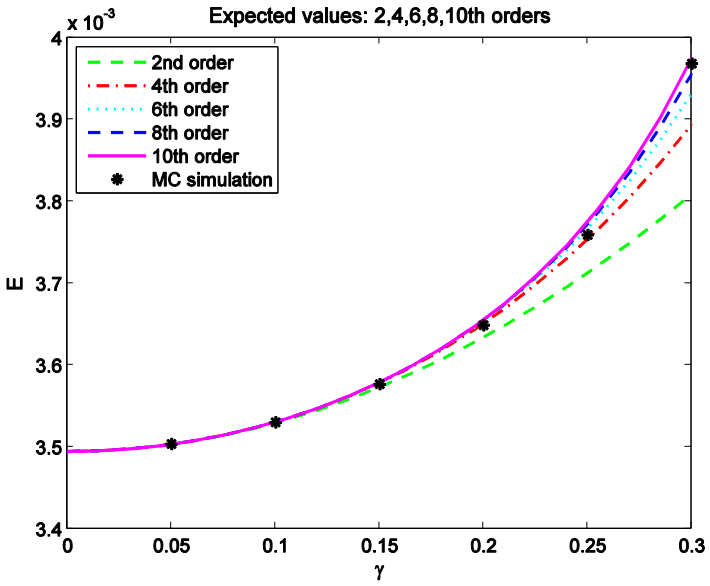

Figure 4.27. Expected values; GS_CS-FEM vs. MCs

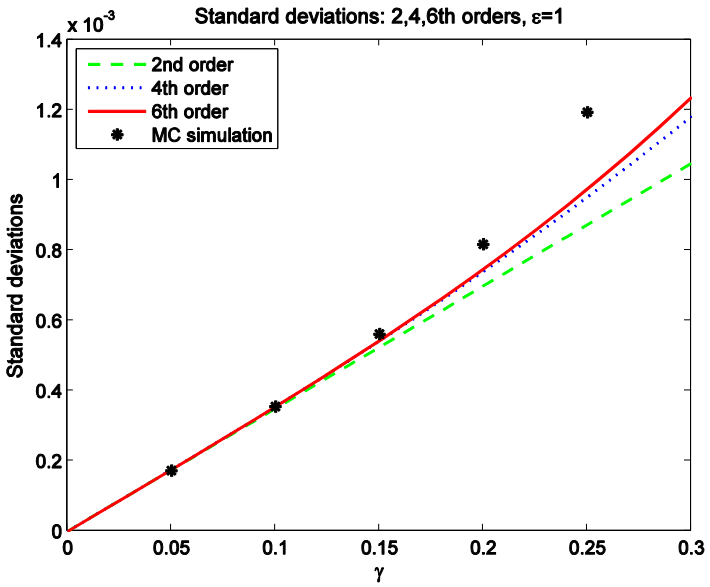

Figure 4.28. Standard deviations; GS_CS-FEM vs. MCs

4.6 Conclusions

In this chapter, a generalized stochastic cell-based smoothed finite element method (GS_CS-FEM) is proposed. The method is applied to both plane stress and plane strain examples. The efficiency and accuracy of the proposed GS_CS-FEM are verified by comparison with results of MCs. The effects of input coefficients of variation and perturbation parameters are investigated, and some conclusions can be drawn as follows:

- The 2^{nd} order approximation may be sufficient for a small input coefficient of variation γ such as less than 0.1, but higher γ needs an approximation with higher order perturbation. For instance, at least 10^{th} order perturbation are required for $\gamma = 0.3$.
- In deterministic computation, it has already proved that the cell-based smoothed finite element method (CS-FEM) can significantly improve accuracy and convergence compared to the FEM [14-15]. As expected, the same level of improvement can be achieved for the probabilistic solutions. This is because the improvement by CS-FEM is achieved by spatial approximation of the strain field. Since the stochastic modeling utilized the same fashion of approximation, the benefit of CS-FEM will be delivered.
- It is expected that there is no technical difficulty in further extending the application of GS_CS-FEM for other input random variables or the applications to other probability distributions.

References

[1] Haldar A and Mahadevan S. 2000. Reliability assessment using stochastic finite element analysis. John Wiley and Sons, NY.

[2] Stefanou G. 2009. The stochastic finite element method: Past, present and future. Computer Methods in Applied Mechanics and Engineering; 198: 1031–1051.

[3] Kamiński M. 2006. On generalized stochastic perturbation-based finite element method. International Journal for Numerical Methods in Biomedical Engineering; 22: 23–31.

[4] Kamiński M. 2010. Generalized stochastic perturbation technique in engineering computations. Mathematical and Computer Modelling; 51: 272–285.

[5] Kleiber M and Hien TD. 1992. The stochastic finite element method. John Wiley and Sons, West Sussex, England.

[6] Çavdar Ö, Bayraktar A and Çavdar A. 2011. Effects of random material and geometrical properties on structural safety of steel-concrete composite systems. International Journal for Numerical Methods in Biomedical Engineering; 27: 1473–1492.

[7] Haldar A and Mahadevan S. 2000. Reliability assessment using stochastic finite element analysis. John Wiley and Sons, NY.

[8] Stefanou G. 2009. The stochastic finite element method: Past, present and future. Computer Methods in Applied Mechanics and Engineering; 198: 1031–1051.

[9] Bathe KJ. 1996. Finite element procedures. MIT Press, Prentice-Hall, Englewood Cliffs, NJ.

[10] Dai KY, Liu GR, and Nguyen TT. 2007. An n-sided polygonal smoothed finite element method (nSFEM) for solid mechanics. Finite Elements in Analysis and Design; 43: 847–860.

[11] Liu GR and Nguyen-Thoi T. 2010. Smoothed finite element methods. CRC Press (Taylor & Francis), Boca Raton.

[12] Kamiński M. 2007. Generalized perturbation-based stochastic finite element method in elastostatics. Computers and Structures; 85: 586–594.

[13] Timoshenko SP and Goodier JN. 1970. Theory of elasticity, 3rd edition. McGraw-Hill, NY.

[14] Liu GR, Nguyen-Thoi T, Dai KY, and Lam KY. 2007. Theoretical aspects of the smoothed finite element method (SFEM). International Journal for Numerical Methods in Engineering; 71: 902–930

[15] Nguyen-Xuan H, Bordas S and Nguyen-Dang H. 2008. Smooth finite element methods: convergence, accuracy and properties. International Journal for Numerical Methods in Engineering; 74: 175–208.

Chapter 5. An Effective Fracture Analysis Method Based on the Virtual Crack Closure-integral Technique Implemented in CS-FEM

5.1 Introduction

In modern fracture mechanics, the well-known Irwin's work [1] uses the Westergaard approach and showed that, for elastic materials, the stresses and displacements near the crack-tip could be described by a single constant, which is related to the strain energy release rate [2]. Likewise, the Eshelby–Cherapanov–Rice *J*-integral [3–6] has then provided a way to calculate the strain energy release rate, or work/energy per unit fracture surface area. In general, almost all the fracture properties of a solid with elastic material can be characterized using a couple of parameters extracted from the near-tip stress and displacement fields. For example, the stress intensity factors (SIF's) K defines the amplitude of the crack tip singularity. Since closed-form analytical solutions for these parameters are only available for some simple problems, numerical modeling techniques such as finite element methods (FEM) and boundary element methods (BEM) are utilized almost exclusively.

To predict facture parameters such as the stress intensity factors, a few classical approaches have been developed including the displacement correlation method (DCM, i.e., displacement extrapolation method [7–10]), domain integral (DI) methods (e.g., interaction integral (I-integral) method [11,12]), stiffness derivative method or virtual crack extension approach (VCE) [13,14], virtual crack closure technique (VCCT) [15,16], etc. In general, most

of these methods could be classified into two categories: the point matching approaches (or direct approaches) and the energy based approaches. The inferring of SIF's by the first category of approaches uses stress or displacement fields near the crack-tip directly and the accuracy depends on the nodal displacement or stress directly, which is hence sensitive to associated mesh in FE computation. On the other hand, the energy based approaches evaluate the energy release rates in the body and relate G to SIF's. The energy based approaches, in general, are applicable to elastic as well as elastic-plastic materials and they perform insensitive to mesh quality at the vicinity of the crack tip/front. Nonetheless, the point matching approach would be usually more simple and easy to implement in FE programming.

Before evaluation of the stress intensity factors, the energy based approaches need firstly to compute the strain energy release rate based on results obtained from finite element analysis (FEA). There are a variety of methods to compute the energy release rates, among which three popular ways are usually used: *J*-integral method (or *I*-integral), virtual crack extension method (VCEM) and virtual crack closure integral method (VCCM or VCCT). The VCEM computes the energy difference during two finite element analyses when a crack extends for a small amount of increment. While the energy in VCCT, which is required to close the crack for one finite element length, is calculated via multiplying the nodal reactions and the opening displacements. This approach was first proposed by Rybicki and Kanninen [15] for 2D crack problems and was later improved by Raju et al. [17,18]. It was also extended for 3D analysis of crack problems by Shivakumar et al. [16]. When inferring the energy release rate from FEA results, the VCCT has several advantages, such as simplicities in computation which involves only the nodal reaction forces at the crack tip/front and opening displacements just behind the tip/front, and convenience

of mode separation when appropriate vector components are utilized in computation of components of the energy release rates.

Over the past two decades, the VCCT has been developed and extended to various aspects. For example, Refs [19,20] used VCCT to treat delamination between the face sheet and the core material of sandwich structures. Xie et al. [21–23] proposed the VCCT formulations for kinking cracks and for a moving delamination front of arbitrary shape. Based on FEA results, Sun and Qian [24] computed the strain energy release rates for interfacial cracks between two isotropic materials. Leski [25] provided the implementation of VCCT in engineering FE calculations and introduced the general conditions of applying VCCT in conjunction with commercial programs (MSC.Patran). In order to extend to 3D problems, Okada et al. [26,27] developed VCCT schemes to compute the energy release rates and stress intensity factors for both linear and quadratic tetrahedral finite elements. Whitcomb [28] computed the strain release rate distributions along a post-buckled embedded delamination including the contact effects. Fawaz [29] performed the sensitivity study of mesh pattern on the accuracy of the calculation of strain energy release rates. In Ref. [30], Krueger presented an overview of historical development of VCCT and a discussion of its applications in engineering. For more details of recent development and applications related to VCCT, we can refer to this review and the references cited therein.

Though the FEM has become the most popular and powerful numerical tool for practical problems in engineering and science including fracture mechanics, it does not mean that it is perfect and no room for improvement. For example, FEM exists the overestimation of stiffness of solid and structures, which may result in locking behavior and inaccuracy in stress solutions [31]. By incorporating the strain smoothing technique [32] into finite element method (FEM),

Liu et al. have formulated a series of smoothed finite element methods (S-FEMs) containing cell-based S-FEM (CS-FEM) [33–35], node-based S-FEM [36,37], edge-based S-FEM [38–40], face-based S-FEM [41,42] and combinations of these techniques [43–45]. Several theoretical aspects of the S-FEM models have been provided in Refs [46–49]. Owing to the strain smoothing operations, the "over-stiff" feature of the standard FEM can be reduced or alleviated and hence the accuracy of both primal and dual quantities can be improved significantly [50]. Moreover, S-FEM does not require the shape function derivatives and S-FEM models developed in elasticity are insensitive to mesh distortion because of the absence of isoparametric mapping [40]. Each of these smoothed FEM has different properties and has been applied to various types of practical mechanics problems. Due to its versatility, the class of S-FEMs has been becoming a simple and effective numerical tool for solving numerous physical problems.

In this work, the VCCT will be formulated and implemented based on the CS-FEM framework. The elements in an FE base mesh will be further subdivided into several smoothing cells (SCs) (e.g., 4 SCs). The Galerkin weak form is used as in FEM, but the strain field at any point in an element is defined as a weighted spatial average over the element. Through such smoothing operation, the obtained smoothed strains will be then used for computing the stiffness matrix. If piecewise-constant weight functions are adopted, area integrations over the domain of cell in the weak form become contour integration along the boundaries of the smoothing cells. As a result, only shape functions themselves (not the derivatives) will be involved in computing the field gradients to obtain the stiffness matrix. Numerical studies [33,51–56] have demonstrated that CS-FEM shows some interesting properties compared to the standard FEM using 4-node isoparametric elements. For examples, (1) CS-FEM can obtain better results than those of FEM in both displacement and energy because of the softening effect; (2) less strict

mesh quality requirements as no coordinate transformation or mapping is involved in CS-FEM (e.g., Abaqus will not run a job with a Jacobian below 0, and requires the Jacobian be great than 0.2 for a solid element and 0.3 for a shell element); (3) construction of shape functions would be easier and flexible than that in the FEM, which practically allows explicit interpolations of field variables; (4) many existing algorithms of FEM can be easily modified and applied to CS-FEM [57,58]. Most importantly, these good features are obtained still within the general frame of FEM, without special procedure except the process of strain smoothing and stiffness assembling.

For numerical evaluation of strain energy release rate or SIF's based on FEA, the domain integral methods usually offer even better accuracy than VCCT. However, the implementation of VCCT is much simpler and the computation cost is always lower, since the associated calculation only involves the nodal reaction forces and opening displacements which are the general outputs of FEA. The work in this chapter will employ the simplicity and convenience of VCCT under the framework of CS-FEM. It will utilize the merits of both VCCT and CS-FEM to formulate a better numerical approach for evaluation of fracture mechanics parameters and then modeling the process of crack propagation. The idea and formulation of CS-FEM for elastic problems has already been introduced in the previous chapter. In Section 2 of this chapter, we will present the techniques for evaluating fracture parameters using VCCT based on outputs of CS-FEM. Some numerical examples will be studied in Section 3 to illustrate the proposed approach. Conclusions are offered in Section 4.

5.2 VCCT for Crack Problems Using CS-FEM Results

5.2.1 Crack Closure Integrals

Irwin [1] introduced the crack closure integral concept in 1950s, which is an energy conservation argument on crack extension [59]. If a crack in a homogenous material is under the loading condition of Mode I (opening mode), the strain energy (per unit area) released during a small crack increment of extension is equivalent to the energy required to close the crack, i.e., the strain energy release rate illustrated in Figure 5.1 can be generally expressed as

$$G_{\mathrm{I}} = \lim_{\Delta l \to 0} \frac{1}{2\Delta l} \int_0^{\Delta l} \sigma_y(\Delta l - r, 0) \Delta v(r, \pi) \mathrm{d}r \tag{5.1}$$

where σ_y is the normal stress along the closed crack surface (line), Δl is the small extension of crack and Δl stands for the opening displacements of y direction for the location along the closed crack surface when the crack is extended.

For Mode II (shearing mode), the similar expression of strain energy release rate using the crack closure integral concept becomes [15]:

$$G_{\mathrm{II}} = \lim_{\Delta l \to 0} \frac{1}{2\Delta l} \int_0^{\Delta l} \tau_{xy}(\Delta l - r, 0) \Delta u(r, \pi) \mathrm{d}r \tag{5.2}$$

where Δu is the corresponding displacements at x direction.

The above two crack closure integrals relate the energy release rates to the crack-tip stress and displacement fields for a small crack extension. Though the integrals are proposed initially for cracks in homogeneous materials, it is worth emphasizing that they are proven to be applicable to interface cracks under mechanical load [60–62], thermal load [63] and extended to variable forms [64].

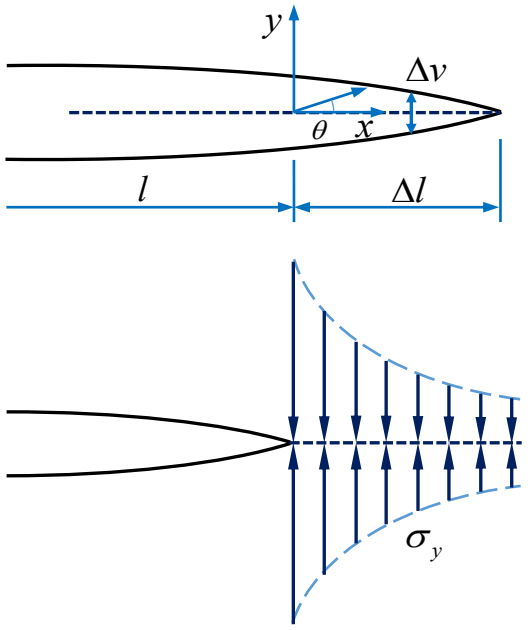

Figure 5.1. Sketch of crack-tip stress and displacement fields used in Irwin's crack closure integral.

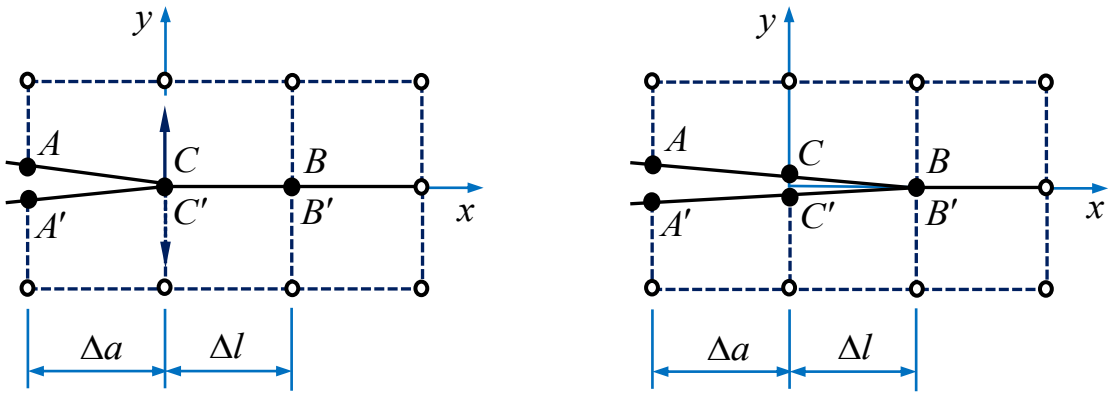

(a) (b)

Figure 5.2. Local mesh configuration used for VCCM.

The implementation of Eq. (5.1) and (5.2) can be performed by two steps: one analysis is to compute the stresses for closing the crack and the other one is to calculate the corresponding

displacements, as depicted in Figure 5.2. If the size of crack-tip elements is small enough, then the expressions can be approximated as

$$G_{\mathrm{I}} \cong \frac{1}{2\Delta l}\int_0^{\Delta l} \sigma_y^{(1)} \Delta v^{(2)} \mathrm{d}x \tag{5.3}$$

$$G_{\mathrm{II}} \cong \frac{1}{2\Delta l}\int_0^{\Delta l} \tau_{xy}^{(1)} \Delta u^{(2)} \mathrm{d}x \tag{5.4}$$

When a CS-FEM (or FEM) technique is adopted for computations, the accuracy of stress values would be low for those nodes near the crack-tip. For the sake of obtaining an accurate solution and easy implementation, the crack closure integrals can be expressed directly in terms of displacements and the internal finite element nodal forces, which are primary variables of the CS-FEM techniques. Also the fracture modes can be easily separated. If the integrals of stress are replaced by the nodal forces, the above equations for a cracked body with thickness B can be then rewritten as

$$G_{\mathrm{I}} \cong \frac{F_{ey}^{(1)} \Delta v_e^{(2)}}{2B\Delta l} \tag{5.5}$$

$$G_{\mathrm{II}} \cong \frac{F_{ex}^{(1)} \Delta u_e^{(2)}}{2B\Delta l} \tag{5.6}$$

5.2.2 VCCT Formulations and Energy Release Rate Extracting

The idea of one-step-analysis virtual crack closure method is assumed that the displacements CC' behind the virtual crack (which is just the original tip for real crack as in Figure 5.2(a)) can be closely approximated by the displacements AA' behind the real crack. In this case the expressions for energy release rates are

$$G_{\mathrm{I}} \cong \frac{F_{Cy}\Delta v_{AA'}}{2B\Delta l} = \frac{1}{2B\Delta l}\left[F_{Cy}\left(v_A - v_{A'}\right)\right] \tag{5.7}$$

$$G_{\mathrm{II}} \cong \frac{F_{Cy}\Delta u_{AA'}}{2B\Delta l} = \frac{1}{2B\Delta l}\left[F_{Cx}\left(u_A - u_{A'}\right)\right] \tag{5.8}$$

Here we will introduce another way to mathematically explain the above formulations, which stands on the assumption that the stress fields around the virtual crack-tip could be approximated closely to those around the real crack-tip [21] (or named as assumption of stress field equivalence). This assumption is actually based on the general common sense: when the geometry dimension, boundary conditions and external loading of a specimen are fixed, an infinitesimal perturbation of crack-tip location would not significantly affect the stress/displacement field. If we consider a linear elastic isotropic material under Mode I loading condition, which has a real crack with its tip at C (or C', in Figure 5.2(a)) and an infinitesimal virtual crack CB before it, the displacement and stress fields can be expressed according to linear elastic fracture mechanics (LEFM, the complete stress and displacement fields for Mode I and Mode II are listed in the Appendix of this chapter):

$$v = \frac{K_{\mathrm{I}}}{2\mu}\sqrt{\frac{r}{2\pi}}\sin\left(\frac{\theta}{2}\right)\left[\kappa + 1 - 2\cos^2\left(\frac{\theta}{2}\right)\right] \tag{5.9}$$

$$\sigma_y = \frac{K_{\mathrm{I}}}{\sqrt{2\pi r}}\cos\left(\frac{\theta}{2}\right)\left[1 + \sin\left(\frac{\theta}{2}\right)\sin\left(\frac{3\theta}{2}\right)\right] \tag{5.10}$$

where K_{I} is the SIF for real crack (the SIF for the virtual crack will be denoted as $\hat{K}_{\mathrm{I}}$ later), $\mu = E/(2+2\nu)$ is the shear modulus, and κ is the bulk modulus. It is noted that the above equations are valid for both real crack and virtual crack due to the assumption of stress field equivalence.

Now the opening displacement in Eq. (5.5), which involves two-steps computation, needs to be calculated. For the real crack (as shown in Figure 5.2(a)), the vertical nodal displacements on upper surface ($\theta = \pi, r = \Delta a$) and lower surface ($\theta = -\pi, r = \Delta a$) can be inferred from Eq. (5.9), giving

$$v_{AA'}^{(1),+} = \frac{\kappa + 1}{2\mu}\sqrt{\frac{\Delta a}{2\pi}}K_{\mathrm{I}} \tag{5.11}$$

$$v_{AA'}^{(1),-} = -\frac{\kappa + 1}{2\mu}\sqrt{\frac{\Delta a}{2\pi}}K_{\mathrm{I}} \tag{5.12}$$

The corresponding opening displacement for the nodes after the crack-tip can be easily evaluated and shown as below

$$\Delta v_{AA'}^{(1)} = v_{AA'}^{(1),+} - v_{AA'}^{(1),-} = \frac{\kappa + 1}{\mu}\sqrt{\frac{\Delta a}{2\pi}}K_{\mathrm{I}} \tag{5.13}$$

The opening displacement for infinitesimal virtual crack (Figure 5.2(b)) can be obtained analogously as

$$\Delta v_{CC'}^{(2)} = v_{CC'}^{(2),+} - v_{CC'}^{(2),-} = \frac{\kappa + 1}{\mu}\sqrt{\frac{\Delta l}{2\pi}}\hat{K}_{\mathrm{I}} \tag{5.14}$$

If we set $\theta = 0°$ in Eq. (5.10), the stress ahead of the crack-tip C for the real crack yields the form as

$$\sigma_y = \frac{K_{\mathrm{I}}}{\sqrt{2\pi r}} \tag{5.15}$$

According to the assumption of stress field equivalence, the corresponding stress for virtual crack-tip shall have the same form as the stress expression in Eq. (5.13). It means the SIF

value for virtual crack-tip would be identical to that for real crack-tip, as the following expression demonstrates:

$$\hat{K}_{\mathrm{I}} = \lim_{r \to 0} \left(\sigma_y \sqrt{2\pi r} \right) = K_{\mathrm{I}} \tag{5.16}$$

Recalling the SIF's expressed in Eq. (5.13) and (5.14) gives

$$\frac{\Delta v_{AA'}^{(1)}}{\Delta v_{CC'}^{(2)}} = \sqrt{\frac{\Delta a}{\Delta l}} \quad \text{or} \quad \Delta v_{CC'}^{(2)} = \sqrt{\frac{\Delta l}{\Delta a}} \Delta v_{AA'}^{(1)} \tag{5.17}$$

Combining this equation with the strain energy release rate of Mode I from Eq. (5.5), it can be rewritten as

$$G_{\mathrm{I}} = \frac{F_{Cy}^{(1)} \Delta v_{CC'}^{(2)}}{2B\Delta l} = \frac{F_{Cy}^{(1)} \Delta v_{AA'}^{(1)}}{2B\Delta l} \sqrt{\frac{\Delta l}{\Delta a}} \tag{5.18}$$

If a uniform mesh size is adopted for the elements before and after the crack-tip C, i.e., $\Delta a = \Delta l$, it may finally obtain the following relation as

$$G_{\mathrm{I}} = \frac{F_{Cy}^{(1)} \Delta v_{AA'}^{(1)}}{2B\Delta l} = \frac{F_{Cy} \Delta v_{AA'}}{2B\Delta l} \tag{5.19}$$

This is exactly the expression for energy release rates of Mode I in Eq. (5.7), which mathematically reveals the mechanism of one-step-analysis for virtual crack closure method. For Mode II problems, analogous procedure of derivation can be followed.

5.2.3 Inclined Crack

In practical problems, cracks are usually not parallel to horizontal or vertical axis as shown in Figure 5.2. Without loss of generality, Figure 5.3 depicts a crack inclined with respect to the axes in global coordinate system and a local coordinate system based on crack-tip. The

corresponding formulations should be then updated according to the local coordinates. The edge length of crack-tip element BC can be written as the following manner:

$$\Delta a = \sqrt{(x_B - x_C)^2 + (y_B - y_C)^2} \tag{5.20}$$

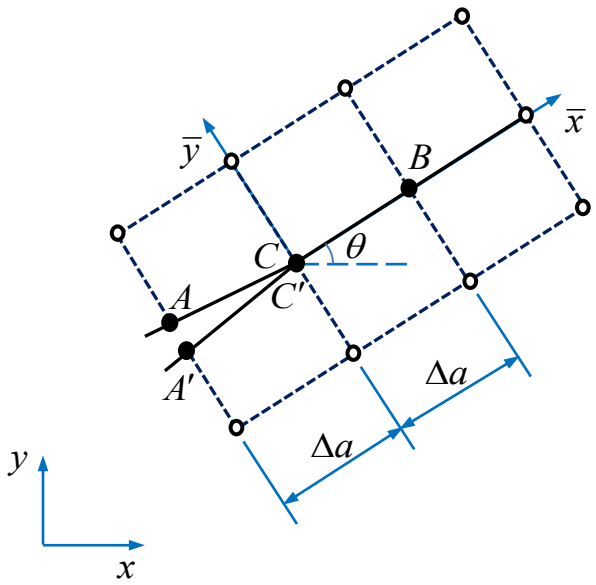

Figure 5.3. Inclined crack in a plane with local coordinates.

The crack inclination angle θ is found as

$$\theta = \arccos\left(\frac{x_B - x_C}{\Delta a}\right) = \arcsin\left(\frac{y_B - y_C}{\Delta a}\right) \tag{5.21}$$

If we project the associated nodal forces and crack opening displacement into local coordinates, it gives

$$\begin{pmatrix} \bar{F}_{Cx} \\ \bar{F}_{Cy} \end{pmatrix} = \begin{bmatrix} \cos\theta & \sin\theta \\ -\sin\theta & \cos\theta \end{bmatrix} \begin{pmatrix} F_{Cx} \\ F_{Cy} \end{pmatrix} \tag{5.22}$$

and

$$\begin{pmatrix} \Delta\bar{u}_{AA'} \\ \Delta\bar{v}_{AA'} \end{pmatrix} = \begin{bmatrix} \cos\theta & \sin\theta \\ -\sin\theta & \cos\theta \end{bmatrix} \begin{pmatrix} \Delta u_{AA'} \\ \Delta v_{AA'} \end{pmatrix} \tag{5.23}$$

Correspondingly, the strain energy release rates can now evaluated as follows:

$$G_{\mathrm{I}} = \frac{\bar{F}_{Cy}\Delta\bar{v}_{AA'}}{2B\Delta a} \text{ and } G_{\mathrm{II}} = \frac{\bar{F}_{Cx}\Delta\bar{u}_{AA'}}{2B\Delta a} \tag{5.24}$$

5.3 Numerical Examples

In this section, several examples are presented to numerically illustrate the applications of proposed technique for elastic fracture mechanics problems. In the first example, a rectangular plate with an edge-crack under uniaxial tension is examined for the method applied under the loading condition of Mode I. The second example is about the edge-crack under mixed-mode loading. The crack propagation of a panel with rivet holes (PMMA beam) is studied in the third example.

5.3.1 Rectangular Plate with an Edge-crack Under Tension

This example analyzes a rectangular plate with a finite single crack under the uniform far-field tension ($\sigma = 1.0\,\mathrm{N/cm^2}$). The basic geometry with the description of symmetric loading is illustrated in Figure 5.4 (a). The width and length of the plate are denoted by W and H, which are set as $W = 5.0\,\mathrm{cm}$ and $H = 10.0\,\mathrm{cm}$. The initial crack length is defined as $a = 1\,\mathrm{cm}$. Plane strain conditions are assumed. A linear elastic simulation is implemented with the material constants: Young's modulus $E = 1\times10^3\,\mathrm{N/cm^2}$ and Poisson's ratio $\nu = 0.3$. The empirical expression of SIF for this problem is

$$K_I = Y\sigma\sqrt{\pi a} \tag{5.25}$$

where a is the crack length, Y is a dimensionless parameter that depends on the geometry with the expression as [65]

$$Y = 1.12 - 0.231(\frac{a}{W}) + 10.55(\frac{a}{W})^2 - 21.72(\frac{a}{W})^3 + 30.39(\frac{a}{W})^4 \tag{5.26}$$

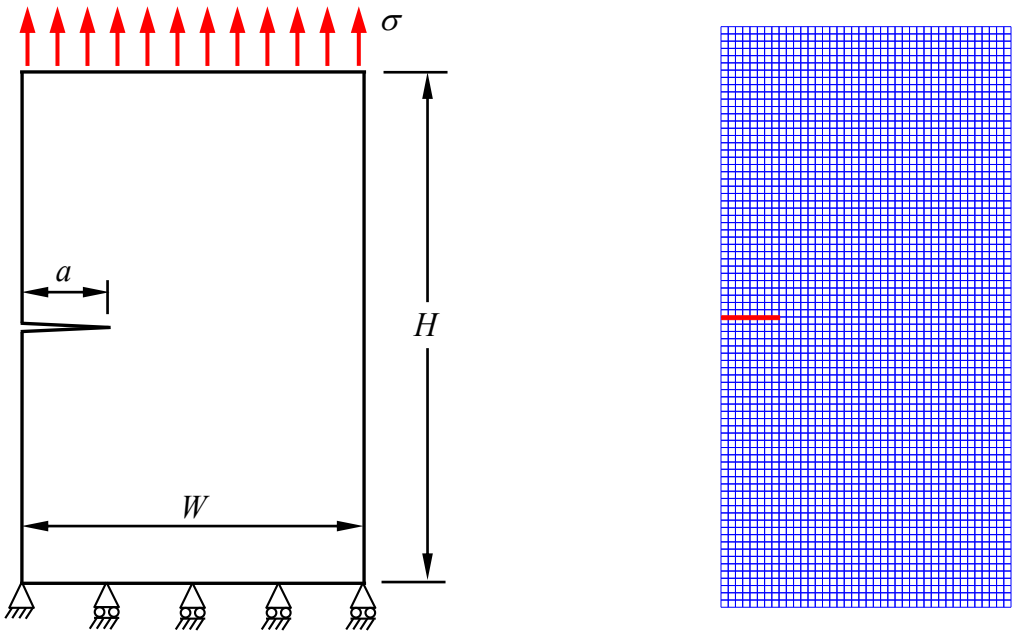

(a) (b)

Figure 5.4. Rectangular plate with an edge-crack under tension and a uniform structured mesh: (a) a sketch of geometry and boundary conditions; and (b) a representative structured mesh.

In Figure 5.4 (b), the domain is discretized by a structured mesh with 4-node quadrilateral (Q4) elements. Figure 5.5(a) shows the comparison of strain energy. It is seen that all the energy curves are closer to reference solution when the mesh becomes finer. For a given set of nodes, the CS-FEM result behaves closer to reference solution than FEM-T3 and FEM-Q4. In Figure 5.5(b), the SIF results of presented method (CS-FEM with VCCT) are compared with those of

conventional method: FEM-T3 with *I*-integral, FEM-Q4 with *I*-integral and FEM-Q4 with VCCT. All solutions of FEM-Q4 with *I*-integral are closer to the reference values than FEM-Q4 with VCCT. While the presented method becomes a good competitor as FEM-Q4 with *I*-integral and performs (slightly) more accurate than it when model adopts more than 1987 nodes.

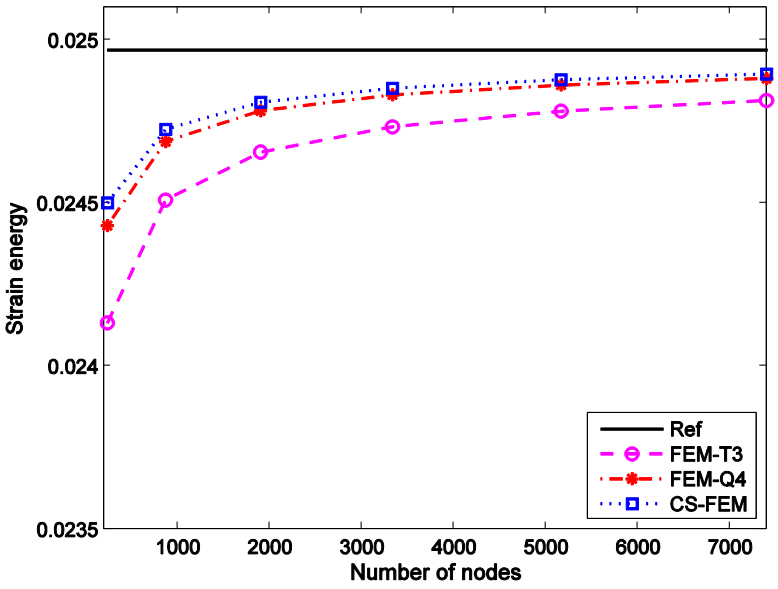

(a)

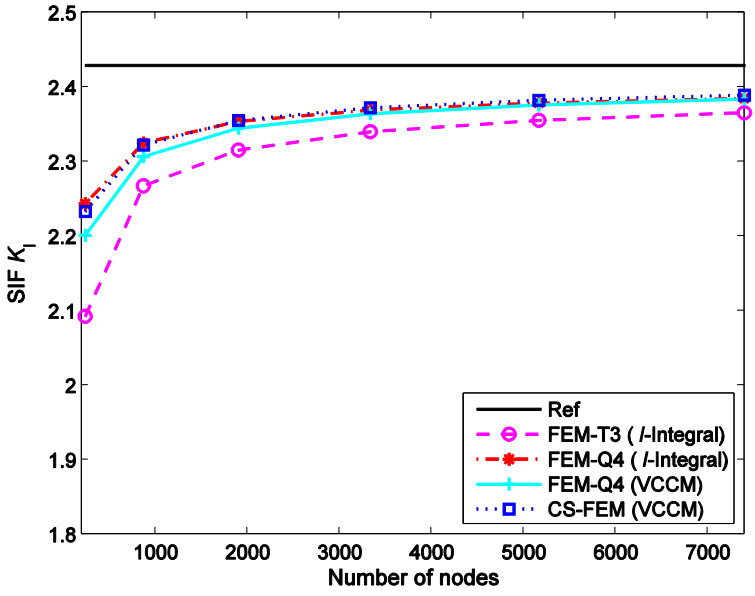

(b)

Figure 5.5. Comparison of different methods for rectangular plate with an edge-crack under tension: (a) strain energy; and (b) stress intensity factor K_1.

5.3.2 Plate with an Edge-crack Under Mixed-mode Loading

The second example deals with the crack in a 2D rectangular plate with an edge crack under a shear loading $\tau = 1.0\,\mathrm{N/cm^2}$, as shown in Figure 5.6(a). The geometry parameters are: width $W = 7.0$ cm, half of length $H = 8.0$ cm, and crack length $a = 3.5$ cm. The material properties are set as Young's modulus $E = 300$ GPa and Poisson's ratio $\nu = 0.25$. The exact stress intensity factors are given as: $K_I = 34Pa\sqrt{mm}$ and $K_{II} = 4.55Pa\sqrt{mm}$.

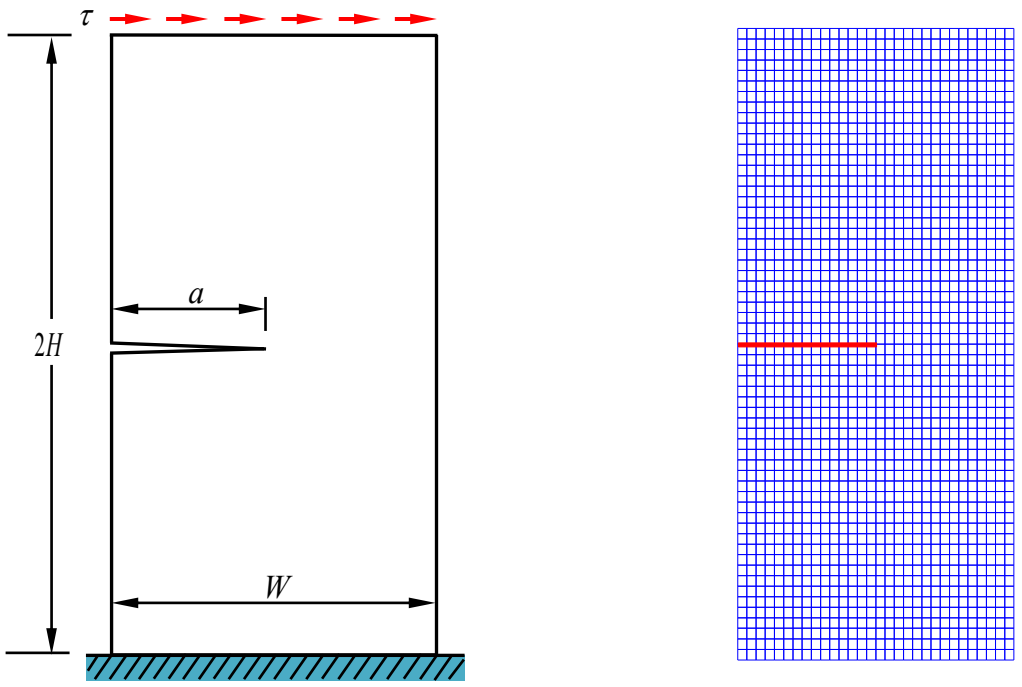

(a) (b)

Figure 5.6. Plate with an edge-crack under shear loading and a representative structured mesh: (a) a sketch of geometry and boundary conditions; and (b) a uniform structured mesh.

Figure 5.7(a) shows the comparison of strain energy. It is seen that all the energy curves are closer to reference solution when the mesh becomes finer. For a given set of nodes, the CS-FEM result behaves closer to reference solution than FEM-T3 and FEM-Q4. The strain energy comparisons between CS-FEM, FEM-T3 and FEM-Q4 are plotted in Figure 5.7(a). Again CS-FEM gains the closest results to reference value. In Figure 5.7(b) and (c), the results from presented method (CS-FEM with VCCT) are compared with those from the other three methods: FEM-T3 with *I*-integral, standard FEM-Q4 with *I*-integral and FEM-Q4 with VCCT. The convergence study of stress intensity factors shows that the proposed method is the most accurate approach among these methods for computation of K_I, and it is between FEM-Q4 with *I*-integral

and FEM-Q4 with VCCT for computation of K_{II}. It is again seen the presented method is a good competitor as FEM-Q4 with *I*-integral.

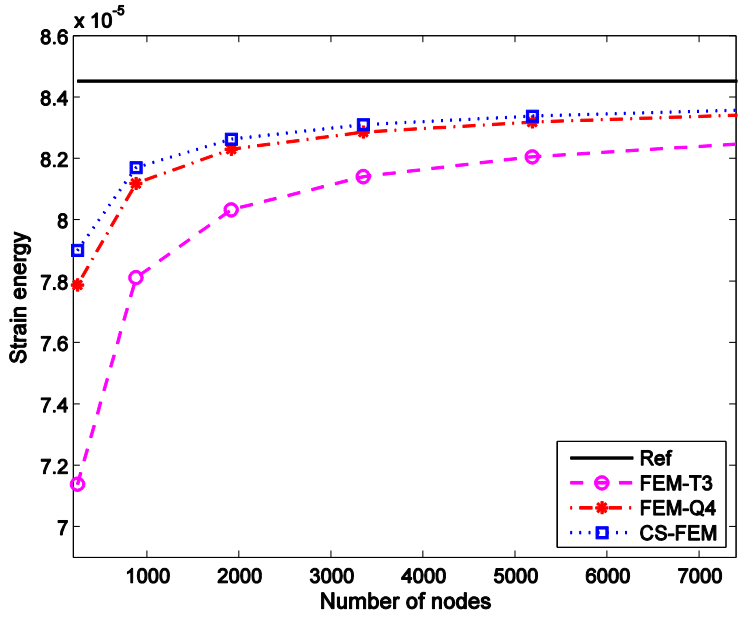

(a)

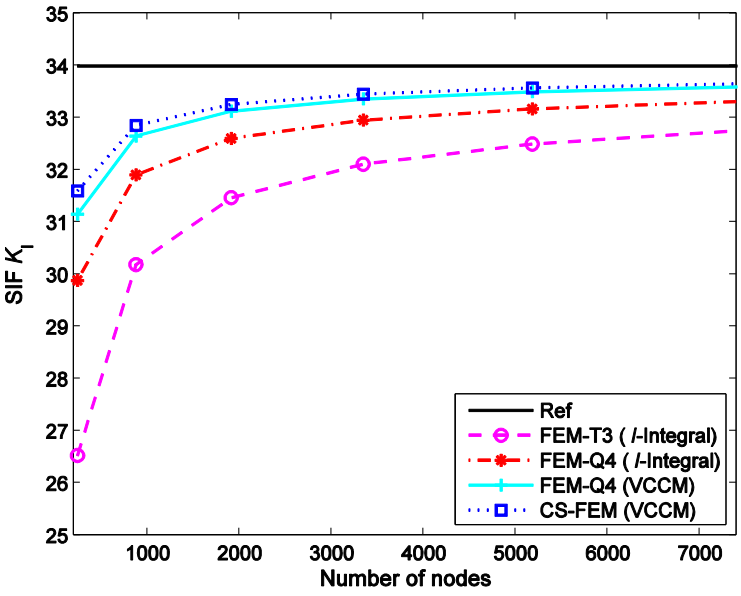

(b)

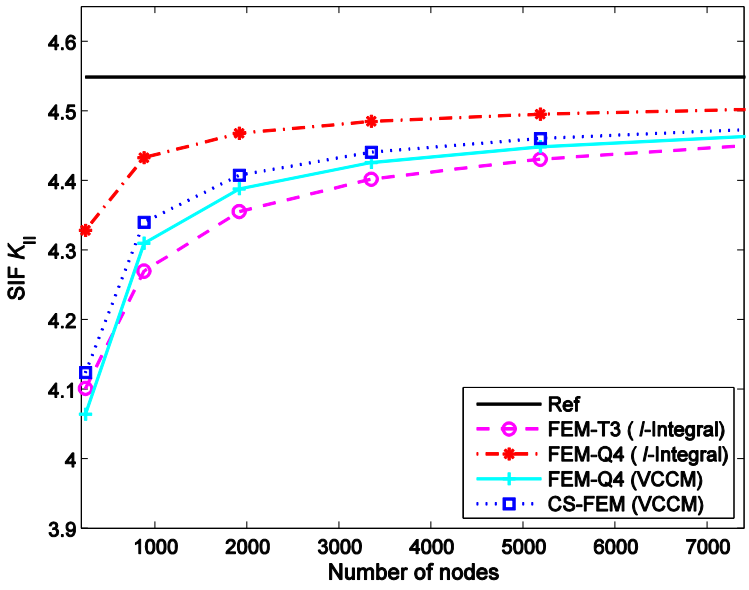

(c)

Figure 5.7. Comparison of different methods for a plate with an edge-crack under shear loading: (a) strain energy; (b) stress intensity factor K_{I}; and (c) stress intensity factor K_{II}.

5.3.3 Crack Propagation of a Panel with Rivet Holes (PMMA beam)

The problem here aims to simulate the crack propagation trajectory under mixed-mode loading. For a crack propagation problem at each time step, one needs to determine whether the crack will growth or not (crack propagation criteria), and then in which direction the crack will propagate (crack kinking criteria). The SIF's, which was introduced in previous subsection, are often utilized for crack propagation criteria. Other available crack propagation criteria are based on energetic parameters and they may use the strain energy release rates [66], the strain energy density [67], etc. The crack growth direction is determined by kinking criteria, which can be categorized into three types [68]:

1) Local approach: based on the local fields around the crack-tip, for instance, the maximum circumferential stress criterion (MCSC) introduced by Erdogan and Sih [69], or the maximum strain criterion (MSC) [70];

2) Global approach: based on the energy distribution throughout the cracked part, such as the maximal strain energy release rate criterion (MSERRC) [71];

3) Micro-void continuum damage model based method: according to the assumption that the void initialization and the void growth control the crack growth direction [72].

In this work, we utilize the MCSC to determine a crack growth direction θ_c such that the circumferential stress $\sigma_{\theta\theta}$ reaches maximum. If a problem under general mixed-mode loadings is considered, the asymptotic near-tip circumferential and shear stresses can be expressed in the tip polar co-ordinate system, giving

$$\begin{Bmatrix}\sigma_{\theta\theta}\\ \sigma_{r\theta}\end{Bmatrix}=\frac{K_{\mathrm{I}}}{4\sqrt{2\pi r}}\begin{Bmatrix}3\cos\left(\frac{\theta}{2}\right)+\cos\left(\frac{3\theta}{2}\right)\\ \sin\left(\frac{\theta}{2}\right)+\sin\left(\frac{3\theta}{2}\right)\end{Bmatrix}+\frac{K_{\mathrm{II}}}{4\sqrt{2\pi r}}\begin{Bmatrix}-3\sin\left(\frac{\theta}{2}\right)-3\sin\left(\frac{3\theta}{2}\right)\\ \cos\left(\frac{\theta}{2}\right)+3\cos\left(\frac{3\theta}{2}\right)\end{Bmatrix} \tag{5.27}$$

After a few manipulations of inferring the maximum circumferential stress [72], the following equation can be established to give

$$K_{\mathrm{I}}\sin\left(\theta_c\right)+K_{\mathrm{II}}\left(3\cos\left(\theta_c\right)-1\right)=0 \tag{5.28}$$

where θ_c represents the angle of crack propagation in the tip local co-ordinate system, which is easily obtained by re-expressing Eq.(5.28) as

$$\theta_c = 2\arctan\left[\frac{1}{4}\left(\frac{K_{\mathrm{I}}}{K_{\mathrm{II}}} \pm \sqrt{\left(\frac{K_{\mathrm{I}}}{K_{\mathrm{II}}}\right)^2 + 8}\right)\right] \tag{5.29}$$

Using this criterion, the equivalent mode I SIF will be then defined as [73]

$$K_{\mathrm{I}eq} = \frac{1}{2}\cos\left(\frac{\theta}{2}\right)\left[K_{\mathrm{I}}\left(1+\cos(\theta)\right) - 3K_{\mathrm{II}}\sin(\theta)\right] \tag{5.30}$$

This equivalent stress intensity factor can provide an input for the fatigue crack growth when applying the classical Paris model to mixed-mode loading.

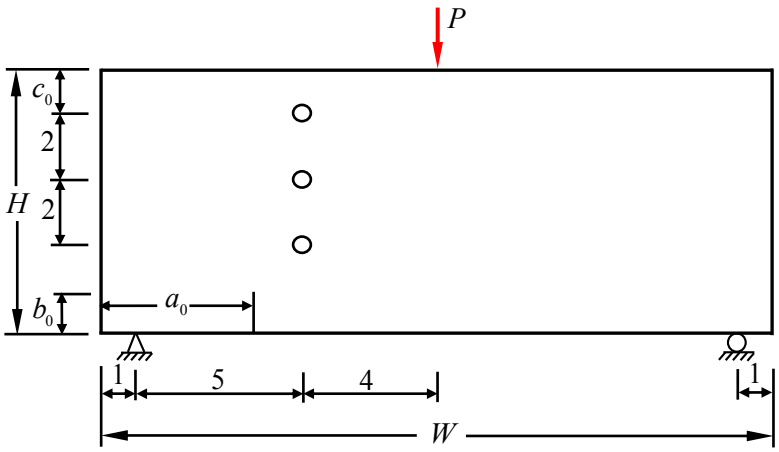

Figure 5.8. The sketch of PMMA beam with three holes subjected to a concentrated loading (dimensions in inches).

Consider a polymethy methacrylate (PMMA) beam with three rivet holes as sketched in Figure 5.8, which has also been studied experimentally or numerically in some references [74–76]. The width of the beam specimen is denoted by W, the height by H, and the radius of each hole by r_0. The length of the initial crack is denoted by a_0 and its distance from the left side of the beam by b_0. The geometric dimensions are set as $t = 0.5''$, W=20″, H=8″, $r_0 = 0.25''$, $a_0 = 4.0''$, $b_0 = 1.0''$ and $c_0 = 1.25''$. The material properties are set as modulus $E = 3.0\times10^5$ PSI

and Poisson's ratio $\nu = 0.3$ .The beam is under the action of vertical concentrated load applied at the center line of the top, which is $P = 1lbf$.

Figure 5.9 plots the initial mesh of the specimen which is discretized with 15853 elements. Figure 5.9(b) and (c) show the contours of von Mises stress distribution on the zoomed deformed configurations at different steps with the crack increment size selected as $0.20''$. In each step of modeling the crack propagation, the mesh here is updated to capture the location of crack-tip and crack line. Figure 5.10 compares the actual crack path and predicted path when the crack grows to a total length of $4.2''$. The predicted crack path shows excellent agreement with some available numerical and experimental results [74,75]

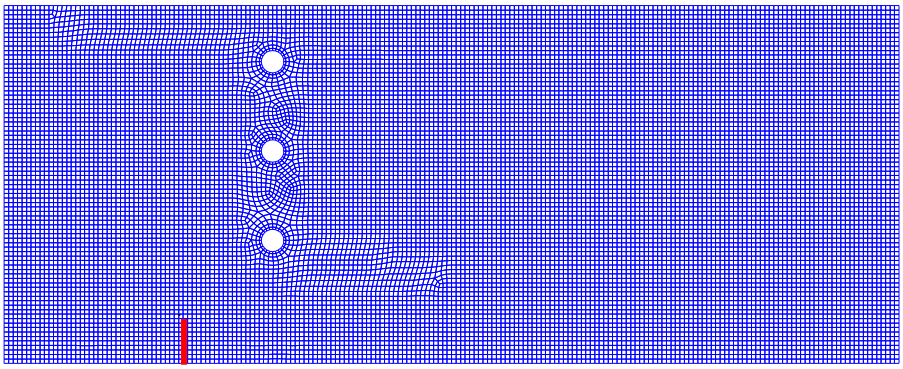

(a)

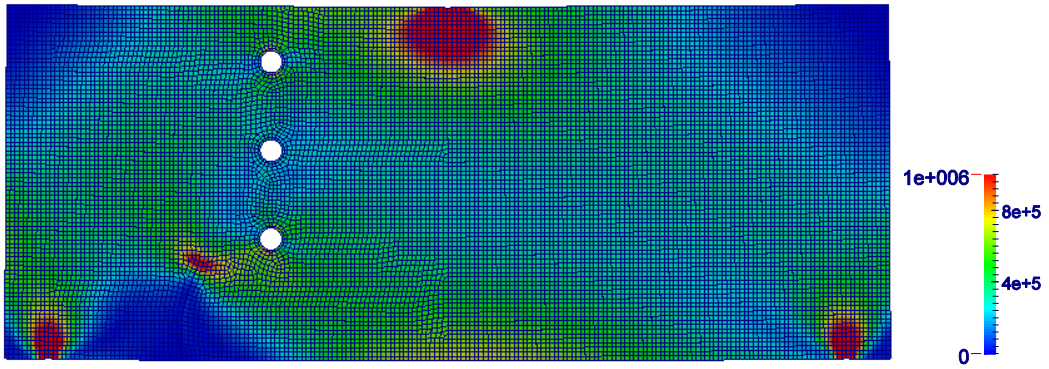

(b)

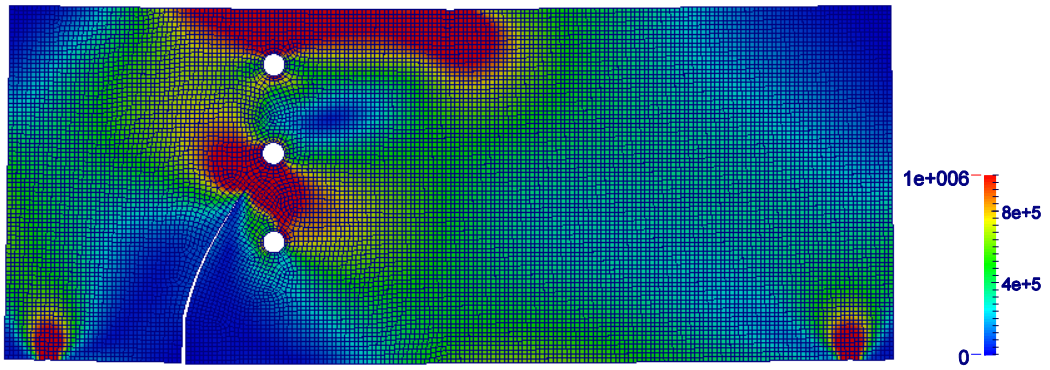

(c)

Figure 5.9. PMMA beam: (a) initial mesh at step 0; and the contours of stress distribution (von Mises stress) and an illustration of zoomed deformation at different steps with the crack increment at 0.20: (b) step 6; and (c) step 17.

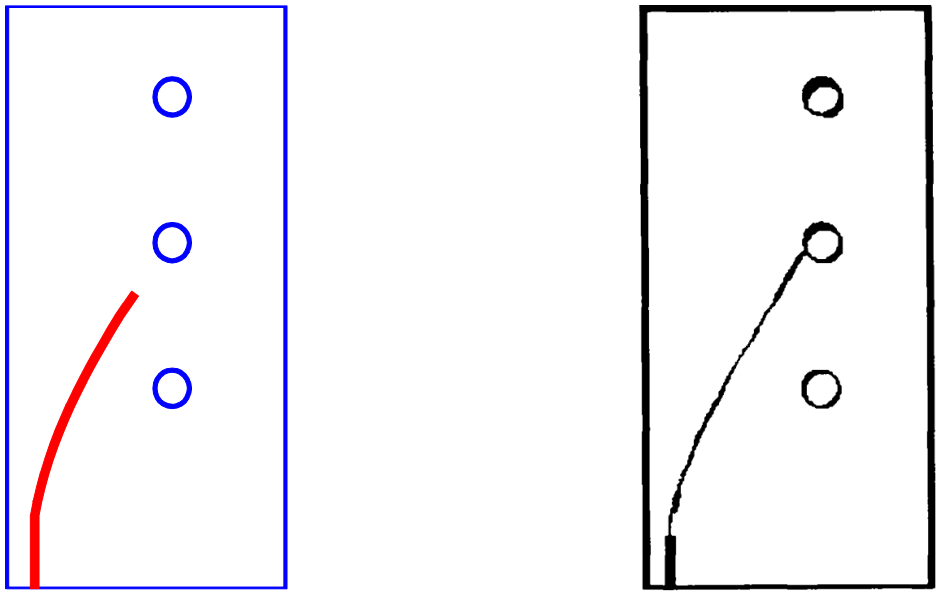

(a) (b)

Figure 5.10. Comparison of trajectories between presented simulation and experiment: (a) prediction; and (b) experiment [76].

5.4 Conclusions

In this study, the VCCT has been developed for evaluation of fracture mechanics parameters and simulation of crack propagation within the framework of CS-FEM. In the implementation, the elements in an FE background mesh are subdivided into four smoothing cells. The cell-wise strain smoothing operations are then applied based on these smoothing cells to obtain the smoothed strains. When piecewise-constant weight functions are adopted, area integrations over the domain of cell become contour integration along the boundaries of the smoothing cells. As a result, only shape functions themselves (not the derivatives) will be involved in computation of the field gradients to form the stiffness matrix. It also has less strict mesh quality requirements since no mapping or coordinate transformation is involved in the CS-FEM. Based on the assumption that an infinitesimal perturbation of crack-tip location shall not affect the stress/displacement field obviously, the mechanism of one-step-analysis feature of VCCT has been presented via an explanation mathematically. The treatment of inclined cracks is also introduced for VCCT by establishing a local coordinate system based on crack-tip.

Several numerical examples have been carried out to validate the proposed method, including evaluation of the fracture parameters and prediction of crack propagation. Although all examples are tested for a single crack, the method has in general suitable for multi-cracked problems. In the first two examples, the strain energy and stress intensity factors have been calculated by proposed method. The comparisons between presented method and conventional FEM using T3 or Q4 elements proved that the presented method is a good competitor as FEM-Q4 with interaction integral method. However, the present formation only used the nodal reaction forces at the crack-tip and the opening displacements just behind the tip, which are the primary variables of the CS-FEM results. It attains same level accuracy as FEM-Q4 with

interaction integral method but does not require much extra effort of post-processing to extract fracture parameters. Also, simulation of crack propagation in an elastic body showed that it is well capable of capturing the actual path of crack propagation and it has good agreement with the experimental results.

Appendix 5.1. Stress and Displacement Fields for Mode I and Mode II in a Linear Elastic, Isotropic Material

The Williams' (1957) [77] solution for stress and displacement fields near the crack-tip can be expressed as

$$\sigma_x = \frac{1}{\sqrt{2\pi r}}\left\{K_{\mathrm{I}}\cos\left(\frac{\theta}{2}\right)\left[1-\sin\left(\frac{\theta}{2}\right)\sin\left(\frac{3\theta}{2}\right)\right]-K_{\mathrm{II}}\sin\left(\frac{\theta}{2}\right)\left[2+\cos\left(\frac{\theta}{2}\right)\cos\left(\frac{3\theta}{2}\right)\right]\right\} \tag{5.31}$$

$$\sigma_y = \frac{1}{\sqrt{2\pi r}}\left\{K_{\mathrm{I}}\cos\left(\frac{\theta}{2}\right)\left[1+\sin\left(\frac{\theta}{2}\right)\sin\left(\frac{3\theta}{2}\right)\right]+K_{\mathrm{II}}\sin\left(\frac{\theta}{2}\right)\cos\left(\frac{\theta}{2}\right)\cos\left(\frac{3\theta}{2}\right)\right\} \tag{5.32}$$

$$\tau_{xy} = \frac{1}{\sqrt{2\pi r}}\cos\left(\frac{\theta}{2}\right)\left\{K_{\mathrm{I}}\sin\left(\frac{\theta}{2}\right)\cos\left(\frac{3\theta}{2}\right)+K_{\mathrm{II}}\left[1-\sin\left(\frac{\theta}{2}\right)\sin\left(\frac{3\theta}{2}\right)\right]\right\} \tag{5.33}$$

$$\sigma_z = \begin{cases} 0 & \text{plane stress} \\ \nu(\sigma_x+\sigma_y) & \text{plane strain} \end{cases} \tag{5.34}$$

$$u = \frac{1}{2\mu}\sqrt{\frac{r}{2\pi}}\left\{K_{\mathrm{I}}\cos\left(\frac{\theta}{2}\right)\left[\kappa-1+2\sin^2\left(\frac{\theta}{2}\right)\right]+K_{\mathrm{II}}\sin\left(\frac{\theta}{2}\right)\left[\kappa+1+2\cos^2\left(\frac{\theta}{2}\right)\right]\right\} \tag{5.35}$$

$$v = \frac{1}{2\mu}\sqrt{\frac{r}{2\pi}}\left\{K_{\mathrm{I}}\sin\left(\frac{\theta}{2}\right)\left[\kappa+1-2\cos^2\left(\frac{\theta}{2}\right)\right]-K_{\mathrm{II}}\cos\left(\frac{\theta}{2}\right)\left[\kappa-1-2\sin^2\left(\frac{\theta}{2}\right)\right]\right\} \tag{5.36}$$

where κ is the bulk modulus, ν and μ are Poisson's ratio and the shear modulus, respectively.

References

[1] Irwin GR. 1957. Analysis of stresses and strains near the end of a crack traversing a plate. Journal of Applied Mechanics; 24: 361–364.

[2] Anderson TL. 1995. Fracture mechanics: Fundamentals and applications, 2nd Edition. CRC Press, Boca Raton.

[3] Eshelby JD. 1956. The continuum theory of lattice defects. In: Seitz F, Turnbull D, editors. Progress in solid state physics, vol. 3: 79–303. Academic Press, New York.

[4] Cherepanov GP. 1967. The propagation of cracks in a continuous medium. Journal of Applied Mathematics and Mechanics; 31(3): 503–512.

[5] Rice JR. 1968. A path independent integral and the approximate analysis of strain concentration by notches and cracks. Journal of Applied Mechanics;35:379–386.

[6] Hutchinson JW. 1968. Singular behaviour at the end of a tensile crack in a hardening material. Journal of the Mechanics and Physics of Solids; 16(1): 13–31.

[7] Chan SK, Tuba IS, and Wilson WK. 1970. On the finite element method in linear fracture mechanics. Engineering Fracture Mechanics; 2(1): 1–17.

[8] Shih CF, deLorenzi H, and German MD. 1976. Crack extension modeling with singular quadratic isoparametric elements. International Journal of Fracture; 12(3): 647–651.

[9] Banks-Sills L and Sherman D. 1986. Comparison of methods for calculating stress intensity factors with quarter-point elements. International Journal of Fracture; 32(2): 127–140.

[10] Fu P, Johnson SM, Settgast RR, and Carrigan CR. 2012. Generalized displacement correlation method for estimating stress intensity factors. Engineering Fracture Mechanics; 88: 90–107.

[11] Stern M, Becker EB, and Dunham RS. 1976. A contour integral computation of mixed-mode stress intensity factors. International Journal of Fracture; 12(3): 359–368.

[12] Yu H, Wu L, Guo L, Wu H, and Du S. 2010. An interaction integral method for 3D curved cracks in nonhomogeneous materials with complex interfaces. International Journal of Solids and Structures; 47: 2178–2189.

[13] Parks DM. 1974. A stiffness derivative finite element technique for determination of crack tip stress intensity factors. International Journal of Fracture; 10-4: 487–502.

[14] Hellen TK. 1975. On the method of virtual crack extensions. International Journal for Numerical Methods in Engineering; 9: 187–207.

[15] Rybicki EF and Kanninen MF. 1977. A finite element calculation of stress intensity factors by a modifiedcrack closure integral. Engineering Fracture Mechanics; 9: 931–938.

[16] Shivakumar KN, Tan PW, and Newman Jr JC. 1988. A virtual crack-closure technique for calculat-ing stress intensity factors for cracked three dimensional bodies. International Journal of Fracture; 36: R43–R50.

[17] Raju IS. 1987. Calculation of strain-energy release rates with higher order and singular finite elements. Engineering Fracture Mechanics; 28: 251–274.

[18] Raju IS, Crews Jr JH, and Aminpour MA. 1988. Convergence of strain-energy release rates for edge delaminated composite laminates. Engineering Fracture Mechanics; 30: 383–396.

[19] Cantwell WJ, Scudamore R, Ratcliffe J, and Davies P. 1999. Interfacial fracture in sandwich laminates. Composites Science and Technology; 59: 2079–2085.

[20] Goswami S and Becker W. 2001. The effect of face sheet/core delamination in sandwich structures under transverse loading. Composite Structures; 54: 515–521.

[21] Xie D, Waas AM, Shahwan KW, Schroeder JA, and Boeman RG. 2004. Computation of energy release rates for kinking cracks based on virtual crack closure technique. CMES: Computer Modeling in Engineering & Sciences; 6: 515–524.

[22] Xie D and Biggers Jr SB. 2006. Strain energy release rate calculation for a moving delamination front of arbitrary shape based on virtual crack closure technique - Part I: Formulation and validation. Engineering Fracture Mechanics; 73(6): 771–785.

[23] Xie D and Biggers Jr SB. 2006. Strain energy release rate calculation for a moving delamination front of arbitrary shape based on virtual crack closure technique - Part II: Sensitivity study on modeling details. Engineering Fracture Mechanics; 73: 786–801.

[24] Sun CT and Qian W. 1997. The use of finite extension strain energy release rates in fracture of interfacial cracks. International Journal of Solids and Structures; 34: 2595–2609.

[25] Leski A. 2007. Implementation of the virtual crack closure technique in engineering FE calculations. Finite Elements in Analysis and Design; 43(3): 261–268.

[26] Okada H and Kamibeppu T. 2005. A virtual crack closure-integral method (VCCM) for three-dimensional crack problems using linear tetrahedral finite elements. CMES: Computer Modeling in Engineering & Sciences: 229–238.

[27] Okada H, Kawai H, and Araki K. 2008. A virtual crack closure-integral method (VCCM) to compute the energy release rates and stress intensity factors based on quadratic tetrahedral finite elements. Engineering Fracture Mechanics; 75(15): 4466–4485.

[28] Whitcomb JD. 1992. Analysis of a laminate with a postbuckled embedded delamination, including contact effects. Journal of Composite Materials; 26: 1523–1535.

[29] Fawaz SA. 1998. Application of the virtual crack closure technique to calculate stress intensity factors for through cracks with an elliptical crack front. Engineering Fracture Mechanics; 59: 327–342.

[30] Krueger R. 2002. The virtual crack closure technique: history, approach and applications. NASA/CR-2002-211628.

[31] Liu GR and Quek SS. 2013. The finite element method: A practical course, 2nd Edition. Butterworth-Heinemann, Oxford.

[32] Chen JS, Wu CT, Yoon S, and You Y. 2001. A stabilized conforming nodal integration for Galerkin mesh-free methods. International Journal for Numerical Methods in Engineering; 50: 435–466.

[33] Liu GR, Dai KY, and Nguyen-Thoi T. 2007. A smoothed finite element for mechanics problems. Computational Mechanics; 39: 859–877.

[34] Liu GR, Zeng W, and Nguyen-Xuan H. 2013. Generalized stochastic cell-based smoothed finite elementmethod (GS_CS-FEM) for solid mechanics, Finite Elements in Analysis and Design;63:51–61.

[35] Bordas SPA and Natarajan S. 2010. On the approximation in the smoothed finite element method (SFEM). International Journal for Numerical Methods in Engineering; 81: 660–670.

[36] Liu GR, Nguyen-Thoi T, and Lam KY. 2009. A node-based smoothed finite element method for upper bound solution to solid problems (NS-FEM). Computers & Structures; 87: 14–26.

[37] Nguyen-Thoi T, Liu GR, Nguyen-Xuan H, and Nguyen-Tran C. 2011. Adaptive analysis using the node-based smoothed finite element method (NS-FEM). International Journal for Numerical Methods in Biomedical Engineering; 27(2): 198–218.

[38] Liu GR, Nguyen-Thoi T, and Lam KY. 2009. An edge-based smoothed finite element method (ES-FEM) for static, free and forced vibration analyses of solids. Journal of Sound and Vibration; 320: 1100–1130.

[39] Zeng W, Liu GR, Kitamura K, and Nguyen-Xuan H. 2013. A three-dimensional ES-FEM for fracture mechanics problems in elastic solids. Engineering Fracture Mechanics; 114: 127–150.

[40] Zeng W, Larsen JM, and Liu GR. 2015. Smoothing technique based crystal plasticity finite element modeling of crystalline materials. International Journal of Plasticity;65:250–268.

[41] Nguyen-Thoi T, Liu GR, Lam KY, and Zhang GY. 2009. A Face-based Smoothed Finite Element Method (FS-FEM) for 3D linear and nonlinear solid mechanics problems using 4-node tetrahedral elements. International Journal for Numerical Methods in Engineering; 78: 324–353.

[42] Li W, Chai Y, Lei M, and Liu GR. 2014. Analysis of coupled structural-acoustic problems based on the smoothed finite element method(S-FEM). Engineering Analysis with Boundary Elements; 42: 84–91.

[43] Zhang Z-Q, Liu GR, and Khoo BC. 2013. A three dimensional immersed smoothed finite element method (3D IS-FEM) for fluid–structure interaction problems. Computational Mechanics; 51(2): 129–150.

[44] Jiang C, Liu GR, Han X, Zhang Z-Q, and Zeng W. 2015. A smoothed finite element method for analysis of anisotropic large deformation of passive rabbit ventricles in

diastole. International Journal for Numerical Methods in Biomedical Engineering; 31(1): e02697 (1–25).

[45] Wu F, Liu GR, Li GY, Liu YJ, and He ZC. 2014. A coupled ES-FEM and FM-BEM for structural acoustic problems. Noise Control Engineering; 62(4): 196–209.

[46] Liu GR, Nguyen-Xuan H, and Nguyen-Thoi T. 2010. A theoretical study on the smoothed FEM (S-FEM) models: Properties, accuracy and convergence rates. International Journal for Numerical Methods in Engineering; 84(10): 1222–1256.

[47] Liu GR. 2010. A G space theory and a weakened weak (W2) form for a unified formulation of compatible and incompatible methods: Part I Theory, Part II applications to solid mechanics problems. International Journal for Numerical Methods in Engineering; 81: 1093–1156.

[48] Liu GR and Nguyen-Thoi T. 2010. Smoothed Finite Element Methods. CRC Press, New York.

[49] Nguyen-Xuan H, Bordas SPA, and Nguyen-Dang H. 2008. Smooth finite element methods: Convergence, accuracy and properties. International Journal for Numerical Methods in Engineering; 74: 175–208.

[50] Dai KY and Liu GR. 2007. Free and forced vibration analysis using the smoothed finite element method (SFEM). Journal of Sound and Vibration; 301: 803–820.

[51] Dai KY, Liu GR, and Nguyen TT. 2007. An n-sided polygonal smoothed finite element method (nSFEM) for solid mechanics. Finite Elements in Analysis and Design; 43(11–12): 847–860.

[52] Nguyen-Thanh N, Rabczuk T, Nguyen-Xuan H, and Bordas SPA. 2008. A smoothed finite element method for shell analysis. Computer Methods in Applied Mechanics and Engineering; 198: 165–177.

[53] Nguyen-Xuan H, Bordas SPA, and Nguyen-Dang H. 2009. Addressing volumetric locking and instabilities by selective integration in smoothed finite elements. Communications in Numerical Methods in Engineering; 25: 19–34.

[54] Bordas SPA, Rabczuk T, Nguyen-Xuan H, Nguyen Vinh P, Natarajan S, Bog T, Do Minh Q, and Nguyen Vinh H. 2010. Strain smoothing in FEM and XFEM. Computers & Structures; 88(23-24): 1419–1443.

[55] Bordas SPA, Natarajan S, Kerfriden P, Augarde CE, Mahapatra DR, and Rabczuk T. 2011. On the performance of strain smoothing for quadratic and enriched finite element approximations (XFEM/GFEM/PUFEM). International Journal for Numerical Methods in Engineering; 86: 637–666.

[56] Nguyen-Xuan H, Vinh Nguyen H, Bordas SPA, Rabczuk T, and Duflot M. 2012. A cell-based smoothed finite element method for three dimensional solid structures. KSCE Journal of Civil Engineering; 16(7): 1230–1242.

[57] Liu GR, Nguyen-Thoi T, Dai KY, and Lam KY. 2007. Theoretical aspects of the smoothed finite element method (SFEM). International Journal for Numerical Methods in Engineering; 71: 902–930.

[58] Bathe K-J. 2014. Finite Element Procedures, 2nd Edition. Klaus-Jürgen Bathe, Watertown, MA.

[59] Narayana KB, George S, Dattaguru B, Ramamurthy TS, and Vijayakumar K. 1994. Modified crack closure integral (MCCI) for 3-d problems using 20-noded brick elements. Fatigue & Fracture of Engineering Materials & Structures; 17(2): 145–157.

[60] Sun CT and Jih CJ. 1987. On strain energy release rates for interfacial cracks in bi-material media. Engineering Fracture Mechanics; 28: 13–20.

[61] Venkatesha KS, Ramamurthy TS, and Dattaguru B. 1996. Generalized modified crack closure integral (GMCCI) and its application to interface crack problems. Computers & Structures; 60: 665–676.

[62] Pathak H, Singh A, and Singh IV. 2013. Fatigue crack growth simulations of homogeneous and bi-material interfacial cracks using element free Galerkin method. Applied Mathematical Modelling; 37: 357–383.

[63] Zhao J-H. 2005. Application of virtual crack closure integral method for interface cracks in low-k integrated circuit devices under thermal load. Engineering Fracture Mechanics; 72: 1361–1382.

[64] Chow WT and Atluri SN. 1995. Finite element calculation of stress intensity factors for interfacial crack using virtual crack closure integral. Computational Mechanics; 16: 417–425.

[65] Nguyen-Xuan H, Liu GR, Nourbakhshnia N, and Chen L. 2012. A novel singular ES-FEM for crack growth simulation. Engineering Fracture Mechanics; 84: 41–46.

[66] Griffith AA, 1920. The phenomena of rupture and flow in solid. Philosophical transactions of the Royal Society of London A; 221: 163–197.

[67] Sih GC and Macdonald B. 1974. Fracture mechanics applied to engineering problems—strain energy density fracture criterion. Engineering Fracture Mechanics; 6: 361–386.

[68] Bouchard PO, Bay F, and Chastel Y. 2003. Numerical modelling of crack propagation: automatic remeshing and comparison of different criteria. Computer Methods in Applied Mechanics and Engineering; 192: 3887–3908.

[69] Erdogan F and Sih GC. 1963. On the crack extension in plane loading and transverse shear. Journal of Basic Engineering; 85: 519–527.

[70] Maiti SK and Smith RA. 1984. Comparison of the criteria for mixed mode brittle fracture based on the preinstability stress–strain field. Part II: pure shear and uniaxial compressive loading. International Journal of Fracture; 24: 5–22.

[71] Hussain MA, Pu SL, and Underwood JH. 1974. Strain energy release rate for a crack under combined Mode I and Mode II. Fracture Analysis: 2–28. ASTM STP 560, Philadelphia.

[72] Zhang X.B. 1992. Etude numérique de la propagation de fissures par la mécanique de la rupture. PhD thesis, thesis no. DU 447, soutenue.

[73] Yan X and Zhang Z. 1992. Mixed mode criteria for the materials with different yield strengths in tension and compression. Engineering Fracture Mechanics; 42(1): 109–116.

[74] Ingraffea AR and Grigoriu M. 1990. Probabilistic fracture mechanics: a validation of predictive capability. Report 90-8. Department of Structural Engineering, Cornell University.

[75] Bittencourt TN, Wawrzynek PA, Ingraffea AR, and Sousa JL. 1996. Quasi-automatic simulation of crack propagation for 2D LEFM problems. Engineering Fracture Mechanics; 52(2): 321–334.

[76] Azocar D, Elgueta M, and Rivara MC. 2010. Automatic LEFM crack propagation method based on local Lepp-Delaunay mesh refinement. Advances in Engineering Software; 41: 111–119.

[77] Williams ML. 1957. On the stress distribution at the base of a stationary crack. Journal of Applied Mechanics; 24: 109–114.

Chapter 6. Edge-Based Smoothing Technique for Modeling Crystal Plasticity

6.1 Introduction

In crystals, the mechanical behaves are essentially anisotropic, i.e., mechanical properties such as plastic deformation are directionally dependent. Microscopically, the properties of anisotropy are related to the forming a crystalline structure (lattices) with certain specific, characteristic orientations during the crystallization, and in reality a variety of crystallographic defects such as twins, dislocations or stacking faults, etc. The continuum crystal plasticity includes considerable models to cope with the anisotropic deformation of crystals, developed since the contributions of pioneers such as Sachs [1] (1928) and Taylor [2] (1938).

Over the past three decades, a large class of research has been conducted to describe the constitutive and numerical aspects for both single crystals (monocrystals) and polycrystals. The numerically tractable constitutive models, incorporating existing knowledge of the physics of crystal deformation and continuum, were invented to tackle crystal mechanical problems subjected to complicated internal and/or external boundary conditions. For single crystal, one of the most used numerical tools is the crystal plasticity finite element method (CPFEM). This method is used with various models and was proposed to study the anisotropic plastic behavior by many investigators [3–13]. Some critical analysis of the behaviors predicted from these models and new explorations can be found in literature [14–21]. Generally, CPFEM evolves the equilibrium of the forces and the compatibility of the displacements employing a weak form of

the principle of virtual work based on certain crystal plasticity constitutive models. CPFEM models possess many advantages, in which one of them is their capability to describe the inelastic deformation and localization processes through encompassing various constitutive formulations for plastic flow and hardening at microscopic crystallographic sliding level, even for complicated geometry or boundary conditions.

Crystal plasticity can be exploited also to study material behaviors of polycrystals from the behavior of individual grains. The reason is that polycrystals are assemblies of large numbers of single crystals (grains), each of which can deform by crystallographic slip with varying orientations. As such, the actual solution of a problem of the macroscopic behaviors of a polycrystal may be a highly complex elastic-plastic boundary value problem for a crowd of anisotropic, continuous and fully contiguous crystallites [22]. To deal with the polycrystal plasticity, a classical approach is exploring some appropriate fashion to average the crystal interactions to describe macroscopic behavior. An early attempt is to assume all grains experience the same state of stress so that it satisfies the equilibrium condition across the grain boundaries but violates the compatibility conditions [1], i.e., finite strains may induce gaps and overlaps between grains. While the Taylor model [2] assumes grains within the aggregate experience the same state of deformation so as to ensure the compatibility conditions; however, the equilibrium condition is neglected. To satisfy both compatibility and equilibrium conditions across the grain boundaries, a self-consistent model was first constructed by Kröner [23] and then further extended [24–28]. In a self-consistent model, each grain is modelled as an inclusion embedded in a homogeneous matrix of surrounding material maintaining mechanical properties of the polycrystal. A number of investigations with new models have been conducted to link the grain level mechanical response to the response of a polycrystalline aggregate, including

developing constrained hybrid model [29], generalized Taylor models [2,30–32] and Green's function fast Fourier transform (FFT) models [33,34], constructing dislocation density-based crystal constitutive equations [35], application of statistical continuum mechanics to study polycrystals [36,37], and so on. Due to the development of computing power over the last few decades, many crystal plasticity models have been integrated into FE simulation tools and successfully applied to numerous practical problems [38,39]. To reduce the CPU time involved in crystal plasticity simulations (especially for large grain assemblies), some computationally efficient strategies have been proposed recently [40–43]. So far, crystal plasticity models based on FE simulations are able to effectively model polycrystals at both microscopic and macroscopic scales. On topics related to kinematics, homogenization and multiscale methods of crystal plasticity modeling, one can refer to the latest review paper [44].

In CPFEM simulation, especially in modeling of polycrystal deformation, the mesh discretization for a domain with a great quantity of grains needs to consider the facility or feasibility. To discretize a domain with internal grain boundaries, the T-mesh (using triangular elements for 2D and tetrahedral elements for 3D) is always easy to generate compared to other mesh types (e.g., quadrilateral mesh for 2D or hexahedral mesh for 3D). However, the conventional FEM models using T-mesh often suffer from poor accuracy, excessive stiffness in shearing/bending, sensitivity of mesh distortion and sometimes rigid behavior of entire mesh, etc. In addition, because of the plastic incompressibility of (single) crystals, an appropriate numerical technique, which can deal with volumetric locking phenomena, is very necessary. Fortunately, the recently proposed smoothed finite element methods (S-FEM) can achieve higher accuracy than the commonly used low order FEM [45]. Based on those good features (e.g., high accuracy and convergence rates, mesh distortion immunity as absence of isoparametric mapping and

volumetric locking free) already obtained for ES-FEM so far, in this chapter we attempt to extend it into crystal plasticity modeling. In this work, we present the formulations and numerical implementation of a hyperelastic-based multiplicative plasticity constitutive model based on the ES-FEM scheme to describe the anisotropic finite strain for rate independent crystal plasticity using a triangular mesh. The implementation is carried out in the general framework of a smoothed Galerkin weak form to avoid volumetric locking and to capture localized failure modes and it involves strain smoothing manipulations over the whole displacement field. The kinematical basis of elastoplastic deformation for the model is the multiplicative decomposition of the deformation gradient by introducing the isoclinic intermediate configuration. The stress update adopts the exponential map-based integration algorithm, which possesses some advantages such as computation of the exponential function through a recursion framework with a straightward manner from the Cayley-Hamilton theorem, avoiding the spectral decomposition of the argument tensors.

The chapter is organized as follows. Section 2 presents the global solution strategy and the idea of the smoothing technique: general framework of the incremental boundary value problem based on Newton-Raphson scheme at finite strains and edge-based gradient smoothing operation. The kinematics of crystal deformation and constitutive laws are laid out in Section 3. Section 4 discusses a planar double slip model and implementation of the stress state update algorithm with return-mapping. In Section 5, the proposed smoothed technique based crystal plasticity finite element modeling procedure is used to study the strain localization in ductile single crystals with two representative numerical examples. Furthermore, the mesoscopic deformation and macro-mechanical behavior of polycrystals are studied in Section 6 by presented procedure with the geometry approximated by the Voronoi tessellation.

6.2 Problem Description and Edge-Based Strain Smoothing Technique

6.2.1 General Framework

Consider a solid referred to an initial configuration $\mathcal{B}_0(X)$, which is open and bounded by smooth boundary $\partial\mathcal{B}_0$ and closure $\overline{\mathcal{B}}_0 := \mathcal{B} \cup \partial\mathcal{B}_0$. Let $[t_n, t_{n+1}]$ be the time interval of interest, and now we assume a process of incremental loading whereby the displacement field of particles mapping over $\mathcal{B}_0$ changes from $\boldsymbol{\varphi}_n$ at time t_n to $\boldsymbol{\varphi}_{n+1} = \boldsymbol{\varphi}_n + \mathbf{u}$ at time t_{n+1}. With these notations in hand, the weak form of equilibrium for conventional FEM at time t_{n+1} according to the virtual principle then reads as

$$\int_{\mathcal{B}_0} \mathbf{P}_{n+1} : \nabla_0 \boldsymbol{\eta} \mathrm{d}\Omega - \int_{\mathcal{B}_0} \mathbf{f}_{n+1}^b \cdot \boldsymbol{\eta} \mathrm{d}\Omega - \int_{\partial\mathcal{B}_0} \mathbf{f}_{n+1}^t \cdot \boldsymbol{\eta} \mathrm{d}\Gamma = 0 \tag{6.1}$$

where $\mathbf{f}_{n+1}^b$ and $\mathbf{f}_{n+1}^t$ denotes the body force and the prescribed traction vector, respectively, $\boldsymbol{\eta}$ defines an admissible virtual displacement field satisfying the homogeneous form of essential boundary conditions, ∇_0 denotes the material gradient, and $\mathbf{P}_{n+1}$ stands for the first Piola-Kirchhoff stress field at the end of the time interval, which can be determined by a general form using some algorithm of stress updating method [46], that is

$$\mathbf{P}_{n+1} = \hat{\mathbf{P}}(\boldsymbol{F}_{n+1}, \boldsymbol{\alpha}_n) \tag{6.2}$$

where $\boldsymbol{\alpha}_n$ represents the set of internal variables and the deformation gradient at state t_{n+1} is given as

$$\boldsymbol{F}_{n+1} = \nabla_0 \boldsymbol{\varphi}_{n+1} \tag{6.3}$$

Substitute Eq.(6.2) and (6.3) into (6.1), we have

$$\int_{\mathcal{B}_0} \left[\hat{\mathbf{P}}(\boldsymbol{F}_{n+1}, \alpha_n) : \nabla_0 \boldsymbol{\eta} - \mathbf{f}_{n+1}^b \cdot \boldsymbol{\eta} \right] \mathrm{d}\Omega - \int_{\partial\mathcal{B}_0} \mathbf{f}_{n+1}^t \cdot \boldsymbol{\eta} \mathrm{d}\Gamma = 0 \tag{6.4}$$

which defines a set of non-linear equations that can be solved to obtain the updated deformation mapping φ_{n+1}. If the Newton-Raphson iteration method is employed, one may arrive at the expression for this finite strain incremental boundary value problem [46], which gives

$$\int_{\mathcal{B}_0} \nabla_0 \boldsymbol{\eta} : \hat{\mathbf{K}}_{n+1} : \nabla_0 \mathbf{u} \mathrm{d}\Omega - \mathbf{r} = 0 \tag{6.5}$$

where $\mathbf{r}$ is the residual force term, and $\hat{\mathbf{K}}_{n+1}$ denotes the consistent tangents， which can be computed trivially for small strains, but would be more cumbersome to derive for finite strain models.

6.2.2 Briefing of Edge-Based Strain Smoothing Technique

The strain smoothing technique was applied in Galerkin mesh-free methods [47], which use the moving least-squares (MLS) and reproducing kernel approximations. The so-called weakened weak (W2) formulation based on the G space theory [48] was subsequently developed by extending the gradient smoothing technique to a class of discontinuous shape functions.

The strain smoothing operation is carried out over the so-called local smoothing domain which can be constructed within elements (e.g., CS-FEM) but more often beyond the elements (e.g., ES-FEM, NS-FEM and FS-FEM). The smoothed strain field $\tilde{\boldsymbol{\varepsilon}}_k$, for computation of stiffness matrix, will be in generally computed by a weighted average of the standard strain field $\boldsymbol{\varepsilon}^h(\mathbf{x})$. For example, the smoothed strain field at a point in a smoothed domain Ω_k^s can be defined by the following operation

$$\tilde{\boldsymbol{\varepsilon}}_k(\mathbf{x}_C) = \int_{\Omega^h} \boldsymbol{\varepsilon}^h(\mathbf{x}) \Phi_k(\mathbf{x} - \mathbf{x}_C) \mathrm{d}\Omega \tag{6.6}$$

where $\Phi_k(\mathbf{x}-\mathbf{x}_C)$ is a distribution function or a smoothing function that satisfies at least unity property such as

$$\Phi_k(\mathbf{x}-\mathbf{x}_C) \geq 0 \text{ and } \int_{\Omega_k^s} \Phi_k(\mathbf{x}-\mathbf{x}_C)\mathrm{d}\Omega = 1 \tag{6.7}$$

For simplicity, the smoothing function is assumed to be a Heaviside-type piecewise constant function defined in the following form

$$\Phi_k(\mathbf{x}-\mathbf{x}_C) = \begin{cases} 1/A_k^s, & \mathbf{x} \in \Omega_k^s \\ 0, & \mathbf{x} \notin \Omega_k^s \end{cases} \tag{6.8}$$

where $A_k^s = \int_{\Omega_k^s} \mathrm{d}\Omega$ is the area of the smoothing domain Ω_k^s. Substituting Eq. (6.8) into Eq. (6.6) and applying the divergence theorem, the smoothed strains would be

$$\tilde{\boldsymbol{\varepsilon}}_k = \frac{1}{A_k^s}\int_{\Omega_k^s} \nabla_S \mathbf{u}^h \mathrm{d}\Omega = \frac{1}{A_k^s}\int_{\Gamma_k^s} \mathbf{n}_k^s(\mathbf{x})\mathbf{u}^h(\mathbf{x})\mathrm{d}\Gamma \tag{6.9}$$

where Γ_k^s is the boundary of the smoothing domain Ω_k^s, and $\mathbf{n}_k^s(\mathbf{x})$ is the outward normal matrix on the boundary Γ_k^s defined by

$$\mathbf{n}_k^s(\mathbf{x}) = \begin{bmatrix} n_{kx}^s & 0 & n_{ky}^s \\ 0 & n_{ky}^s & n_{kx}^s \end{bmatrix}^T \tag{6.10}$$

in which n_{kx}^s and n_{ky}^s are the unit outward normal components in *x*-axis and *y*-axis, respectively.

The idea of ES-FEM is applying the smoothing operation on the smoothing domain Ω_k^s associated with the edge which is created by connecting two endpoints of the edge to centroids of corresponding adjacent element(s) as sketched in Figure 3.3. Based on the formulations already introduced in Eq. (3.12)–(3.17), the smoothed strain-displacement matrix for ES-FEM using triangle elements can be assembled by

$$\tilde{\mathbf{B}}_I = \frac{1}{A_k^s}\sum_{j=1}^{n_k^e}\frac{1}{3}A_j^e\mathbf{B}_j^e \tag{6.11}$$

where $\mathbf{B}_j^e = \sum_{I\in S_j^e}\mathbf{B}_I$ is the compatible strain-displacement matrix for j th element attached to edge k. The expression of matrix $\mathbf{B}_I(\mathbf{x})$ for the node I in triangle elements is defined as

$$\mathbf{B}_I(\mathbf{x}) = \nabla_S \mathbf{N}_I(\mathbf{x}) = \begin{bmatrix} \dfrac{\partial N_I(\mathbf{x})}{\partial x} & 0 & \dfrac{\partial N_I(\mathbf{x})}{\partial y} \\ 0 & \dfrac{\partial N_I(\mathbf{x})}{\partial y} & \dfrac{\partial N_I(\mathbf{x})}{\partial x} \end{bmatrix}^T \tag{6.12}$$

Due to the use of the triangular elements with the linear shape functions, the entries of matrix $\mathbf{B}_I(\mathbf{x})$ are constants, and so are the entries of matrix $\mathbf{B}_j^e$ and $\tilde{\mathbf{B}}_I$. In a similar fashion, the smoothed element discrete spatial gradient operator (strain-displacement matrix) involving finite deformation and strains for computing of smoothed consistent spatial tangent modulus later will be of the form

$$\tilde{\mathbf{G}}_I = \frac{1}{A_k^s}\sum_{j=1}^{n_k^e}\frac{1}{3}A_j^e\mathbf{G}_j^e \tag{6.13}$$

where $\mathbf{G}_j^e$ is the element discrete spatial gradient operator of element j and its associated form for plane problems is given as

$$\mathbf{G}_j^e = \begin{bmatrix} \dfrac{\partial N_1(\mathbf{x})}{\partial x} & 0 & \dfrac{\partial N_2(\mathbf{x})}{\partial x} & 0 & \dfrac{\partial N_3(\mathbf{x})}{\partial x} & 0 \\ 0 & \dfrac{\partial N_1(\mathbf{x})}{\partial x} & 0 & \dfrac{\partial N_2(\mathbf{x})}{\partial x} & 0 & \dfrac{\partial N_3(\mathbf{x})}{\partial x} \\ \dfrac{\partial N_1(\mathbf{x})}{\partial y} & 0 & \dfrac{\partial N_2(\mathbf{x})}{\partial y} & 0 & \dfrac{\partial N_3(\mathbf{x})}{\partial y} & 0 \\ 0 & \dfrac{\partial N_1(\mathbf{x})}{\partial y} & 0 & \dfrac{\partial N_2(\mathbf{x})}{\partial y} & 0 & \dfrac{\partial N_3(\mathbf{x})}{\partial y} \end{bmatrix} \tag{6.14}$$

The smoothed consistent spatial tangent modulus $\tilde{\mathbf{K}}_T$ for an associated smoothing domain is computed as

$$\tilde{\mathbf{K}}_T = \int_{\Omega_k^s} \tilde{\mathbf{G}}^T \tilde{\mathfrak{c}} \tilde{\mathbf{G}} d\Omega = \tilde{\mathbf{G}}^T \tilde{\mathfrak{c}} \tilde{\mathbf{G}} A_k^s \tag{6.15}$$

where $\tilde{\mathfrak{c}}$ is the smoothed elastoplastic consistent tangent, and the expression of the associated elastoplastic consistent tangent for planar double slip single crystal model will be introduced in Section 4. The corresponding smoothed internal force will be obtained using a comparable fashion of smoothing as follows

$$\tilde{\mathbf{f}}^{\text{int}} = \int_{\Omega_k^s} \tilde{\mathbf{B}}^T \tilde{\boldsymbol{\sigma}} d\Omega = \tilde{\mathbf{B}}^T \tilde{\boldsymbol{\sigma}} A_k^s \tag{6.16}$$

where the smoothed Cauchy stress $\tilde{\boldsymbol{\sigma}}$ here can be computed through a completely analogous operation of gradient smoothing as mentioned. Once the smoothed consistent spatial tangent modulus matrix and the smoothed internal force vector for each smoothing cells are obtained, the discrete global stiffness matrix and internal force vector for the system will be assembled similarly to the procedure of standard FEM.

6.3 Kinematics of Crystal Deformation and Constitutive Model

The pioneering work of kinematics of crystal plasticity theory had been outlined by [6,49–53]. The basic constitutive description of crystal plasticity here follows the framework laid out by [6,54,55], with the variation of the integration algorithm and numerical implementation in the next section outlined by [46,56]. The mechanical response of inelastic deformation of crystalline is dominated by crystallographic slip, in which the other mechanisms such as the sliding effect of grain boundaries, twinning or diffusion are not considered.

6.3.1 Kinematics of Crystal Plastic Deformation

The material is presumed to flow through the crystal lattice owing to dislocation motions. During the process, the crystal lattice undergoes rigid rotation and stretching, which can be recovered via complete unloading of the material. Although these two deformation modes arise simultaneously, they can be multiplicatively decomposed [50] locally in mathematical models by introducing the intermediate configuration as shown in Figure 6.1, i.e., considering the multiplicative decomposition [57–58], the deformation gradient is specified as

$$\boldsymbol{F} = \boldsymbol{F}^e \boldsymbol{F}^p \tag{6.17}$$

where elastic deformation and rigid body motions are typically considered to be included in $\boldsymbol{F}^e$, and $\boldsymbol{F}^p$ describes locally a plastic intermediate (or unrotated) configuration which is supposed to be obtained by the evolution constitutive equation $\dot{\boldsymbol{F}}^p = \partial(\boldsymbol{F}^p)/\partial t$ with the initial condition $\boldsymbol{F}_t^p(t = t_0) = 1$ at the reference configuration [59].

In Figure 6.1, a pair of orthonormal slip system vectors (initial slip direction vector $\boldsymbol{s}_0^\alpha$ and initial slip plane normal vector $\boldsymbol{n}_0^\alpha$) defined the α th slip system in initial (or undeformed) configuration; the unit slip system vectors $\boldsymbol{s}^\alpha$ and $\boldsymbol{n}^\alpha$ remain orthonormal since $\boldsymbol{s}_0^\alpha \cdot \boldsymbol{n}_0^\alpha = \boldsymbol{s}^\alpha \cdot \boldsymbol{n}^\alpha = 0$.

Through the polar decomposition of $\boldsymbol{F}^e$, we can define the rotation tensor $\boldsymbol{R}^e$ and the right stretch tensor $\boldsymbol{U}^e$ as follows

$$\boldsymbol{F}^e = \boldsymbol{R}^e \boldsymbol{U}^e \tag{6.18}$$

Then the unit vectors $\boldsymbol{s}^\alpha$ and $\boldsymbol{n}^\alpha$ will take the form

$$\boldsymbol{s}^{\alpha} = \boldsymbol{R}^{e}\boldsymbol{s}_{0}^{\alpha} \text{ and } \boldsymbol{n}^{\alpha} = \boldsymbol{R}^{e}\boldsymbol{n}_{0}^{\alpha} \tag{6.19}$$

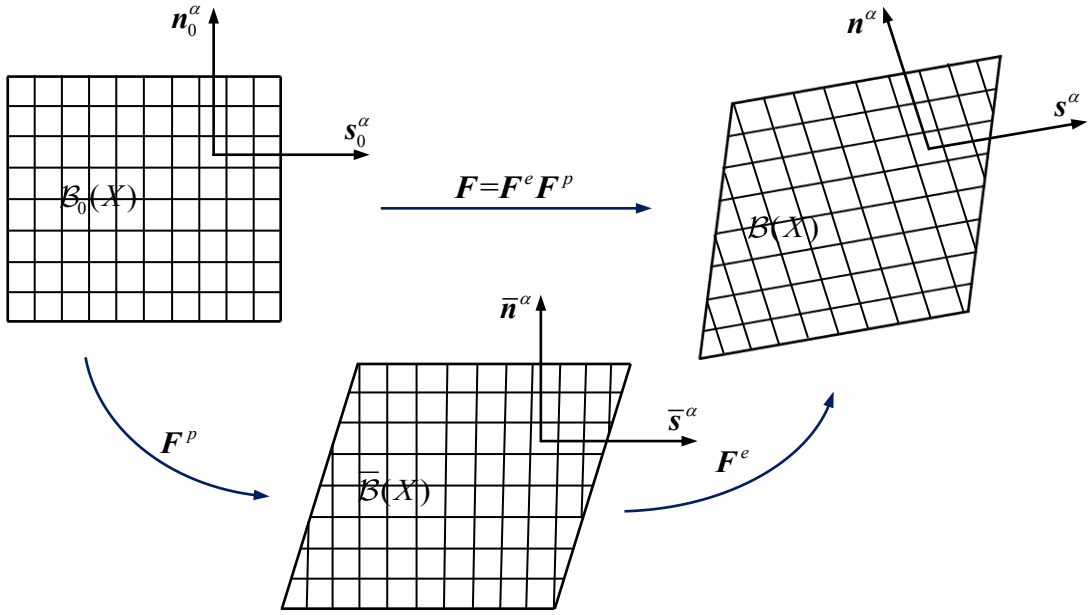

Figure 6.1. Illustration of kinematics of elastoplastic deformation of crystalline solid deformation by crystallographic slip: multiplicative decomposition of deformation gradient, $\boldsymbol{F} = \boldsymbol{F}^e\boldsymbol{F}^p$ (involving the initial configuration $\mathcal{B}_0(X)$, intermediate configuration $\bar{\mathcal{B}}(X)$, and deformed configuration $\mathcal{B}(X)$).

The plastic velocity gradient in the intermediate configuration can be represented as the sum of plastic shearing rates ($\dot{\gamma}^{\alpha}$) for all active crystallographic slip systems by [6, 51]

$$\boldsymbol{L}^{p} = \dot{\boldsymbol{F}}^{p}\left(\boldsymbol{F}^{p}\right)^{-1} = \sum_{\alpha=1}^{N_{as}} \dot{\gamma}^{\alpha}\boldsymbol{s}^{\alpha} \otimes \boldsymbol{n}^{\alpha} \tag{6.20}$$

where N_{as} is the number of active slip systems, γ^{α} is the plastic increment within the slip system.

6.3.2 Constitutive Laws

In this subsection, we present the constitutive relations of a general finite strain, rate-independent, multisurface elastoplastic model of crystals. The model is formulated based on the framework of hyperelastic-based multiplicative plasticity integrating the ES-FEM scheme to describe the anisotropic finite strain continuum crystal plasticity.

The mechanisms of inelastic deformation of crystals resulting from shear deformations occurring on one or more slip systems have been mentioned previously, but no description was given yet to reckon the stresses required to initiate and sustain the deformation. A crystal deforms plastically only when the stress component on a slip plane and in the slip direction reaches the critical resolved shear stress. The resolved shear stress on a system is evaluated as follows

$$\tau^{\alpha} = \boldsymbol{S} : \boldsymbol{s}^{\alpha} \otimes \boldsymbol{n}^{\alpha} \tag{6.21}$$

where $\boldsymbol{S}$ denotes the second Piola-Kirchhoff stress (PK2), which is symmetric and is defined via the relation as

$$\boldsymbol{S} = \boldsymbol{C}^{e} : \boldsymbol{E} = J\boldsymbol{F}^{e-1}\boldsymbol{\sigma}\boldsymbol{F}^{e-\mathrm{T}} \tag{6.22}$$

where $\boldsymbol{C}^{e}$ is the fourth order elastic constant matrix, $\boldsymbol{E} = \frac{1}{2}(\boldsymbol{F}^{e\mathrm{T}} \cdot \boldsymbol{F}^{e} - \boldsymbol{I})$ is the Lagrangian finite strain tensor, $\boldsymbol{\sigma}$ is the Cauchy stress tensor which has a relation with the Kirchhoff stress tensor $\boldsymbol{\tau}$ or PK2 stress via

$$\boldsymbol{\sigma} = J^{-1}\boldsymbol{\tau} = J^{-1}\boldsymbol{F}^{e} \cdot \boldsymbol{S} \cdot \boldsymbol{F}^{eT} \tag{6.23}$$

It is noted that both the PK2 stress and Cauchy stress (and hence the Kirchhoff stress) are symmetric. Using above equations and the rotation tensor defined in Eq. (6.18), the resolved shear stress can be rewritten as

$$\tau^{\alpha} = \boldsymbol{R}^{eT}\boldsymbol{\tau}\boldsymbol{R}^{e} : \boldsymbol{s}^{\alpha} \otimes \boldsymbol{n}^{\alpha} \tag{6.24}$$

To model the reversibility of crystalline material behavior subjected to large strains, accounting both for nonlinear behavior and large shape changes, a hyperelastic law is adopted in constitutive relation. Assume the strain energy density function arisen by elastic contribution is denoted by W^e, the Kirchhoff stress $\boldsymbol{\tau}$ in Eq. (6.24) can be obtained in terms of $\boldsymbol{F}^e$ as

$$\boldsymbol{\tau} = \frac{\partial W^e}{\partial \boldsymbol{F}^e} \cdot \boldsymbol{F}^{e\mathrm{T}} \tag{6.25}$$

The evaluation of yield functions for rate-independent elastoplastic model of FCC crystals here is determined by the relationship in terms of the resolved shear stress and the critical resolved shear stress. For the α^{th} slip system, it would be

$$f^\alpha(\tau^\alpha(\boldsymbol{\tau}^{\mathrm{tr}}), \tau_y^\alpha) = \tau^\alpha(\boldsymbol{\tau}^{\mathrm{tr}}) - \tau_{cr}^\alpha, \quad \alpha = 1,2,...,N_{as} \tag{6.26}$$

where τ_{cr}^α is the critical resolved shear stress for the α^{th} slip system, $\tau^\alpha(\boldsymbol{\tau}^{\mathrm{tr}})$ is the resolved shear stress related to the trial state of stress $\boldsymbol{\tau}^{\mathrm{tr}}$ in the general return-mapping procedure. Note that f^α would be anisotropic functions of τ^α. The plastic slip for an associated slip system may commence when $f^\alpha > 0$, that is, the state of resolved shear stress exceeds the corresponding anisotropic yield surface [60]. The set of systems for which $\tau^\alpha = \tau_{cr}^\alpha$ is called as the set of potentially active or critical systems [6].

It is worthwhile to note that the critical resolved shear stress $\tau^\alpha(\boldsymbol{\tau}^{\mathrm{tr}})$ depends on both the strain and the history of strain if hardening behavior is involved. After first introduced in Taylor's dislocation model [61], a number of flow rules have been developed to describe the hardening behavior of crystals for both rate-independent (e.g., References [26,52,62–68]) and rate-dependent (e.g., References [5,7,46,69–73]). The general form of the constitutive laws for

slip (shear) on α th slip system (the current strain hardening state) can be expressed as the following evolution equation [4]

$$\dot{\tau}_{cr}^{\alpha} = \sum_{\beta=1}^{N_{as}} h_{\alpha\beta}\dot{\gamma}^{\beta}, \quad \alpha = 1,2,...,N_{as} \tag{6.27}$$

where $h_{\alpha\beta}$ are slip-plane plastic hardening moduli that characterize the work hardening rate of the crystal, the sum ranges over all activated slip systems. The diagonal components $h_{\alpha\alpha}$ ($\beta = \alpha$) represent self-hardening on a slip system and off diagonal terms $h_{\alpha\beta}$ ($\beta \neq \alpha$) denote latent hardening, viz., hardening of one slip system due to slip on another [74]. In this study, the classical, commonly used Taylor isotropic hardening rule is employed where the self and latent hardening are considered equal. Besides, the resolved critical stress is assumed to be a function of a single internal variable γ, or so-called the Taylor cumulative shear strain on all slip system, i.e.

$$\gamma = \sum_{\alpha=1}^{N_{as}} \int_0^t \left|\dot{\gamma}^{\alpha}\right| \mathrm{d}t \tag{6.28}$$

6.4 Planar Double Slip Model and Numerical Implementation

The actual crystal plastic deformation in physics may comprise a number of slip systems, e.g., face centered cubic (fcc) crystals have 12 slip systems. In most situations, the slip initiation and shear band formation is observed in crystals undergoing multi-slip, often with a double mode of primary-conjugate slip [4]. Although the theory in the previous section is applicable for general three-dimensional slip geometry, we employ the planar primary-conjugate double slip geometry as sketched in Figure 6.2, due to its simplicity of implementation.

6.4.1 A Planar Double Slip Model

To study the plane deformation of fcc crystals under certain crystallographic orientations and external loading, only two effective slip systems (other than 12 slip system in general fcc structures) with both of their slip directions and slip plane normal vectors lie in the drawing plane with loading and deformation. In Figure 6.2, θ_0 represent the initial orientation of slip systems 1 and ϕ_0 is the angle between systems 1 and 2. The mirrored slip systems 3 and 4 have the relations with systems 1 and 2 as

$$\left\langle s^3, n^3 \right\rangle = \left\langle -s^1, n^1 \right\rangle, \ \left\langle s^4, n^4 \right\rangle = \left\langle -s^2, n^2 \right\rangle \tag{6.29}$$

Observing from the mirrored pairs of slip systems, the compatible active slip sets would be

$$\begin{gathered} \langle 1\rangle, \langle 2\rangle, \langle 3\rangle, \langle 4\rangle \text{ (when the set has one system)} \\ \text{or: } \langle 1,2\rangle, \langle 2,3\rangle, \langle 3,4\rangle, \langle 4,1\rangle \text{ (when the set has two systems)} \end{gathered} \tag{6.30}$$

According to constitutive theory of a compressible Neo-Hookean type model [12], the stored energy function is defined as

$$W^e = \frac{1}{2}\kappa \ln^2[J^e] + \frac{1}{2}\mu(\boldsymbol{F}^e_{iso} : \boldsymbol{F}^e_{iso} - 3) \tag{6.31}$$

where κ and μ denote the bulk modulus and shear modulus, respectively. Here, the equation introduced the tensor $\boldsymbol{F}^e_{iso}$, the isochoric component of the elastic left Cauchy–Green strain tensor, which gives,

$$\boldsymbol{F}_{iso}^{e} = (J^{e})^{-1/3}\boldsymbol{F}^{e} \text{ with } J^{e} = \det(\boldsymbol{F}^{e}) \tag{6.32}$$

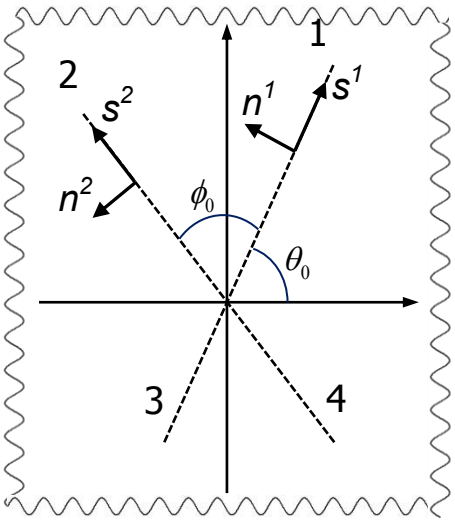

Figure 6.2. Schematic drawing of a planar double-slip crystal model.

Utilize Eq. (6.25), the Kirchhoff stress then can be evaluated as

$$\boldsymbol{\tau} = \kappa \ln[J^{e}]\boldsymbol{I} + \mu \,\mathrm{dev}[\boldsymbol{F}_{iso}^{e} : \boldsymbol{F}_{iso}^{e}] \tag{6.33}$$

Note that the inner products by hydrostatic components of Kirchhoff stress will be eliminated as the slip system tensors are deviatoric intrinsically. Then if we substitute Eq. (6.33) into Eq. (6.24), it leads to the resolved shear stress

$$\tau^{\alpha} = \mu(\boldsymbol{R}^{e})^{T}[\boldsymbol{F}_{iso}^{e}(\boldsymbol{F}_{iso}^{e})^{T}]\boldsymbol{R}^{e} : \boldsymbol{s}^{\alpha} \otimes \boldsymbol{n}^{\alpha} = \mu \boldsymbol{C}_{iso}^{e} : \boldsymbol{s}^{\alpha} \otimes \boldsymbol{n}^{\alpha} \tag{6.34}$$

where $\boldsymbol{C}_{iso}^{e} = (\boldsymbol{R}^{e})^{T}[\boldsymbol{F}_{iso}^{e}(\boldsymbol{F}_{iso}^{e})^{T}]\boldsymbol{R}^{e} = (\boldsymbol{F}_{iso}^{e})^{T}\boldsymbol{F}_{iso}^{e}$ represents the isochoric right Cauchy-Green strain tensor. Then a simple constitutive formulation of the Schmid stresses based on the Neo-Hookean type model can be inferred as

$$\tau^{\alpha} = \mu \bar{\boldsymbol{s}}^{\alpha} \cdot \bar{\boldsymbol{n}}^{\alpha} \quad \text{with } \bar{\boldsymbol{s}}^{\alpha} = \boldsymbol{F}_{iso}^{e} \boldsymbol{s}^{\alpha} \text{ and } \bar{\boldsymbol{n}}^{\alpha} = \boldsymbol{F}_{iso}^{e} \boldsymbol{n}^{\alpha} \tag{6.35}$$

here the pairs of Eulerian vectors ($\bar{\boldsymbol{s}}^{\alpha}$, $\bar{\boldsymbol{n}}^{\alpha}$) of the slip systems are computed through mapping the orthonormal slip system vectors ($\boldsymbol{s}^{\alpha}$, $\boldsymbol{n}^{\alpha}$) by the unimodular part $\boldsymbol{F}_{iso}^{e}$ of the elastic deformation gradient.

6.4.2 State Update Algorithm

The exponential map algorithm for isotropic elastoplastic response in computational multiplicative elasto-plasticity is available in literature (e.g., [75–79]). For the case of anisotropic monocrystalline plasticity, the implementation of the exact exponential map algorithm utilizes the simple representation of the resolved shear stress τ^{α} expressed in Eq. (6.34), which is based on the corresponding backward-Euler time discretization.

Applying an incremental procedure, the incremental update of the trial elastic deformation gradient in pseudo-time interval $\left[t_n, t_{n+1}\right]$ can be expressed as

$$\boldsymbol{F}_{n+1}^{e\,\mathrm{tr}} = \boldsymbol{F}_{inc} \boldsymbol{F}_{n}^{e} \tag{6.36}$$

where $\boldsymbol{F}_{n}^{e}$ is the elastic deformation gradient at the beginning of the time step, and $\boldsymbol{F}_{inc}$ is the incremental deformation gradient. The associated trial unimodular part $\boldsymbol{F}_{iso}^{e}$ is then to be evaluated by the incremental form of Eq. (6.32) and the trial Schmid stresses are easily written as

$$\tau_{n+1}^{\alpha\,\mathrm{tr}} = \mu \bar{\boldsymbol{s}}^{\alpha\,\mathrm{tr}} \cdot \bar{\boldsymbol{n}}^{\alpha\,\mathrm{tr}} \quad \text{with } \bar{\boldsymbol{s}}^{\alpha\,\mathrm{tr}} = \boldsymbol{F}_{iso}^{e\,\mathrm{tr}} \boldsymbol{s}^{\alpha} \text{ and } \bar{\boldsymbol{n}}^{\alpha\,\mathrm{tr}} = \boldsymbol{F}_{iso}^{e\,\mathrm{tr}} \boldsymbol{n}^{\alpha} \tag{6.37}$$

Once the trial stresses are obtained, we need to check that the trial state is within the elastic domain or lies on the yield surface when the return-mapping algorithm applied, viz., check the yielding function

$$f^{\alpha\,\mathrm{tr}} = \tau_{n+1}^{\alpha\,\mathrm{tr}} - \tau_{cr}^{\alpha}(\gamma_{n+1}^{\mathrm{tr}}) = \mu\bar{\boldsymbol{s}}^{\alpha\,\mathrm{tr}} \cdot \bar{\boldsymbol{n}}^{\alpha\,\mathrm{tr}} - \tau_{cr}(\gamma_{n+1}^{\mathrm{tr}}), \text{ with } \alpha = 1,2,...,N_{as} \tag{6.38}$$

If $f^{\alpha\,\mathrm{tr}} \le 0$, it locates in the elastic state, then the incremental plastic multipliers will be set to be zero and stress state will be set to trial state directly; Otherwise, the plastic multipliers for active systems should be non-negative, and it can be expressed by accumulative form of the corrector $\delta\gamma_{n+1}^{\alpha}$ in the $k^{\,\mathrm{th}}$ Newton-Raphson scheme as

$$\Delta\gamma_{n+1,k}^{\alpha} := \Delta\gamma_{n+1,k-1}^{\alpha} + \delta\gamma_{n+1}^{\alpha} \text{ with } \sum_{\alpha,\beta\in\mathcal{A}} \delta\gamma_{n+1}^{\alpha}\mathbb{J}^{\alpha\beta} = -f^{\alpha} \tag{6.39}$$

where $\mathcal{A}$ is an active working set and the coefficients of the Jacobian $\mathbb{J}^{\alpha\beta}$ can be computed in the following manner:

$$\mathbb{J}^{\alpha\beta} = \mu\left(\bar{\boldsymbol{s}}^{\alpha} \otimes \boldsymbol{n}^{\alpha} + \boldsymbol{n}^{\alpha} \otimes \boldsymbol{s}^{\alpha}\right) : \left[\boldsymbol{F}_{iso}^{e\,\mathrm{tr}} \cdot \mathrm{D}_e : \left(\boldsymbol{s}^{\alpha} \otimes \boldsymbol{n}^{\alpha}\right)\right] + \frac{d\tau_{cr}}{d\gamma} \tag{6.40}$$

where D_e represents the derivative of the exponential map at $-\sum_{\alpha\in\mathcal{A}} \Delta\gamma^{\alpha}(\boldsymbol{s}^{\alpha} \otimes \boldsymbol{n}^{\alpha})$.

When the plastic return-mapping is applied for active working set, the corresponding yield function involving $\Delta\gamma$ yields

$$f^{\alpha}(\Delta\gamma) = \mu\bar{\boldsymbol{s}}^{\alpha}(\Delta\gamma) \cdot \bar{\boldsymbol{n}}^{\alpha}(\Delta\gamma) - \tau_{cr}(\gamma_{n+1}(\Delta\gamma)), \text{ with } \alpha \in \mathcal{A} \tag{6.41}$$

To find the pairs of Eulerian vectors ($\bar{\boldsymbol{s}}^{\alpha}$, $\bar{\boldsymbol{n}}^{\alpha}$) in Eq. (6.41), the Eq. (6.37) can be employed, and the corresponding term $\boldsymbol{F}_{iso}^{e}(\Delta\gamma)$ by the exponential map-based update algorithm leads to

$$\boldsymbol{F}_{iso}^{e}(\Delta\gamma) = \boldsymbol{F}_{iso}^{e\,\mathrm{tr}}\boldsymbol{P}_{iso}^{e}, \text{ with } \boldsymbol{P}_{iso}^{e} = \exp\left[-\sum_{\alpha\in\mathcal{A}} \Delta\gamma^{\alpha}(\boldsymbol{s}^{\alpha} \otimes \boldsymbol{n}^{\alpha})\right] \tag{6.42}$$

The updated elastic deformation gradient and Kirchhoff stress at the end of the interval $[t_n, t_{n+1}]$ would be obtained via Eq. (6.32) and (6.33), we now arrive at

$$\boldsymbol{F}^e_{n+1} = J^{1/3}\boldsymbol{F}^e_{iso} \text{ and } \boldsymbol{\tau}_{n+1} = \kappa \ln[J^e_{n+1}]\boldsymbol{I} + \mu \,\mathrm{dev}[\boldsymbol{F}^e_{iso}(\boldsymbol{F}^e_{iso})^T] \tag{6.43}$$

Concerning the elastoplastic consistent tangents for the stress updating algorithm above, here the tedious derivation will not be presented and we adopt the similar expression of algorithmic moduli employed by Reference [11], that is

$$\begin{aligned}\mathfrak{c} &= \kappa(1+\ln[J^e])\tilde{\mathbf{1}}\otimes\tilde{\mathbf{1}} - 2\kappa\ln[J^e]\tilde{\mathbb{I}} \\ &+ \frac{2}{3}\mu \mathrm{tr}[\boldsymbol{F}^e_{iso}(\boldsymbol{F}^e_{iso})^T][\tilde{\mathbb{I}} - \frac{1}{3}\tilde{\mathbf{1}}\otimes\tilde{\mathbf{1}}] - \frac{2}{3}[\mathrm{dev}[\boldsymbol{\tau}]\otimes\tilde{\mathbf{1}} + \tilde{\mathbf{1}}\otimes\mathrm{dev}[\boldsymbol{\tau}]] \\ &- \sum_{\alpha\in\mathcal{A}}\sum_{\beta\in\mathcal{A}} \mathrm{G}^{\alpha\beta-1}\mu\,\mathrm{dev}[\boldsymbol{s}^\alpha\otimes\boldsymbol{n}^\alpha + \boldsymbol{n}^\alpha\otimes\boldsymbol{s}^\alpha]\otimes\mu\,\mathrm{dev}[\boldsymbol{s}^\beta\otimes\boldsymbol{n}^\beta + \boldsymbol{n}^\beta\otimes\boldsymbol{s}^\beta]\end{aligned} \tag{6.44}$$

The step-by-step algorithm procedure for implementing the stress updating algorithm discussed above is summarized in the Appendix of this chapter.

6.5 Applications to Single Crystal Plasticity

In this section, the numerical procedure proposed will be carried out for single crystal plasticity with examples of the planar slip single crystal model in the context of rate-independent localization computation.

6.5.1 Planar Tension with Symmetric Localization

Strain localization is regarded as a typical instability phenomenon of materials in solid mechanics. The studied problem involves different failure modes: the specimen appears to be the fashion of homogeneous deformation in the early stage of loading, followed by a localization mode of shear bands formation which is superposed by diffuse necking at high strain levels [13]. In the numerical example here, the geometry with the description of symmetric displacement-controlled loading under plane strain conditions is illustrated in Figure 6.3(a). The geometry

parameters are set as: width $W = 20\,\text{mm}$, and length $H = 60\,\text{mm}$. The material parameters are chosen to be: Young modulus $E = 55.4911\,\text{GPa}$, Poisson's ratio $\nu = 0.315$; and the hardening function $\tau_y(\gamma) = y_0 + y_{0,\infty}\left[1 - \exp(-\gamma/\gamma_0)\right] + h\gamma$, with the parameters $\gamma_0 = 0.0929$, $h = 0.0010$ GPa, flow stress $y_0 = 0.0600\,\text{GPa}$ and $y_{0,\infty} = 0.0480\,\text{GPa}$.

The initial orientation of the first slip system (as indicated in Figure 6.2) is assumed to be $\theta_0 = 60.0°$ w.r.t the horizontal direction and the angle between the second slip system and the first one is $\phi_0 = 60.0°$, i.e., the crystal lattice is oriented symmetrically with respect to the axis of tension. The specimen will be deformed up to a prescribed elongation of $\Delta D = 5.0\,\text{mm}$ at both ends in the vertical direction. A material imperfection in the center of the specimen as sketched by a square in Figure 6.3(a) is assumed to trigger the strain localization and the computations presented here are considered as a plane deformation under plane strain condition. Figure 6.3(b) shows a similar experiment of the formation of macroscopic bands conducted by [80].

By exploiting the symmetry along the centerlines of the specimen, only one quadrant of the specimen subjected to appropriate boundary conditions is necessary to discretize and analyze. Because of the plastic incompressibility of single crystals, some special elements such as *Q1E4* enhanced incompatible elements [81] or *F*-bar elements [82] were utilized to tackle the phenomenon of volumetric locking in their previous work for similar problems. In the ES-FEM scheme, the domain is discretized with a base mesh of constant strain triangle elements (CST or T3), and then followed by the construction of strain smoothing, which is performed within elements but more often beyond the elements (meshfree concepts). Without loss of generality, the model adopts a free initial unstructured mesh, which is versatile for the generation of meshes for complex geometries. In this example, the performance of proposed formulations and

algorithms implemented using ES-FEM is compared with FEM by same initial grid plotted in Figure 6.5(a). Figure 6.4 plots the reactions along the constrained edge against the associated prescribed elongation, for both FEM and ES-FEM. The ES-FEM model has two cases: a coarse mesh case with 2432 elements and a fine mesh one with 9704 elements as shown in Figure 6.5(a). Similar to the typical stress-strain curve of ductile materials, the reaction increases slowly after a yield point and it will continue to rise along the deformation until it reaches the peak point, i.e., edge displacement about 3.8 mm. After this point, it decreases with unstable phenomenon occurs which is due to the rather abrupt rotation of the crystal lattice along the shear bands in softer orientation geometrically. At the descending stage of reaction, the FEM model with fine mesh behaves stiffer than ES-FEM model, no matter using coarse mesh or fine mesh. The mesh sensitivity study of ES-FEM model indicated by comparison of reaction displacement curves (coarse mesh and fine mesh) shows the reactions are almost identical before the onset of reaction descending stage, and the variance along the drop stage is also smaller than references [11–12]. It is also worthwhile to note that the ES-FEM model with fine mesh behaves slightly softer than the coarse one after the curves reach the associated peak reactions. Figure 6.5(b) and (c) depicts the deformed configurations of specimen simulated by FEM at the stage $\Delta D = 4.5\,\text{mm}$ and the final stage with $\Delta D = 5.0\,\text{mm}$, respectively. And Figure 6.5(d) and (e) show the deformation/localization simulated by ES-FEM for the specimen stretched up to $\Delta D = 4.5\,\text{mm}$ and $\Delta D = 5.0\,\text{mm}$ ($\Delta D / H = 16.667\%$). To gain better visualization, the quarter model with initial and deformed mesh is mirrored to other three quadrants. We noted that this reflecting mapping generates a horizontal line in the middle of the grid of full model, but actually it does not affect the computation. For FEM case, it fails to model the shear bands in localization analysis when the specimen stretched up to $\Delta D = 4.5\,\text{mm}$ shown in Figure 6.5(b). Two crossed

shear bands are observed in final configuration plotted in Figure 6.5(c), but they are not fully developed compared to references [11,56]. In the deformed configurations in Figure 6.5(d) and (e) obtained by ES-FEM, it is observed that a pair of symmetric crossed shear bands with the cross angle of about 77.4°, i.e., the slip direction rotates from the initial angle 60.0° to 51.3°. Large deformation/strain occurs within elements along the shear band and this phenomena is also consistent with some available references [4,9,11,12,83]. Therefore, the proposed ES-FEM scheme here is demonstrated to be capable of modeling the shear bands development during single crystal deformation in this numerical test.

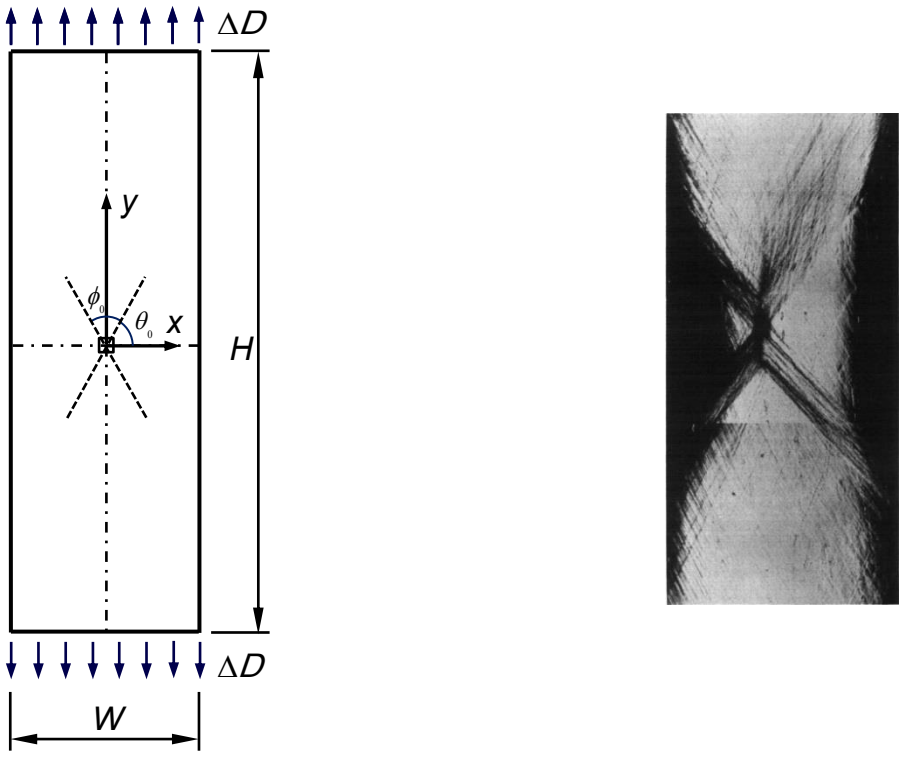

(a) (b)

Figure 6.3. Planar double-slip crystal specimen: (a) schematic drawing of the geometry and mechanical boundary condition used in our example, and (b) experimental observation of a specimen of single crystal of Al-2.8%wt Cu (Photo taken from Asaro, 1979 [84]).

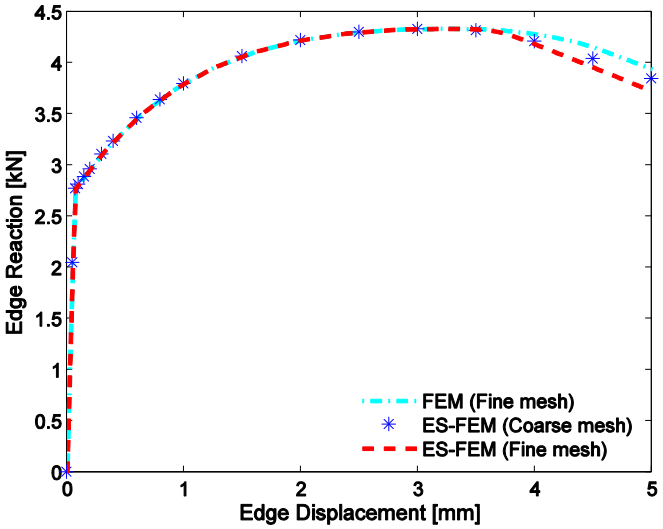

Figure 6.4. The edge reactions against the elongation of prescribed edge.

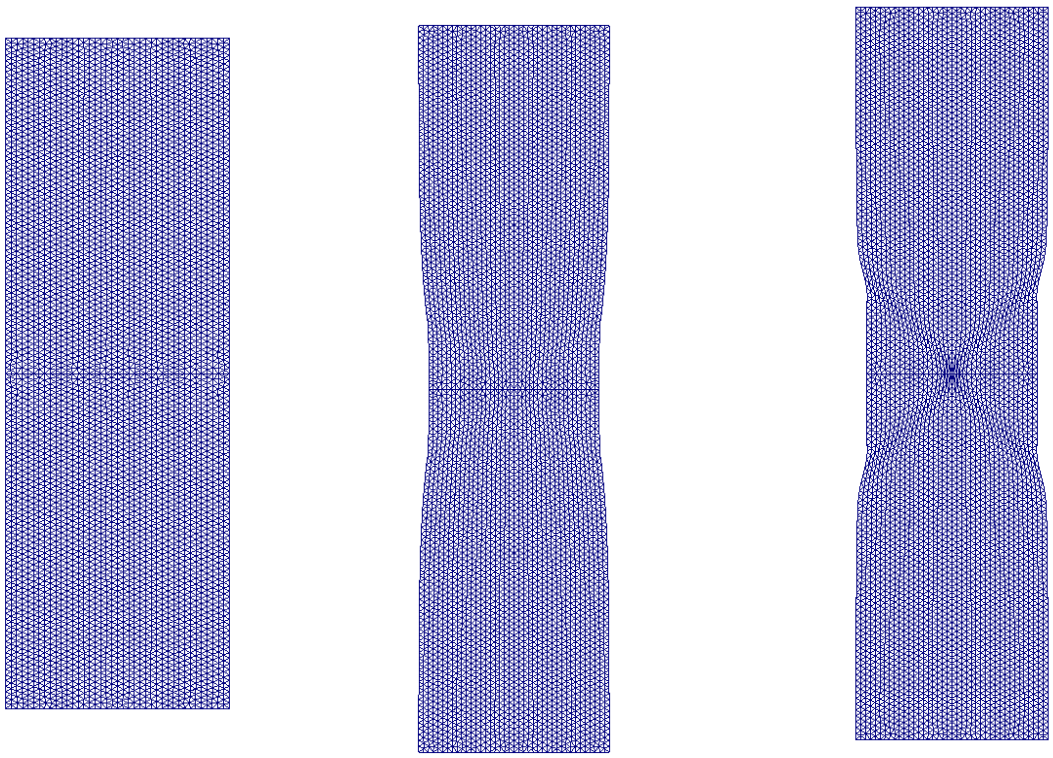

(a) (b) (c)

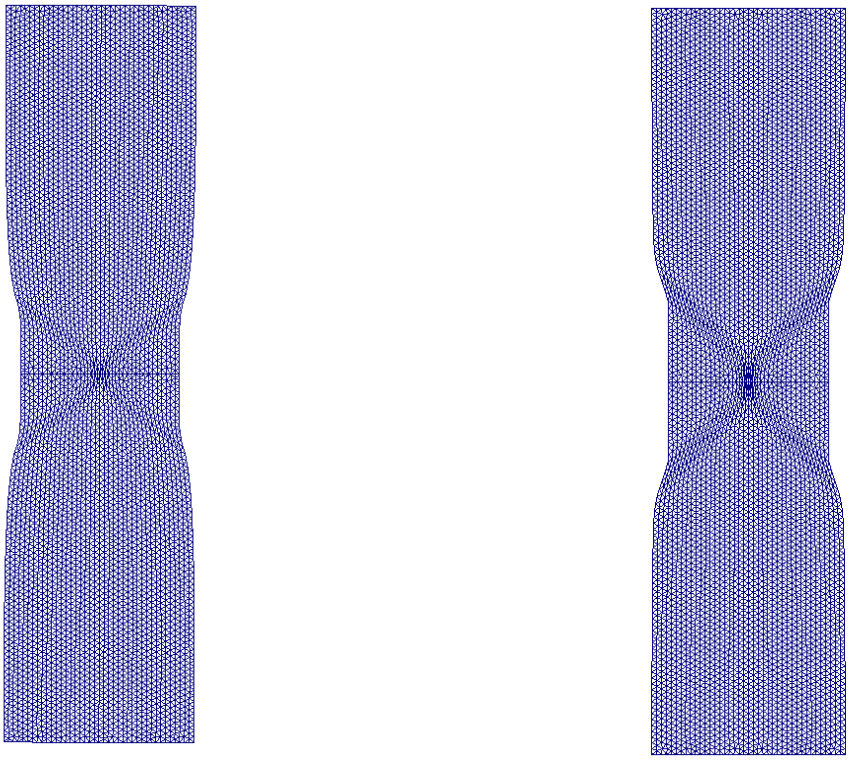

(d) (e)

Figure 6.5. Initial grid and deformed configuration of numerical model: (a) domain discretization with a basic unstructured mesh of 4×2426 CST elements (b) and (c) show the deformed configurations at the stage of $\Delta D = 4.5$ mm simulated by FEM and ES-FEM, respectively; and (d) and (e) show the deformation /localization of the specimen at the final stage with $\Delta D = 5.0$ mm ($\Delta D / H = 16.667\%$) simulated by FEM and ES-FEM, respectively.

6.5.2 Planar Tension with Unsymmetric Localization

This example is included in order to study the strain localization in single crystal when the double slip systems are not symmetrically disposed about the loading axis. The basic geometry with the description of horizontal displacement-controlled loading is illustrated in Figure 6.6. The dimensions of are: $W = 60\,\text{mm}$ and $H = 20\,\text{mm}$. The specimen deforms up to a prescribed elongation $\Delta D = 9.0\,\text{mm}$ at both left and right ends. To exclude the rigid motion of

specimen, the middle node at each end is constrained at vertical direction. The material parameters are the same as the previous example. The initial orientation of the first slip system is assumed to be $\theta_0 = -15.0°$ w.r.t the horizontal direction and the relative angle between the slip systems is $\phi_0 = 60.0°$. The specimen has been discretized using a base mesh of 2426 CST elements in Figure 6.7(a). The outcome of deformation obtained by the proposed method is provided in Figure 6.7(b) and (c). In Figure 6.7(c), a strong localization and associated softening along the narrow shear band shows that plastic flow has localized on the one of the slip planes. It has been known that distorted mesh in standard FEM cause relatively or even dramatically poor results and sometimes is computationally infeasible (e.g., this example). Again, the extended ES-FEM scheme for finite strain applied in this example has been proved to be successful to model the strain localization accompanied with large shear deformation due to insensitivity of large mesh distortion. Compared to conventional linear FEM scheme, such advantages to avoid volumetric locking without using special elements [56] or increasing the total degrees of freedom show S-FEM is a promising technique in numerical simulations for similar problems of strain localization [85,86].

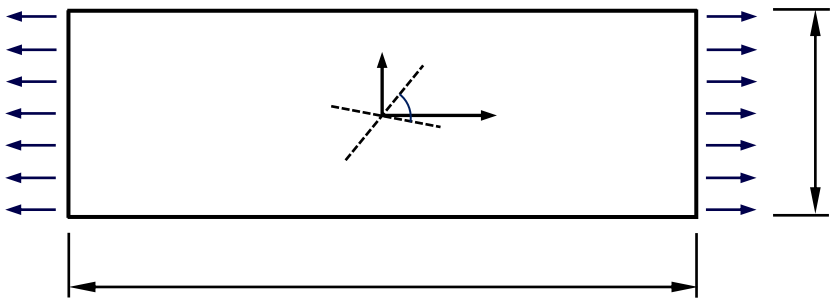

Figure 6.6. A sketch of the geometry with boundary conditions.

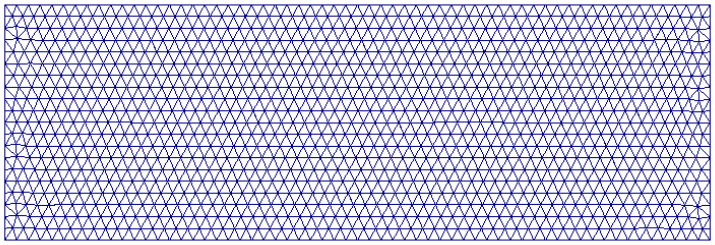

(a)

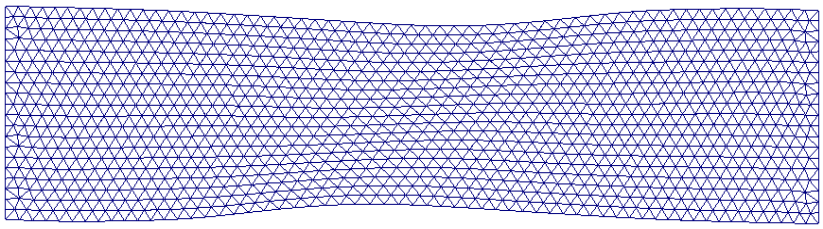

(b)

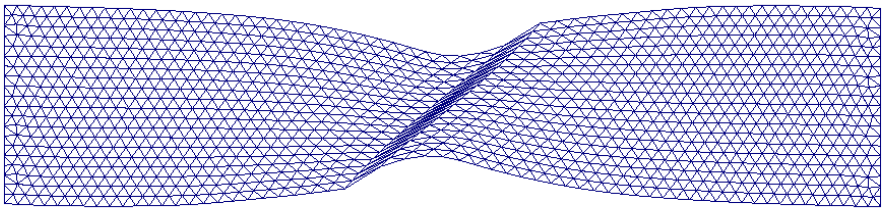

(c)

Figure 6.7. Initial grid and deformed configuration: (a) domain discretization using CST elements; (b) Deformed configuration at the stage of $\Delta D = 6.3$ mm; and (c) unsymmetric localization of the specimen at a final elongation $\Delta D = 9.0$ mm.

6.6 Polycrystalline Plasticity Modeling

In polycrystalline materials the microstructure consists of continuous aggregates of single crystal grains connected by grain boundaries [87], and it then involves prediction of stress-strain behavior and texture by associating the grain subdivision with the geometrically necessary dislocation. Polycrystal plasticity relates the macromechanical behavior of polycrystalline materials to fundamental mechanisms of single crystal deformation. In this work, we focus on the stress and deformation behavior through exploring the smoothed technique based crystal plasticity finite element computation. Since stress/strain distributions depend on grain size, shape, orientation and their distributions, the FE micromechanics modeling of the behavior of polycrystalline aggregates should accommodate the realistic mesoscopic features, including the morphology of the grains. The Voronoi tessellation (VT) [37,88–92], regarded as an excellent candidate to generate polycrystalline grains for geometrical consideration in a stochastic manner, will be implemented to model the polycrystalline aggregates with random grain structure. In our numerical example here, the Voronoi tessellation [93] is also employed to build a random tessellation of the continuous problem domain. It is anticipated to predict the mesoscopic stress/strain field distribution involving crystalline slip dominated inelastic behavior under finite strain scheme. The representative volume element (RVE) size will be also investigated through assessing the macroscopically homogeneous behavior. In schematic description of the problem depicted in Figure 6.8(a), a specimen with the dimension $W = 800\,\mu\text{m}$ and $H = 400\,\mu\text{m}$ under the constraints illustrated is chosen to represent the polycrystalline structure domain. A representative microstructure with 150 random grain cells by VT is plotted in Figure 6.8(b). Figure 6.8(c) and (d) illustrate the domain discretization using CST elements for two typical virtual grain microstructures generated by VT (200 grains and 300 grains), where varied color

relate to a number of random grain orientations. It can be viewed as an aggregation of randomly orientated monocrystals which may endure plastic deformation of anisotropic finite strain. The study will focus on the deformation, elastoplastic behavior and macroscopic responses under monotonic tensile loading condition.

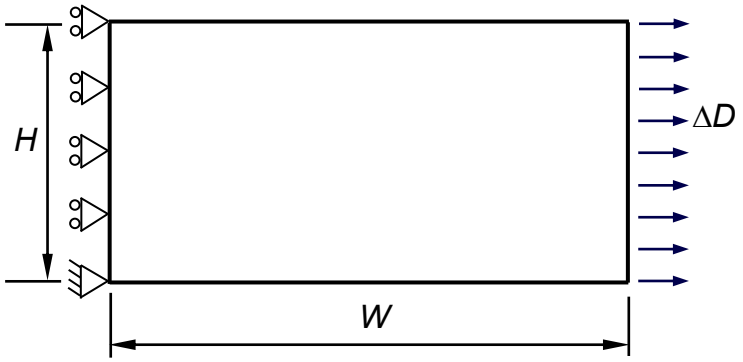

(a)

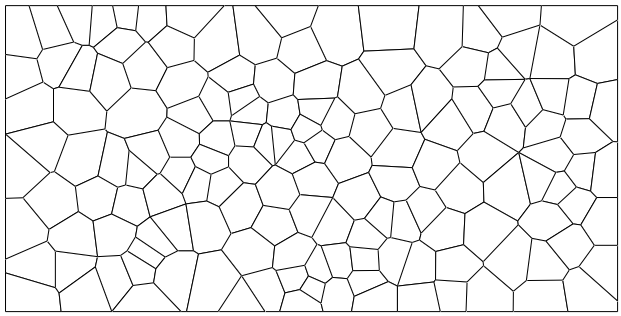

(b)

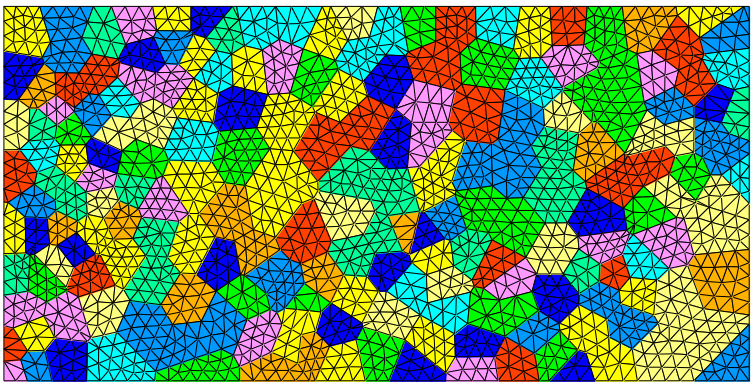

(c)

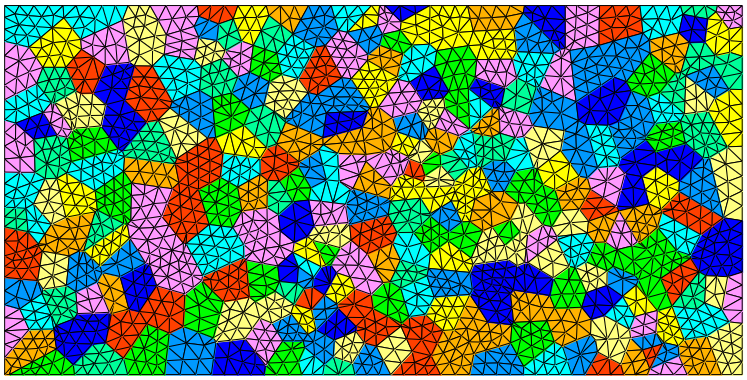

(d)

Figure 6.8. A polycrystalline specimen subjected to tension: (a) A sketch of geometry and boundary conditions; (b) A representative microstructure with 150 random grain cells by Voronoi Tessellation; (c) and (d) show the domain discretization using CST elements for representative synthetic microstructure comprised of 200 grains and 300 grains generated by Voronoi tessellation.

The numerical computation for the model is carried out by a displacement controlled loading, which is subjected to plane strain monotonic tension up to a final displacement of 10% total length of specimen in the horizontal direction. The equivalent von Mises stress of the specimen on deformed configurations for microstructures with 200 grain cells and 300 grain cells with random initial crystal orientations is shown in Figure 6.9(a) and (b). The local

equivalent stresses are up to almost 500% of macroscopic equivalent stress (Figure 6.10). At some grain boundaries, the stress varies considerably, which is mainly due to the incompatible deformation of associated contiguous grains. These plots of stress distributions clearly illustrate the stress and locations of stress concentration varying from grain to grain and it shows the extremely inhomogeneity of polycrystalline aggregates at mesoscale level.

To study the stress-strain behavior at grain level, the choice of RVE (the sufficient amount of grains that effectively includes a sampling of microstructural heterogeneities) is necessary to statistically represent the global material behavior. An appropriate RVE size would be the smallest volume over which the sample of material is stable and insensitive to the effect of the initial grain orientations and macroscopic boundary conditions. A series of numerical analysis of stress-strain analysis using ES-FEM are performed to estimate the size of RVE. Six different grain structures with 100, 150, 200, 250, 300, 350 grains each are constructed to perform the computation. Figure 6.10 compares the macroscopic equivalent stress against the strain of these polycrystalline aggregates with different grain amounts. Despite the differences in grains structures with different grain amount, morphology and orientations, these simulations exhibit similar macroscopic responses under monotonic tensile loading condition. In general, the strength of aggregates with more grain cells is a little higher than the one with fewer cells. It is mainly because that the overall response of aggregates with more constituents possesses a good performance of homogenized properties and has less effect of local heterogeneity. This feature indicates that the ensemble averages of mechanical properties of polycrystalline samples reflect microstructural heterogeneities to a certain extent, especially when analyzing aggregates with a small amount of grains (e.g., 100 grains). However, the convergence study of six different stress-strain curves in Figure 6.10 shows that with 300 grains or more for our example (with the same

level of mesh size, i.e., without considering the effect of element size), the macro-mechanical behavior of interest are almost independent of variations in the grain structures, i.e., sufficiently large samples behave homogeneously and statistically equivalently regardless of the effect of random grain orientations.

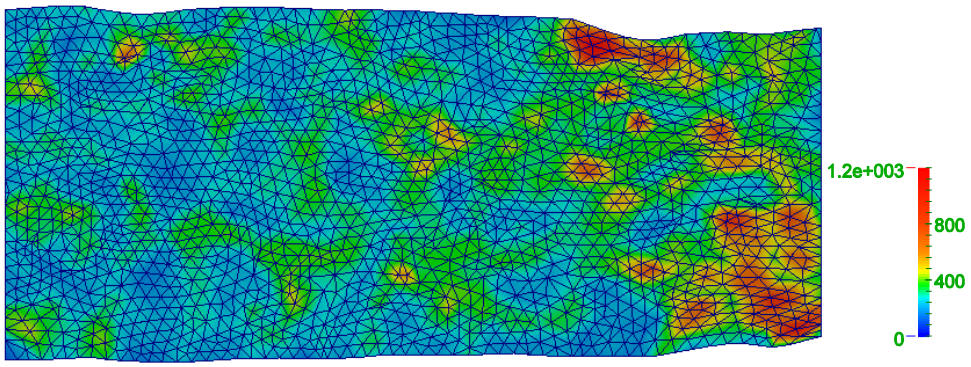

(a)

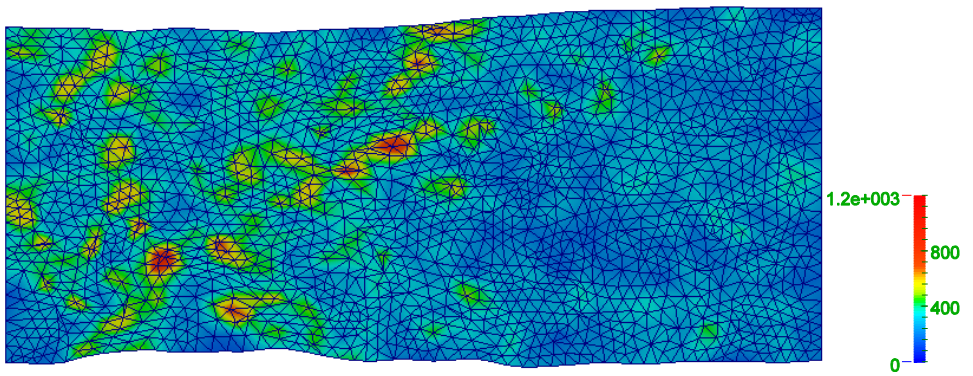

(b)

Figure 6.9. The equivalent stress (MPa) of specimen on the deformed configuration: (a) grain structure with 200 cells; and (b) grain structure with 300 cells.

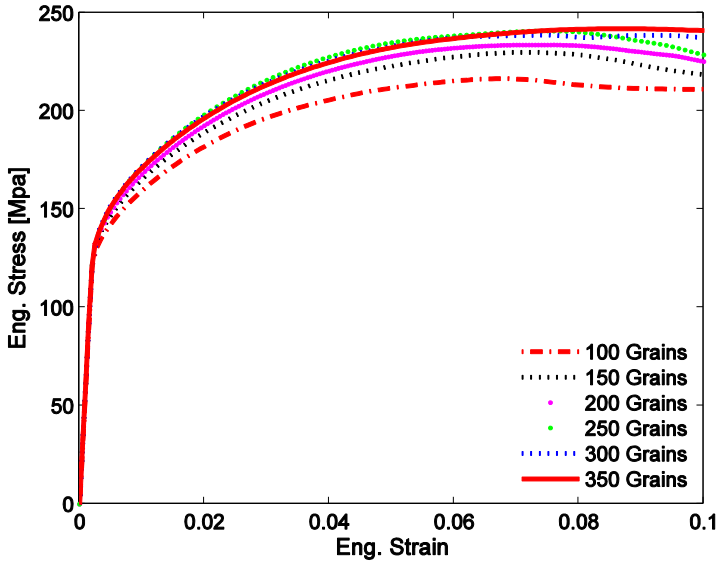

Figure 6.10. The equivalent stress-strain curves of various grain structures: 100, 150, 200, 250, 300 and 350 grain cells.

6.7 Conclusions

A computational framework for smoothed finite element modeling of crystalline plasticity at finite strains has been developed and the applicability of the method for both single crystal and polycrystalline simulation has been demonstrated in a 2D ES-FEM setting. In view of plastic incompressibility of single crystals and large mesh distortion in shear band localization of plastic deformations, the ES-FEM with good performance reported in elastic solid are employed successfully to cope with such problems for crystal plasticity at finite strains. The constitutive model utilizes the hyperelastic-based multiplicative plasticity framework on the basis of the theory of crystallographic slip, which involves a crystal kinematics described based on the local multiplicative decomposition of the deformation gradient into elastic and plastic components. The return-mapping algorithm with exponential map method is used for stress updates of the planar crystal model.

The performance of the proposed formulations has been illustrated firstly in single crystal plasticity by strain localization problems. The onset of localization and successive shear band development are consistent with literatures, in which special elements such as *Q1E4* elements or *F*-bar elements are exploited to capture strain localization phenomena and cope with geometric nonlinearity at large deformation. We conclude the reason essentially is that smoothed models (e.g., ES-FEM model), even with a basic T-mesh of linear elements, can provide a softening effect provided by the smoothing operations to the compatible FEM models.

Since a smoothing domain in a smoothed model usually involves part of adjacent elements, the number of associated supporting nodes is more than that to an element. This leads to increasing of bandwidth of the global stiffness matrix (or consistent spatial tangent matrix) and higher computational cost for smoothed models, compared to the corresponding standard FEM models with the same sets of nodes. Besides, the smoothing operations will also consume some computation time. In ES-FEM models, the CPU time is usually 30-40% more than FEM models. On the other hand, smoothed models often generate higher accuracy results, thus when we evaluate the efficiency of computation (computation time for the same accuracy) in terms of the error estimator versus computational cost, the S-FEM models perform more efficient than the standard FEM models [94]. Moreover, the low-order displacement-based FEM exhibits an overly stiff behavior (locking) which can be improved/resolved by using higher-order elements with a sufficiently large number of nodes per element or mesh refinement by increasing sufficiently the number of elements. This will definitely increase the number of degrees of freedom and/or Gauss integration points, which reduces the computational efficiency and brings computational complexity. Furthermore, because of the absence of isoparametric mapping enabled by the strain

smoothing operation, smoothed models are less sensitive to the quality of the initial mesh and mesh distortion during the large deformation procedure.

To illustrate the present framework and formulations, several typical numerical problems have been studied. In our single crystal plasticity examples, the free unstructured T-mesh is adopted to simulate the single crystalline strain localization with a large mesh distortion during the shear band(s) development. The results demonstrate the model's capability to capture shear localization phenomena and show good agreement through compared with several other published references. Furthermore, the proposed algorithmic framework has been also applied to polycrystalline modeling. The mesoscopic stress/displacement fields and macroscopic behavior of polycrystalline aggregates have been studied through modeling the virtual microstructure constructed by the Voronoi tessellation technique. Numerical results demonstrate that the framework is well capable of modeling the deformation and elastoplastic behavior of polystalline grain structure at mesoscopic level. The analysis is limited to plane models due to the high computational efforts, but the proposed framework is however equally extendable to three-dimensional cases.

Appendix 6.1. Stress Update Algorithm for the Rate-Independent Planar Single Crystal Model

(i) Elastic predictor

1. For load increment $n+1$
2. For Newton-Raphson iteration k
3. Find the incremental deformation gradient $\boldsymbol{F}_{inc}^{k} = \boldsymbol{I} + \nabla_n[\Delta \mathbf{d}]$, then compute the trial state, (k now implied)

$$\boldsymbol{F}_{n+1}^{e\,\mathrm{tr}} = \boldsymbol{F}_{inc}\boldsymbol{F}_{n}^{e}$$

4. Compute $J = \det[\boldsymbol{F}_{n+1}]$ and evaluate isochoric component of the elastic left Cauchy–Green strain tensor

$$\boldsymbol{F}_{iso}^{e} = J^{-1/3}\boldsymbol{F}^{e}$$

5. Obtain the trial values of resolved Schmid stresses on each slip system α

$$\tau_{n+1}^{\alpha\,\mathrm{tr}} = \mu \bar{\boldsymbol{s}}^{\alpha\,\mathrm{tr}} \cdot \bar{\boldsymbol{n}}^{\alpha\,\mathrm{tr}} \quad \text{with } \bar{\boldsymbol{s}}^{\alpha\,\mathrm{tr}} = \boldsymbol{F}_{iso}^{e\,\mathrm{tr}}\boldsymbol{s}^{\alpha} \text{ and } \bar{\boldsymbol{n}}^{\alpha\,\mathrm{tr}} = \boldsymbol{F}_{iso}^{e\,\mathrm{tr}}\boldsymbol{n}^{\alpha}$$

6. Check for consistency

If $f^{\alpha\mathrm{tr}} = \tau_{n+1}^{\alpha\,\mathrm{tr}} - \tau_{cr}(\gamma_{n+1}) \le 0$ for all $\alpha \in \mathcal{A}$, set $\boldsymbol{F}_{n+1}^{e} = J^{1/3}\boldsymbol{F}_{iso}^{e}$, and go to (iii)

Else first define estimate $\mathcal{A} = \{\alpha \in \mathcal{A} \mid f^{\alpha\mathrm{tr}} > 0\}$ for active working set, and go to (ii)

(ii) Return mapping algorithm

7. Set initial values for plastic multiplier(s) for all $\alpha \in \mathcal{A}$

$$\Delta\gamma^{\alpha} = 0$$

8. Compute for active systems $\alpha, \beta \in \mathcal{A}$

1) Compute the Jacobian matrix using Eq. (6.40)

2) Update multiplier(s) by Newton-Raphson correction

$$\Delta\gamma_{n+1}^{\alpha} = \Delta\gamma_{n+1}^{\alpha} + \delta\gamma_{n+1}^{\alpha} \text{ with } \sum_{\alpha,\beta\in\mathcal{A}} \delta\gamma_{n+1}^{\alpha}\mathbb{J}^{\alpha\beta} = -f^{\alpha}$$

3) Update $\boldsymbol{F}_{iso}^{e}$ (Eq. (6.42)) and γ_{n+1}

$$\gamma_{n+1} = \gamma_n + \sum_{\alpha\in\mathcal{A}} \Delta\gamma^{\alpha}$$

4) Evaluate for yielding according to Eq. (6.41)

9. Check for convergence

If $\left|f^{\alpha}\right| \le 0$, for all $\alpha \in \mathcal{A}$, converged, then go to 10

Else go to 8.

10. Check the Kuhn-Tucker conditions (Simo and Hughes, 1998)

If $\left|f^{\alpha}\right| \leq 0$ for any active slip system α ($\alpha = 1,2,...,N_{as}$) or $\Delta\gamma^{\alpha} \geq 0$ for all $\alpha \in \mathcal{A}$, valid converged solution, exit and go to next step
Else go to 7.

(iii) Stress state updating

11. Update stress state variables
Use Eq. (6.43) to update the Kirchhoff stress, and then compute the corresponding Cauchy stress.

References

[1] Sachs G. 1928. Zur ableilung einer fleissbedingung. Zeitschrift Des Vereines Deutscher Ingenieure; 72: 734–736.

[2] Taylor GI. 1938. Plastic strain in metals. Twenty-eighth May Lecture to the Institute of Metals 307–325.

[3] Mandel J. 1973. Equations constitutives et directeurs dans les milieux plastiques et viscoplastiques. International Journal of Solids and Structures; 9: 725–740.

[4] Peirce D, Asaro RJ, and Needleman A. 1982. An analysis of nonuniform and localized deformation in ductile single crystals. Acta Metallurgica; 30: 1087–1119.

[5] Peirce D, Asaro RJ, and Needleman A. 1983. Material rate dependence and localized deformation in crystalline solids. Acta Metallurgica; 31: 1951–1976.

[6] Asaro RJ. 1983. Micromechanics of Crystals and Polycrystals. Advances in Applied Mechanics; 23: 1–115.

[7] Asaro RJ and Needleman A. 1985. Overview no. 42 Texture development and strain hardening in rate dependent polycrystals. Acta Metallurgica; 33: 923–953.

[8] Havner KS. 1992. Finite plastic deformation of crystalline solids. Cambridge University Press, Cambridge.

[9] Rashid MM and Nemat-Nasser S. 1995. A constitutive algorithm for rate-dependent crystal plasticity. Computer Methods in Applied Mechanics and Engineering; 94: 201–228.

[10] Borja R and Wren JR. 1993. Discrete micromechanics of elastoplastic crystals. International Journal for Numerical Methods in Engineering; 36: 3815–3840.

[11] Miehe C. 1996. Exponential map algorithm for stress updates in anisotropic multiplicative elastoplasticity for single crystals. International Journal for Numerical Methods in Engineering; 39: 3367–3390.

[12] Miehe C. 1996. Multisurface thermoplasticity for single crystals at large strains in terms of eulerian vector updates. International Journal of Solids and Structures; 33: 3103–3130.

[13] Steinmann P and Stein E. 1996. On the numerical treatment and analysis of finite deformation ductile single crystal plasticity. Computer Methods in Applied Mechanics and Engineering; 129: 235–254.

[14] Busso EP, Cailletaud G. 2005. On the selection of active slip systems in crystal plasticity; 21(11): 2212–2231.

[15] Ling X, Horstemeyer MF, and Potirniche GP. 2005. On the numerical implementation of 3D rate-dependent single crystal plasticity formulations. International Journal for Numerical Methods in Engineering; 63: 548–568.

[16] Kuchnicki SN, Cuitiño AM, and Radovitzky RA. 2006. Efficient and robust constitutive integrators for single-crystal plasticity modeling. International Journal of Plasticity; 22: 1988–2011.

[17] Li HW, Yang H, and Sun ZC. 2008. A robust integration algorithm for implementing rate dependent crystal plasticity into explicit finite element method. International Journal of Plasticity; 24: 267–288.

[18] Kuroda M. 2011. On large-strain finite element solutions of higher-order gradient crystal plasticity. International Journal of Solids and Structures; 48: 3382–3394.

[19] Anand L, Aslan O, and Chester SA. 2012. A large-deformation gradient theory for elastic–plastic materials: Strain softening and regularization of shear bands. International Journal of Plasticity; 30-31: 116–143.

[20] Niordson CF and Kysar JW. 2014. Computational strain gradient crystal plasticity. Journal of the Mechanics and Physics of Solids; 62: 31–47.

[21] Bargmann S, Reddy BD, and Klusemann B. 2014. A computational study of a model of single-crystal strain-gradient viscoplasticity with an interactive hardening relation. International Journal of Solids and Structures; 51: 2754–2764.

[22] Asaro RJ and Lubarda VA. 2006. Mechanics of Solids and Materials. Cambridge University Press, New York.

[23] Kröner E. 1958. Kontinuumstheorie der Versetzungen und Eigenspannungen. Springer-Verlag, Berlin.

[24] Budiansky B and Wu TT. 1961. Theoretical Prediction of Plastic Strains of Polycrystals. Technical Report. Division of Engineering and Applied Physics, Harvard University.

[25] Hill R. 1965. A self-consistent mechanics of composite materials. Journal of the Mechanics and Physics of Solids; 13: 213–222.

[26] Hutchinson JW. 1970. Elastic-plastic behavior of polycrystalline metals and composite. Proceedings of the Royal Society of London. Series A: Mathematical, Physical and Engineering Sciences; 319: 247–272.

[27] DeBotton G and Castañeda PP. 1995. Variational estimates for the creep behaviour of polycrystals. Proceedings of the Royal Society of London. Series A: Mathematical and Physical Sciences; 448(1932): 121–142.

[28] Segurado J, Lebensohn RA, Llorca J, and Tomé CN. 2012. Multiscale modeling of plasticity based on embedding the viscoplastic self-consistent formulation in implicit finite elements. International Journal of Plasticity; 28: 124–140.

[29] Parks D. 1990. Polycrystalline plastic deformation and texture evolution for crystals lacking five independent slip systems. Journal of the Mechanics and Physics of Solids; 38: 701–724.

[30] Mathur KK, Dawson PR, and Kocks UF. 1990. On modeling anisotropy in deformation processes involving textured polycrystals with distorted grain shape. Mechanics of Materials; 10: 183–202.

[31] Kalidindi SR and Anand L. 1992. An approximate procedure for predicting the evolution of crystallographic texture in bulk deformation processing of fcc metals. International Journal of Mechanical Sciences; 34: 309–329.

[32] Habraken AM and Duchêne L. 2004. Anisotropic elasto-plastic finite element analysis using a stress-strain interpolation method based on a polycrystalline model. International Journal of Plasticity; 20: 1525–1560.

[33] Lebensohn RA, Kanjarla AK, and Eisenlohr P. 2012. An elasto-viscoplastic formulation based on fast Fourier transforms for the prediction of micromechanical fields in polycrystalline materials. International Journal of Plasticity; 32-33: 59–69.

[34] Eisenlohr P, Diehl M, Lebensohn RA, and Roters F. 2013. A spectral method solution to crystal elasto-viscoplasticity at finite strains. International Journal of Plasticity; 46: 37–53.

[35] Lee MG, Lim H, Adams BL, Hirth JP, and Wagoner RH. 2010. A dislocation density-based single crystal constitutive equation. International Journal of Plasticity; 26: 925–938.

[36] Garmestani H, Lin S, Adams BL, and Ahzi S. 2001. Statistical continuum theory for large plastic deformation of polycrystalline materials. Journal of the Mechanics and Physics of Solids; 49: 589–607.

[37] Zhang L, Dingreville R, Bartel T, and Lusk MT. 2011. A stochastic approach to capture crystal plasticity. International Journal of Plasticity; 27: 1432–1444.

[38] Watanabe I and Terada K. 2010. A method of predicting macroscopic yield strength of polycrystalline metals subjected to plastic forming by micro-macro de-coupling scheme. International Journal of Mechanical Sciences; 52: 343–355.

[39] Kim JH, Lee MG, Kim D, and Barlat F. 2013. Numerical procedures for predicting localization in sheet metals using crystal plasticity. Computational Materials Science; 72: 107–115.

[40] Rousselier G and Leclercq S. 2006. A simplified "polycrystalline" model for viscoplastic and damage finite element analyses. International Journal of Plasticity; 22: 685–712.

[41] Mahesh S. 2010. A binary-tree based model for rate-independent polycrystals. International Journal of Plasticity; 26: 42–64.

[42] Knezevic M and Savage DJ. 2014. A high-performance computational framework for fast crystal plasticity simulations. Computational Materials Science; 83: 101–106.

[43] Knezevic M, Drach B, Ardeljan M, and Beyerlein IJ. 2014. Three dimensional predictions of grain scale plasticity and grain boundaries using crystal plasticity finite element models. Computer Methods in Applied Mechanics and Engineering; 277: 239–259.

[44] Roters F, Eisenlohr P, Hantcherli L, Tjahjanto DD, Bieler TR, and Raabe D. 2010. Overview of constitutive laws, kinematics, homogenization and multiscale methods in crystal plasticity finite-element modeling: Theory, experiments, applications. Acta Materialia; 58: 1152–1211.

[45] Liu GR, Dai KY, and Nguyen TT. 2007. A smoothed finite element method for mechanics problems. Computational Mechanics; 39: 859–877.

[46] Cuitino AM and Ortiz M. 1992. Computational Modelling of Single Crystals. Modelling and Simulation in Materials Science and Engineering; 1: 225–263.

[47] Chen JS, Wu CT, Yoon S, and You Y. 2001. A stabilized conforming nodal integration for Galerkin meshfree method. International Journal for Numerical Methods in Engineering; 50: 435–466.

[48] Liu GR. 2010. A G space theory and a weakened weak (W2) form for a unified formulation of compatible and incompatible methods: Part I theory, Part II applications to solid mechanics problems. International Journal for Numerical Methods in Engineering; 81: 1093–1156.

[49] Hill R. 1966. Generalized constitutive relations for incremental deformation of metal crystals by multislip. Journal of the Mechanics and Physics of Solids; 14: 95–102.

[50] Lee EH. 1969. Elastic-Plastic Deformation at Finite Strains. Journal of Applied Mechanics, Transactions ASME; 36: 1–6.

[51] Rice JR. 1971. Inelastic constitutive relations for solids: An internal-variable theory and its application to metal plasticity. Journal of the Mechanics and Physics of Solids; 19: 433–455.

[52] Hill R and Rice JR. 1972. Constitutive analysis of elastic-plastic crystals at arbitrary strain. Journal of the Mechanics and Physics of Solids; 20: 401–413.

[53] Hill R and Havner KS. 1982. Perspectives in the mechanics of elastoplastic crystals. Journal of the Mechanics and Physics of Solids; 30: 5–22.

[54] Goh CH, Neu RW, and McDowell DL. 2003. Crystallographic plasticity in fretting of Ti-6AL-4V. International Journal of Plasticity; 19: 1627–1650.

[55] Marin EB. 2006. On the formulation of a crystal plasticity model. Sandia National Laboratories, CA, SAND2006-4170.

[56] de Souza Neto EA, Perić P, and Owen DRJ. 2008. Computational Methods for Plasticity: Theory and Applications. John Wiley & Sons.

[57] Meissonnier FT, Busso EP, and O'Dowd NP. 2001. Finite element implementation of a generalised non-local rate-dependent crystallographic formulation for finite strains. International Journal of Plasticity; 17(4): 601–640.

[58] Rossiter J, Brahme A, Simha MH, Inal K, and Mishra R. 2010. A new crystal plasticity scheme for explicit time integration codes to simulate deformation in 3D microstructures: Effects of strain path, strain rate and thermal softening on localized deformation in the aluminum alloy 5754 during simple shear. International Journal of Plasticity; 26(12): 1702–1725.

[59] Mandel J. 1965. Generalisation de la theorie de plasticite de W. T. Koiter. International Journal of Solids and Structures; 1(3): 273–295.

[60] Kocks UF. 1970. The relation between polycrystal deformation and single-crystal deformation. Metallurgical and Materials Transactions; 1(5): 1121–1143.

[61] Taylor GI. 1934. The Mechanism of Plastic Deformation of Crystals. Part I. Theoretical. Proceedings of the Royal Society, Series A: Mathematical, Physical and Engineering Sciences; 145: 362–387.

[62] Asaro RJ and Rice JR. 1977. Strain localization in ductile single crystals. Journal of the Mechanics and Physics of Solids; 25: 309–338.

[63] Franciosi P. 1985. The concepts of latent hardening and strain hardening in metallic single crystals. Acta Metallurgica; 33: 1601–1612.

[64] Anand L and Kothari M. 1996. A computational procedure for rate-independent crystal plasticity. Journal of the Mechanics and Physics of Solids; 44: 525–558.

[65] Schröder J and Miehe C. 1997. Aspects of computational rate-independent crystal plasticity. Computational Materials Science; 9: 168–176.

[66] McGinty RD and McDowell DL. 2006. A semi-implicit integration scheme for rate independent finite crystal plasticity. International Journal of Plasticity; 22(6): 996–1025.

[67] Zuo QH. 2011. On the uniqueness of a rate-independent plasticity model for single crystals. International Journal of Plasticity; 27(8): 1145–1164.

[68] Gurtin ME and Reddy BD. 2014. Gradient single-crystal plasticity within a miseshill framework based on a new formulation of self- and latenthardening. Journal of the Mechanics and Physics of Solids; 68(0): 134–160.

[69] Hutchinson JW. 1976. Bounds and Self-Consistent Estimates for Creep of Polycrystalline Materials. Proceedings of the Royal Society of London. Series A: Mathematical, Physical and Engineering Sciences; 348: 101–127.

[70] Chang YW and Asaro RJ. 1981. An experimental study of shear localization in aluminum-copper single crystals. Acta Metallurgica; 29; 241–257.

[71] Bassani JL and Wu T-Y. 1991. Latent Hardening in Single Crystals II. Analytical Characterization and Predictions. Proceedings of the Royal Society, Series A: Mathematical, Physical and Engineering Sciences; 435: 21–41.

[72] Anand L and Kalidindi SR. 1994. The process of shear band formation in plane strain compression of FCC metals: Effects of crystallographic texture. Mechanics of Materials; 17: 223–243.

[73] McGinty RD and McDowell DL. 1999. Multiscale polycrystal plasticity. Journal of Engineering Materials and Technology; 121, 203–209.

[74] McGinty RD. 2001. Multiscale representation of polycrystalline inelasticity. Ph.D Thesis. Georgia Institute of Technology, Atlanta.

[75] Weber G and Anand L. 1990. Finite deformation constitutive equations and a time integration procedure for isotropic, hyperelastic-viscoplastic solids. Computer Methods in Applied Mechanics and Engineering; 79: 173–202.

[76] Eterovic AL and Bathe KJ. 1990. A hyperelastic-based large strain elasto-plastic constitutive formulation with combined isotropic-kinematic hardening using the logarithmic stress and strain measures. International Journal for Numerical Methods in Engineering; 30: 1099–1114.

[77] Simo JC. 1992. Algorithms for static and dynamic multiplicative plasticity that preserve the classical return mapping schemes of the infinitesimal theory. Computer Methods in Applied Mechanics and Engineering; 99: 61–112.

[78] Perić D, Owen DRJ, and Honnor ME. 1992. A model for finite strain elasto-plasticity based on logarithmic strains: Computational issues. Computer Methods in Applied Mechanics and Engineering; 94: 35–61.

[79] Yamakawa Y, Hashiguchi K, and Ikeda K. 2010. Implicit stress-update algorithm for isotropic Cam-clay model based on the subloading surface concept at finite strains. International Journal of Plasticity; 26: 634–658.

[80] Chang YW and Asaro RJ. 1980. Lattice rotations and shearing in crystals. Archive of Applied Mechanics; 32: 369–388.

[81] Simo JC and Armero F. 1992. Geometrically non-linear enhanced strain mixed methods and the method of incompatible modes. International Journal for Numerical Methods in Engineering; 33: 1413–1449.

[82] De Souza Neto EA, Andrade Pires FM, and Owen DRJ. 2005. F-bar-based linear triangles and tetrahedra for finite strain analysis of nearly incompressible solids. Part I: Formulation and benchmarking. International Journal for Numerical Methods in Engineering; 62: 353–383.

[83] Needleman A, Asaro RJ, Lemonds J, and Peirce D. 1985. Finite element analysis of crystalline solids. Computer Methods in Applied Mechanics and Engineering; 52: 689–708.

[84] Asaro RJ. 1979. Geometrical effects in the inhomogeneous deformation of ductile single crystals. Acta Metallurgica; 27: 445–453.

[85] Li S, Hao W, and Liu WK. 2000. Mesh-free simulations of shear banding in large deformation. International Journal of Solids and Structures; 37: 7185–7206.

[86] Borg U. 2007. Strain gradient crystal plasticity effects on flow localization. International Journal of Plasticity; 23: 1400–1416.

[87] Lim H, Lee MG, Kim JH, Adams BL, and Wagoner RH. 2011. Simulation of polycrystal deformation with grain and grain boundary effects. International Journal of Plasticity; 27: 1328–1354.

[88] Ghosh S, Lee K, and Moorthy S. 1995. Multiple scale analysis of heterogeneous elastic structures using homogenization theory and Voronoi cell finite element method. International Journal of Solids and Structures; 32: 27–62.

[89] Moorthy S and Ghosh S. 1998. Particle cracking in discretely reinforced materials with the voronoi cell finite element model. International Journal of Plasticity; 14(4): 805–827.

[90] Barbe F, Decker L, Jeulin D, and Cailletaud G. 2001. Intergranular and intragranular behavior of polycrystalline aggregates. Part 1: F.E. model. International Journal of Plasticity; 17(4): 513–536.

[91] Kovač M and Cizelj L. 2005. Modeling elasto-plastic behavior of polycrystalline grain structure of steels at mesoscopic level. Nuclear Engineering and Design; 235: 1939–1950.

[92] Ghosh S. 2011. Micromechanical analysis and multi-scale modeling using the Voronoi cell finite element method. CRC Press, Taylor & Francis.

[93] Talischi C, Paulino GH, Pereira A, and Menezes IFM. 2012. PolyMesher: A general-purpose mesh generator for polygonal elements written in Matlab. Journal of Structural and Multidisciplinary Optimization; 45(3): 308–328.

[94] Nguyen-Xuan H, Liu GR, Bordas S, Natarajan S, and Rabczuk T. 2013. An adaptive singular ES-FEM for mechanics problems with singular field of arbitrary order. Computer Methods in Applied Mechanics and Engineering; 253: 252–273.

Chapter 7. A Beta Finite Element Method (βFEM) of Coupled Edge/Face and Node Based Smoothing Techniques for Mechanics Problems

The edge-based (for 2D) and face-based (for 3D) strain smoothing techniques are found to be able to produce more accurate solutions than standard FEM, and offer lower bounds (for force driven problems). The node-based smoothing technique, on the other hand has a unique property of producing upper bound solutions. In this chapter, a novel smoothed finite element method (S-FEM) is proposed, where the smoothing domains are formed based on both edges (faces for 3D) and nodes. An adjustable parameter β is introduced to control the ratio of the area of edge-based/face-based and node-based smoothing domains. As presented, a nearly exact solution in strain energy can be obtained by tuning the parameter, making use of the important property that the exact solution is bonded by the solutions of NS-FEM and ES/FS-FEM. Standard patch tests are likewise satisfied. For numerical illustration of the features, a number of numerical examples (static, dynamic, linear and nonlinear) have shown that the present βFEM method is found to be ultra-accurate, insensitive to mesh quality, temporal stability and capability for modeling objects with complex geometry, and offers alleviation of volumetric locking, etc. In the section of applications in modeling crystal plasticity, several representative examples are studied to demonstrate the capability of proposed method for capturing the strain localization and dealing with plastic incompressibility. The proposed method and algorithm are also performed to simulate the mechanical behavior of polycrystalline aggregates through modeling the synthetic microstructure constructed by the Voronoi tessellation technique.

7.1 Introduction

The standard constant finite elements such as 3-node triangular or 4-node tetrahedral elements (T-elements) were popular and preferred in practical mechanics problems for many years, as they offer many of the advantages such as convenience in FE implementation, high mesh quality, adaptive analysis with mesh rezoning, etc. And sometimes triangular/ tetrahedral mesh (T-mesh) would be the only option for mesh generation of complex geometries. However, compared to quadrilateral/hexahedral meshes, a T-mesh using constant strain T-elements has its own numerical drawbacks including the inaccuracy, shear and volumetric locking due to excessive stiffness, especially for large deformation problems. As such, it is usually not recommended to use T-mesh in commercial FEM software packages.

Procedures for tackling locking and accuracy of FEM include supplementing the element displacement field with additional nodes and utilizing reduced numerical integration rules to calculate the element stiffness matrix. However, these procedures are not applicable or compatible with constant strain T-elements. T-mesh with second-order or higher-order elements is thought to be a good option to avoid the locking issues, but it would be ineffective for extremely large deformation problems due to intermediate nodes [1,2]. In order to deal with these element defects of T-mesh, a number of researchers made efforts to improve it and some advances have occurred in the last 30 years. For example, Allman [3,4] improved the accuracy of triangle elements by using vertex connectors which included rotations. However, it exhibited an unusual type of zero energy mode, in addition to the rigid body movements. Reference [5] made a critical assessment of the Allman's triangular membrane element with drilling degrees of freedom by the way of examining the performance of the element combined with a triangular plate bending element. Huang et al. [6] modified Allman's triangular planar element with drilling

degrees of freedom and dealt with spurious energy mode by an introduced constraint which ensures that a drilling degree of freedom is a true rotation in elasticity. Piltner and Taylor [7] developed enhanced triangle elements to deal with nearly incompressible plane strain problems. However, the requirement of more degrees of freedom has limited the practical applications of these methods. In References [8,9], elements with rotational freedom were also designed to improve the bending performance or stiffness matrices for plane triangular elements. Reference [10] proposed a weighted least-squares formulation for deriving constant strain T-elements, which claimed to be possible to eliminate volumetric locking. Reference [11] introduced a node-based uniform strain element for T-mesh and it is capable in avoiding the volumetric locking and reduce the effects of shear locking for static linear elastic problems. Reference [12] used bubble function displacements in conjunction with the assumed strain formulation to construct triangular solid shell elements for precluding the membrane locking effect.

The S-FEM [13–19] introduces the gradient/strain smoothing techniques to FEM settings and uses direct (no mapping) point interpolation for computing shape functions. The gradient/strain smoothing techniques using Green's theorem were also exploited for the quasi-conforming elements for plates and shells [20], stabilizing nodal integration of meshfree methods [21,22] and natural element method [23]. The idea of S-FEM is to utilize a standard first-order finite element mesh (in particular T-mesh) to build numerical models with good performance [24]. The essential idea of S-FEM is to construct the compatible strain field in a Galerkin weak form model to produce some good properties. Compared to the element-based implementation for the standard FEM, the S-FEM techniques evaluate the weak form based on smoothing domains. The construction of smoothing domains can be located within the elements but more often beyond the elements, which would bring in the information from the neighboring elements.

According to different fashions in the creation of smoothing domains, a variety of S-FEM models were proposed: the cell-based smoothed FEM (CS-FEM) [16,19], node-based smoothed FEM (NS-FEM) [18], edge based smoothed FEM (ES-FEM) [15] and face-based smoothed FEM (FS-FEM) [25], etc. Compared to the standard FEM, the overestimation behavior of stiffness values shall be reduced or alleviated and hence the accuracy of both primal and dual quantities can be improved significantly [26]. In addition, the evaluation of shape function derivatives involved in FEM would be avoided in S-FEM and S-FEM models applied in elasticity are insensitive to mesh distortion when compared to standard FEM due to the absence of isoparametric mapping [27,28]. Furthermore, an S-FEM model would utilize the background mesh as the corresponding standard FEM model and it does not require the introduction of additional degrees of freedom.

The numerical studies have already demonstrated that S-FEMs show a few superiorities over standard FEM [24]. Among these S-FEMs, the ES-FEM (or FS-FEM for 3D) possesses some properties such as: i) ES-FEM/FS-FEM can produce a solution with properties of super-convergence and accuracy compared to a corresponding FEM model; ii) it usually generates a lower bound to the exact solution in terms of strain energy, but still has the feature of overestimation of stiffness; iii) it can use T-mesh which would be conveniently generated especially for complex geometries; iv) the ES-FEM/FS-FEM models would be always stiffer than NS-FEM, partially due to the number of edges being always larger than the number of nodes with a background T-mesh; v) the vibration models using ES-FEM/FS-FEM are often temporally stable and there are no spurious non-zeros energy modes found in free vibration analysis [24]. Meanwhile, the NS-FEM has some interesting properties [29–31]: i) it has the unique upper bound property in strain energy as it may extremely soften the over-stiffness of the

corresponding standard FEM model; ii) it achieves accurate and often super-convergent properties of stress solutions; iii) it is effective in overcoming volumetric locking; iv) it works effectively with T-mesh; v) it performs spatially stable but possibly would be temporally instable with non-zero-energy spurious modes.

Considering the fact that ES-FEM is capable of producing an the accurate solution from the lower bound (better than standard FEM) and the NS-FEM can approximate the solution from the upper bound, a mixed smoothed FEM model can be naturally conceived in order to obtain the exact or close-to-exact solution measured in a norm. Another fascinating aspect is that the mixed smoothed FEM would be versatile and may inherit the merits from both ES-FEM and NS-FEM. In this work, a novel ultra-accurate beta finite element method (βFEM) based on T-mesh is proposed and then applied in different mechanics problems. In βFEM, the smoothing domains will be constructed by a mixed edge-based and node-based smoothing technique, in which the parameter $\beta \in [0,1]$ tunes the portion of area of the edge-based and node-based smoothing domains. The idea of βFEM can be regarded as a utilization of the overestimation property of ES-FEM/FS-FEM and the unique under-estimation property of NS-FEM using T-elements, and hence can be "tuned" to have good features of both. Since both the NS-FEM and ES-FEM with T-elements are spatially stable [24], the presented βFEM would be stable and guarantees the convergence. In addition, the scheme ensures the variational consistency and the compatibility of the displacement field, by which ensures reproducing linear field exactly [32–35].

The work aims to propose and formulate the novel βFEM for solid mechanics problems with first-order triangular or tetrahedral mesh, using the mixed edge-based/face-based and node-based strain smoothing techniques. The governing equation and different smoothing techniques utilized in this work will be briefly introduced in Section 2. The idea of βFEM for both 2D and

3D problems will be presented in Section 3. Section 4 considers the implementation aspects for vibration analysis and large deformation problems which will be shown in subsequent numerical examples. The standard patch test and numerical examples will be discussed in Section 5 and 6. In Section 7, the method is performed to model rate-independent crystal plasticity problems by a proper constitutive integration scheme already introduced in Chapter 6. The conclusion will be summarized in the last section.

7.2 Brief of Problem and Strain Smoothing Techniques

The target of our βFEM is to solve the solid mechanics problems using the weakened weak (W^2) Galerkin formulation [33]. For example, consider an elastic deformable body occupying domain Ω, subjected to body force $\mathbf{f}^b$ and traction $\mathbf{f}^t$ on natural boundary Γ_t. The object undergoes arbitrary virtual displacements with the compatible virtual strains $\delta\boldsymbol{\varepsilon}$ and internal displacement $\delta\mathbf{u}$. The dynamic equilibrium equations, which contain the inertial and damping forces, are described in the following form:

$$\int_\Omega \delta\boldsymbol{\varepsilon}^{\mathrm{T}}\mathbf{D}\boldsymbol{\varepsilon}\mathrm{d}\Omega - \int_\Omega \delta\mathbf{u}^{\mathrm{T}}[\mathbf{b}-\rho\ddot{\mathbf{u}}-c\dot{\mathbf{u}}]\mathrm{d}\Omega - \left(\int_\Omega \delta\mathbf{u}^{\mathrm{T}}\mathbf{f}^b\mathrm{d}\Omega + \int_{\Gamma_t}\delta\mathbf{u}^{\mathrm{T}}\mathbf{f}^t\mathrm{d}\Gamma\right) = 0 \tag{7.1}$$

where $\mathbf{D}$ is the Hooke matrix of elastic constants which is related to modulus E and Poisson's ratio ν. For a static problem, the second term in Eq. (7.1) will vanish. The strain tensor $\boldsymbol{\varepsilon}$ can be expressed by displacement $\mathbf{u}$ using a compatibility relation:

$$\int_\Omega \delta\boldsymbol{\varepsilon}^{\mathrm{T}}\mathbf{D}\boldsymbol{\varepsilon}\mathrm{d}\Omega - \int_\Omega \delta\mathbf{u}^{\mathrm{T}}[\mathbf{b}-\rho\ddot{\mathbf{u}}-c\dot{\mathbf{u}}]\mathrm{d}\Omega - \left(\int_\Omega \delta\mathbf{u}^{\mathrm{T}}\mathbf{f}^b\mathrm{d}\Omega + \int_{\Gamma_t}\delta\mathbf{u}^{\mathrm{T}}\mathbf{f}^t\mathrm{d}\Gamma\right) = 0 \tag{7.2}$$

where ∇^s is the symmetric gradient of the displacement field. In FEM, the displacement $\mathbf{u}$ and $\delta\mathbf{u}$ will be approximated using trial functions by the following expression:

$$\mathbf{u}^h(\mathbf{x}) = \sum_{I=1}^{\mathrm{NP}} \mathbf{N}_I(x)\mathbf{d}_I \quad \text{and} \quad \delta\mathbf{u}^h(\mathbf{x}) = \sum_{I=1}^{\mathrm{NP}} \mathbf{N}_I(x)\delta\mathbf{d}_I \tag{7.3}$$

where $\mathbf{N}_I$ represents the a matrix of shape functions, $\mathbf{d}_I$ is the vector of the associated nodal displacements, and NP is the total number of the nodal variables of the element.

The S-FEM techniques evaluate the smoothed strain based on associated smoothing domains and the manipulation will be derived from the compatible strains of finite element expressed in Eq. (7.3). Hereafter in this section, the fashions of strain smoothing techniques involved in βFEM will be presented. Since the edge-based smoothing technique has already been introduced in previous chapters, we only present here the 3D face-based smoothing technique and node-based smoothing technique.

7.2.1 Briefing of Face-Based Strain Smoothing

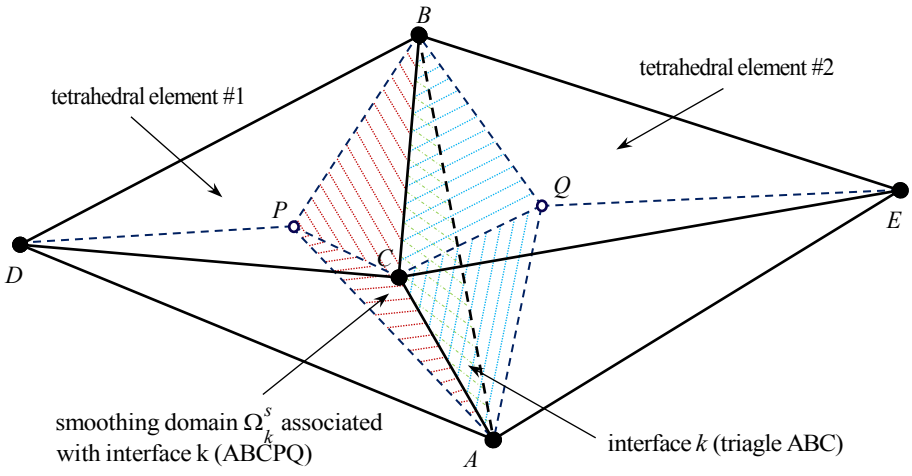

Figure 7.1. A face-based smoothing domain Ω_k^s constructed from two adjacent tetrahedral elements based on their interface k.

Analogous to 2D ES-FEM, the FS-FEM creates smoothing domains associated with faces of tetrahedral elements such that $\Omega \approx \bigcup_{k=1}^{N_{face}} \Omega_k^s$ and $\Omega_i^s \cap \Omega_j^s = \varnothing$ for $i \neq j$, in which N_{face} is the number of faces for all elements in the problem domain. For tetrahedral elements sketched in Figure 7.1, the smoothing domain associated with the face k can be constructed through connecting the triangle vertices (A, B and C) and the two centroids of the two attached elements (P and Q), i.e., the triangular bipyramid. By applying the face-based smoothing operation [36], the smoothed strain-displacement matrix may have a similar formulation expressed as

$$\tilde{\mathbf{B}}_I = \frac{1}{V_k^s} \sum_{j=1}^{n_k^e} \frac{1}{4} V_j^e \mathbf{B}_j^e \tag{7.4}$$

where n_k^e is the number of elements attached to the face ($n_k^e = 1$ for the boundary faces and $n_k^e = 2$ for interior faces), $\mathbf{B}_j^e$ is the standard compatible strain-displacement matrix for j^{th} element attached to face k . The matrix $\mathbf{B}_I(\mathbf{x})$ for the node I in tetrahedral elements is expressed as

$$\mathbf{B}_I(\mathbf{x}) = \nabla_S \mathbf{N}_I(\mathbf{x}) = \begin{bmatrix} \frac{\partial N_I(\mathbf{x})}{\partial x} & 0 & 0 & \frac{\partial N_I(\mathbf{x})}{\partial y} & 0 & \frac{\partial N_I(\mathbf{x})}{\partial z} \\ 0 & \frac{\partial N_I(\mathbf{x})}{\partial y} & 0 & \frac{\partial N_I(\mathbf{x})}{\partial x} & \frac{\partial N_I(\mathbf{x})}{\partial z} & 0 \\ 0 & 0 & \frac{\partial N_I(\mathbf{x})}{\partial z} & 0 & \frac{\partial N_I(\mathbf{x})}{\partial y} & \frac{\partial N_I(\mathbf{x})}{\partial x} \end{bmatrix}^T \tag{7.5}$$

7.2.2 Briefing of Node-Based Strain Smoothing

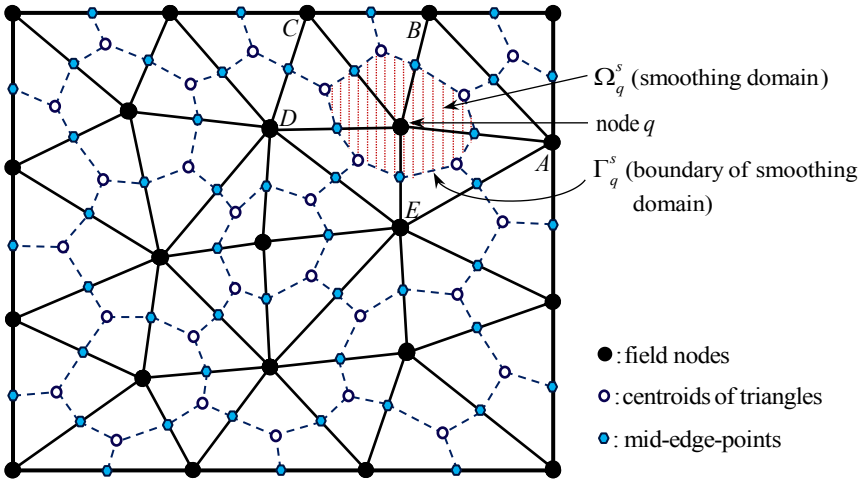

Figure 7.2. Division of a problem domain into triangular elements and node-based smoothing domains. For example, the smoothing domain Ω_q^s for node q is a polygon with $2n_q^e$ sides (where n_q^e is the number of elements surrounding node q).

The node-based strain smoothing technique constructs smoothing domains for the strain field associated with the nodes [37], which is different from the edge-based strain smoothing technique. In Figure 7.2, the smoothing domain Ω_q^s is created by connecting the centroid points of the surrounding elements and the middle points of associated edges. The set of supporting nodes S_q^s for the node-based smoothing domain are all nodes belonging to the surrounding elements of node q, e.g., the nodes $\{A, B, C, D, E\}$ for the smoothing domain associated to node q in Figure 7.2. For the domain, it can be also viewed as the combination of the sub-domains of all the elements involving node q. Through a similar fashion of the edge-based smoothing

operation, which was introduced in previous chapters, the smoothed strain-displacement matrix of NS-FEM $\bar{\mathbf{B}}_I$ can be evaluated as

$$\bar{\mathbf{B}}_I = \frac{1}{A_q^s}\sum_{l=1}^{n_q^e}\frac{1}{3}A_l^e\mathbf{B}_l^e \quad \text{with} \quad A_q^s = \int_{\Omega_q^s} d\Omega = \frac{1}{3}\sum_{l=1}^{n_q^e}A_l^e \tag{7.6}$$

where n_q^e is the number of elements around node q, A_l^e is the area of l^{th} element around node q, $\mathbf{B}_l^e = \sum_{I\in S_l^e}\mathbf{B}_I$ is the compatible strain-displacement matrix for l^{th} element associated to node q, which has the form of Eq. (6.12) for node $I \in S_q^s$ if triangle elements are used.

For 3D NS-FEM, the implementation is quite similar as 2D NS-FEM and the variable of area needs to be replaced by the associated volume in formulation in Eq. (7.6). The set of supporting nodes S_q^s would be all of the nodes belonging to the elements which contain this node q.

7.3 The Idea and Properties of Beta Finite Element Method

7.3.1 The Idea of βFEM

In order to implement the βFEM using T-mesh (triangles for 2D and tetrahedrons for 3D), the background T-elements (shown in Figure 7.3) are further divided into two different types of smoothing domains: the node-base smoothing domains (the domain surrounding a node shown with red dotted lines) and the edge-based smoothing domains (the domain attached an edge/face indicated with green dashed lines). The portion of the area of edge/face-based and node-based smoothing domains will be tuned by a parameter β. In Figure 7.3, the length of an edge of a triangle/tetrahedral element is assumed to be "L". If we adopt the scale factor β to

tune the dividing points (H and G), the length of segments on the edge has relations such as: $l_1 = l_3 = (1-\beta)\dfrac{L}{2}$ and $l_2 = \beta L$. If we take a 2D problem as our example, the area of three sub-domains by the node-based smoothing technique in an element (three quadrilaterals at three corners of a triangle element k) would be $\dfrac{1}{3}(1-\beta^2)A_k^e$. The sub-domains by the edge-based smoothing technique in element k , i.e., three pentagons attached to middle segment of associated edges depicted with green dashed lines in Figure 7.3, also have an identical area $\dfrac{1}{3}\beta^2 A_k^e$.

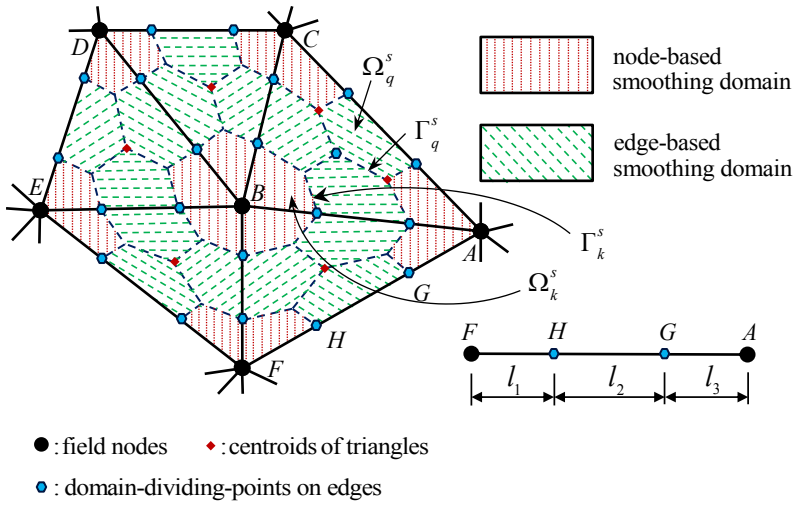

Figure 7.3. Division of representative elements into smoothing domains using βFEM-T3: the node-base smoothing domains are shown by red dotted lines and the edge-based smoothing domains indicated with green dashed lines.

It can be noticed that βFEM using T-elements can be regarded as a combination of the features from both the NS-FEM and ES-FEM, since the smoothing domains are established based on both edge-based and node-based smoothing techniques.

If we choose $(\tilde{\bullet}), (\bar{\bullet})$ and $(\hat{\bullet})$ to represent the physical quantities computed by the ES/FS-FEM, NS-FEM and βFEM respectively, the area of smoothing domain of βFEM ($\hat{A}^s$) has the following relationship with the area of the edge-based smoothing domain ($\tilde{A}^s$) and the node-based smoothing domain ($\bar{A}^s$):

$$\hat{A}^s = \tilde{A}^s + \bar{A}^s \tag{7.7}$$

with

$$\tilde{A}^s = \beta^2 \hat{A}^s \quad \text{and} \quad \bar{A}^s = (1-\beta^2)\hat{A}^s, \ \beta \in [0,1] \tag{7.8}$$

For 3-D problems, Eq. (7.7) and (7.8) would be expressed in forms as

$$\hat{V}^s = \tilde{V}^s + \bar{V}^s \tag{7.9}$$

$$\tilde{V}^s = \beta^3 \hat{V}^s \quad \text{and} \quad \bar{V}^s = (1-\beta^3)\hat{V}^s, \ \beta \in [0,1] \tag{7.10}$$

where $\hat{V}^s$ denotes the volume of the smoothing domain for 3-D problems.

In a βFEM scheme, the smoothed strain-displacement matrix $\tilde{\mathbf{B}}_I$ for Ω_k^s is defined by

$$\tilde{\mathbf{B}}_I = \frac{1}{A_k^s}\sum_{j=1}^{n_k^e}\frac{1}{3}\beta^2 A_j^e \mathbf{B}_j^e \ \text{ or } \ \tilde{\mathbf{B}}_I = \frac{1}{V_k^s}\sum_{j=1}^{n_k^e}\frac{1}{4}\beta^3 V_j^e \mathbf{B}_j^e \tag{7.11}$$

The smoothed strain-displacement matrix $\bar{\mathbf{B}}_I$ for Ω_q^s will be of the form

$$\bar{\mathbf{B}}_I = \frac{1}{A_q^s}\sum_{l=1}^{n_q^e}\frac{1}{3}(1-\beta^2) A_l^e \mathbf{B}_l^e \ \text{ or } \ \bar{\mathbf{B}}_I = \frac{1}{V_q^s}\sum_{l=1}^{n_q^e}\frac{1}{4}(1-\beta^3) V_l^e \mathbf{B}_l^e \tag{7.12}$$

We now can obtain the smoothed stiffness matrix $\tilde{\mathbf{K}}_{IJ}^{(k)}$ for smoothing domain Ω_k^s, which gives

$$\tilde{\mathbf{K}}_{IJ}^{(k)} = \int_{\Omega_k^s} \tilde{\mathbf{B}}_I^T \mathbf{D} \tilde{\mathbf{B}}_J \mathrm{d}\Omega = \beta^2 \tilde{\mathbf{B}}_I^T \mathbf{D} \tilde{\mathbf{B}}_J A_k^s \tag{7.13}$$

For node-based smoothing domain Ω_q^s, the smoothed stiffness matrix $\bar{\mathbf{K}}_{IJ}^{(q)}$ or smoothed tangent stiffness matrix $\bar{\mathbf{K}}_{T\,IJ}^{(q)}$ would be obtained by a similar fashion as follows

$$\bar{\mathbf{K}}_{IJ}^{(q)} = \int_{\Omega_q^s} \bar{\mathbf{B}}_I^T \mathbf{D} \bar{\mathbf{B}}_J \mathrm{d}\Omega = (1-\beta^2) \bar{\mathbf{B}}_I^T \mathbf{D} \bar{\mathbf{B}}_J A_q^s \tag{7.14}$$

Since the portion of area of edge-based and node-based smoothing domains (or ES/FS-FEM and NS-FEM) will be tuned by β, the global stiffness matrix will be assembled by contributions from both of them. Therefore the global stiffness matrix $\hat{\mathbf{K}}$ for βFEM can be assembled from the $\tilde{\mathbf{K}}_{IJ}^{(k)}$ and $\bar{\mathbf{K}}_{IJ}^{(q)}$ as follows

$$\hat{\mathbf{K}} = \sum_{k=1}^{N_e} \tilde{\mathbf{K}}_{IJ}^{(k)} + \sum_{q=1}^{N_n} \bar{\mathbf{K}}_{IJ}^{(q)} \tag{7.15}$$

where N_e and N_n denote the number of total edges and total nodes in the system.

7.3.2 Properties of βFEM

The properties of ES-FEM and NS-FEM, including the displacement compatibility, variational consistency, solution continuity, etc., have been analyzed or discussed [24,32–34]. Since the continuous scalar factor β for βFEM can be regarded as a knob controlling the contributions from the NS-FEM and ES-FEM, it indicates that we may obtain a continuous solution function from the solution of the NS-FEM to that of ES-FEM if the factor β varies from 0 to 1. Therefore, the βFEM possesses some properties of both NS-FEM and ES-FEM due to this fact. If we take an elastic static problem as our example and we denote the strain field of an elastic problem computed by ES-FEM and NS-FEM as $\tilde{\boldsymbol{\varepsilon}}$ and $\bar{\boldsymbol{\varepsilon}}$ respectively, the potential energy functional of βFEM can be determined by the virtual work principle also used for standard FEM, given by

$$\widehat{\Pi}(\hat{\mathbf{u}},\beta)=\widehat{\Pi}^{\text{int}}(\hat{\mathbf{u}})-\widehat{\Pi}^{\text{ext}}(\hat{\mathbf{u}})=\tilde{\Pi}^{\text{int}}(\hat{\mathbf{u}})+\bar{\Pi}^{\text{int}}(\hat{\mathbf{u}})-\widehat{\Pi}^{\text{ext}}(\hat{\mathbf{u}}) \tag{7.16}$$

For isotropic linear elastic material, the Eq. (7.16) can be written as

$$\widehat{\Pi}(\hat{\mathbf{u}},\beta)=\int_{\Omega}\frac{1}{2}\tilde{\boldsymbol{\varepsilon}}^{\mathrm{T}}(\hat{\mathbf{u}})\mathbf{D}\tilde{\boldsymbol{\varepsilon}}(\hat{\mathbf{u}})\mathrm{d}\Omega+\int_{\Omega}\frac{1}{2}\bar{\boldsymbol{\varepsilon}}^{\mathrm{T}}(\hat{\mathbf{u}})\mathbf{D}\bar{\boldsymbol{\varepsilon}}(\hat{\mathbf{u}})\mathrm{d}\Omega-\int_{\Omega}\mathbf{f}^{b}\cdot\hat{\mathbf{u}}\mathrm{d}\Omega-\int_{\Gamma_{t}}\mathbf{f}^{t}\cdot\hat{\mathbf{u}}\mathrm{d}\Gamma \tag{7.17}$$

where $\hat{\mathbf{u}}$ defines an admissible virtual displacement field satisfying the given essential boundary conditions, the given continuous scalar factor $\beta\in[0,1]$, $\mathbf{D}$ stands for the elasticity tensor. If we perform variation to $\hat{\mathbf{u}}$ using the chain rule, the above equation becomes

$$\delta\widehat{\Pi}(\hat{\mathbf{u}},\beta)=\delta\int_{\Omega}\tilde{\boldsymbol{\varepsilon}}^{\mathrm{T}}(\hat{\mathbf{u}})\mathbf{D}\tilde{\boldsymbol{\varepsilon}}(\hat{\mathbf{u}})\mathrm{d}\Omega+\delta\int_{\Omega}\bar{\boldsymbol{\varepsilon}}^{\mathrm{T}}(\hat{\mathbf{u}})\mathbf{D}\bar{\boldsymbol{\varepsilon}}(\hat{\mathbf{u}})\mathrm{d}\Omega-\int_{\Omega}\delta\hat{\mathbf{u}}\mathbf{f}^{b}\mathrm{d}\Omega-\int_{\Gamma_{t}}\delta\hat{\mathbf{u}}\mathbf{f}^{t}\mathrm{d}\Gamma \tag{7.18}$$

From above equations, we can find some important properties as follows:

Property 1 (variational consitence). The βFEM is variational consistent for both 2D and 3D problems.

For a problem domain Ω, it can be discretized into edge/face-based smoothing cells Ω_k^s associated with N_{ed} (or N_{face}) edges/faces and node-based smoothing cells Ω_q^s associated with N_n nodes. If we substitute the approximation (7.3) and (3.12) (similar form for node-based smoothing cells) into Eq. (7.18) and utilize the arbitrary property of variation, the equation of interest for an element would be obtained as following

$$\mathbf{K}^{\text{two-field}}\mathbf{d}=\mathbf{f} \tag{7.19}$$

where $\mathbf{f}$ is the force vector and $\mathbf{K}^{\text{two-field}}$ denotes the smoothed stiffness matrix leading to

$$\mathbf{K}^{\text{two-field}}=\int_{\Omega_k^s}\tilde{\mathbf{B}}_I^T\mathbf{D}\tilde{\mathbf{B}}_J\mathrm{d}\Omega+\int_{\Omega_q^s}\bar{\mathbf{B}}_I^T\mathbf{D}\bar{\mathbf{B}}_J\mathrm{d}\Omega \tag{7.20}$$

Noted that the first term follows ES-FEM and second term follows NS-FEM, and both of them are variationally consistent [23].

Property 2 (bound property). The βFEM is variational consistent for both 2D and 3D problems.

If the factor is set as $\beta = 0$, the βFEM scheme becomes the same as the NS-FEM, which processes the underestimation of stiffness values and exact strain energy as reported [28,36]. The upper bound property is then ensured, which will be confirmed in numerical examples in Section 6.

When we choose $\beta = 1$, the βFEM is essentially the same as the ES/FS-FEM. The stiffness would be overestimated [26,32,38–40], though its accuracy would be better than standard FEM. This leads to the low bound property of βFEM.

The solution of βFEM shall be within the narrow interval which bounds the exact solution, owing to the fact that ES-FEM generates the nearly exact solution from the lower bound and NS-FEM produces the unique upper bound solution (noted that this interval would be narrower than αFEM [37], as the solution of ES-FEM is closer to exact solution from lower bound than standard FEM);

Property 3 (solution continuity property). If the scaling factor β changes from 0.0 to 1.0, the property of underestimation of stiffness will become overestimation, continuously, and the solution of βFEM would be a continuous function of β from the solution of the NS-FEM and that of ES-FEM.

Property 4 (exact solution property). It is possible to find the exact (or close-to-exact) solution(s) of strain energy during the procedure of tuning the factor due to the solution continuity property [24].

Property 5 (temporal stability property). Even with a small portion of ES-FEM (choosing a small value of β), the constructed stiffness matrix exhibits the properties of overestimation, which can alleviate the temporal instability brought by the pure NS-FEM.

7.4 Implementation Aspects

This section will briefly introduce the implementation aspects for numerical examples, including the formulations for free vibration analysis and large deformation problems.

7.4.1 Formulations for Free Vibration Problem

The general discrete form of Eq. (7.1) for vibration analysis using βFEM gives the form as

$$\mathbf{M}\ddot{\mathbf{d}} + \mathbf{C}\dot{\mathbf{d}} + \hat{\mathbf{K}}\mathbf{d} = \mathbf{f} \tag{7.21}$$

where $\mathbf{M}$, $\mathbf{C}$ and $\hat{\mathbf{K}}$ are the matrices of mass, damping and stiffness. If the terms of damping and external forces are not considered, the above equation can be simplified into a free vibration problem with a homogenous form:

$$\mathbf{M}\ddot{\mathbf{d}} + \hat{\mathbf{K}}\mathbf{d} = \mathbf{0} \tag{7.22}$$

where the mass matrix can adopt lumped mass matrix or consistent mass matrix. The general solution of Eq. (7.22) can be assumed as [41]

$$\mathbf{d} = \boldsymbol{\varphi}\exp(\mathrm{i}\omega t) \tag{7.23}$$

in which the eigenvector $\boldsymbol{\varphi}$ and natural frequency ω can be determined by the eigenvalue equation as following:

$$(-\mathbf{\Lambda M}+\widehat{\mathbf{K}})\boldsymbol{\psi}=0 \tag{7.24}$$

and

$$\mathbf{\Lambda}=\text{diagonal}(\omega_1^2,\omega_2^2,...,\omega_n^2)=\text{diagonal}(\lambda_1,\lambda_2,...,\lambda_n) \tag{7.25}$$

$$\boldsymbol{\psi}=[\boldsymbol{\varphi}_1,\boldsymbol{\varphi}_2,...,\boldsymbol{\varphi}_n] \tag{7.26}$$

where $\boldsymbol{\varphi}_r$ is the eigenvector associated with the eigenvalue λ_r ($r=1,2...,n$).

We can also define modal stiffness k_r and modal mass m_r of the system as

$$k_r=\boldsymbol{\varphi}_r^T\mathbf{K}\boldsymbol{\varphi}_r,\ r=1,2...,n \tag{7.27}$$

$$m_r=\boldsymbol{\varphi}_r^T\mathbf{M}\boldsymbol{\varphi}_r,\ r=1,2...,n \tag{7.28}$$

In this case the natural frequency can now be evaluated using the following relationship:

$$\omega_r=\sqrt{k_r/m_r},\ r=1,2...,n \tag{7.29}$$

7.4.2 Nonlinear Problems with Large Deformation

For nonlinear problems with large deformation, it can be solved by an incremental process. If we introduce the tangent stiffness matrix ${}^t\mathbf{K}$ and internal force vector $\mathbf{f}^I$, the FEM equilibrium equation of large deformation according to the total Lagrange formulation [24,38–40] becomes

$${}^t\mathbf{K}\mathbf{d}=\mathbf{f}^R=\mathbf{f}^E-\mathbf{f}^I \tag{7.30}$$

In finite element computations, the tangent stiffness matrix is frequently split into linear part ${}^t\mathbf{K}_L$ and nonlinear part ${}^t\mathbf{K}_{NL}$, then we can rewrite the above equation using βFEM as

$$({}^t\widehat{\mathbf{K}}_L+{}^t\widehat{\mathbf{K}}_{NL})\mathbf{d}=\mathbf{f}^E-\widehat{\mathbf{f}}^I \tag{7.31}$$

where the linear part

$$ {}^{t}\widehat{\mathbf{K}}_{L}=\sum_{k=1}^{N_e}\beta^2\tilde{\mathbf{B}}_{L}^{T}\mathbf{D}\tilde{\mathbf{B}}_{L}V_{k}^{s}+\sum_{q=1}^{N_n}(1-\beta^2)\bar{\mathbf{B}}_{L}^{T}\mathbf{D}\bar{\mathbf{B}}_{L}V_{q}^{s} \tag{7.32} $$

the contribution, ${}^{t}\widehat{\mathbf{K}}_{NL}$, is defined as

$$ {}^{t}\widehat{\mathbf{K}}_{NL}=\sum_{k=1}^{N_e}\beta^2\tilde{\mathbf{B}}_{NL}^{T}\tilde{\mathbf{S}}\tilde{\mathbf{B}}_{NL}V_{k}^{s}+\sum_{q=1}^{N_n}(1-\beta^2)\bar{\mathbf{B}}_{NL}^{T}\bar{\mathbf{S}}\bar{\mathbf{B}}_{NL}V_{q}^{s} \tag{7.33} $$

and the internal force vector reads

$$ \widehat{\mathbf{f}}^{I}=\sum_{k=1}^{N_e}\beta^2\tilde{\mathbf{B}}_{L}^{T}\left\{\tilde{\mathbf{S}}\right\}V_{k}^{s}+\sum_{q=1}^{N_n}(1-\beta^2)\bar{\mathbf{B}}_{L}^{T}\left\{\bar{\mathbf{S}}\right\}V_{q}^{s} \tag{7.34} $$

where the matrix $\tilde{\mathbf{B}}_{L}$, $\bar{\mathbf{B}}_{L}$, $\tilde{\mathbf{B}}_{NL}$, $\bar{\mathbf{B}}_{NL}$, $\tilde{\mathbf{S}}$, $\bar{\mathbf{S}}$, $\left\{\tilde{\mathbf{S}}\right\}$ and $\left\{\bar{\mathbf{S}}\right\}$ can be smoothed from $\mathbf{B}_{L}$, $\mathbf{B}_{NL}$, $\mathbf{S}$ and $\{\mathbf{S}\}$ via a similar fashion presented in Section 2. The expressions of these matrices ($\mathbf{B}_{L}$, $\mathbf{B}_{NL}$, $\mathbf{S}$ and $\{\mathbf{S}\}$) for 3D problems are given as (2D expressions would be easily obtained [24])

$$ \mathbf{B}_{L}=\begin{bmatrix} F_{11}N_{1,1} & F_{21}N_{1,1} & F_{31}N_{1,1} \\ F_{12}N_{1,2} & F_{22}N_{1,2} & F_{32}N_{1,2} \\ F_{13}N_{1,3} & F_{23}N_{1,3} & F_{33}N_{1,3} \\ F_{11}N_{1,2}+F_{12}N_{1,1} & F_{21}N_{1,2}+F_{22}N_{1,1} & F_{31}N_{1,2}+F_{32}N_{1,1} \\ F_{12}N_{1,3}+F_{13}N_{1,2} & F_{22}N_{1,3}+F_{23}N_{1,2} & F_{32}N_{1,3}+F_{33}N_{1,2} \\ F_{13}N_{1,1}+F_{11}N_{1,3} & F_{23}N_{1,1}+F_{21}N_{1,3} & F_{33}N_{1,1}+F_{31}N_{1,3} \end{bmatrix} \begin{matrix} F_{11}N_{1,1} & \cdots & F_{31}N_{4,1} \\ F_{12}N_{1,2} & \cdots & F_{32}N_{4,2} \\ F_{13}N_{1,3} & \cdots & F_{33}N_{4,3} \\ F_{11}N_{1,2}+F_{12}N_{1,1} & \cdots & F_{31}N_{4,2}+F_{32}N_{4,1} \\ F_{12}N_{1,3}+F_{13}N_{1,2} & \cdots & F_{32}N_{4,3}+F_{33}N_{4,2} \\ F_{13}N_{1,1}+F_{11}N_{1,3} & \cdots & F_{33}N_{4,1}+F_{31}N_{4,3} \end{matrix} \tag{7.35} $$

where the deformation gradient tensor $\mathbf{F}$ is defined by

$$\mathbf{F}=\left(\frac{\partial \mathbf{x}}{\partial \mathbf{X}}\right)^{T}=\begin{bmatrix} F_{11} & F_{12} & F_{13} \\ F_{21} & F_{22} & F_{23} \\ F_{31} & F_{32} & F_{33} \end{bmatrix} \tag{7.36}$$

The matrices $\mathbf{B}_{NL}$ and $\mathbf{S}$ are given by

$$\mathbf{B}_{NL}=\begin{bmatrix} N_{1,1} & 0 & 0 & N_{2,1} & \ldots & 0 \\ N_{1,2} & 0 & 0 & N_{2,2} & \ldots & 0 \\ N_{1,3} & 0 & 0 & N_{2,3} & \ldots & 0 \\ 0 & N_{1,1} & 0 & 0 & \ldots & 0 \\ 0 & N_{1,2} & 0 & 0 & \ldots & 0 \\ 0 & N_{1,3} & 0 & 0 & \ldots & 0 \\ 0 & 0 & N_{1,1} & 0 & \ldots & N_{4,1} \\ 0 & 0 & N_{1,2} & 0 & \ldots & N_{4,2} \\ 0 & 0 & N_{1,3} & 0 & \ldots & N_{4,3} \end{bmatrix} \tag{7.37}$$

and

$$\mathbf{S}=\begin{bmatrix} S_{11} & S_{12} & S_{13} & 0 & 0 & 0 & 0 & 0 & 0 \\ S_{12} & S_{22} & S_{23} & 0 & 0 & 0 & 0 & 0 & 0 \\ S_{13} & S_{23} & S_{33} & 0 & 0 & 0 & 0 & 0 & 0 \\ 0 & 0 & 0 & S_{11} & S_{12} & S_{13} & 0 & 0 & 0 \\ 0 & 0 & 0 & S_{12} & S_{22} & S_{23} & 0 & 0 & 0 \\ 0 & 0 & 0 & S_{13} & S_{23} & S_{33} & 0 & 0 & 0 \\ 0 & 0 & 0 & 0 & 0 & 0 & S_{11} & S_{12} & S_{13} \\ 0 & 0 & 0 & 0 & 0 & 0 & S_{12} & S_{22} & S_{23} \\ 0 & 0 & 0 & 0 & 0 & 0 & S_{13} & S_{23} & S_{33} \end{bmatrix} \tag{7.38}$$

The second Piola-Kirchhoff stress tensor (PK2) holds the form as

$$\{\mathbf{S}\}=\begin{bmatrix} S_{11} & S_{22} & S_{33} & S_{12} & S_{23} & S_{31} \end{bmatrix}^{T}=\mathbf{D}\begin{bmatrix} E_{11} & E_{22} & E_{33} & 2E_{12} & 2E_{23} & 2E_{31} \end{bmatrix}^{T} \tag{7.39}$$

where the Green–Lagrange strain tensor **E** of elements can be defined from the deformation gradient tensor, which reads

$$\mathbf{E}=\frac{1}{2}\left(\mathbf{F}^{T}\mathbf{F}-\mathbf{I}\right)=\begin{bmatrix} E_{11} & E_{12} & E_{13} \\ E_{21} & E_{22} & E_{23} \\ E_{31} & E_{32} & E_{33} \end{bmatrix} \tag{7.40}$$

7.5 Standard Patch Test

7.5.1 A Standard Patch Test for 2D Problems

To assess the convergence of the presented βFEM, the satisfaction of patch tests is an essential requirement. In Figure 7.4, a simple domain is discretized using "patch" of irregular triangular elements indicated by red color. The left and bottom edges are constrained at the horizontal and vertical directions, respectively. The right and top edges are assumed to be stretched to 10% of the original length at the horizontal and vertical directions, respectively. To pass the patch test, the computed displacements of all the interior nodes should follow exactly (to machine precision) the same linear function of the displacements imposed along the edges, viz.,

$$u=0.1x \quad \text{and} \quad v=0.1y \tag{7.41}$$

In order to examine the numerical convergence rate, the following displacement error norm can be defined

$$e_d=\frac{\sum_{i=1}^{\text{ndof}}\left|u_i-u_i^h\right|}{\sum_{i=1}^{\text{ndof}}\left|u_i\right|}\times 100\% \tag{7.42}$$

where u_i and u_i^h are the exact and numerical solution of displacements, respectively.

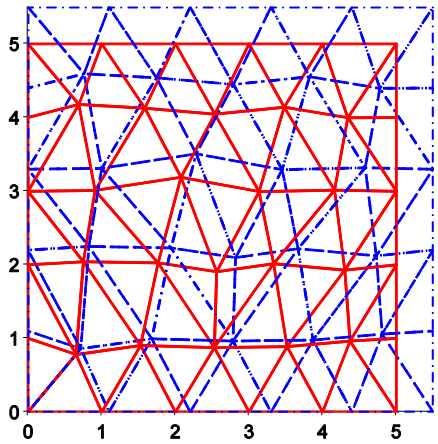

Figure 7.4. A 2D patch test for βFEM using triangular mesh.

The deformed configuration is plotted by blue dash-dot lines in Figure 7.4. In Table 7.1, the numerical results show that this simple square model is able to pass the designed patch test within machine precision for any value of $\beta \in [0,1]$. Therefore, the displacement compatibility is ensured and the convergence of numerical solutions (toward exact results) would be confirmed.

Table 7.1 Displacement error norm for 2D patch test

β	0.0000	0.2000	0.4853*	0.6324*	0.8000	0.9000	1.0000
e_d	5.2170e-14	4.2645e-14	2.8359e-14	2.6369e-14	2.4734e-14	2.8786e-14	2.7933e-14

* Random generated number

7.5.2 Irons First-order Patch Test for 3D Problems

Consider a 3D cube with side length 10 mm and elastic parameters $E = 6.895 \times 10^3$ MPa and $v = 0.25$. On the exterior boundaries, linear displacements are prescribed as following:

$$\begin{aligned} u &= 0.0005*(2x+y+z) \\ v &= 0.0005*(x+2y+z) \\ w &= 0.0005*(x+y+2z) \end{aligned} \tag{7.43}$$

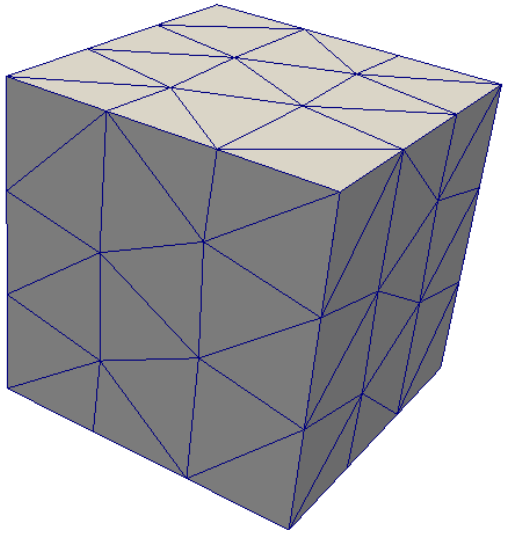

Figure 7.5. A 3D cubic patch test for βFEM using tetrahedral mesh.

The domain needs to be discretized by irregular elements with at least one interior node, e.g., Figure 7.5. To pass this patch test, the displacements of all the interior nodes should follow exactly the same function of the imposed displacement on exterior boundaries. The displacement error norms calculated by Eq. (7.43) are listed in Table 7.2. Again it passed the conducted patch test at machine precision and the displacement compatibility would be ensured.

Table 7.2 Displacement error norm for 3D patch test

β	0.0000	0.2000	0.4218*	0.6555*	0.7500	0.9000	1.0000
e_d	8.1157e-16	4.0579e-16	1.1159e-16	3.0434e-16	6.0868e-16	4.0579e-16	7.1012e-16

* Random generated number

7.6 Numerical Examples and Discussions

In this section, several representative numerical examples are illustrated. In the first two examples, the well-known Cook's membrane problem and cantilever beam problem under plane

stress conditions is studied for comparisons of accuracy and solution bounds. An elastic infinite plate with a circular hole considered as a plane strain problem is tested for accuracy and simple volumetric locking in the third example. The fourth example tests the property of temporal stability of βFEM by analysis of free vibration of an automobile connecting bar. The fifth and sixth examples examine the accuracy of proposed 3D βFEM. A human molar tooth example is simulated in the seventh example, which shows the application of our method for modeling of an object with moderately complex geometry. The last example extends to the analysis of a geometrically non-linear problem with large deformation.

7.6.1 Cook's Membrane: Study of Accuracy and Solution Bounds

As a standard test for combined bending and shear response with moderate distortion, Cook's membrane problem [42] is shown in Figure 7.6. The problem consists of a tapered panel clamped at the left boundary and subjected to an in-plane shearing traction at the free right edge. The volume force would not be considered and the plane stress conditions are assumed. The material parameters are chosen as: Young's modulus $E = 3\times10^7$ Pa and Poisson's ratio $\nu = 1/3$. Following References [7,43], we set the geometrical dimensions as $l_1 = 48$, $l_2 = 44$ and $l_3 = 16$, and the loading $P = 1$, where P is the resultant of the uniformly distributed shear traction. The reference value of the vertical displacement for the middle of the right edge is 23.9642 [44] and the reference strain energy of membrane is 12.015 [42].

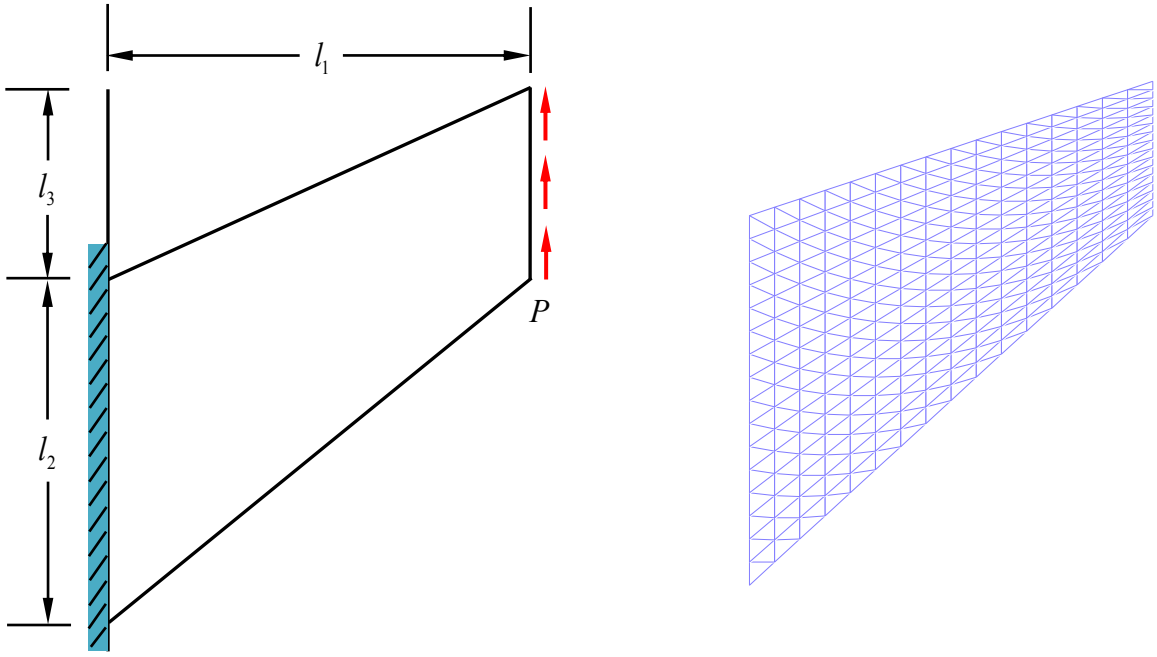

(a) (b)

Figure 7.6. Cook's membrane problem: (a) geometry and loads and (b) domain discretization by 16×16 triangular base mesh.

In order to test the accuracy and convergence behavior of the βFEM, the problem has been discretized into structured meshes with $N\times N$ edge density of the mesh. Figure 7.7 and Figure 7.8 compare the results obtained by several different methods with four different spatial discretizations. Figure 7.7 shows comparisons of displacements at right tip-center of the membrane from different methods. The bound properties of strain energy are investigated and compared in Figure 7.8. It is evident that the βFEM (with $\beta=0.9$) generates the most accurate solutions (or close-to-reference solutions) among all these methods. The FEM and ES-FEM produce stiffer solutions of displacement and behavior of the overestimation property of stiffness, which approximate the reference solutions from the lower-bound of displacement or energy. While the NS-FEM produces "overly-soft" solutions because of the underestimation behavior, which reflects the unique property of upper-bound. Regardless of the value of parameter β, the

numerical results of βFEM would be within the narrow interval bounded by the solutions of ES-FEM and NS-FEM.

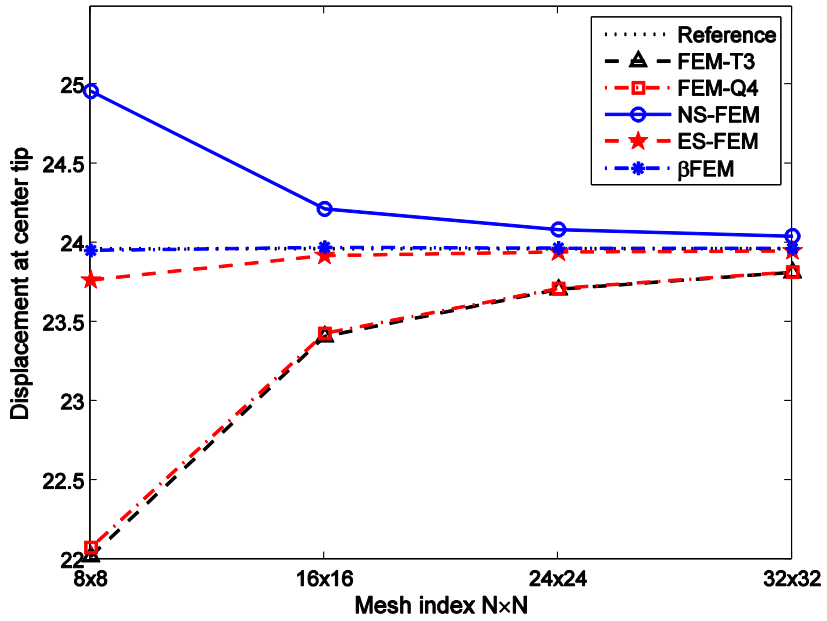

Figure 7.7. Comparisons of displacements at tip-center from different methods for Cook's membrane problem.

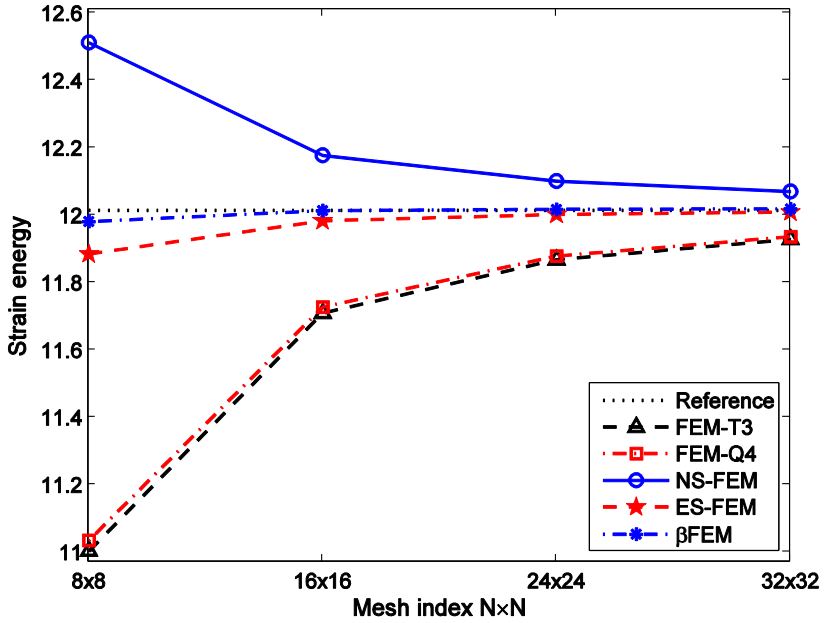

Figure 7.8. Solution bounds of energy for Cook's membrane problem.

7.6.2 Cantilever Beam Under a Tip Load: Study of Accuracy and Solution Bounds

In this example, a rectangular cantilever linear elastic beam with length L and height H is studied here. The beam is fixed along the left side edge and subjected to a parabolic traction P at the free end as shown in Figure 7.9(a). The beam is assumed to be a plane stress problem with unit thickness. The analytical solution of displacements can be found in reference [45], which reads as follows

$$\begin{aligned} u_x &= \frac{P}{6EI}\left[(6L-3x)xy+(2+\nu)y\left(y^2-\frac{H^2}{4}\right)\right] \\ u_y &= -\frac{P}{6EI}\left[(4+5\nu)\frac{H^2x}{4}+(3L-x)x^2+3\nu y^2(L-x)\right] \end{aligned} \tag{44}$$

The corresponding stresses can be expressed as

$$\sigma_{xx}(x,y)=\frac{P(L-x)y}{I};\ \sigma_{yy}(x,y)=0;\ \tau_{xy}(x,y)=\frac{P}{2I}\left(y^2-\frac{D^2}{4}\right) \tag{45}$$

where I is the moment of inertia for the beam and can be written as $I=H^3/12$ for this problem. The related geometry/loading parameters and material properties are given as: $L=2.4$ m, $H=0.6\,\text{m}$, $P=5000\,\text{N}$, Young's modulus $E=3\times10^7\,\text{Pa}$ and Poisson's ratio $v=0.3$.

(a)

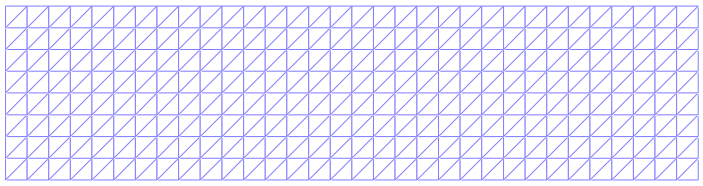

(b)

Figure 7.9. Computation model of cantilever beam: (a) sketch of geometry and loading; (b) domain discretization using 512 triangular (or 256 quadrilateral) elements.

In Figure 7.9(b), a sample mesh using 512 triangular elements (or 256 quadrilateral elements with the same number of nodes) is illustrated. To check the accuracy of βFEM, the displacement values along the neutral axis obtained by different methods are compared in Figure 7.10. The bound properties of strain energy are investigated and compared in Figure 7.11. From these numerical results, it reveals several facts as: (1) compared to analytical solution, the FEM-

T3, FEM-Q4, ES-FEM produce stiffer solutions of deformation and show the overestimation property of stiffness, which can evaluate the exact solution from the lower-bound of deformation or energy; (2) the ES-FEM solution is the most accurate one among these methods from the lower-bound, and it behaves even (slightly) more accurately than FEM-Q4; (3) the NS-FEM generates "overly-soft" solution due to the underestimation behavior, which brings on the unique property of the upper-bound; (4) βFEM can achieve the super-accurate or close-to-exact solution when it adopts the proper value of adjustable parameter β. For example, $\beta \in [0.8, 0.95]$ for this problem works well compared to the analytical solution; (5) the numerical results of βFEM is within the interval bounded by the solutions of ES-FEM and NS-FEM.

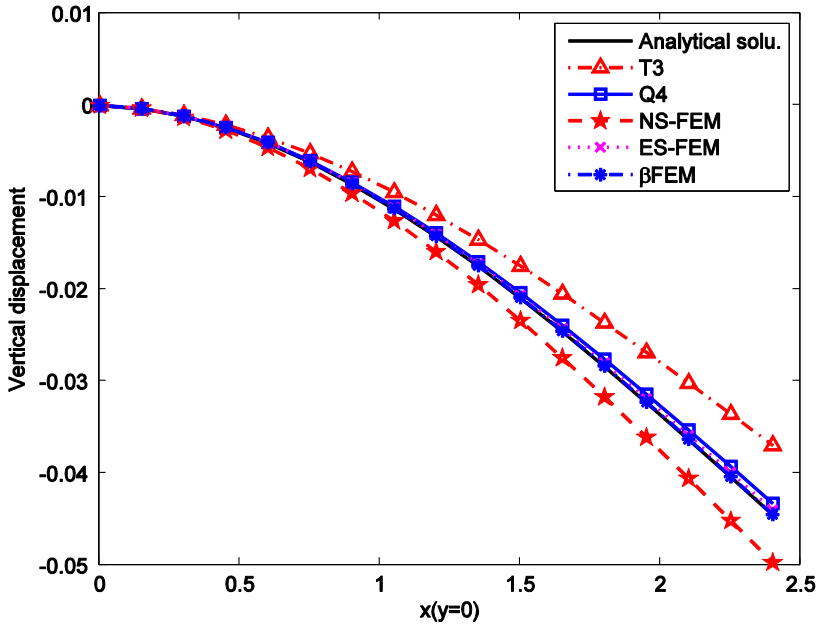

Figure 7.10. Vertical displacement at central line ($y = 0$) using the mesh with 85 nodes.

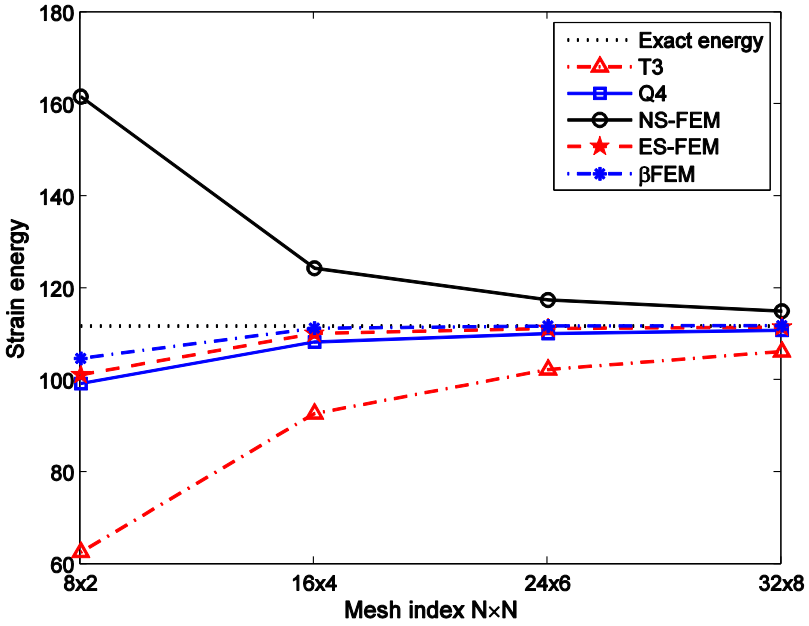

Figure 7.11. Solution bounds of energy for the problem of cantilever beam.

7.6.3 Infinite Plate with a Circular Hole: Test for Accuracy and Volumetric Locking

Figure 7.12 illustrates a plate with a central circular hole subjected to a unidirectional tensile stress of $p = 0.98\times10^{6}\,\mathrm{N/m^2}$ at infinity in the x direction. Since the stress concentration around the hole is highly localized and decays very rapidly, essentially disappearing when the distance to the center is greater than $5a$, only a finite plate with $L = 5a$ is necessary to be modeled. Here one quarter (upper right quadrant) of the plate is chosen and discretized into T3 or Q4 elements, owing to the symmetry of problem. The symmetry boundary conditions are imposed along the left and bottom edges and the inner edge of the hole is traction free. Plane strain condition is considered and the geometrical parameters are assumed as $a = 0.2\,\mathrm{m}$ and $L = 1.0\,\mathrm{m}$. The exact solution for displacement components is given as [45]

$$
\begin{aligned}
u_x &= \frac{pa}{8\mu}\left[\left(2\frac{a}{r}+\frac{r}{a}\right)(1+\kappa)\cos\theta+2\frac{a}{r}\left(1-\frac{a^2}{r^2}\right)\cos 3\theta\right] \\
u_y &= \frac{pa}{8\mu}\left[\left(2\frac{a}{r}-\frac{r}{a}\right)(1-\kappa)\sin\theta+2\frac{a}{r}\left(1-\frac{a^2}{r^2}\right)\sin 3\theta\right]
\end{aligned}
\tag{46}
$$

where the shear modulus $\mu = E/(2(1+\nu))$ and bulk modulus $\kappa = 3-4\nu$ for plane strain conditions, (r,θ) are the polar coordinates with counterclockwise measured θ. The exact solution for the stress is given as [45]

$$
\begin{aligned}
\sigma_{11} &= p\left[1-\frac{a^2}{r^2}\left(\frac{3}{2}\cos 2\theta+\cos 4\theta\right)+\frac{3a^4}{2r^4}\cos 4\theta\right] \\
\sigma_{22} &= p\left[-\frac{a^2}{r^2}\left(\frac{1}{2}\cos 2\theta-\cos 4\theta\right)-\frac{3a^4}{2r^4}\cos 4\theta\right] \\
\tau_{12} &= p\left[-\frac{a^2}{r^2}\left(\frac{1}{2}\sin 2\theta+\sin 4\theta\right)+\frac{3a^4}{2r^4}\sin 4\theta\right]
\end{aligned}
\tag{47}
$$

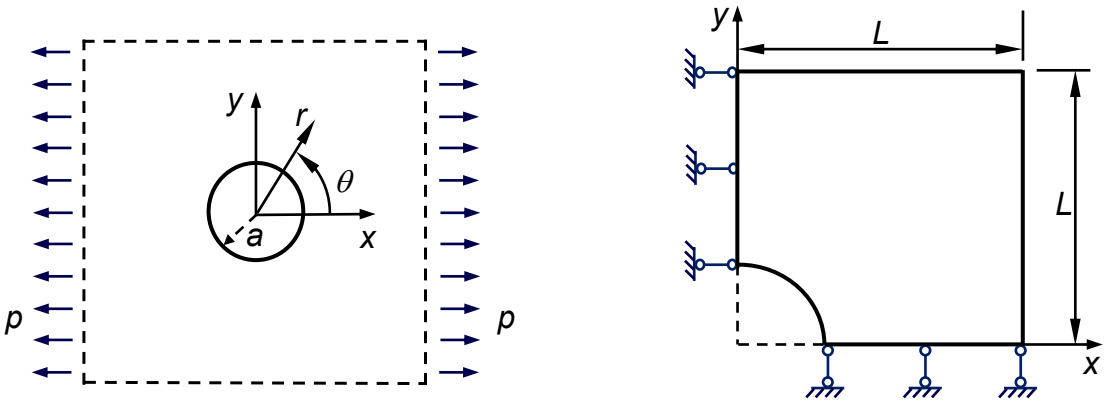

Figure 7.12. An infinite plate with a circular hole and its quarter model.

In order to investigate the strain energy, the energy curves against the mesh index are compared and plotted in Figure 7.12. Here the parameters are set to be: Young's modulus $E = 90$ MPa, Poisson's ratio $\nu = 0.3$, and $\beta = 0.84$. The figure shows that the values of strain

energy obtained using NS-FEM are always larger than the reference exact energy and those computed from other methods. On the other side, the curves computed using FEM-T3, FEM-Q4, ES-FEM and βFEM are lower than the exact one. Moreover, the presented βFEM provides the most accurate results which can be regarded as the close-to-exact solution among these methods. These phenomena also indicate the reference/exact solution is always bounded from both sides: by NS-FEM from the upper-bound of energy or deformation and by FEM-T3, FEM-Q4 or ES-FEM from the lower-bound. Tuning the value of the scaling factor β in βFEM, the solutions will be shifted from above to below of the exact one and the features of both NS-FEM and ES-FEM would be inherited when the factor $\beta \in (0,1)$ is selected.

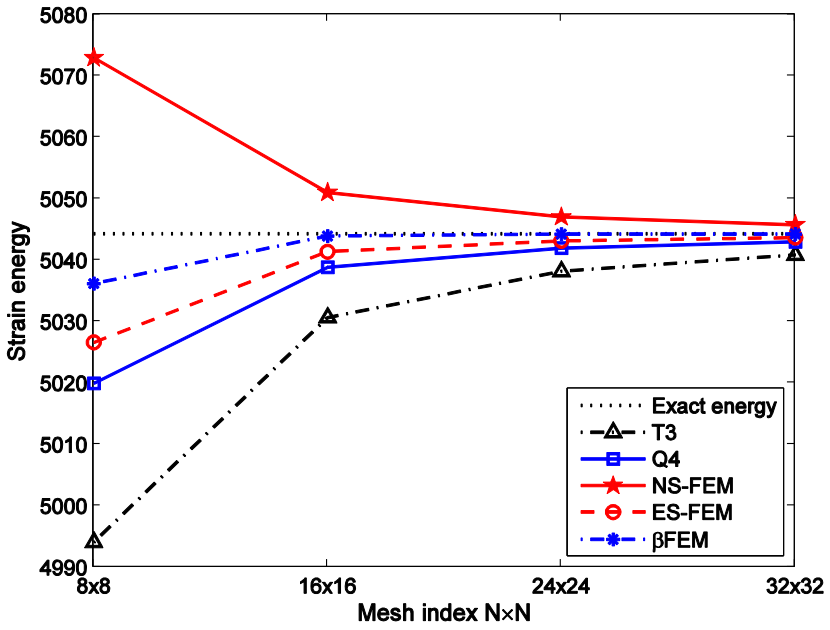

Figure 7.13. Solution bounds of energy for the problem of infinite plate with a circular hole.

For the volumetric locking issue in the nearly incompressible elastic materials under plane strain condition, we can test the problem via setting the Poisson's ratio as values being close to 0.5, i.e., $\nu = 0.4 / 0.49 / 0.499 / 0.4999 / 0.49999 / 0.499999 / 0.4999999$. Table 7.3 and

Figure 7.14 shows the displacement error norms at different Poisson's ratios for FEM-T3, FEM-Q4, ES-FEM, and βFEM with $\beta = 0$ (i.e., NS-FEM) and $\beta = 1 - \nu$. Obviously both the standard FEM using T3 and Q4 suffer from the volumetric locking. While the βFEM, which inherits the property of NS-FEM, is immune from volumetric locking and suitable for treating near incompressible situations. The case $\beta = 0$ for βFEM also verified the property: the NS-FEM is effective in overcoming volumetric locking.

Table 7.3 Displacement error norm for infinite plate with a circular hole

Mesh	Poisson's Ratio	FEM-T3	FEM-Q4	ES-FEM	βFEM ($\beta = 0$)	βFEM ($\beta = 1 - \nu$)
16x16	0.4	1.08677	0.29847	0.14065	0.90085	0.85173
16x16	0.49	3.96202	1.80973	0.43391	0.85934	0.84933
16x16	0.499	7.34553	7.67250	1.89630	0.85573	0.85450
16x16	0.4999	8.35639	15.12191	4.59207	0.85556	0.85543
16x16	0.49999	8.49039	17.45636	7.37184	0.85554	0.85553
16x16	0.499999	8.50438	17.75544	8.23398	0.85554	0.85554
16x16	0.4999999	8.50579	17.78638	8.34642	0.85554	0.85554

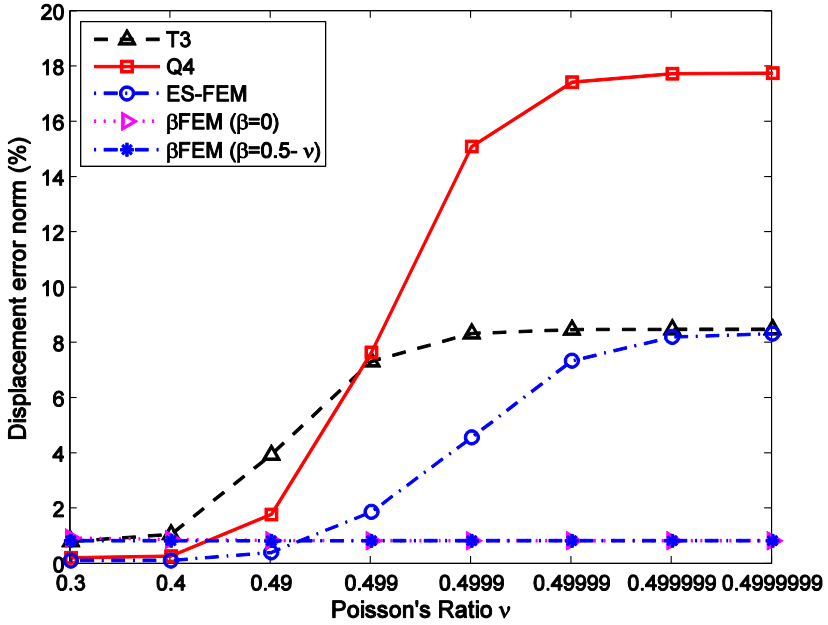

Figure 7.14. Displacement error norms vs. different Poisson's ratios.

7.6.4 Free Vibration Analysis of an Automobile Connecting Rod: Test for Temporal Stability

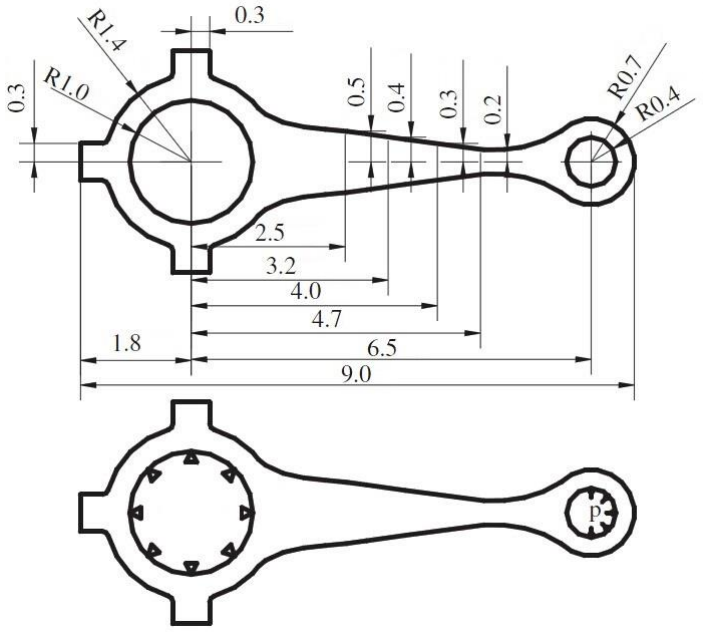

Figure 7.15. Geometry and boundary conditions of an automobile connecting rod [15].

As NS-FEM is found to be temporally instable and may have non-zero-energy spurious modes [30], this example will test the temporal stability of βFEM by performing a free vibration analysis for an automobile connecting rod. The geometrical dimensions, boundary conditions and loading are illustrated in Figure 7.15, with $p = 1$MPa. The inside circumference for the left side is fixed at both directions. The material parameters are chosen as: Young's modulus $E = 3\times10^7$ Pa, Poisson's ratio $\nu = 1/3$, and mass density $\rho = 7.8\times10^3$ kg/m^3 for plane stress analysis. The domain is discretized by a triangle mesh using 472 nodes for T-mesh based methods (FEM-T3, NS-FEM, ES-FEM and βFEM) and 511 nodes for FEM-Q4 as a comparison.

Table 7.4 First 12 natural frequencies (Hz) for the automobile connecting rod

Mesh	472 nodes and 736 T3 elements					511 nodes and 404 Q4 elements
Method	FEM-T3	NS-FEM	ES-FEM	βFEM ($\beta = 0.8$)	βFEM ($\beta = 0.9$)	FEM-Q4 (Abaqus)
Frequencies (Hz)	470.37	417.68	442.70	434.15	438.23	439.74
	2130.96	1911.17	2023.13	1987.24	2004.50	2017.5
	4907.22	4683.20	4864.00	4839.24	4851.83	4858.8
	5234.04	4746.23	4994.71	4903.62	4947.87	5010.4
	9453.83	7742.60	8967.82	8763.59	8864.36	9022.2
	11889.09	8167.72	11293.10	10963.85	11131.13	11220
	13906.91	9841.74	12748.38	12231.46	12487.51	12747
	16337.07	10800.20	15426.02	15075.44	15251.90	15240
	16728.28	13271.05	15524.57	15095.27	15292.12	15412
	19935.52	14056.13	19319.98	18980.37	19151.17	18628
	20387.98	14358.80	19712.42	19346.70	19531.13	19571
	20706.67	15890.19	19926.97	19533.44	19729.33	19918

Table 7.4 lists the first 12 natural frequencies. It is observed that the FEM-T3 has the largest value of frequency and the NS-FEM has the lowest value at each mode, which clearly

demonstrates the overly-stiff behavior of FEM-T3 and overly-soft feature of NS-FEM for frequency analysis. All the natural frequencies solved by βFEM ($\beta = 0.8$ and $\beta = 0.9$) are bounded between the results from ES-FEM (upper) and NS-FEM (lower). The mode shapes obtained by NS-FEM and βFEM ($\beta = 0.8$) are presented in Figure 7.16 and Figure 7.17. It is apparent that the spurious non-zero modes (e.g., modes 5, 9, 11 and 12) exhibited in NS-FEM have vanished in ES-FEM. This example confirms that the βFEM with a proper parameter β can approach the exact solutions and effectively eliminate the temporal instability and spurious modes, which may have existed in NS-FEM.

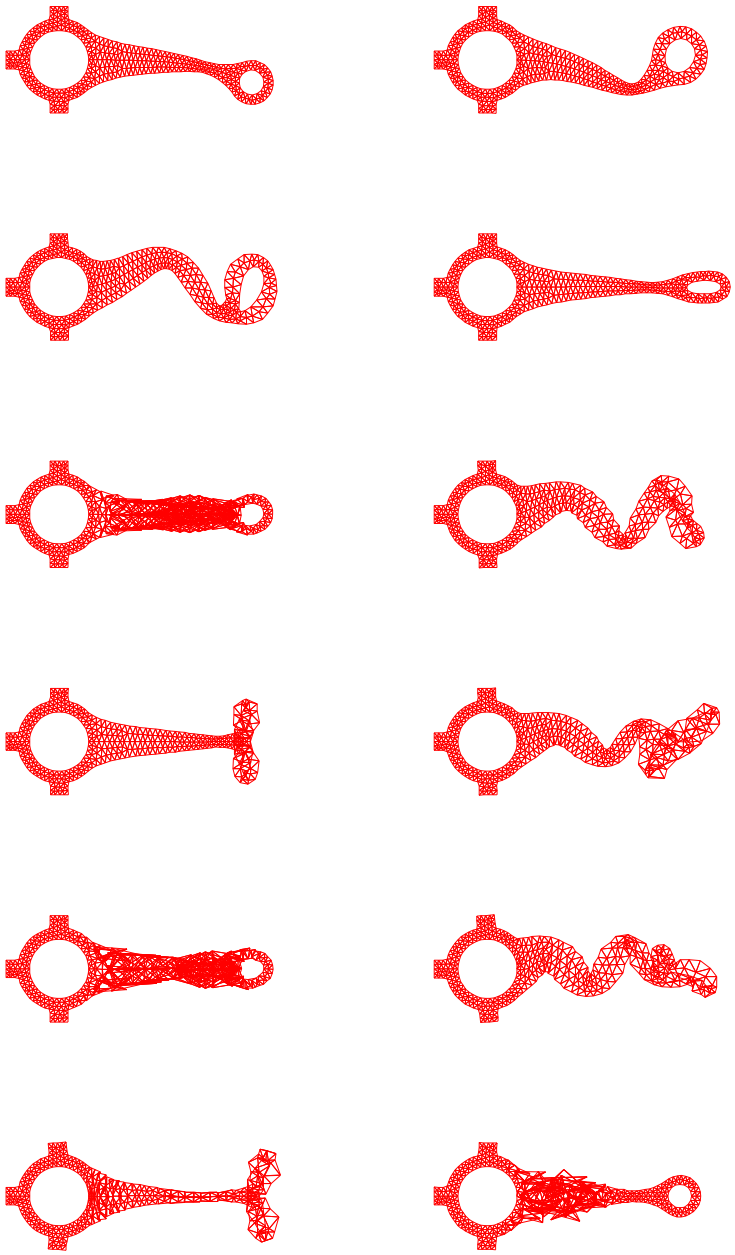

Figure 7.16. First 12 modes of the connecting rod obtained by NS-FEM.

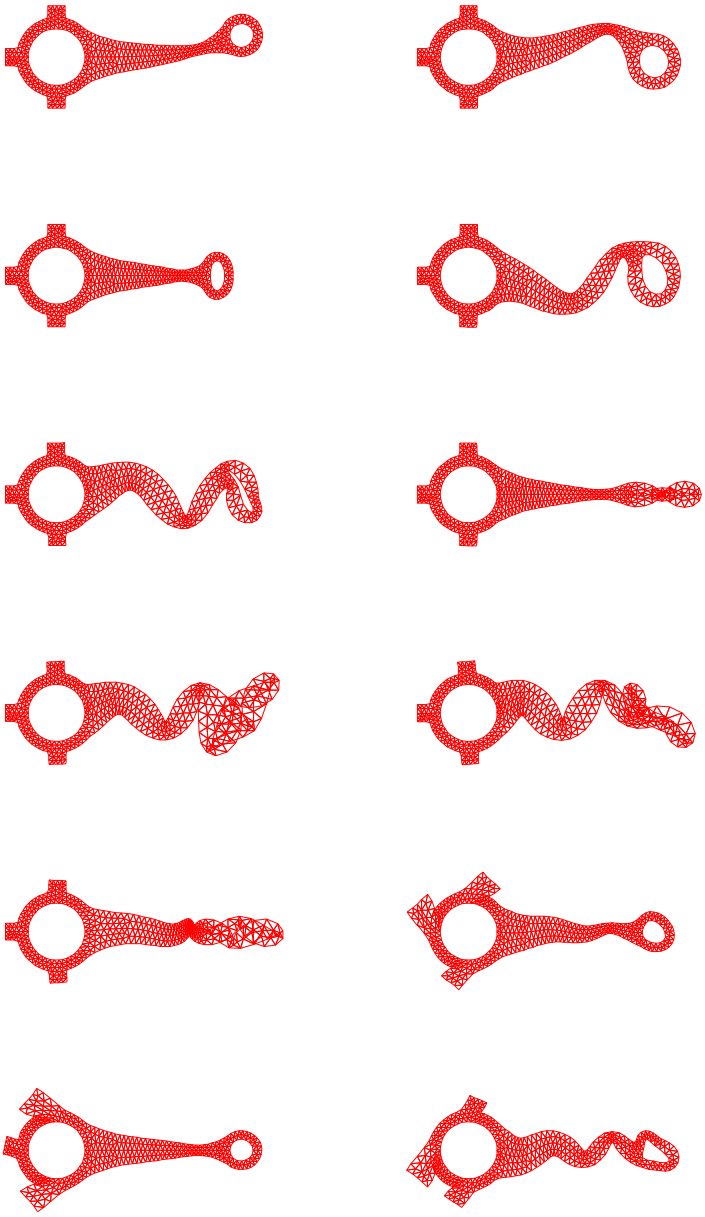

Figure 7.17. First 12 modes of the connecting rod obtained by βFEM.

7.6.5 A 3D Cantilever of Cubic Shape: Accuracy Study

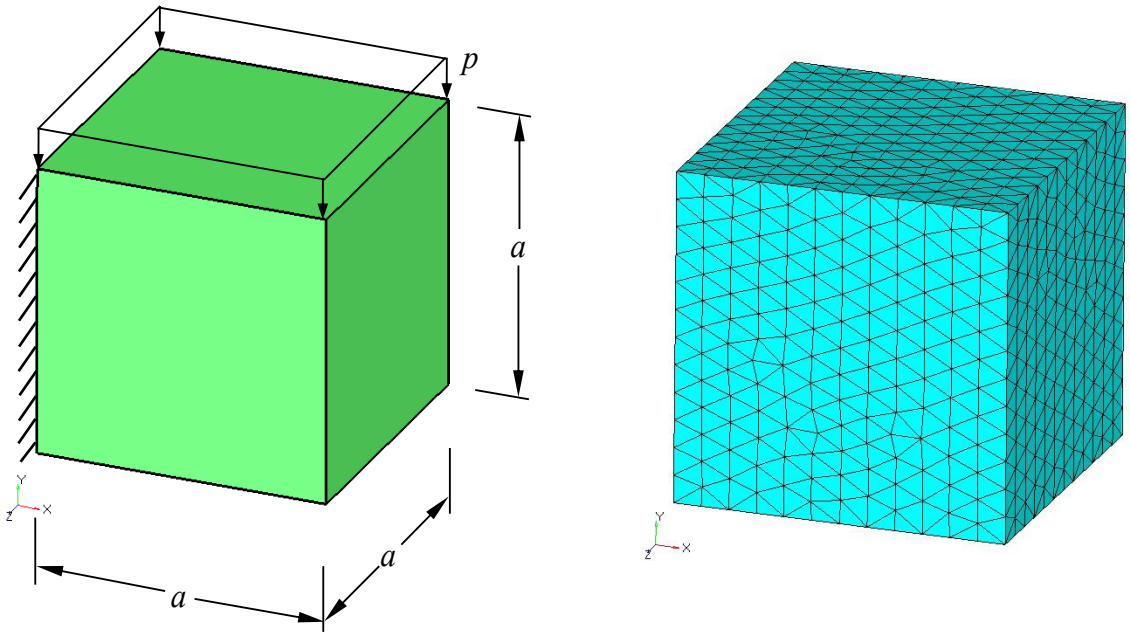

(a) (b)

Figure 7.18. A cubic cantilever submitted to a uniform pressure on its upper face: (a) geometry and (b) domain discretization by tetrahedral mesh.

This example considers a 3D cantilever with cubic shape as shown in Figure 7.18(a), submitted to a uniform pressure on its top face. The input parameters are set as: $a = 1.0$, $p = 1.0$, $E = 1.0$ and $v = 0.25$. The exact solution of strain energy is unknown for this problem, but a reference solution is available in [46], which applied Richardson's extrapolation [47] on the solutions of hexahedral super-elements. The approximation of strain energy reported in this reference is 0.950930. Another reference solution of strain energy is 0.9486 [25], which was obtained from FEM model with very fine mesh using second-order 10-node tetrahedral elements (T-10). In βFEM computations, three types of mesh structure (M1: 203 nodes and 611 elements; M2: 554 nodes and 1936 elements; and M3: 1418 nodes and 5554 elements, shown in Figure 7.18(b)) are adopted. The estimated values of energy obtained from different values of

β are plotted and compared in Figure 7.19. To approximate good results, it is noted that the parameter $\beta \in [0.6, 0.8]$ is suggested to adopt for this problem. For mesh structure M2 and M3, the close-to-reference solution can be obtained at $\beta \cong 0.7$.

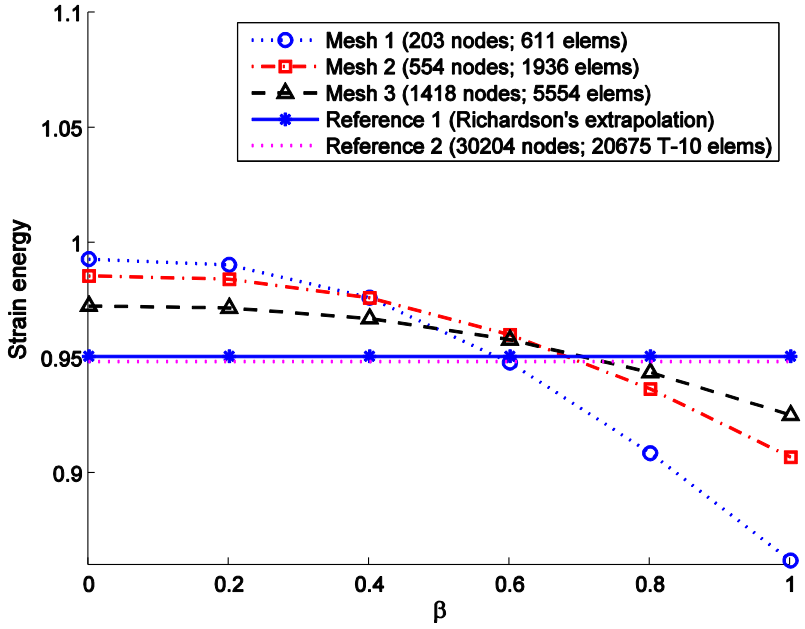

Figure 7.19. Strain energy of cubic cantilever obtained by βFEM.

7.6.6 A 3D L-shaped Block: Accuracy Study

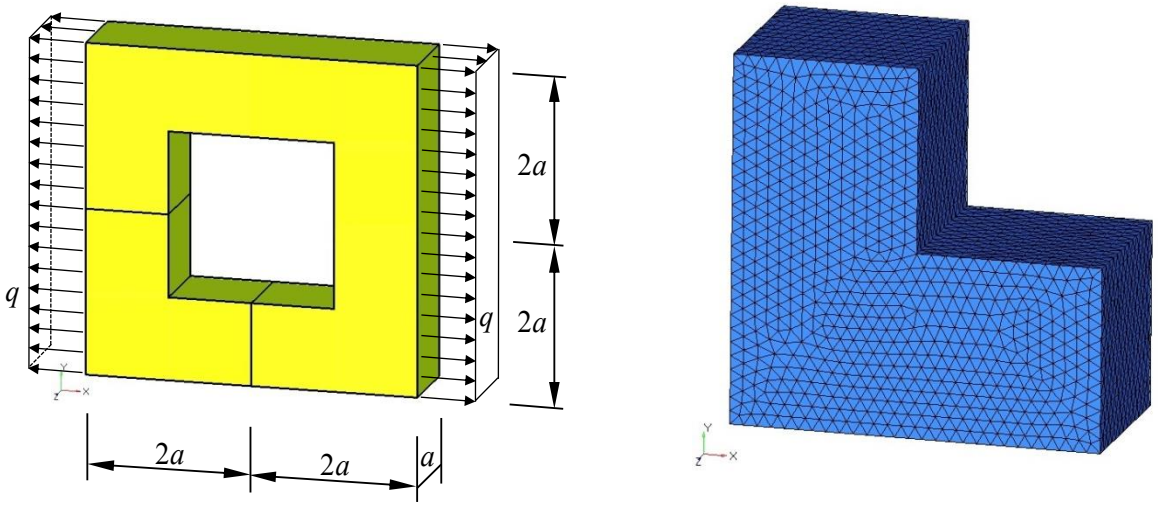

(a) (b)

Figure 7.20. A 3D L-shaped problem and its quarter model: (a) geometry and (b) a quarter model discretized by tetrahedral mesh.

Now consider a 3D square block with a rectangular parallelepiped hole illustrated in Figure 7.20(a), which is submitted to a uniform traction q on left and right side faces. Since the problem is biaxial symmetry, only a quadrant of the block (L-shaped) is modeled as shown in Figure 7.20(b). The parameters are assumed to be: $a=1.0$, $q=1.0$, $E=1.0$ and $v=0.3$. Cugnon [48] provided an approximation of the reference strain energy to be 6.19985060. The results of strain energy computed from βFEM are plotted in Figure 7.21, which indicate that the parameter $\beta \in [0.75, 0.8]$ is recommended to get the close-to-reference solutions.

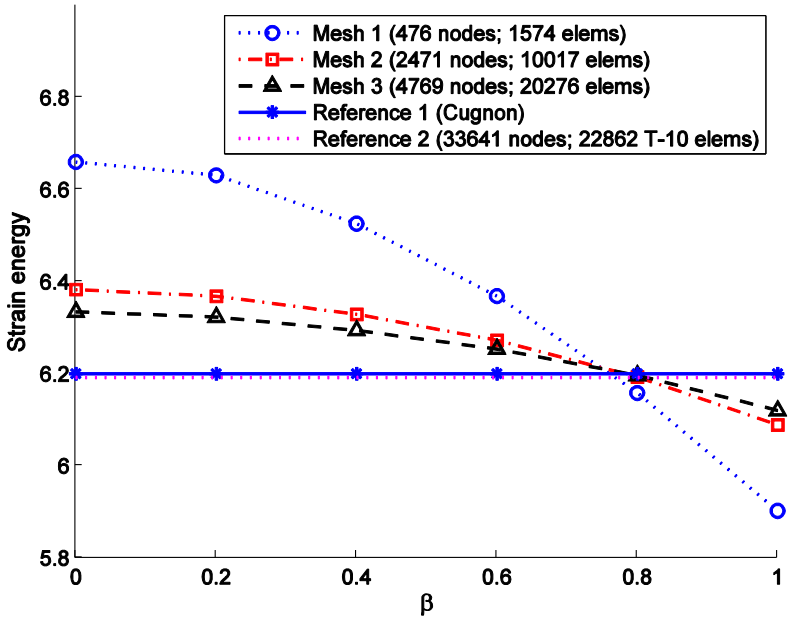

Figure 7.21. Strain energy of the 3D L-shaped problem obtained by βFEM.

7.6.7 A Molar Tooth: Analysis for Problem with Complex Geometry

In this example, a human mandibular molar tooth under vertical pressure shown in Figure 7.22 will be simulated. The aim of the present study is to show the advantage of βFEM in modeling object with moderate complex shape of geometry, since the adopted element type (tetrahedron) is the only option to discretize arbitrary irregular complex shapes. Fixed zero-displacement at the three spatial dimensions are assigned to the nodes below the horizontal plane at $z = 0.6$. As the data of true loading of mastication would be a stochastic event and will be difficult to decide, here we assume a uniformly vertical downward loading applied at the surface above the horizontal plane $z = 10.2$ (above the lowest point of top surface). The value of total force using for analysis is set to be 225 N [49]. The material is assumed to be a homogeneous

and isotropic material which has the same properties as tooth enamel: $E = 84.1\,\text{GPa}$ [50] and $v = 0.30$ [51].

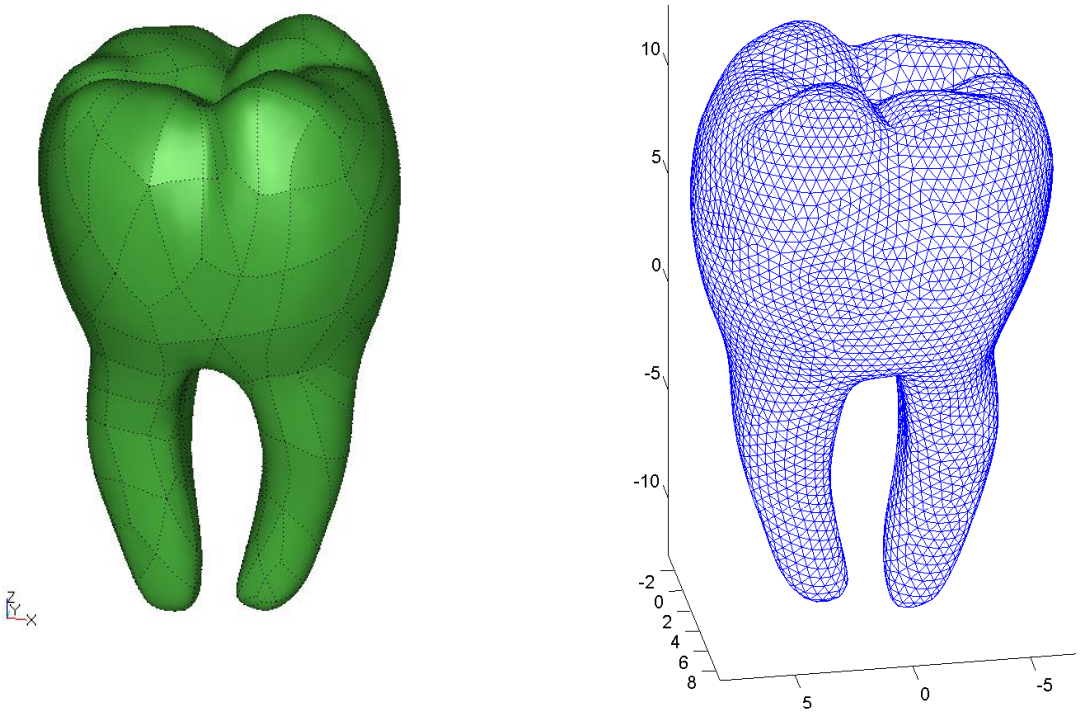

(a) (b)

Figure 7.22. A human molar tooth and its mesh: (a) geometry and (b) a model discretized by T-mesh using 33968 tetrahedral elements.

The stress distribution obtained from presented βFEM is displayed in Figure 7.23 and it is compared with the FEM result obtained from Abaqus, which utilizes the same mesh structure and loading/boundary conditions. It is noticed that the input data of this problem is simplified and some assumptions are made as the related experimental data is unknown. However, the potential use of the present method is already demonstrated for investigating the stress distribution of dental structures. And it is valuable in the field of creating patient-specific models

for clinical operations of tooth restoration and dental implants. The study here also shows the capability of our βFEM in modeling complex 3D geometry for medical applications and mimicking biological systems with irregular shapes.

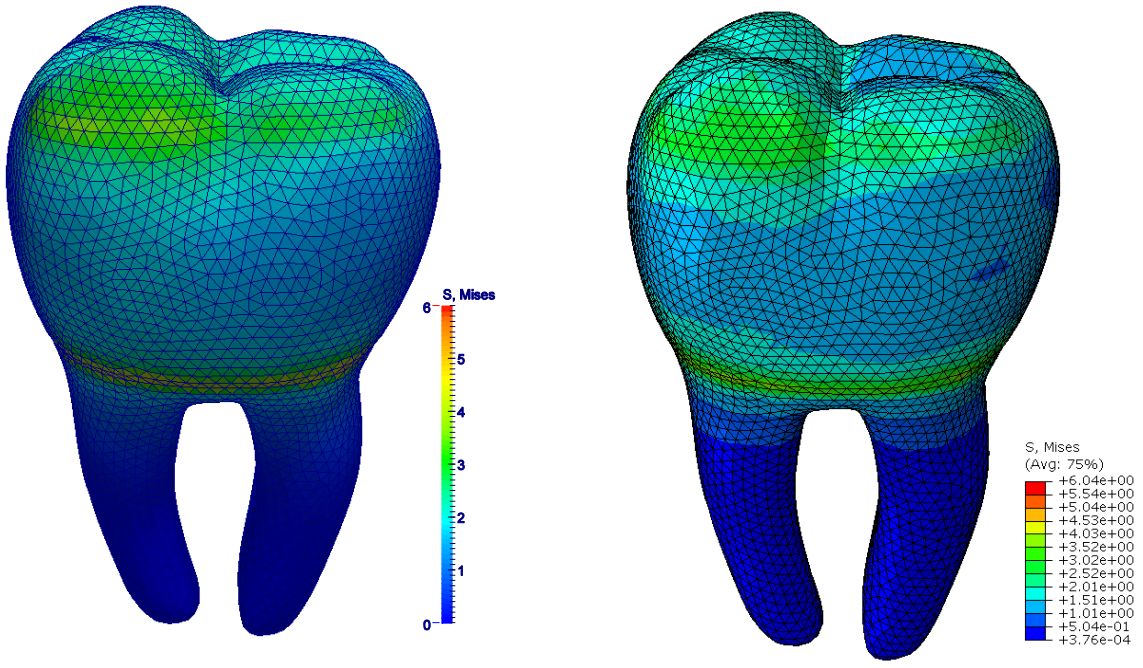

(a) (b)

Figure 7.23. Stress distribution of molar tooth models using T-mesh: (a) βFEM model and (b) FEM model by Abaqus.

7.6.8 A 3D Cantilever Beam Subjected to a Regular Distributed Load: Analysis for Large Deformation Problem

A large deformation analysis of a 3D cantilever beam is performed using βFEM in this example. The geometrical dimensions of the beam are given as: $2\text{cm}\times 2\text{cm}\times 10\text{cm}$. The beam is constrained at its left end and subjected to a regular distributed loading at its right end. The material parameters are set as $E = 30\,\text{GPa}$ and $v = 0.30$. The domain is discretized by a mesh

using 117 nodes and 298 elements. The geometrically nonlinear analysis is based on total Lagrange formulation using 10 increment steps ($\text{nsteps} = 10$) with $\Delta f = 2\,\text{kN/cm}^2$ in each step. In Figure 7.24, the initial grid and deformed final configuration for the model are shown. The tip deflections / vertical displacements (cm) at each load step obtained by different methods are compared in Table 7.5 and Figure 7.25. It is apparent in each step, the problem converges quickly as all the iterations at each step are no more than 5. Compared to linear problem, the nonlinear large deformation analysis models will be stiffer and unpliable to bend. The deflections obtained by βFEM ($\beta = 0.65$) are softer than those from FEM-T4 and FS-FEM, and they are closer to the model using eight node hexahedral elements (FEM-H8) [24] with fine mesh.

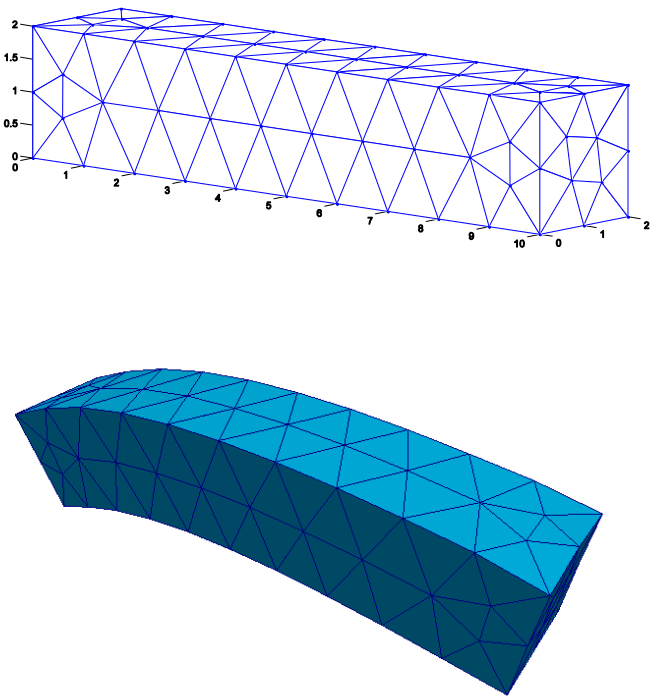

Figure 7.24. Initial mesh and deformed final configuration of the 3D cantilever beam problem obtained by βFEM based on geometrically nonlinear analysis.

Table 7.5 Tip deflections (cm) at each load step for 3D cantilever beam.

Load step (n)	FEM-T4 (linear, 1322 nodes)	FEM-T4 (nonlinear, 117 nodes)	FS-FEM (nonlinear, 117 nodes)	FEM-H8 (nonlinear, 1323 nodes)	βFEM (nonlinear, 117 nodes)
1	0.2364	0.1333 (3)*	0.1486 (3)	0.2421 (3)	0.1969 (3)
2	0.4728	0.2658 (3)	0.2962 (2)	0.4522 (3)	0.4016 (5)
3	0.7092	0.3988 (2)	0.4448 (2)	0.6405 (3)	0.6047 (3)
4	0.9456	0.5320 (2)	0.5940 (2)	0.8205 (3)	0.7985 (2)
5	1.1819	0.6641 (2)	0.7419 (2)	1.0022 (4)	0.9907 (2)
6	1.4183	0.7949 (2)	0.8880 (2)	1.1762 (4)	1.1840 (2)
7	1.6547	0.9242 (2)	1.0321 (2)	1.3495 (4)	1.3735 (2)
8	1.8911	1.0519 (2)	1.1741 (2)	1.5222 (4)	1.5590 (2)
9	2.1275	1.1779 (2)	1.3138 (2)	1.6943 (4)	1.7390 (2)
10	2.3639	1.3022 (2)	1.4510 (2)	1.8656 (4)	1.9131 (2)

* The number in the bracket is the iterations in each step.

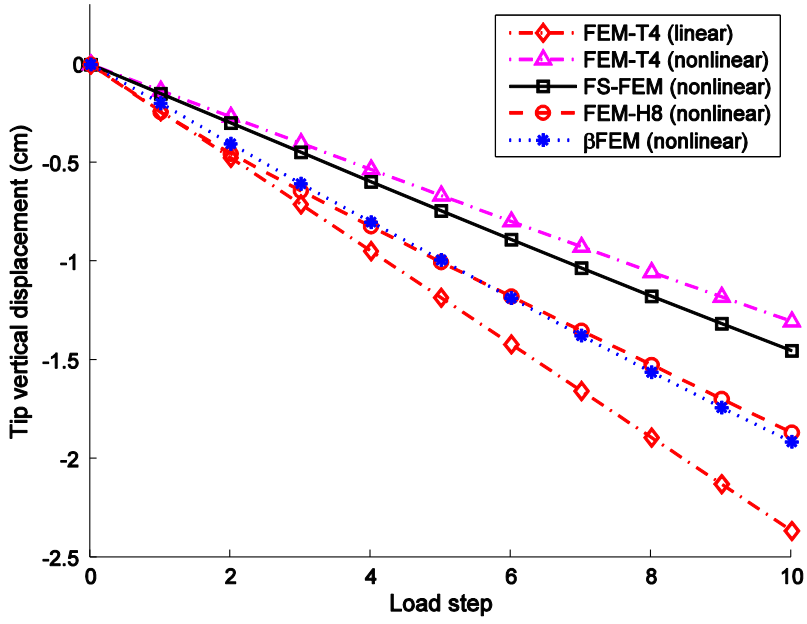

Figure 7.25. Tip deflection (cm) at each load step for the 3D cantilever beam problem.

7.7 Applications in Crystal Plasticity

The method is illustrated and verified by the (static, dynamic, linear and nonlinear) elastic problems in the previous section. This section will apply the method into nonlinear crystal plasticity problems at finite strain. In such cases, the exact solutions are usually difficult to be obtained, but the capability of this method will be shown in handling plastic incompressibility of single crystals as well as capturing strain localization phenomena. The work is based on βFEM scheme and it comprises the framework and formulations of anisotropic finite strain rate-independent single crystal plasticity model introduced in Chapter 6. The numerical procedure proposed for single crystal plasticity is carried out in several examples (1, 2, and 3) with the planar slip models for single crystals in the context of rate-independent localization computations. The proposed method and algorithms are also applied to model the mechanical behavior of bicrystal and polycrystalline aggregate in the last two examples.

7.7.1 Planar Tension of Single Crystal with Symmetric Localization

In this example sketched in Figure 7.26, we consider the localization of a rectangular single crystal strip under plane strain conditions, which has been studied using ES-FEM in previous chapter (Section 6.5.1). The material parameters for calculation are set to be the same as the ES-FEM. The initial crystallographic orientation of the first slip plane is assumed to be $\theta_0 = 30.0°$ w.r.t the horizontal direction and the angle between the second slip system and the first one is $\phi_0 = 120.0°$, i.e., the crystal lattice is oriented symmetrically with respect to the axis of tension. In Section 6.5.1, the maximum stretching at both ends by ES-FEM is $\Delta D = 5.0\,\text{mm}$. In this example studied by βFEM, the specimen is able to be deformed up to a prescribed elongation of $\Delta D = 5.5\,\text{mm}$ at both ends in the horizontal direction. In order to trigger the

localization of the geometrically perfect specimen, a material imperfection is assumed in the center of the specimen as shown in Figure 7.26. Again by exploiting the symmetry along the centerlines of the specimen, only one quadrant of the specimen subjected to appropriate boundary conditions is modeled and analyzed.

To implement the simulation by βFEM, the domain is discretized with a base mesh of constant strain triangle elements (CST or T3), and then followed by the construction of strain smoothing domains for βFEM as illustrated in Figure 7.3. Without loss of generality, here the specimen utilizes free unstructured mesh with 4×709 triangle elements for coarse mesh model (Figure 7.27(a)) and 4×2426 elements for fine mesh model (Figure 7.27(b)). In this example, the performance of proposed formulations and algorithms implemented using βFEM is compared with standard FEM based on the same initial fine mesh plotted in Figure 7.27(b). Figure 7.27(c), (d) and (e) plot the shear stresses on deformed configurations simulated by FEM at the elongation length of $\Delta D = 4.0, 4.5, 5.0$ mm ($2\Delta D/W = 13.333\%, 15.000\%, 16.667\%$). Figure 7.27(f), (g), (h) and (i) plot the corresponding shear stresses on deformed configurations simulated by βFEM at the stage $\Delta D = 4.0, 4.5, 5.0, 5.5$ mm. Apparently the FEM model is not able to reflect the evident phenomena of strain localization when the specimen stretched up to $\Delta D = 4.0$ mm as shown in Figure 7.27(c). Actually it can be regarded as an essentially homogeneous deformation mode. Moreover, it fails to model the shear bands for the elongation $\Delta D = 4.5$ mm shown in Figure 7.27(d). Two crossed shear bands are observed in final configuration plotted in Figure 7.27(e), but they are not fully developed compared to references [52,53]. While the shear stresses and deformation in Figure 7.27(f) simulated by βFEM using a same structure of mesh depicts the formation of shear bands starting at least from $\Delta D = 4.0$ mm. Figure 7.27(g) and (h) shows the ongoing deformation of shear band mode and the final

configuration is depicted in Figure 7.27(i), which highlights a pair of symmetric crossed shear bands with the cross angle of about $102.6°$, i.e., the slip direction rotates from the initial angle $30.0°$ to $38.7°$. Large deformation/strain occurs within elements along the shear band and this evolution of distributions also matches some available references [52,54–57]. Therefore, the proposed βFEM has proved to be successful for modeling the shear bands development and strain localization in this numerical example.

Figure 7.28 plots the edge loading of specimen against the associated deflection. The βFEM adopts a coarse mesh model shown in Figure 7.27(a) and a fine mesh model shown in Figure 7.27(b). The loading increases slowly after a yield point and it continues to rise along the increasing deformation until it reaches the maximum point at about $\Delta D = 3.83\,\text{mm}$. After this peak point, it decreases with unstable phenomenon occurs, which is caused by the rather abrupt rotation of the crystal lattice along the shear bands in softer orientation geometrically. In the increasing stage, the differences of three curves are not evident. However, the βFEM models using both coarse mesh and fine mesh behave softer than FEM model using fine mesh during the load dropping/necking stage. This is consistent with the onset of localized shear band development indicated in Figure 7.27(f). The mesh sensitivity study of βFEM shows that the loading are almost identical before the beginning of reaction descending stage, and the variance along the droping stage is also smaller than references [52,57]. This demonstrates the high accuracy of the exponential map-based integration scheme which we exploited. It is also necessary to know that the βFEM model with fine mesh behaves slightly softer than the coarse one during the necking stage of specimen.

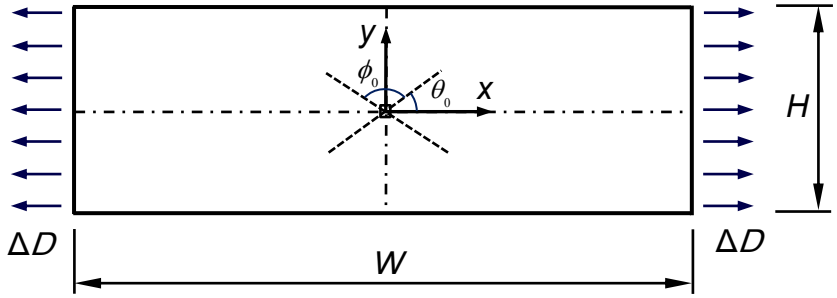

Figure 7.26. Geometry and mechanical boundary condition for planar double-slip crystal specimen with symmetric initial crystallographic orientations.

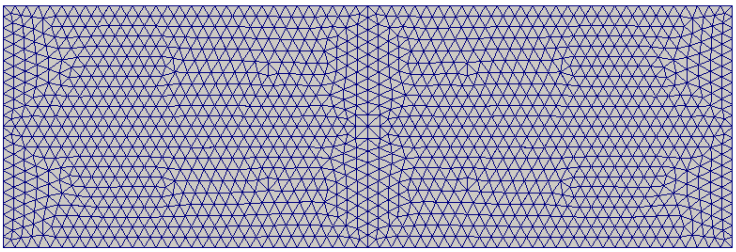

(a)

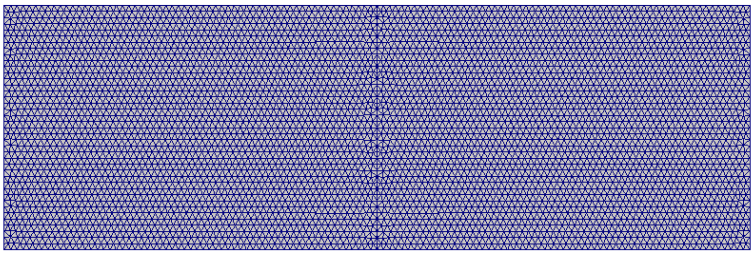

(b)

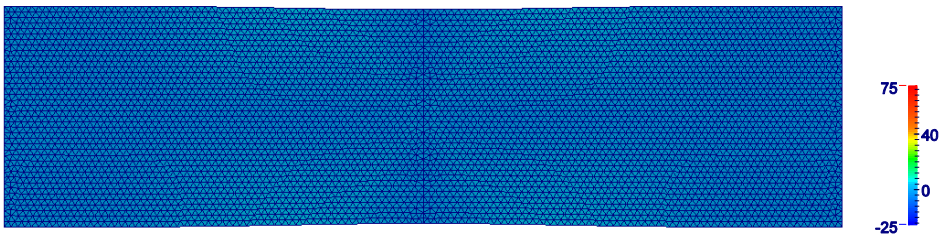

(c)

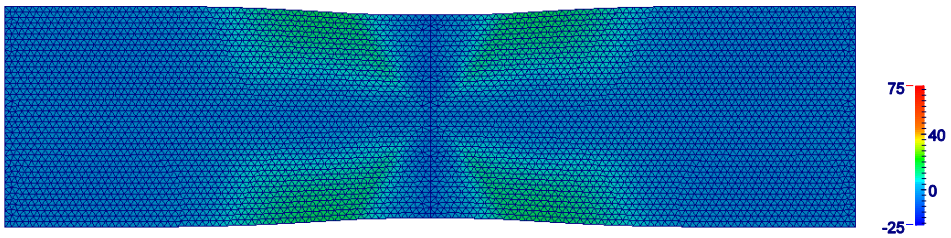

(d)

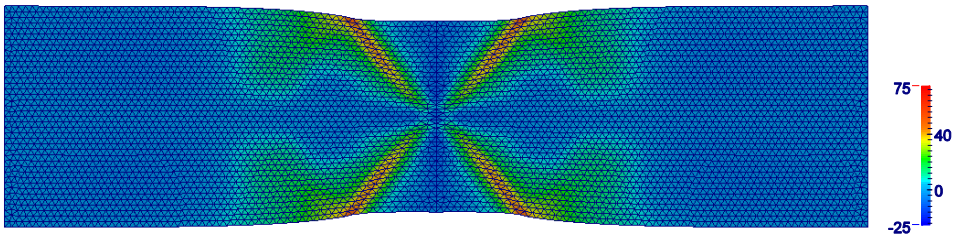

(e)

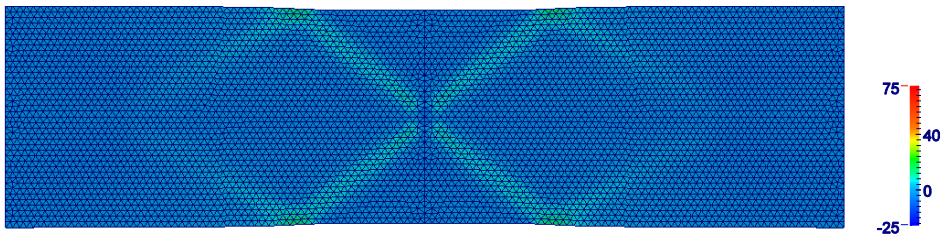

(f)

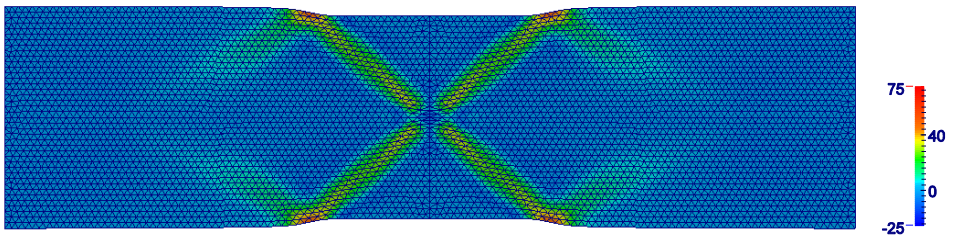

(g)

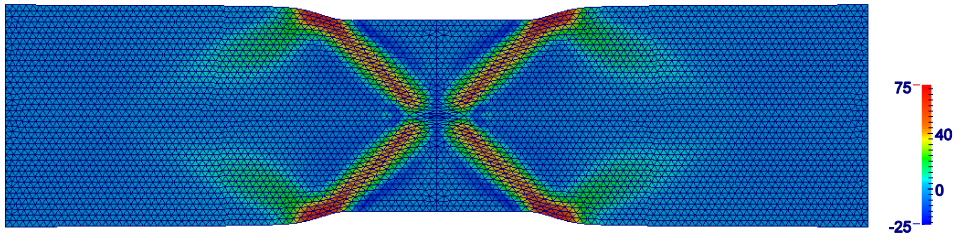

(h)

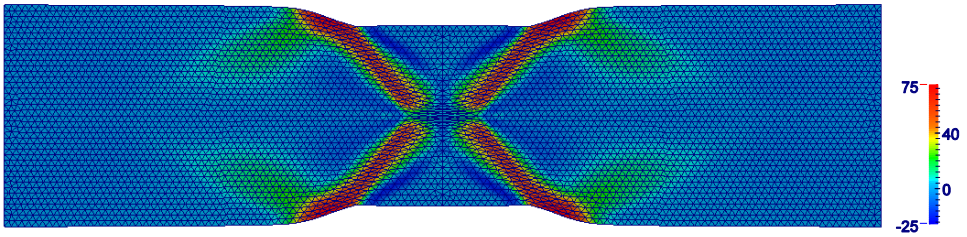

(i)

Figure 7.27. Initial mesh and shear stresses on deformed configuration for numerical models: (a) and (b) domain discretization by a basic unstructured mesh with 4×709 elements and 4×2426 elements, respectively; (c), (d) and (e) show the shear stresses on deformed configurations simulated by FEM at the elongation stage of $\Delta D=4.0$ mm, $\Delta D=4.5$ mm and $\Delta D=5.0$ mm, respectively; (f), (g), (h) and (i) show the shear stresses on deformed configurations simulated by βFEM at the elongation stage of $\Delta D=4.0$ mm, $\Delta D=4.5$ mm, $\Delta D=5.0$ mm and $\Delta D=5.5$ mm, respectively.

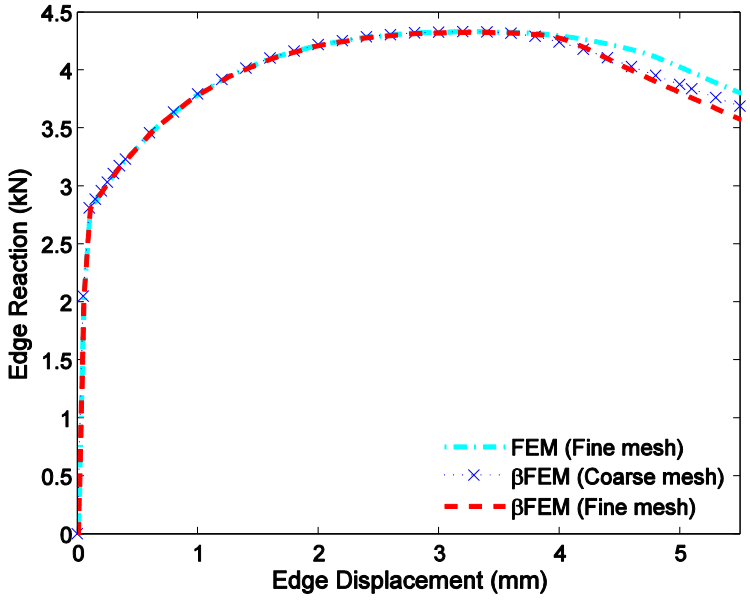

Figure 7.28. The edge reactions against the elongation of prescribed edge.

7.7.2 Tension of a Crystal Strip with Initial Edge Imperfection

We now consider the localization of a rectangular strip with different arrangements of the internal structure, which are characterized by the initial orientations under plane strain conditions. The geometrical dimensions of the strip sample are characterized by the relation $\text{width}/\text{length} = 6\text{mm}/15.4\text{mm}$. An initial geometrical imperfection as a square hole with $\text{size} = 0.3\text{mm}$ on the center of left-hand side of the specimen is used to initiate shear bands by concentrating the stress in its vicinity, which is depicted in Figure 7.29(a). In a displacement-controlled numerical test the specimen is deformed by a prescribed vertical elongation 1.54mm at both top and bottom ends. The initial crystallographic orientation angles for two slip systems in three strip samples are set to be $+60°/-60°$, $+75°/-45°$, and $+45°/-75°$, respectively. In Figure 7.29(b), (c) and (d), the orientations of the localized bands of stress depend on the

arrangement of the initial internal structure, i.e., the initial crystallographic orientation angles in this example. In all samples we have observed the patterns with slip bands development or stress concentrations. The first sample in Figure 7.29(b) leads to two slip bands which are emanated from the initial geometrical imperfection and approximately orientated under ±46.6° w.r.t. the horizontal axis ($\Delta D = 1.309\text{mm}$). The second and third samples have bands with stress concentration on the final deformed configuration. However, it seems the shear bands are hard to be formed and developed for the sample with unsymmetric slip systems (w.r.t. horizontal axis or loading direction), compared to the sample with symmetric lattice orientations. In this example, the comparison study reveals the fact that the crystal matter is mechanically anisotropic as its deformation patterns depend on the direction of mechanical loading. This is associated with the internal crystal structure and the orientation dependence of the activation of the crystallographic deformation mechanisms.

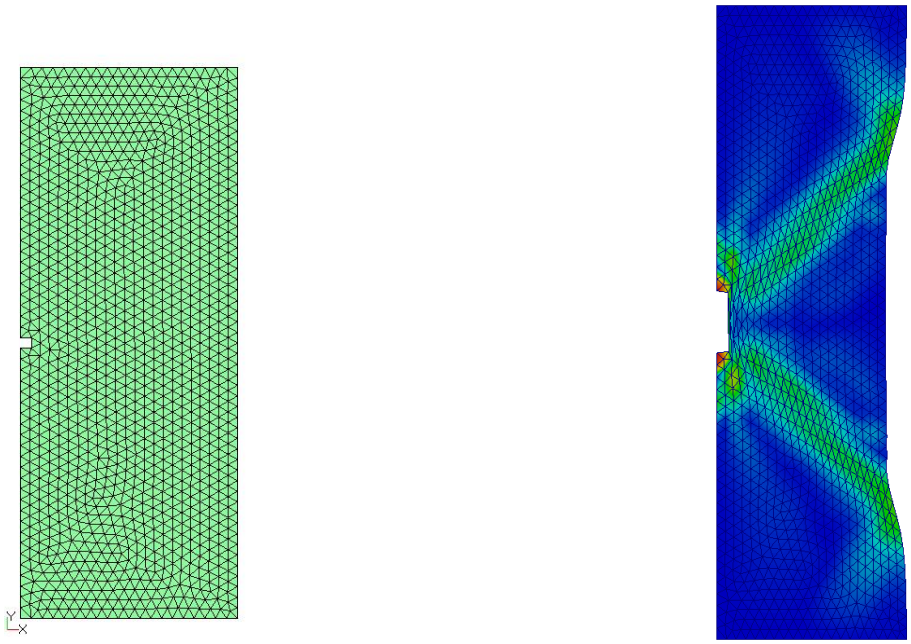

(a) (b)

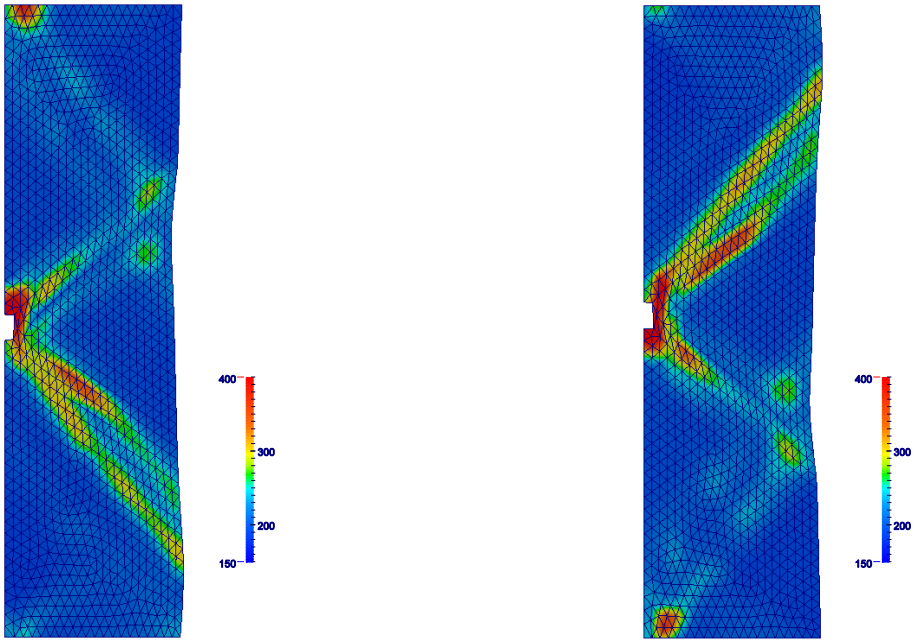

(c) (d)

Figure 7.29. Tension of a crystal strip with initial edge imperfection: (a) initial mesh; and shear stress on deformed configuration when: (b) $\theta_0 = 60°$; (c) $\theta_0 = 75°$; and (d) $\theta_0 = 45°$.

7.7.3 Necking of a Single Crystal Strip in Tension

This benchmark of crystal plasticity concerns the necking of an f.c.c. single crystal strip when the double slip systems are not symmetrically disposed about the loading axis. The geometrical dimensions of the specimen are characterized by the relation $W/H = 20\text{mm}/60\text{mm}$, which are depicted in Figure 7.30(a). The top and bottom edges are constrained the contraction along the horizontal direction. And we prescribe the vertical displacement on both ends with the elongation up to $\Delta D = 8.0\,\text{mm}$ ($2\Delta D/H = 26.667\%$). The material parameters are the same as in the previous example. The initial lattice orientation angle is assumed to be $\theta_0 = 45.0°$ w.r.t the horizontal direction and the relative angle between the slip systems is $\phi_0 = 60.0°$. The crystalline

orientations are then asymmetrical w.r.t the vertical axis and the entire specimen should be discretized. Herein the material imperfection for triggering the localization is no longer required. Similar problem has been studied in [58] using *Q1*/*P0*-type finite elements for same geometry with free contraction of the ends. In Figure 7.30(b), the deformed configuration remains in an essentially homogeneous deformation mode when the ends are stretched up to $\Delta D = 4.0\,\text{mm}$. The developments of the shear band are depicted in Figure 7.30(c), (d) and (e). In contrast to the first crystal example, which results in the symmetrical shear bands, this example shows the development of necking with an asymmetrical shear band due to its priori unsymmetrical slip systems. In the final configuration depicted in Figure 7.30(e), a strong localization and associated softening along the narrow shear band shows that plastic flow has localized on the one of the slip planes. As we know, the standard FEM with distorted mesh during the large deformation procedure may lead to relatively or even dramatically poor results and sometimes is computationally infeasible (e.g., this example). While the proposed βFEM used in this example is successfully modeled the strain localization accompanied with large shear deformation in a narrow band, which reflects its feature of insensitivity for large mesh distortion problems. The βFEM can then be a promising tool to treat the similar problems of strain localization due to its advantages to avoid volumetric locking without using special elements [53,58] or increasing the degrees of freedom of a system.

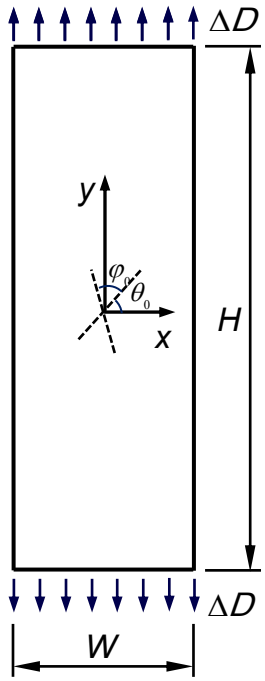

(a)

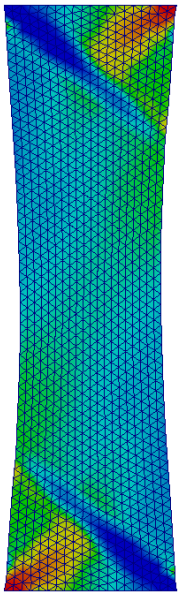

(b)

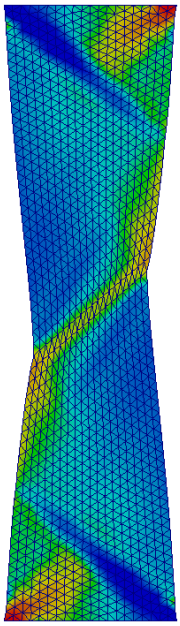

(c)

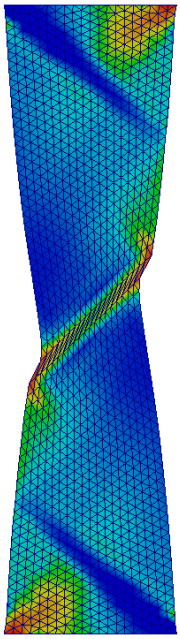

(d)

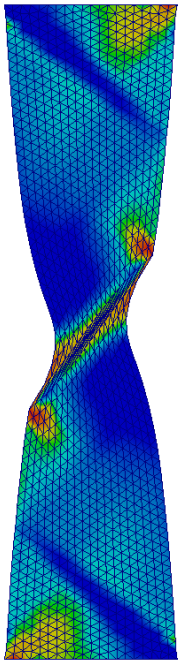

(e)

Figure 7.30. Asymmetrical localization of a crystalline strip in tension: (a) geometrical dimensions initial crystal orientation; (b) shear stress distribution on deformed configuration at the stage of $\Delta D = 4.0$ mm; (c) $\Delta D = 5.75$ mm; (d) $\Delta D = 6.5$ mm; (e) final deformed configuration at $\Delta D = 8.0$ mm.

7.7.4 Deformation of a Bi-crystal

In Figure 7.31(a), a bi-crystal strip, which is made up of two adhered parts with identical geometrical dimensions, is discretized by triangular mesh with 2236 elements. The initial geometry of the problem is set as: 80×35. The left end of specimen is clamped at both horizontal and vertical directions. The strip is stretched up to $\Delta D = 9.6$ at the right side end, which is constrained in vertical direction. The initial crystallographic orientation angle is chosen to be $\theta_0^L = 45.0°$ for the left crystal and $\theta_0^R = 15.0°$ for the right crystal w.r.t the horizontal direction. The angle between the slip systems remains $60.0°$. Here we assume the grain boundary between the two crystals is perfect, without any possibility of glide or separation. Figure 7.31(b) and (c) show the spatial distribution of shear band and shear stress in the bi-crystal. Obviously the initiation locations of the shear band are clearly at the constrained left corner and the junction at the top edge, i.e., the locations with possible stress concentrations. The stress is certainly higher in the shear band areas. For example, a band of concentrated stress in the left-side crystal develops with an orientation of approximately 38° in Figure 7.31(b) w.r.t. the horizontal axis of the strip. While the requirement of bi-crystal compatibility at the grain boundary hardens the right bi-crystal, as long as the slip systems themselves harden with continuing deformation.

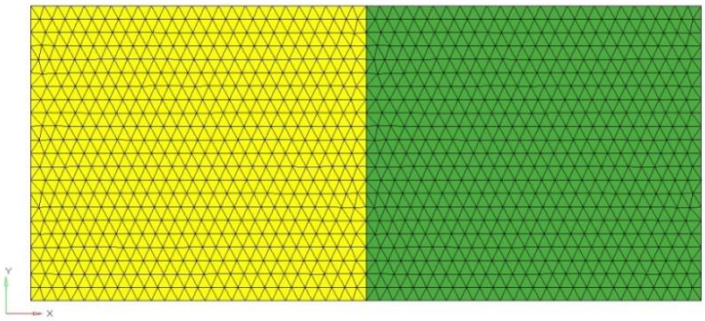

(a)

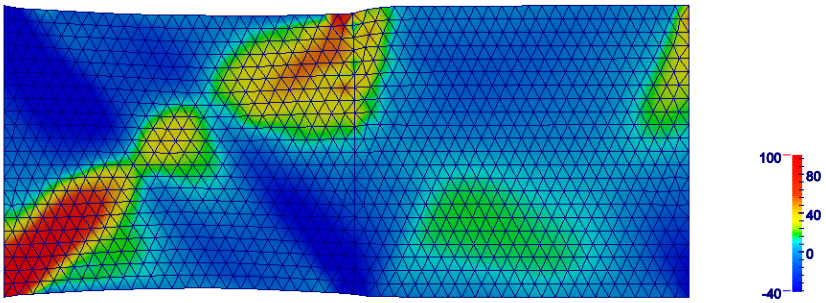

(b)

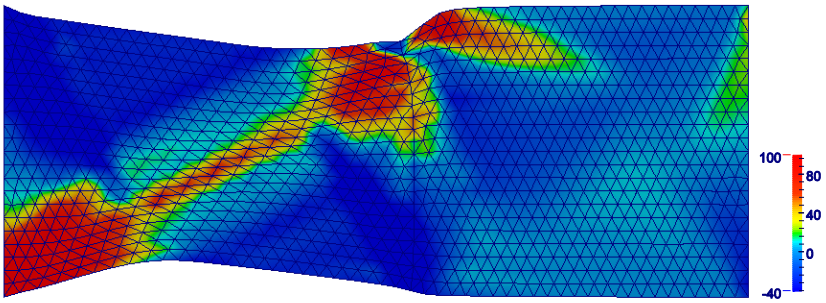

(c)

Figure 7.31. Deformation and distribution of shear stress of a bi-crystal strip in tension: (a) initial mesh; (b) shear stress on deformed configuration after an extension of 3% ; (b) shear stress on deformed configuration at a final extension of 12% .

7.7.5 Simulation of Polycrystalline Plasticity

The crystal plasticity is also extendable to predict the behavior of the polycrystalline aggregate from the behaviors of individual grains. Synthetic polycrystalline plasticity models can be generated using stochastic methods such as Voronoi tessellation [59–62], which is able to treat the mesoscopic features, including representing the realistic morphology of the grains. In this example, we focus on the effective polycrystalline behavior which is derived from inelastic material behavior of the basic constituents (e.g., monocrystals). The βFEM using T-elements is utilized to obtain numerical solutions of strain and stress fields, which involve crystalline slip dominated inelastic behavior under large strain scheme. We anticipate it can predict the heterogeneous stress distribution inside individual grains and the overall properties of polycrystals. The Voronoi Tessellation (VT) [63] is employed to build a random polycrystalline structure for the numerical example. In Figure 7.32(a), a schematic diagram of the specimen with the dimension $W = 100\,\mu\text{m}$ and $H = 30\,\mu\text{m}$ under the constraints is illustrated. A representative microstructure with 200 random grain cells by VT is plotted in Figure 7.33(a). Figure 7.33(b) illustrates the domain discretization using triangle elements for virtual grain microstructures in Figure 7.33(a), where varied colors relate to a number of random lattice orientations of grains. The specimen can then be viewed as an aggregation of randomly orientated monocrystals which accommodate the associated continuous deformation.

Other than quadrilateral elements, discretization of the Voronoi polygons into triangular finite elements is straightforward. Unfortunately, the computational accuracy of triangular finite elements is generally poor [64]. However, the proposed βFEM using triangular elements can achieve high accuracy compared to FEM using quadrilateral elements, or even other S-FEM methods. In this example, the Voronoi polygons plotted in Figure 7.33(a) is discretized into

2674 elements. To implement the numerical computation, a displacement controlled loading with a final 15% of nominal strain has been applied in the horizontal direction. Figure 7.33(c) shows the equivalent stress of specimen on deformed configuration for polycrystalline microstructures with 200 grains shown in Figure 7.33(b). The local equivalent stresses are up to about 600% of macroscopic nominal equivalent stress. The stress varies considerably at some grain boundaries, which is mainly resulted from the incompatible deformation of associated contiguous grains. The diagram of stress distributions clearly show the stress and locations of stress concentration varying from grain to grain. Therefore, the local fields of stress and deformation reflect the extreme inhomogeneity of mechanical property of polycrystalline aggregates at mesoscale level. Figure 7.34 depicts the macroscopic equivalent stress-strain curves associated with the microstructures with 200 grains (Figure 7.33(a)) and 50 grains. Compared to the single crystal example, the curves are not so smooth after the maximum loading. This is essentially due to the non-uniform grain microstructures and non-concurrent onset of localization. The regular localized shear band development in single crystals is also blocked under the compatibility conditions between irregular/complex grain boundaries. It is also interesting to note that the strength of aggregates with 200 grain cells behaves a little higher than the one with 50 cells, though simulations exhibit similar macroscopic responses under monotonic tensile loading condition. This phenomenon of macroscopic overall response shows the analyzed aggregates with more grains will be effected less from local heterogeneity and then own a good performance of homogenized properties.

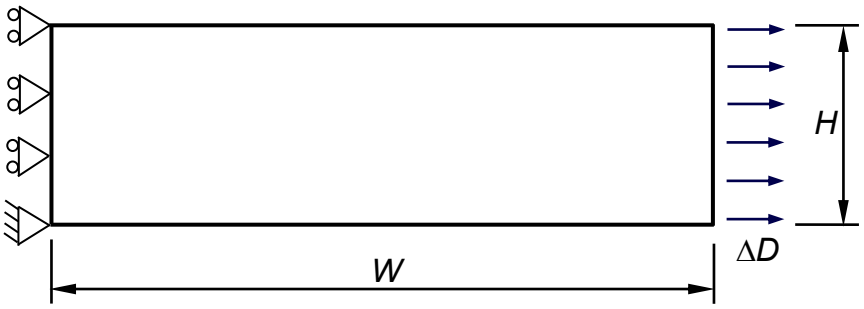

Figure 7.32. Geometry and boundary condition for a polycrystalline specimen.

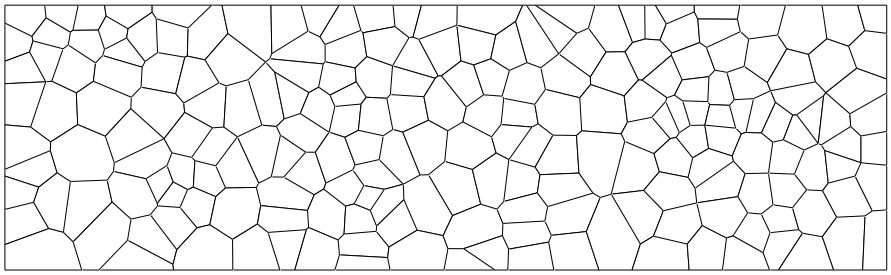

(a)

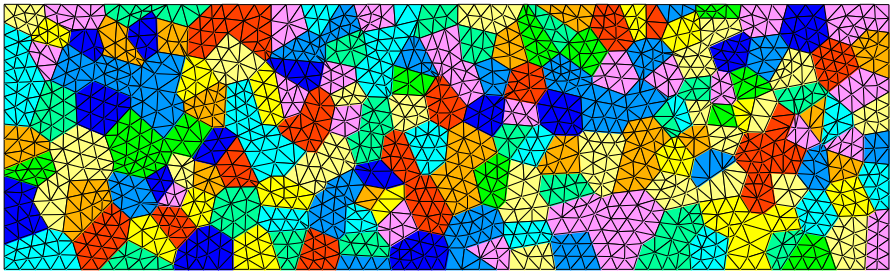

(b)

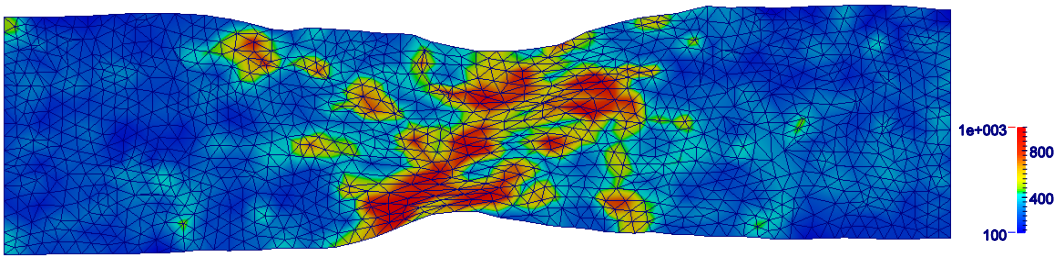

(c)

Figure 7.33. Mesoscopic microstructure representation and stress distribution: (a) Voronoi tessellation of the polycrystalline structure with random lattice orientations of grains; (b) mesh discretization using triangular elements; (c) stress distribution under tension.

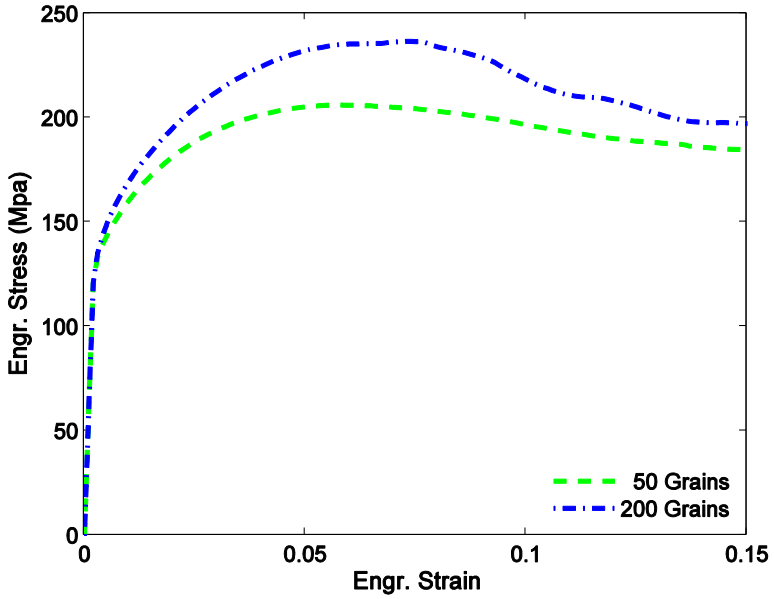

Figure 7.34. The engineering stress-strain curves for two different microstructures with 50 and 200 grain cells.

7.8 Conclusion Remarks

In this work, a novel smoothed technique based beta finite element method (βFEM) has been developed and applied for both 2D and 3D solid mechanics problems. For βFEM, smoothing domains generated from both edge-based (2D)/face-based (3D) and node-based strain smoothing techniques are employed to construct a smoothed model. A key aspect of the method is that it inherits the features of both ES-FEM/FS-FEM and NS-FEM. Standard patch tests are likewise satisfied. Through the present framework of formulations and numerical discussions by

examples, the major characteristics of the proposed method has been demonstrated and verified, including high accuracy, insensitivity to mesh quality or distortion, immunity or alleviation of volumetric locking, temporal stability and capability for modeling objects with complex geometry. After numerical investigation of accuracy and volumetric locking in elastic problem, the method is then performed to model rate-independent planar crystal plasticity problems, including single crystal, bi-crystal and polycrystalline structures. From these studies, some remarks can be concluded as following:

(1) An adjustable parameter β controls the portion of area of edge-based/face-based and node-based smoothing domains. In the context of elasticity, it is promising to find nearly exact solution in strain energy due to solution shifting by tuning the adjustable parameter, since the exact solution would be within the narrow interval bounded by the solutions of βFEM with $\beta = 0$ and $\beta = 1$.

(2) The method can be immune from volumetric locking and no special treatments are required for solids of nearly incompressible materials. This feature is inherited from NS-FEM by properly choosing the parameter β of βFEM, and the ES-FEM/FS-FEM may not possess this property due to its inherent features.

(3) Temporal instability and spurious modes existed in NS-FEM can be eliminated by proposed βFEM model with a proper parameter β. However, the effective way to find such a parameter needs to be further studied.

(4) The method is effective in analysis of solid mechanics problems for both linear and geometrically nonlinear cases.

(5) Due to the fact that tetrahedral mesh can be efficiently generated for complex geometry using fully automatic procedure, the method has a lot of potential and capabilities for applications in areas with complex shapes (such as biomedical, automotive, and aerospace engineering) as it is essentially the T-mesh based algorithms.

(6) Numerical results of modeling crystal plasticity attest the capabilities of treating plastic incompressibility and volumetric locking. The phenomena of strain localization and shear band development show good agreement with literatures, in which some special elements such as *Q1E4* elements, *Q1/P0* elements or *F*-bar elements are utilized to capture strain localization phenomena and handle geometric nonlinearity at large deformation. We conclude the reason essentially is that our βFEM models, even with a basic T-mesh of linear elements, have the important property of softening effects compared with the corresponding FEM models. On the other hand, because of the absence of isoparametric mapping enabled by the strain smoothing operation, βFEM models are less sensitive to the quality of the grid configuration, even for severely distorted mesh during the large deformation process.

(7) The proposed method and algorithms are also applied to simulate a bi-crystal specimen and polycrystalline aggregates. Numerical results demonstrated that the method along with the numerical framework is performed successfully for the predictions of the anisotropic deformation and elastoplastic behaviors of bi-crystal and polycrystalline grain structure.

References

[1] Liu GR and Quek SS. 2013. The Finite Element Method: A Practical Course, 2nd edition. Butterworth-Heinemann, Oxford.

[2] Onishi Y and Amaya K. 2014. A locking-free selective smoothed finite element method using tetrahedral and triangular elements with adaptive mesh rezoning for large deformation problems. International Journal for Numerical Methods in Engineering; 99(5): 354–371.

[3] Allman DJ. 1984. A compatible triangular element including vertex rotations for plane elasticity analysis. Computers and Structures; 19(2): 1–8.

[4] Allman DJ. 1988. Evaluation of the constant strain triangle with drilling rotations. International Journal for Numerical Methods in Engineering; 26(12): 2645–2655.

[5] Chen HC. 1992. Evaluation of allman triangular membrane element used in general shell analyses. Computers and Structures; 43(5): 881–887.

[6] Huang M, Zhao Z, and Shen C. 2010. An effective planar triangular element with drilling rotation. Finite Elements in Analysis and Design; 46: 1031–1036.

[7] Piltner R. and Taylor RL. 2000. Triangular finite elements with rotational degrees of freedom and enhanced strain modes. Computers and Structures; 75: 361–368.

[8] Bergan PG and Felippa CA. 1985. A triangular membrane element with rotational degrees of freedom. Computer Methods in Applied Mechanics and Engineering; 50: 25–69.

[9] Cook RD. 1991. Modified formulations for nine-DoF plane triangles that include vertex rotations. International Journal for Numerical Methods in Engineering; 31: 825–835.

[10] Dohrmann CR, Key SW, Heinstein MW, and Jung J. 1998. A least squares approach for uniform strain triangular and tetrahedral finite elements. International Journal for Numerical Methods in Engineering; 42: 1181–1197.

[11] Dohrmann CR, Heinstein MW, Jung J, and Key SW, Witkowski WR. 2000. Node-based uniform strain elements for three-node triangular and four-node tetrahedral meshes. International Journal for Numerical Methods in Engineering; 47: 1549–1568.

[12] Hong WI, Kim YH, and Lee SW. 2001. An assumed strain triangular solid shell element with bubble function displacements for analysis of plates and shells. International Journal for Numerical Methods in Engineering; 52(4): 455–469.

[13] Liu GR, Nguyen-Thoi T, Dai KY, and Lam KY. 2007. Theoretical aspects of the smoothed finite element method (SFEM). International Journal for Numerical Methods in Engineering; 71(8): 902–930.

[14] Nguyen-Thoi T, Liu GR, Dai KY, and Lam KY. 2007. Selective smoothed finite element method. Tsinghua Science and Technology; 12(5): 497–508.

[15] Liu GR, Nguyen-Thoi T, and Lam KY. 2009. An edge-based smoothed finite element method (ES-FEM) for static, free and forced vibration analyses in solids. Journal of Sound and Vibration; 320: 1100–1130.

[16] Liu GR, Dai KY, and Nguyen-Thoi T. 2007. A smoothed finite element for mechanics problems. Computational Mechanics; 39(6): 859–877.

[17] Zeng W, Liu GR, Kitamura Y, and Nguyen-Xuan H. 2013. A three-dimensional ES-FEM for fracture mechanics problems in elastic solids. Engineering Fracture Mechanics; 114: 127–150.

[18] Liu GR, Nguyen-Thoi T, and Lam KY. 2009. A node-based smoothed finite element method for upper bound solution to solid problems (NS-FEM). Computers and Structures; 87: 14–26.

[19] Liu GR, Zeng W, and Nguyen-Xuan H. 2013. Generalized stochastic cell-based smoothed finite elementmethod (GS_CS-FEM) for solid mechanics. Finite Elements in Analysis and Design; 63: 51–61.

[20] Tang LM, Chen WJ, and Liu XY. 1983. String net function approximation and quasi-conforming technique. In Hybrid and Mixed Finite Element Methods, Chapter 9, Atluri SA et al. (eds). Wiley: New York.

[21] Chen JS, Wu CT, Yoon S, and You Y. 2001. A stabilized conforming nodal integration for Galerkin mesh-free methods. International Journal for Numerical Methods in Engineering; 50(2):435–466.

[22] Hu M, Liu MB, Xie MW, and Liu GR. 2015. Three-dimensional run-out analysis and prediction of flow-like landslides using smoothed particle hydrodynamics. Environmental Earth Sciences; 73(4): 1629–1640.

[23] Yoo JW, Moran B, and Chen J-S. 2004. Stabilized conforming nodal integration in the natural-element method. International Journal for Numerical Methods in Engineering; 60(5): 861–890.

[24] Liu GR and Nguyen-Thoi T. 2010. Smoothed Finite Element Methods. CRC Press, Taylor and Francis Group: New York.

[25] Nguyen-Thoi T, Liu GR, and Lam KY. 2009. A face-based smoothed finite element method (FS-FEM) for 3D linear and nonlinear solid mechanics problems using 4-node tetrahedral elements. International Journal for Numerical Methods in Engineering; 78: 324–353.

[26] Dai KY and Liu GR. 2007. Free and forced vibration analysis using the smoothed finite element method (SFEM). Journal of Sound and Vibration; 301(3–5): 803–820.

[27] Chen L, Liu GR, Nourbakhsh-Nia N, and Zeng K. 2010. A singular edge-based smoothed finite element method (ES-FEM) for bimaterial interface cracks. Computational Mechanics; 45(2-3): 109–125.

[28] Jiang Y, Liu GR, Zhang YW, Chen L, and Tay TE. 2011. A singular ES-FEM for plastic fracture mechanics. Computer Methods in Applied Mechanics and Engineering; 200(45): 2943–2955.

[29] Liu GR and Zhang GY. 2008. Upper bound solution to elasticity problems: A unique property of the linearly conforming point interpolation method (LC-PIM). International Journal for Numerical Methods in Engineering; 74: 1128–1161.

[30] Jiang C, Liu GR, Han X, Zhang ZQ, and Zeng W. 2015. A smoothed finite element method for analysis of anisotropic large deformation of passive rabbit ventricles in diastole. International Journal for Numerical Methods in Biomedical Engineering; 31(1): e02697 (1–25).

[31] Nguyen-Thoi T, Liu GR, and Nguyen-Xuan H. 2009. Additional properties of the node-based smoothed finite element method (NS-FEM) for solid mechanics problems. International Journal of Computational Methods; 6(4): 633–666.

[32] Liu GR, Nguyen-Xuan H, and Nguyen-Thoi T. 2010. A theoretical study on the smoothed FEM (S-FEM) models: Properties, accuracy and convergence rates. International Journal for Numerical Methods in Engineering; 84(10): 1222–1256.

[33] Liu GR. 2010. A G space theory and a weakened weak (W2) form for a unified formulation of compatible and incompatible methods: Part I theory. International Journal for Numerical Methods in Engineering; 81: 1093–1126.

[34] Liu GR. 2010. A G space theory and a weakened weak (W2) form for a unified formulation of compatible and incompatible methods: Part II applications to solid mechanics problems. International Journal for Numerical Methods in Engineering; 81: 1127–1156.

[35] Zhang ZQ and Liu GR. 2011. An edge-based smoothed finite element method (ES-FEM) using 3-node triangular elements for 3D non-linear analysis of spatial membrane structures. International Journal for Numerical Methods in Engineering; 86(2): 135–154.

[36] Nguyen-Thoi T, Liu GR, Vu-Do HC, and Nguyen-Xuan H. 2009. A face-based smoothed finite element method (FS-FEM) for visco-elastoplastic analyses of 3D solids using tetrahedral mesh. Computer Methods in Applied Mechanics and Engineering; 198(41–44): 3479–3498.

[37] Liu GR, Nguyen-Thoi T, and Lam KY. 2008. A novel alpha finite element method (αFEM) for exact solution to mechanics problems using triangular and tetrahedral elements. Computer Methods in Applied Mechanics and Engineering; 197 (45–48): 3883–3897.

[38] Bathe KJ. 2014. Finite Element Procedures (2nd edn). Klaus-Jürgen Bathe: Watertown, MA.

[39] De Borst R, Crisfield MA, Remmers JJC, and Verhoosel CV. 2012. Nonlinear Finite Element Analysis of Solids and Structures (2nd edn). Wiley: West Sussex, UK.

[40] Reddy JN. 2004. An Introduction to Nonlinear Finite Element Analysis. Oxford University Press: Oxford.

[41] Wu F, Liu GR, Li GY, and He ZC. 2014. A new hybrid smoothed FEM for static and free vibration analyses of Reissner–Mindlin Plates. Computational Mechanics: 1–26.

[42] Cook RD. 1974. Improved two-dimensional finite element. Journal of the Structural Division; ASCE 100 (ST6): 1851–1863.

[43] Taylor RL, Beresford PJ, and Wilson EL. 1976. A non-conforming element for stress analysis. International Journal for Numerical Methods in Engineering; 10: 1211–1219.

[44] Fredriksson M, and Ottosen NS. 2004. Fast and accurate four-node quadrilateral. International Journal for Numerical Methods in Engineering; 61: 1809–1834.

[45] Timoshenko SP. and Goodier JN. 1970. Theory of elasticity (3rd edn)., McGraw-Hill: New York,.

[46] Pereira OJBA. 2008. Hybrid equilibrium hexahedral elements and super-elements. Communications in Numerical Methods in Engineering; 24(2): 157–165.

[47] Richardson LF. 1910. The approximate arithmetical solution by finite differences of physical problems involving differential equations, with an application to the stresses in a masonry dam. Transactions of the Royal Society of London, Series A; 210: 307–357.

[48] Cugnon F. 2000. Automatisation des calculs elements finis dans le cadre de la methode-p, Universite de Lie, Ph.D. Thesis.

[49] Magne P. 2007. Efficient 3D finite element analysis of dental restorative procedures using micro-CT data. Dental Materials; 23(5): 539–548.

[50] Craig RG, Peyton FA, and Johnson DW. 1961. Compressive properties of enamel, dental cements, and gold. Journal of Dental Research; 40: 936–945.

[51] Anusavice KJ and Hojjatie B. 1988. Influence of incisal length of ceramic and loading orientation on stress distribution in ceramic crowns. Journal of Dental Research; 67: 1371–1375.

[52] Miehe C. 1996. Exponential map algorithm for stress updates in anisotropic multiplicative elastoplasticity for single crystals. International Journal for Numerical Methods in Engineering; 39: 3367–3390.

[53] de Souza Neto EA, Perić P, and Owen DRJ. 2008. Computational Methods for Plasticity: Theory and Applications. John Wiley & Sons.

[54] Peirce D, Asaro RJ, and Needleman A. 1982. An analysis of nonuniform and localized deformation in ductile single crystals. Acta Metallurgica; 30: 1087–1119.

[55] Asaro RJ and Needleman A. 1985. Overview no. 42 Texture development and strain hardening in rate dependent polycrystals. Acta Metallurgica; 33: 923–953.

[56] Rashid MM and Nemat-Nasser S. 1995. A constitutive algorithm for rate-dependent crystal plasticity. Computer Methods in Applied Mechanics and Engineering; 94: 201–228.

[57] Miehe C. 1996. Multisurface thermoplasticity for single crystals at large strains in terms of eulerian vector updates. International Journal of Solids and Structures; 33: 3103–3130.

[58] Miehe C and Schotte J. 2004. Crystal plasticity and evolution of polycrystalline microstructure, in: E. Stein, R. de Borst, T.J.R. Hughes (Eds.), in: Solid and structures, in: Encyclopedia of computational mechanics, vol. 2. John Wiley & Sons, Ltd., West Sussex, England; 267–289.

[59] Ghosh S, Lee K, and Moorthy S. 1995. Multiple scale analysis of heterogeneous elastic structures using homogenization theory and Voronoi cell finite element method. International Journal of Solids and Structures; 32: 27–62.

[60] Barbe F, Decker L, Jeulin D, and Cailletaud G. 2001. Intergranular and intragranular behavior of polycrystalline aggregates. Part 1: F.E. model. International Journal of Plasticity; 17(4): 513–536.

[61] Ghosh S. 2011. Micromechanical analysis and multi-scale modeling using the Voronoi cell finite element method. CRC Press, Taylor & Francis.

[62] Zhang P, Balint D, and Lin J. 2011. An integrated scheme for crystal plasticity analysis: Virtual grain structure generation. Computational Materials Science; 50(10): 2854–2864.

[63] Talischi C, Paulino GH, Pereira A, and Menezes IFM. 2012. PolyMesher: A general-purpose mesh generator for polygonal elements written in Matlab. Journal of Structural and Multidisciplinary Optimization; 45(3): 308–328.

[64] Kovač M and Cizelj L. 2005. Modeling elasto-plastic behavior of polycrystalline grain structure of steels at mesoscopic level. Nuclear Engineering and Design; 235: 1939–1950.

Chapter 8. Summary

From the discussions in previous chapters, S-FEM can be regarded as a special linear version of smoothed point interpolation methods, which is established using the generalized smoothed Galerkin weak form theoretically on G space theory. The objective of S-FEM is to construct numerical models with good performance under a general framework of the standard finite element method. This is achieved by the implementation of some generalized gradient smoothing operations on strains, which will alter the assumed strain field in a proper fashion. The smoothing operations in S-FEM can be performed over smoothing domains, which would be located within the elements: CS-FEM, but more often beyond elements: bringing in the information from the adjacent elements, including NS-FEM, ES-FEM and FS-FEM.

Compared to the standard linear displacement finite element method (LFEM), S-FEM can overcome some inherited drawbacks existed in LFEM, such as stress inaccuracy, sensitivity to element distortion, unstable/volumetric locking phenomena, etc. It can be seen that the class of S-FEMs has become a simple and effective tool for analysis of a few advanced types of solid mechanics problems.

The present study was motivated by the development of novel smoothing techniques based methods with better performance for computational solid mechanics. We developed S-FEM in computational mechanics with several aspects and successfully conducted numerial applications of these methods for analysis of different types of problems. These proposed methods can solve problems more accurately than conventional methods, provide alternatives to

standard FEM with easy implementation, or tackle some problems which standard linear FEM would be not able to handle. A summary of the work can be provided as following:

- The generalized stochastic cell-based smoothed finite element method (GS_CS-FEM) is proposed for stochastic analysis based on the generalized stochastic perturbation technique. Numerical examples for problems with large uncertainties are presented and the efficiency and accuracy of the GS_CS-FEM are verified by the comparison with results from Monte Carlo simulations.
- The virtual crack closure integral technique (VCCT) has been developed for evaluation of fracture mechanics parameters and simulation of crack propagation within the framework of CS-FEM. The mechanism of one-step-analysis feature of VCCT has been introduced mathematically based on the assumption that an infinitesimal perturbation of crack-tip location shall not obviously affect the stress/displacement field. In numerical examples, the comparisons of strain energy and stress intensity factors between the presented technique and conventional methods show that it is a good competitor of accuracy as FEM-Q4 with the interaction integral method. While the present scheme only employs the information of displacement openings behind the crack-tip and the nodal forces at the crack-tip, it also successfully predicts the crack growth trajectory with excellent agreement between numerical results and the experimental observations.
- A computational framework of S-FEM for modeling anisotropic crystalline plasticity has been presented to simulate the mechanical behavior of crystal materials with rate-independence. The ES-FEM technique has been extended to deal with finite strains in a nonlinear incremental integration procedure based on the Newton-Raphson scheme. The constitutive model utilizes the hyperelastic-based multiplicative plasticity framework on

the basis of the theory of crystallographic slip. The performance of the proposed formulations has been illustrated firstly in single crystal plasticity by strain localization problems. The predictions of onset of localization and successive shear band development are verified by literature with special elements such as *Q1E4* elements or *F*-bar elements. We conclude that the reason essentially is that smoothed models are able to provide a softening effect provided by the smoothing operations to the compatible FEM models. Moreover, the proposed formulations and algorithms are also implemented to explore the mesoscopic and macroscopic elaso-plastic behavior of polycrystalline aggregates through modeling the synthetic microstructure constructed by the Voronoi tessellation technique.

- Finally, a novel smoothed techniques based beta finite element method (βFEM) has been developed and applied for both 2D and 3D solid mechanics problems. Smoothing domains generated from both edge-based/face-based and node-based strain smoothing techniques are employed to construct a smoothed model. A key aspect of the method is that it inherits the features of both ES-FEM/FS-FEM and NS-FEM, such as ultra-accuracy, insensitivity to mesh quality or distortion, alleviation of volumetric locking, etc. Numerical results for 2D and 3D problems validated that the present method gives super-accurate solutions for both linear and nonlinear problems. The attractive features inherited from both ES-FEM/FS-FEM and NS-FEM have been confirmed, including high accuracy, immunity from volumetric locking, temporal stability during vibration and capability for modeling an object with complex geometry. It is argued that βFEM is a viable versatile alternative to standard FEM and possesses some promising advantages. The developed βFEM has also performed in modeling rate-independent crystal plasticity

problems. Numerical results attest to its capabilities of treating plastic incompressibility and volumetric locking. The proposed method is also implemented to mimic the mechanical behavior of polycrystalline aggregates successfully.

Journal Publications

- Zeng W, Liu GR, Nguyen-Thoi T, and Jiang C. 2015. A beta finite element method (βFEM) of coupled edge/face and node based smoothing techniques for mechanics problems. International Journal for Numerical Methods in Engineering, under review.
- Zeng W, Liu GR, Jiang C, Dong XW, Chen HD, and Jiang Y. 2015. An effective fracture analysis technique based on the virtual crack closure-integral method implemented in CS-FEM. Applied Mathematical Modelling, under review.
- Zeng W, Liu GR, Li D, and Dong XW. 2015. A smoothing technique based beta finite element method (βFEM) for crystal plasticity modeling. Computers & Structures, under review.
- Zeng W, Larsen JM, and Liu GR. 2015. Smoothing technique based crystal plasticity finite element modeling of crystalline materials. International Journal of Plasticity; 65: 250–268.
- Zeng W, Liu GR, Kitamura Y, and Nguyen-Xuan H. 2013. A three-dimensional ES-FEM for fracture mechanics problems in elastic solids. Engineering Fracture Mechanics; 114(0): 127–150.
- Liu GR, Zeng W, and Nguyen-Xuan H. 2013. Generalized stochastic cell-based smoothed finite element method (GS_CS-FEM) for solid mechanics. Finite Elements in Analysis and Design; 63: 51–61.

- Jiang C, Liu GR, Han X, Zhang Z-Q, and Zeng W. 2015. A smoothed finite element method for analysis of anisotropic large deformation of passive rabbit ventricles in diastole. International Journal for Numerical Methods in Biomedical Engineering; 31(1): e02697 (1–25).
- Dong XW, Liu GR, Li ZL, and Zeng W. 2015. Smoothed Particle Hydrodynamic (SPH) modeling of shot peening process. Modelling and Simulation in Materials Science and Engineering, under review.
- Jiang C, Zhang Z-Q, Liu GR, Han X, and Zeng W. 2015. An edge-based/node-based selective smoothed finite element method using tetrahedrons for cardiovascular tissues. Engineering Analysis with Boundary Elements; 59: 62–77.
- Chen HD, Wang Q, Liu GR, Zeng W, Sun J, He L, Bui TQ. Dynamic brittle crack propagation modeling using a five-node crack-tip singular edge-based smoothed element with local refined mesh. International Journal of Solids and Structures, under review.